ISTANBUL TECHNICAL UNIVERSITY ★ GRADUATE SCHOOL

# DESIGN AND ANALYSIS OF INTERIOR PERMANENT MAGNET MACHINES EQUIPPED WITH NOVEL SEMI-OVERLAPPING WINDINGS FOR ELECTRIC VEHICLE APPLICATIONS

**Ph.D. THESIS**

**Tayfun GUNDOGDU**

**Department of Electrical Engineering**

**Electrical Engineering Programme**

**MARCH 2021**

ISTANBUL TECHNICAL UNIVERSITY ★ GRADUATE SCHOOL

# DESIGN AND ANALYSIS OF INTERIOR PERMANENT MAGNET MACHINES EQUIPPED WITH NOVEL SEMI-OVERLAPPING WINDINGS FOR ELECTRIC VEHICLE APPLICATIONS

**Ph.D. THESIS**

**Tayfun GUNDOGDU**
**(504122004)**

**Department of Electrical Engineering**

**Electrical Engineering Programme**

**Thesis Advisor: Prof. Dr. Guven KOMURGOZ KIRIS**

**MARCH 2021**

**İSTANBUL TEKNİK ÜNİVERSİTESİ ★ LİSANSÜSTÜ EĞİTİM ENSTİTÜSÜ**

# ELEKTRİKLİ ARAÇ UYGULAMALARI İÇİN YENİ YARI KESİŞEN SARGILARLA DONANIMLI GÖMÜLÜ KALICI MIKNATISLI MAKİNALARIN TASARIMI VE ANALİZİ

**DOKTORA TEZİ**

**Tayfun GÜNDOĞDU**
**(504122004)**

**Elektrik Mühendisliği Anabilim Dalı**

**Elektrik Mühendisliği Programı**

**Tez Danışmanı: Prof. Dr. Güven KÖMÜRGÖZ KIRIŞ**

**MART 2021**

Tayfun GÜNDOĞDU, a Ph.D. student of ITU Graduate School student ID 504122004, successfully defended the thesis entitled "DESIGN AND ANALYSIS OF INTERIOR PERMANENT MAGNET MACHINES EQUIPPED WITH NOVEL SEMI-OVERLAPPING WINDINGS FOR ELECTRIC VEHICLE APPLICATIONS", which he prepared after fulfilling the requirements specified in the associated legislations, before the jury whose signatures are below.

**Thesis Advisor :** **Prof. Dr. Güven KÖMÜRGÖZ KIRIŞ** ..............................
Istanbul Technical University

**Jury Members :** **Assoc. Prof. Dr. Murat YILMAZ** .............................
Istanbul Technical University

**Prof. Dr. Necibe Füsun OYMAN SERTELLER** ..................
Marmara University

**Asst. Prof. Dr. Derya Ahmet KOCABAŞ** ..............................
Istanbul Technical University

**Prof. Dr. Erkan MEŞE** ..............................
Ege University

**Date of Submission : 22 December 2020**
**Date of Defense : 03 March 2021**

***I would like to dedicate this Ph.D. thesis to my loving family and to Turkish field marshal, revolutionary statesman, author, and the founding father of the Republic of Turkey, Gazi Mustafa Kemal Atatürk.***

**FOREWORD**

I am very grateful for the support and encouragement I received during the development of this thesis. I would like to thank my supervisors Prof. Dr. Güven KÖMÜRGÖZ KIRIŞ for her kind guidance, continuous support and valuable suggestions for many years. Also, I would like express my sincere gratitude to my former superviser Prof. Zi-Qiang ZHU at the University of Sheffield. Without his instructive and insightful advices, support and guidance, I would have not been in the position of producing high quality research.

I would like to thank the steering committee members Prof. Dr. Necibe FÜSUN OYMAN SERTELLER and Assoc. Prof. Dr. Murat YILMAZ for their valuable suggestions. I am grateful for the academic staff and colleagues I met while being a member in the Electrical Engineering Department of Istanbul Technical University. Thank you, Prof. Dr. Özcan KALENDERLI, Prof. Dr. Serhat ŞEKER, Prof. Dr. Faik MERGEN, Prof. Dr. Aydoğan ÖZDEMIR, Prof. Dr. Lale TÜKENMEZ ERGENE, Prof. Dr. Mustafa BAĞRIYANIK, Prof. Dr. Ömer USTA, Prof. Dr. İstemihan GENÇ, Assoc. Prof. Özgür ÜSTÜN, Assoc. Prof. Ömer GÜL, Asst. Prof. Derya A. KOCABAŞ, Prof. Dr. Emine AYAZ, Dr. A. Saffet ALTAY, Dr. Murat IMERYÜZ, Dr. Taşdemir AŞAN, Dr. M. Onur GÜLBAHÇE, Kubilay ATALAY, Abdullah POLAT, Dr. Aytuğ FONT, Dr. M. Alparslan ZEHIR, Emrah SALMAN and Furkan BAŞKUR for their undergraduate and postgraduate courses, precious advice and valuable technical discussions. I would also like to acknowledge the support provided by former and past colleagues in the EMD Group of the Sheffield University. In particular, to Dr. Petrica TARAS, Dr. Zhongze WU, Dr. Yang GUANG, Dr. Hanlin ZHAN, Dr. Shaoshen XUE, Dr. Han YANG, Dr. Yafeng ZHANG, Dr. Ibrahim A. A. AFINOWI, Dr. Iain M. URQUHART and Dr. James DEXTER for their support, interesting and helpful discussions, and willingness to share their knowledge related to electromagnetic field analysis, machine control, Matlab codes, and test equipment. I am grateful for the friends I met while being a member in the EMD Group of the University of Sheffield. I would like to thank Dr. Izgun GUNSAL, Dr. Huseyin CELIKAG, Dr. Fernando ALVAREZ-GONZALES, Dr. Yasuhiro KATAOKA, Dr. Jun-Tao SHI, Dr. Xiao. GE, and Dr. Di WU for the many pleasant moments and conversations. A special thanks to Akım Metal R&D Mechatronics Team for technical support during the manufacturing of the prototype.

I would also like to thank my parents for their selfless love, unconditional support and immense encouragement.

Last, but not the least, my special and deep gratitude goes to my wife, Dr. Burcu GÜNDOĞDU for her love and support. Without her patience and proofreading, the writing quality of this work would be significantly worse. The happiness and comfort you give me are my most precious gifts.

March 2021

Tayfun GUNDOGDU
(Ph.D., M.Sc., B.Sc.)

**TABLE OF CONTENTS**

**Page**

## ABBREVIATIONS

| | |
|---|---|
| **2-D** | : Two dimentional |
| **3-D** | : Three dimentional |
| **3L** | : Triple layer |
| **AC** | : Alternative current |
| **DL** | : Double layer |
| **EMF** | : Electromotive force |
| **EV** | : Electric vehicle |
| **FEA** | : Finite-element analysis |
| **FEM** | : Finite-element method |
| **FFT** | : Fast Fourier transform |
| **FSCW** | : Fractional-slot concentrated winding |
| **GCD** | : Greatest common divisor |
| **HEV** | : Hybrid electric vehicle |
| **IPM** | : Interioer permanent-magnet |
| **ISDW** | : Integer-slot distributed winding |
| **LD** | : Large dimension |
| **MMF** | : Magnetomotive force |
| **NSW** | : Novel semi-overlapped winding |
| **ORG** | : Original |
| **PM** | : Permanent-magnet |
| **S/P** | : Slot/pole combination |
| **SL** | : Single layer |
| **THD** | : Total harmonic distortion |

## SYMBOLS

| | |
|---|---|
| $\boldsymbol{A_c}$ | : Cross-sectional area of slot |
| $\boldsymbol{B_m}$ | : AC flux component amplitude |
| $\boldsymbol{\cos\varphi}$ | : Power factor |
| $\boldsymbol{D_{so}}$ | : Outer diameter of stator |
| $\boldsymbol{I_{e_{PM}}}$ | : Eddy currents in PMs |
| $\boldsymbol{I_e}$ | : Eddy current amplitude |
| $\boldsymbol{I_{e\_PM}}$ | : Eddy current amplitude induced in PMs |
| $\boldsymbol{I_s}$ | : Stator current |
| $\boldsymbol{L_d}$ | : *d*-axis inductance |
| $\boldsymbol{L_{dq}}$ | : *dq*-axis mutual inductance |
| $\boldsymbol{L_q}$ | : *q*-axis inductance |
| $\boldsymbol{N_c}$ | : Number of coils per phase |
| $\boldsymbol{N_h}$ | : Amplitude of the $h^{\text{th}}$ order harmonic |
| $\boldsymbol{N_t}$ | : Number of turns per slot |
| $\boldsymbol{P_{PM}}$ | : Permanent-magnet loss |
| $\boldsymbol{P_{PM}}$ | : PM loss |
| $\boldsymbol{P_{add}}$ | : Additional loss |
| $\boldsymbol{P_{core}}$ | : Core loss |
| $\boldsymbol{P_{cu}}$ | : Copper loss |
| $\boldsymbol{P_{in}}$ | : Input power |
| $\boldsymbol{P_{out}}$ | : Output power |
| $\boldsymbol{S_{pm}}$ | : Conductivity of the PM material |
| $\boldsymbol{T_{e_{avg}}}$ | : Time averaged torque |
| $\boldsymbol{T_{PM}}$ | : PM or aligment torque component |
| $\boldsymbol{T_{rel}}$ | : Reluctance torque component |
| $\boldsymbol{i_d}$ | : *d*-axis current |
| $\boldsymbol{i_q}$ | : *q*-axis current |
| $\boldsymbol{k_f}$ | : Slot fill factor |

| | |
|---|---|
| $\boldsymbol{k_{wh\_final}}$ | : New winding factor after phase shifting process |
| $\boldsymbol{k_{wh\_initial}}$ | : Initial winding factor |
| $\boldsymbol{k_{w1}}$ | : Fundamental winding factor |
| $\boldsymbol{l_{av}}$ | : Average length |
| $\boldsymbol{l_{av\_FSCW}}$ | : Average length of one phase coil of stator windings with FSCW |
| $\boldsymbol{l_{av\_ISDW}}$ | : Average length of one phase coil of stator windings with ISDW |
| $\boldsymbol{l_{av\_NSW}}$ | : Average length of one phase coil of stator windings with NSW |
| $\boldsymbol{l_{axial}}$ | : Axial length |
| $\boldsymbol{l_{end\_FSCW}}$ | : Average end-winding length of one phase coil of stator windings with FSCW |
| $\boldsymbol{l_{end\_ISDW}}$ | : Average end-winding length of one phase coil of stator windings with ISDW |
| $\boldsymbol{l_{end\_NSW}}$ | : Average end-winding length of one phase coil of stator windings with NSW |
| $\boldsymbol{l_{stack}}$ | : Stack length |
| $\boldsymbol{r_w}$ | : Average winding radius |
| $\boldsymbol{y_c}$ | : Coil pitch |
| $\boldsymbol{\beta_h}$ | : Phase angle of the $h^{th}$ order harmonic |
| $\boldsymbol{\gamma_d}$ | : Phase angle between the current vector and the rotor $d$-axis |
| $\boldsymbol{\theta_{phm}}$ | : Mechanical angular displacement |
| $\boldsymbol{\theta_m}$ | : Space angle at a point of interest in the air-gap |
| $\boldsymbol{\lambda_{PM}}$ | : PM flux component |
| $\boldsymbol{\rho_{cu}}$ | : Resistivity of coppe |
| $\boldsymbol{\sigma_{PM}}$ | : Conductivity of the PM material |
| $\boldsymbol{\omega_r}$ | : Rotor angular speed |
| $\boldsymbol{\Delta T}$ | : Torque ripple |
| $\boldsymbol{I}$ | : Phase current amplitude |
| $\boldsymbol{P}$ | : Pole number |
| $\boldsymbol{S}$ | : Stator slot number |
| $\boldsymbol{TPV}$ | : Torque per volume |
| $\boldsymbol{W}$ | : Average radial length of the end-winding (from slot to slot) |
| $\boldsymbol{f}$ | : Synchronous frequency |
| $\boldsymbol{h}$ | : Harmonic order |
| $\boldsymbol{r}$ | : Periodicity |
| $\boldsymbol{t}$ | : Time |

| | |
|---|---|
| $\boldsymbol{\alpha}$ | **:** Phase shifting angle |
| $\boldsymbol{\eta}$ | **:** Efficiency |

**LIST OF TABLES**

**Page**

**LIST OF FIGURES**

**Page**

# DESIGN AND ANALYSIS OF INTERIOR PERMANENT MAGNET MACHINES EQUIPPED WITH NOVEL SEMI-OVERLAPPING WINDINGS FOR ELECTRIC VEHICLE APPLICATIONS

## SUMMARY

In this thesis, to meet the key expectations of the 21$^{st}$ century from electrical machines such as cost-effectiveness, higher power and/or torque density, efficient energy consuptions, a novel winding topology comprising semi-overlapped windings has been proposed. In addition, single-excited synchronous machines having novel winding topology is investigated with specific relations to the short end-winding length with low magnetomotive force (MMF) harmonics, improved torque density and efficiency, and flux-weakening (FW) capability topics.

Because of the major advantages of fractional-slot concentrated windings (FSCWs) over integer-slot distributed windings (ISDWs), such as very short-end winding length, high slot fill factor, good field weakening and better fault-tolerant capabilities, etc., an interior permanent magnet (IPM) machine equipped with FSCWs is designed and investigated, comprehensively. It has been validated that the significantly high level of MMF harmonics of FSCW configuration causes a substantial increase in the rotor losses. To reduce these losses, different MMF harmonic reduction methods, including phase-winding coils with a different number of turns, multilayer winding with phase shifting, and stator with flux barriers have been implemented. However, it has been revealed that the influence of these methods on the MMF harmonic reduction is insignificant. Therefore, a novel semi-overlapping winding (NSW) topology having concentric windings with a different number of turns per coil arm is introduced. The major advantages of such winding over ISDWs (overlapping) and FSCWs (non-overlapping) are having very short-end winding lengths and significantly low MMF harmonic content, respectively. It has been demonstrated that the proposed winding topology promises significant superiorities such as improved efficiency with substantially reduced total axial length, low eddy current losses, and low risk of irreversible magnet demagnetisation over overlapping and non-overlapping winding topologies.

The effectiveness of the proposed NSW topology by demonstrating its implemention into different synchronous machine technologies, namely IPM, synchronous reluctance machine (SynRM), permanent-magnet assisted SynRM (PMaSynRM), and double salient reluctance machine (DSRM) is investigated. It is found that the electromagnetic performance characteristics of these machines with the proposed NSW topology are comparable to design with ISDW and FSCW topologies. Moreover, it has also been revealed that the implementation of proposed NSWs into the reluctance machines results with higher torque and power output than that of FSCWs.

To be able to increase the torque density, reduce the torque ripple, and improve the efficiency, a systematic design optimization approach compromising single-objective individual and multi-objective global optimization methods is also proposed. Thanks

to the proposed optimization approach, more sensitive geometry parameters to the torque and torque ripple are identified and the optimal solutions is reached much more quickly.

Finally, a systematic analysis on the sole impact of key design parameters, including number of turns, stack length, distance and angle between V-shaped magnets, rotor yoke thickness, magnetic bridge width and thickness, and number of magnet segments, on the FW capability of NSW IPM machines is performed. It has been revealed that number of turns per phase, stack length, and width of main magnetic bridge have a significant effect on the FW capability while distance between magnets has a trivial effect.

It has been concluded that thanks to the proposed NSW topology, electrical machines having a shorter end-winding length (compact structure), higher torque density, higher efficiency, low torque ripple, good FW capability and low risk of irreversible magnet demagnetization can be designed.

**ELEKTRİKLİ ARAÇ UYGULAMALARI İÇİN YENİ YARI KESİŞEN SARGILARLA DONANIMLI GÖMÜLÜ KALICI MIKNATISLI MAKİNALARIN TASARIMI VE ANALİZİ**

# ÖZET


Bu tezde, 21. yüzyılın elektrik makinelerinden beklentileri arasında yer alan; maliyet etkinliği, yüksek güç ve/veya moment yoğunluğu, ve verimli enerji tüketimini karşılamak için; yarı kesişen sargılardan oluşan yeni bir sargı tekniği önerilmiştir. Ayrıca, yeni sargı topolojisinin uygulandığı elektrik makinasına kazandırmış olduğu avantajlar arasında yer alan; düşük manyetomotor kuvvet (MMK) harmonikleri, geliştirilmiş moment yoğunluğu, yüksek verimlilik, akı zayıflatma yeteneği ve kısa sargı sonu uzunluğu gibi konular detaylı bir şekilde incelenmiştir.

Dünya genelinde üretilen elektrik enerjisinin %65'inden fazlası elektrik motorları tarafından tüketilmektedir. Ülkemizde ise bu oran %70'e tekabül etmektedir. Öte yandan, dünya genelinde üretilen elektrik enerjisinin 93%'ünden fazlası elektrik generatörleri tarafından üretilmektedir. Bu nedenle, döner elektrik makinalarının verimliliklerindeki iyileştirmeler, güç tüketiminin azaltılmasında ve dolayısıyla ülkelerin ekonomik büyümesine büyük katkı sağlamaktadır. Ayrıca, verimli enerji tüketiminin 21. yüzyılın küresel iklim değişikliğiyle ilgili sorunların çözülmesinin anahtarı olduğu son zamanlarda fark edilmiştir. Özellikle karayolu ulaşımının elektrifikasyonu; sera etkisine katkıda bulunan $CO_2$ emisyonunun azaltılmasında en önemli katkıyı sağlayacağı anlaşılmıştır. Bu yüzden, karayolu taşımacılığında enerji kullanımının 2050 yılına kadar, elektrifikasyonun hakim olacağı sonucu, BP Enerji şirketi tarafından ön görülmüştür. Sonuç olarak, küresel ısınma, yenilenemeyen enerji kaynaklarının ayrıştırılması ve ekonomik büyüme sorunları ile ilgili artan endişeler nedeniyle, elektrik makinalarının enerji verimliliği tasarımı, önemli bir araştırma alanı olarak ortaya çıkmaktadır.

Kesirli oluklu konsantre sargıların (ISDW), klasik oluklu dağıtılmış sargılara (FSCW) göre sahip olduğu; oldukça kısa sargı sonu uzunluğu, daha yüksek oluk doldurma faktörü, daha iyi alan zayıflatma kapasitesi ve daha iyi hata töleransı gibi avantajlardan dolayı, bu sargı tekniği kullanılarak tasarlanmış; 12-oluk/8-kutup (12S/8P) kombinasyonuna sahip gömülü mıknatıslı senkron (IPM) makinanın elektromanyetik performans karakteristikleri ayrıntılı bir şekilde incelenmiştir. Burada, tasarımların doğruluğunu kontrol edebilmek için, tasarım ve işletme spesifikasyonları 2010 Toyota Prius IPM makinası ile aynı seçilmiştir. FSCW ailesine ait 12S/8P kombinasyonunun altharmoniği bulunmamasına rağmen, bu sargı yapısına sahip makinalarının, oldukça yüksek MMK harmonikleri nedeniyle, rotor kayıplarında önemli bir artış olduğu doğrulanmıştır. Bu kayıpları azaltmak için, farklı tur sayısına sahip faz bobinleri, fazları kaydırılmış çok tabakalı sargı yapısı, stator akı bariyerleri gibi farklı MMK harmonik azaltma yöntemleri uygulanmıştır. Ancak, kullanılan bu yöntemlerin, MMK harmoniklerini azaltmakta oldukça yetersiz olduğu ortaya çıkmıştır. Bu sebeple, düşük MMK harmonik ve kısa sargı sonu uzunluğu talebini karşılamak için; her bir bobin

kolunda farklı tur sayısına sahip konsantirik tip yarı kesişen sargı (NSW) topolojisi geliştirilmiştir. Bu sargı modelinin temel yapısal özellikleri şu şekilde sıralanabilir: (a) yeni bir stator yapısına gerek duymaz (ISDW topolojisine sahip bir sargının yerine stator geometrisinde bir değişikliğe gidilmeden kullanılabilir); (b) bobin ve faz adımlarını herhangi bir stator olur ve kutup sayısına göre hesap etmek oldukça kolaydır; (c) sargı tabaka sayısını oluk ve kutup sayısına bağlı olarak elde etmek mümkündür. Optimum sargı yapısını belirlemek için yapılan çalışmalar sonucunda, oluk sayısı, tabaka sayısı ve bobin kolları arasındaki tur sayıları arttıkça, hava aralığı harmoniklerinin azaldığı ve hava aralığı akısının temel bileşen değerinin arttığı gözlemlenmiştir. Geliştirilen sargı yapısının kesişen sargı (ISDW) tekniğine göre çok daha kısa sargı sonu uzunluğu ve kesişmeyen sargı (FSCW) tekniğine göre çok daha az MMK harmonikleri bulunmaktadır. Önerilen sargı topolojisinin, kesişen ve kesişmeyen sargı topolojilerine göre; büyük ölçüde azaltılmış toplam eksenel uzunluk, düşük girdap akımı kayıpları, düşük geri mıknatıs demanyetizasyon riski ve arttırıllmış verimlilik gibi önemli üstünlükler vaat ettiği gösterilmiştir.

Önerilen YKS topolojisinin IPM makinası, senkron relüktans makinası (SynRM), kalıcı mıknatıs destekli SynRM (PMaSynRM) ve çift çıkıntılı relüktans makinaları (DSRM) gibi farklı tiplerdeki senkron makinalara uygulanmasındaki etkinliği araştırılmıştır. Bu araştırma için kesişen ve kesişmeyen sargı yapılarının etkisi de hesaba katılmıştır. Dolayısı ile aynı tasarım ve işletme spesifikasyonlarına fakat farklı sargı ve rotor topolojilerine sahip toplamda 12 adet senkron makinanın, elektromanyetik performans kıyaslaması ayrınrılı bir şekilde yapılmıştır. Kesişen ve yarı kesişen sargılar için 24S/4P ve kesişmeyen sargı sargı için 6S/4P oluk/kutup kombinasyonları seçilmiştir. Yapılan analizler sonucu; ele alınan makinaların; sargı endüktansları, akı yoğunluğu ve akı çizgi dağılımları, sargılarda endüklenen gerilimler, hava aralığı akı yoğunlukları, mıknatıs demayetizasyon riskleri, moment, moment dalgalılığı, moment yoğunluğu, güç kayıpları, çıkış gücleri, ve verim değerleri kıyaslanmıştır. Önerilen sargı tekniği ile tasarlanan bu makinaların, elektromanyetik performans karakteristiklerinin, ISDW ve FSCW teknikleri ile tasarlanmış senkron makinalar ile karşılaştırılabilir olduğu bulunmuştur. Dahası, önerilen NSW ile tasarlanmış relüktans makinalarının, FSCW tasarımlarına göre daha yüksek moment ve güç çıkışı verdiği ortaya çıkmıştır.

Yüksek hızlardaki dayanıklılığından ve iyi bir alan zayıflatma karakteristiğine sahip olduğundan seçilen IPM rotor topolojisi önerilen NSW yapısı ile tasarlanmış ve akabinde çıkış performans parameterelerini geliştirebilmek için optimize edilmiştir. Burada, tek amaçlı bireysel ve çok amaçlı küresel optimizasyon yöntemlerinin sistematik bir şekilde uygulanması ile optimizasyon gerçekleştirilmiştir. Yapılan optimizasyonun amacı moment yoğunluğunu ve verimi en üst seviyeye çıkarmak, moment dalgalılığını ise en düşük seviyeye indirmek olarak belirlenmiştir. Genetik algoritma, optimizasyon algoritması olarak seçilmiştir. Hassiyet analizleri sonucunda, stator bölme oranı, stator diş genişlik oranı, stator oluk yüksekliği, rotor iç ve dış köprü çapları, akı bariyer kalınlığı, mıknatıs genişlik ve kalınlıkları, stator oluk açıklığının yükseklik ve genişlik parametreleri; optimize edilecek tasarım parametreleri olarak seçilmiştir. Önerilen optimizasyon yaklaşımı sayesinde, maksimum verim koşulunda elde edilebilecek maksimum moment ve minimum moment dalgalılığı hızlı bir şekilde (klasik optimizasyon yöntemlerine göre daha az iterasyon ile) elde edilmiştir.

Son olarak, önerilen sargı yapısı ile tasarlanan bir IPM makinanın alan zayıflatma karakteristikleri ayrıntılı bir şekilde incelenmiştir. Ayrıca, faz başına tur sayısı, istif uzunluğu, mıknatısların konumu, rotor boyunduruk kalınlığı, akı bariyer köprüsünün boyutları, mıknatıs segment sayısı gibi temel tasarım parametrelerinin, alan zayıflatma karakterisiğine olan etkileri araştırılmıştır. Alan zayıflatma performansındaki değişimlerinin sebebini açıklayabilmek için: (a) mıknatıs akı katsayısı; (b) ters çıkıntı oranı; (c) manyetik doyma seviyeleri incelenmiştir. Moment bileşenlerinden relüktans momentinin, alan zayıflatma performansı ile doğru orantılı bir ilişkiye sahip olduğu belirlenmiştir. Yani, eğer incelenen parametere relüktans momentini arttırıyorsa, alan zayıflatma karakteristiğinin daha iyi olacağı tahmin edilebilir sonucuna varılmıştır. Yapılan çalışmalar sonucunda, sargı tur sayısı, istif uzunluğu ve ana manyetik köprü genişliğinin alan zayıflatma kapasitesi üzerinde önemli bir etkiye sahip olduğu, mile yakın uçtaki mıknatıslar arasındaki mesafenin ise önemsiz bir etkiye sahip olduğu ortaya çıkmıştır. Ayrıca, prototipi üretilen makina için kayıp ve verim haritaları ile birlikte moment ve güç–hız eğrileri elde edilmiştir.

Önerilen NSW topolojisi sayesinde, daha kısa sargı sonu uzunluğuna (kompakt yapı), daha yüksek moment yoğunluğuna, daha yüksek verime, düşük moment dalgalanmasına, iyi bir alan zayıflatma kapasitesine ve düşük mıknatıs demanyetizasyon riskine sahip elektrik makinelerinin tasarlanabileceği sonucuna varılmıştır.

# 1. GENERAL INTRODUCTION

More than 65% of the world's generated electrical power is consumed by electric motors [1]. This percentage corresponds to 70% in Turkey [2]. On the other hand, more than 93% of the world's generated electrical power is generated by electric generators [3]. Therefore, improvements in the efficiency of electric motors make significant imprints on reduction of power consumption and hence provides a great contribution to the economic growth of nations. Furthermore, it has recently been realized that efficient energy consumption is the key to solve the 21st century global issues on climate change. Particularly, electrification of road transportation makes the most significant imprints on reduction of $CO_2$ emission contributing to the greenhouse effect. Thus, it has been concluded that the use of energy in road transport is dominated by electrification by 2050 [4]. Consequently, due to the increasing concerns on the global warming, non-renewable energy sources sortage and economic growth issues, the energy efficiecnt design of electrical machines emerging as important area of research.

Electric machines have gained more and more interest with the emergence and evolution of renewable energy and automation technologies. They play critically important roles in several applications, such as electric vehicles (EVs), rail transportation, drones, wind power generation, aerospace, industrial robots, etc [5]-[11]. Conventional electrical machines having either permanent-magnets (PMs) or conductors on their rotors have been extensively used to satisfy the requirements for high torque/power density and efficiency in these applications. As investigated in this thesis, to further increase the power density and cost-effectiveness of electrical machines without sacrificing or even improving the efficiency is one of the main research topics of recent years.

## 1.1 Introduction

With growing concerns of the shortage of global fossil fuels, energy efficiency, and environmental impacts, the conventional vehicles having internal combustion engines are likely to be eliminated in future transportation as reported in BP energy outlook report 2020 edition [4]. EVs have the ability to provide an ultimate solution for sustainable transportation, particularly if they can be powered by electricity generated from renewable energy sources. Figure 1 and 2 illustrate that the road transport will be dominated by EVs and correspondily the global $CO_2$ emission level will be decrease significantly by 2050. Detailed describtions of the legents of the figures (scenarios) are given in Table 1.1.

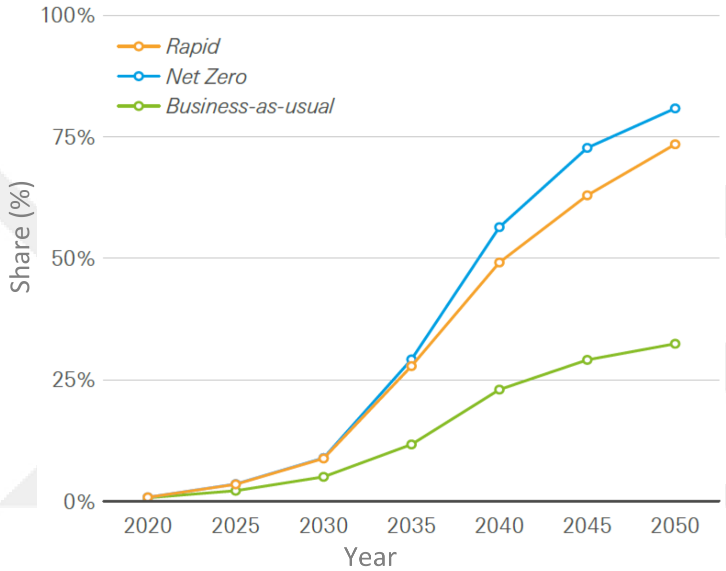


**Figure 1.1 :** Share of car, bus, and truck vehicle kilometres electrified [4].

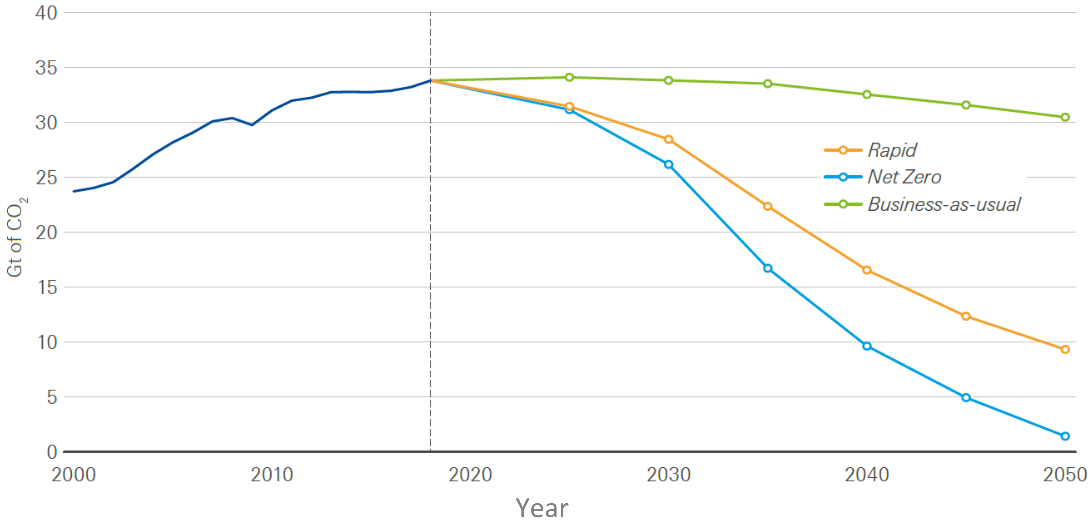


**Figure 1.2 :** Share of car, bus, and truck vehicle kilometres electrified [4].

**Table 1.1 :** Descriptions of scenarios for Figures 1 and 2.

| Scenario | Description |
|---|---|
| Rapid Transition Scenario (Rapid) | includes a number of policy initiatives, accompanied by a substantial rise in carbon prices and assisted by more concrete measures in the industry, which bring about a 70 per cent decrease in carbon emission from energy consumption by 2050. |
| Net Zero Scenario (Net Zero) | assumes that the policy steps included in Rapid are both complementary and enhanced by substantial changes in the behaviour and expectations of society, which further accelerate the reduction in carbon emissions. |
| Business-as-usual Scenario (BAU) | assumes assumes that public policies, innovations and social preferences continue to change. |

In [4], it has been predicted that energy use in road transport is dominated by two major trends: (a) increasing electrification and (b) improving vehicle efficiency. Concequently, the global $CO_2$ emissions from energy use fall by more than 95% by 2050, mainly in line with a number of scenarios consistent with limiting temperature rises to 1.5° Celsius. Although EVs for road transportation have already been available on the market, EV research and development remain faced with many challenges.

### 1.2 Electrical Machines Used in EV Applications

For many years, the research on investigation of cost-effective electric traction machines having higher power density and efficiency has been going on. Many electric machine types having different design topologies have been proposed and successfully applied to EVs as shown in Table 1.2 [12]-[20]. The interior permanent-magnet (PM) machine (IPM) and induction machine (IM) are two types of machines used widely in EV propulsion systems as summarised in Table 1.2. The PM machines equipped with high-energy rare earth permanent magnets (SmCo or NdFeB) have been the first choice for high performance traction machines because of their high torque and/or power densities and power characteristic over a wide speed range.

IM is favourable because of its simplicity, robustness and mature manufacturing technology and control method. Further, IM is cheaper than PM machines, which makes it popular in the market. However, because the magnetic field of IM is established by the magnetizing part of stator current, the power factor is not as high as

PM machines, which leads to lower power density. Further, the constant power region of IM is not as wide as IPM and SPM, although usually up to 4:1 constant power region can be realized. The overall efficiency of IM is usually lower than IPM, except in the high speed region, which is due to no need of large stator current to counteract PM magnetic field. There are several comparison studies on the traction machines used in EV applications in the existing literature [21]-[23].

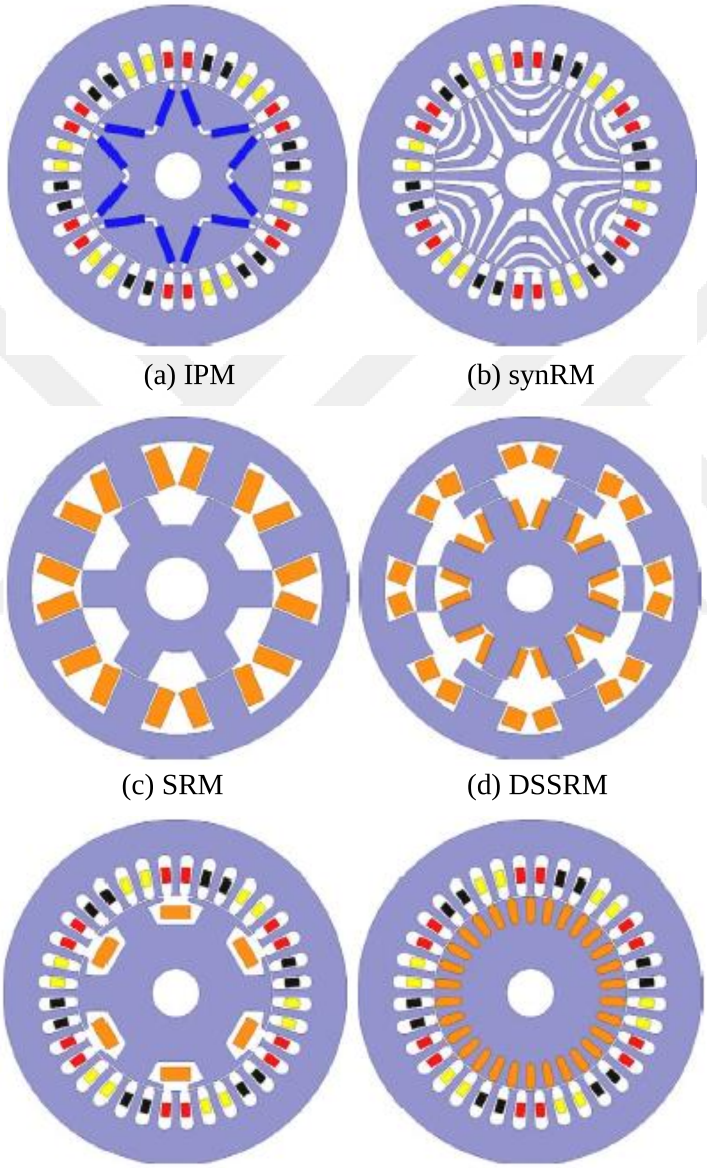

(a) IPM (b) synRM

(c) SRM (d) DSSRM

(e) EESM (f) IM

**Figure 1.3 :** Machine topologies mainly used in the EV Marked.

The vast majority of these studies have been compared three major machine topologies namely, IPM, IM, and switched reluctance machines (SRMs) (see Figure 1.3). SRMs has different stator and rotor topologies such as synchronous reluctance Machine (synRM), double-stator SRM (DSSRM), and electrically excited synchronous machine (EESM). However, among these topologies, synRM and SRM are more frequently used in the EV applications. There are several good candidates for PM-less machines for EVs, and no clear winner among them.

All topologies presented here have some advantages to highlight, but also disadvantages that makes the special requirements for each application crucial for where the choice falls [21]-[23].

- When low cost, simple control and efficiency is preferred over torque and power density, the synRM could be a good option. The main challenges are in the design, balancing between air gap channel design and solidity, and between rotor to stator air gap size and manufacturing cost.
- When robustness, high speeds, low cost and manufacturability is preferred over efficiency, smoothness and silence, the SRM could be a reliable option. The main challenges are to minimize torque ripple, vibrations and noise with design and current control, as well as optimizing performance with materials and design.
- With less vibrations and noise, but a slightly more complicated structure, the DSSRM is an interesting option to the SRM.
- For high controllability over a wide operation range, but lower torque density and higher losses, the EESM is an alternative to consider. Some of the main challenges are cooling the rotor windings or otherwise manage the thermal constraints, and supplying the rotor current with as little extra volume and maintenance needed as possible.
- When reliability, robustness, low cost is preferred over efficiency and controllability, the IM is a good choice. Among the challenges are improving the control and balancing between peak torque and speed range.
- Some of the topologies are mature and widely used, some are barely more than concepts in its cradle. They are all promising in their own ways, but they are also all in need of more research and development.

In [23], an IPM, SRM, and IM with the same outer-diameter, stack length, and pole number have been quantitatively compared. The 2-D cross-sections of the compared machines are illustrated in Figure 1.4. Obtained results are summarized in Table 1.3. Among the compared machines, it is clear that the IPM machine has the highest efficiency in all different torque levels. On the other hand, IM has higher efficiency than the SRM machine in all different torque levels except for the highest torque case. Since the flux weakening performance of the SRM machine with fractional-slot concentrated windings (FSCW) is better than the IM, the SRM has higher power density at high speeds. Since the overall performance of IPM machines are satisfactory in the EV applications, more attention has been given to design and optimization of IPM machines [21].

**Table 1.2 :** Top 20 EV sales in the world in 2015 and machine topologies [20].

| | **Manuf.** | **Model** | **Sales** | **Share** | **Topology** |
|---|---|---|---|---|---|
| **1** | Tesla | Model S | 50366 | 9.2% | IM |
| **2** | Nissan | Leaf | 43870 | 8.0% | PM |
| **3** | Mitubishi | Outlander | 43259 | 7.9% | PM |
| **4** | BYD | Qin | 31898 | 5.8% | PM |
| **5** | BMW | i3 | 24089 | 4.4% | PM |
| **6** | Kandi | K11 Panda | 20390 | 3.7% | PM |
| **7** | Renault | Zeo | 18846 | 3.4% | EE |
| **8** | BYD | Tang | 18375 | 3.4% | PM |
| **9** | Chevrolet | Volt | 17508 | 3.2% | PM |
| **10** | VW | Golf GTE | 17282 | 3.2% | PM |
| **11** | BAIC | E-Series | 16488 | 3.0% | PM |
| **12** | Zoyte | Cloud 100 | 15467 | 2.8% | IM |
| **13** | VW | e-Golf | 15356 | 2.8% | PM |
| **14** | Audi | A3 e-Tron | 11962 | 2.2% | PM |
| **15** | Roewe | 550 | 10711 | 2.0% | PM |
| **16** | JAC | i EV | 10420 | 1.9% | PM |
| **17** | Ford | Fusion Energi | 9894 | 1.8% | PM |
| **18** | Ford | C-Max Energi | 9643 | 1.8% | PM |
| **19** | Kandi | K10 | 7665 | 1.4% | PM |
| **20** | Kia | Soul | 7510 | 1.4% | PM |
| **21+** | Rest | | 147217 | 26.9% | |
| | Total | | 548210 | 100% | |

**Table 1.3 :** Comparison of loss and efficiency at typical operating points [23].

| 48/8 IPMSM | | | | | | |
|---|---|---|---|---|---|---|
| Torque (Nm) | Speed (rpm) | $I_d/I_q$ (A) | Core loss (W) | PM loss (W) | Copper loss (W) | Effi (%) |
| 30 | 3000 | −20.5/20.9 | 173.0 | 0.098 | 96.04 | 97.14 |
| 50 | 1000 | −18.7/36.3 | 52.7 | 0.012 | 186 | 95.51 |
| 50 | 5000 | −80.2/21.1 | 552.4 | 1.328 | 766.6 | 95.06 |
| 300 | 1500 | −184.8/151.6 | 185.7 | 5.7 | 6376.7 | 87.43 |

| 12/8 IPMSM | | | | | | |
|---|---|---|---|---|---|---|
| Torque (Nm) | Speed (rpm) | $I_d/I_q$ (A) | Core loss (W) | PM loss (W) | Copper loss (W) | Effi (%) |
| 30 | 3000 | −21/16.2 | 161.3 | 37.4 | 61.4 | 97.23 |
| 50 | 1000 | −10.2/30.1 | 65.5 | 4.2 | 87.9 | 96.99 |
| 50 | 5000 | −65.4/23 | 298.5 | 651 | 418.1 | 94.89 |
| 300 | 1500 | −149.2/222.4 | 221.4 | 182.3 | 6238 | 87.31 |

| 48/36 IM | | | | | | |
|---|---|---|---|---|---|---|
| Torque (Nm) | Speed (rpm) | $I_d/I_q$ (A) | Core loss (W) | Rotor copper loss (W) | Stator copper loss (W) | Effi (%) |
| 30 | 3000 | 16.2/34.2 | 97.6 | 95.1 | 121.5 | 96.83 |
| 50 | 1000 | 24.2/51.3 | 35.9 | 214.9 | 273.8 | 91.04 |
| 50 | 5000 | 11.1/75 | 110.8 | 458.1 | 488.7 | 96.25 |
| 300 | 1500 | 108.2/44.6 | 74.2 | 5019.1 | 6083.1 | 79.02 |

| 12/8 SRM | | | | | | |
|---|---|---|---|---|---|---|
| Torque (Nm) | Speed (rpm) | $I_{peak}$ (A) | Turn ON turn OFF electric angle | Core loss (W) | Copper loss (W) | Effi (%) |
| 30 | 3000 | 60 | 0–120 | 886.2 | 163.6 | 90.99 |
| 50 | 1000 | 80 | 0–120 | 379.1 | 282.9 | 88.47 |
| 50 | 5000 | 80 | 18–138 | 1346.2 | 296 | 93.8 |
| 300 | 1500 | 350 | 25–145 | 1019.2 | 6222.7 | 86.13 |

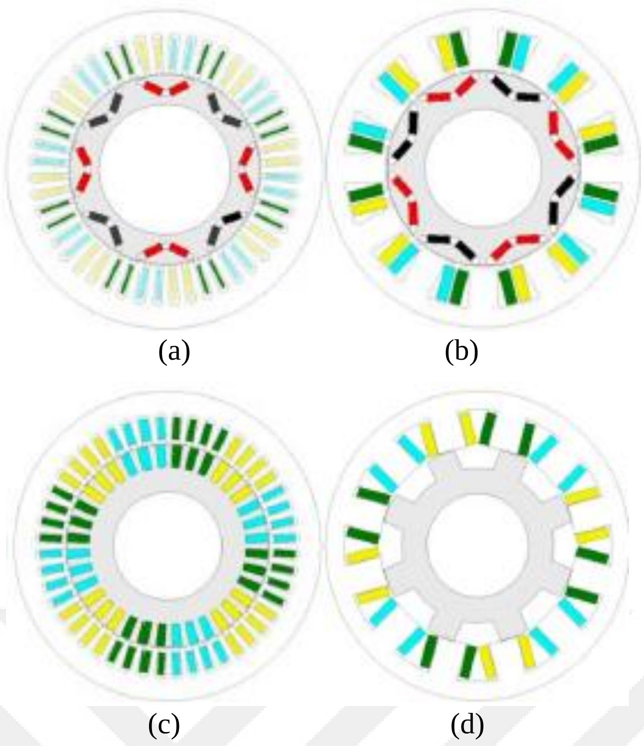


**Figure 1.4 :** Cross-section view of: (a) 48/8 IPMSM; (b) 12/8 IPMSM; (c) 48/36 IM; and (d) 12/8 SRM [23].

### 1.2.1 PM machines used in EV applications

In the early 19th century, the first PM excitation mechanisms were intrroduced to electrical machines [24]. However, as a result of using very poor performance hard magnetic materials and not utilization of variable frequency power supplies, the use of PM machines was very limited. The invention of Alnico in 1930s, and than the availability of high energy density rare earth SmCo in the 1970s and NdFeB since 1983 was a breakthrough in PM machine technology and their performance. Moreover, by the advancement of the elementary technologies, including electromagnetic material technology, computer-aided design technology, control and drive circuit technologies, etc., the performance of PM machines continues to improved rapidly.

The PM machines offer substantial advantages as listed follows.

- Simple contraction and very low maintenance requirement;
- Quite high power and/or torque densities;
- Good dynamic performance and robustness against the enviroment;
- High controllability;
- High efficiency;

• High power factor.

In general, the PM machines for continuos operation are catagorized into three groups as (1) DC commutator; (2) DC brushless; and (3) AC synchronous. The construction of a PM DC commutator motor is similar to a DC motor with the electromagnetic excitation system replaced by PMs. The only difference between DC and AC PM machines is in the control and shape of the excitation voltage. DC PM machines have square or trapezoidal shaped excitation waveform while AC PM machines have sinusoudal excitation waveform. In this thesis, AC PM (PMSM), currently the most preffered topology, will be investigated.

The PMSMs are classified by the location, position, and shape of the PMs in the rotor. In addition, the stator windings can be designed as eighter overlapping or non-overlapping as illustrated in Figure 1.5.

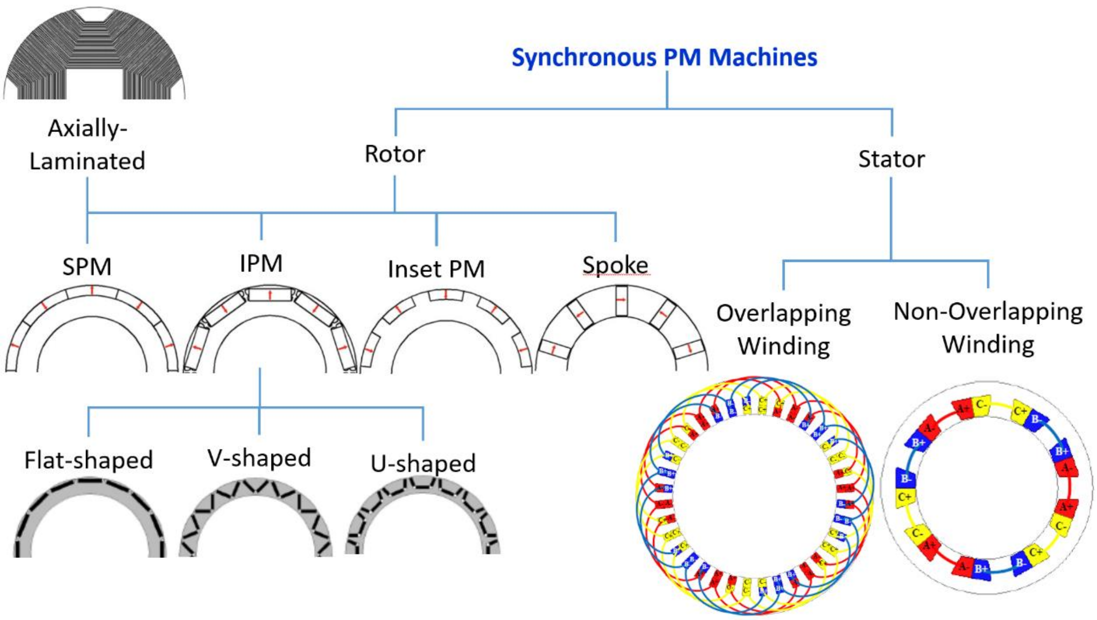


**Figure 1.5 :** PMSM topologies.

### 1.2.2 Stator structure and wires

The stators of PMSMs are occupied either overlapping or non-overlapping windings as shown in Figure 1.6. Each winding topology has its own advantages and disadvantages as shown. The integer slot distributed winding (ISDW) topology is the most preferred one because of the low MMF harmonic content, low rotor losses and very low risk of irreversible demagnetization issues. On thee other hand, as consequenece of excessive rotor losses, particularly magnet losses induced by eddy currents, the fractional slot concentrated windings (FSCWs) mostly are not preferred in EV applications. Because, since the FSCWs are characterized by high MMF harmonic content, the resultant eddy current losses in PMs can be significant. Hence, these losses cause a significant temperature rise and may result in irreversible demagnetization of PMs, particularly in applications requiring high electric loading and/or high speed. Therefore, design of stator windings having very short end-windings with low MMF harmonics is very favorable for electrical machines used in EV applications.

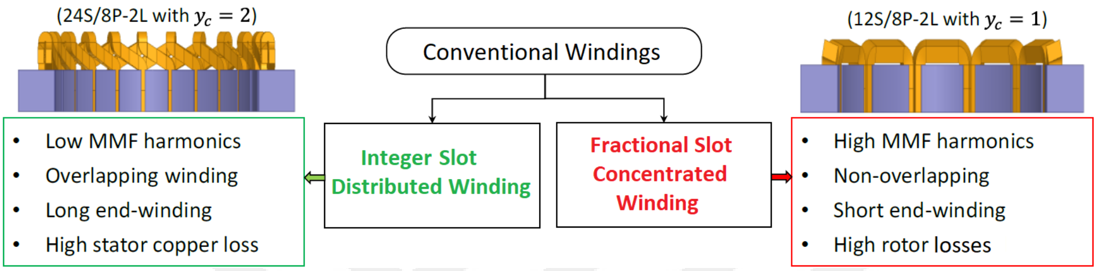


**Figure 1.6 :** The key properties of conventional windings employed in electrical machines.

In recent years, the demand for cost-effective and high-power density EVs has grown although the electric drive represents only 5% of the EV's overall cost [25]. A simple way to reduce the size of the machine is to increase the rated rotor speed and hence the fundamental frequency [26], [27]. In addition, the common approach to increase power density is to optimize the slot filling factor, in order to reduce copper loss and improve the thermal conductivity [28]. The rectangular conductors or hairpin winding technologies providing a high slot fill factor can be implemented. Rectangular conducters, however, have an inherent drawback in high-speed applications. As a consequence of having large size, they generate excessive AC losses at high-frequencies. Thus, the large solid conductors are typically split into smaller strands and connected in parallel. To be able to reduce the AC losses in windings, transposition of the strands in the bundle along the length of the slot and implementation of Litz wire is proposed [29]-[35]. However, transposition of the strands, in order words, "twisting the strands" results with reduced slot fill factor, increased DC resistance and hence DC copper loss. In addition, the termal performance and mechanical stability of the strands are adversely affected by transposition [36]-[38]. Moreover, the Litz wire suffers from lower copper fill factor and reduced effective thermal conductivity [29], [39].

### 1.2.3 Rotor structure

Basically, there exists three groups of rotor structure for PMSMs as: surface mounted PM (SPM), inset PM, and buried or interior PM (IPM) as shown in Figure 1.7. The SPM and inset PM structures have PMs exposed to the air-gap and they usually have high reluctance torque component. The IPM structure has its PMs buried inside the rotor with a higher capability for flux-weakening as a result of having much higher *q*-axis inductance than *d*-axis inductance.

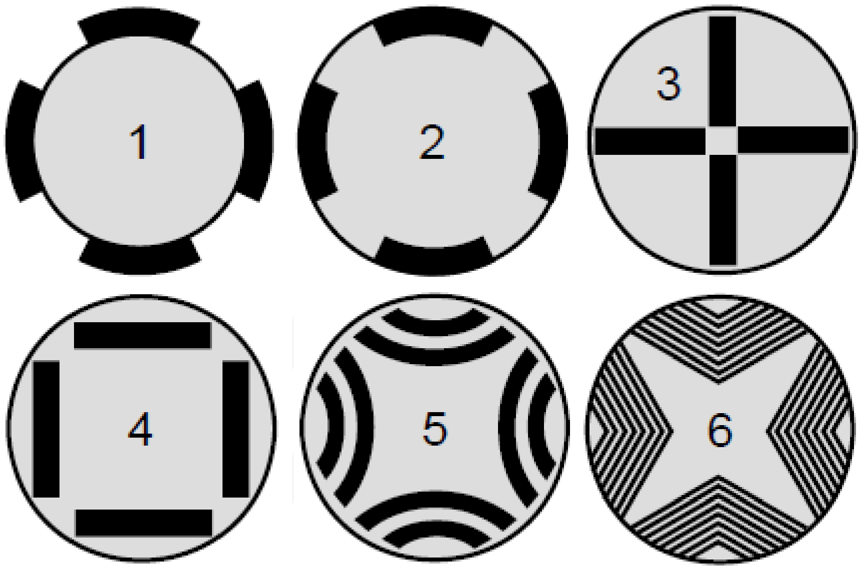


**Figure 1.7 :** The most common rotor types of PMSMs.

The key characteristics and properties of the most common rotor types illustrated in Figure 1.7 are summarized as follows.

1. **SPM**: non-salient strucutre, usually used in diversity of arrangements;
2. **Inset PM**: iron poles between magnets, offers useful reluctance torque;
3. **Spoke**: the flux concentration enhances PM flux with ferrite magnets, very low reluctance torque;
4. **Single-barrier IPM**: the simplest IPM rotor type ensuring very wide flux-weakening performance characteristics;
5. **Multiple-barrier IPM**: improved reluctance torque and saliency ratio but has increased manufacturing costs, more barriers gives higher saliency but more complex construction;

6. **Axially-laminated PM**: the highest possible saliency ratio but difficult to construct commercially.

In the existing literature, many researchers have been investigated the performance characteristics of PMSMs having different rotor topologies. In [21], four different rotor topologies whose structures are illustrated in Figure 1.8 have been investigated.

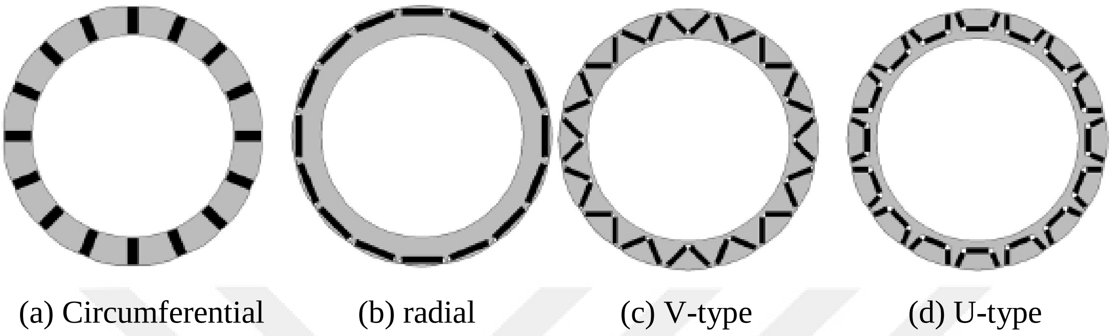


**Figure 1.8 :** Four IPM machine rotor configurations [21].

From the results of the compartive study, the following conclusions for large pole-pairs and fractional slots IPM machines have been obtained.

- For non-overlapping winding, V-type and U-type rotor configurations exhibit better torque and power capabilities.
- For overlapping winding, although the torque capability is a little lower, circumferential rotor configuration has better flux-weakening capability.
- Radial rotor configuration exhibits better demagnetization capability under the condition that different configurations have the same volume of permanent magnets.

In a similar study, the SPM machines have also been considered and its electromagnetic performance has been compared with the IPM machines with different rotor topologies [22]. The considered rotor topologies are shown in Figure 1.9. This paper compares the calculated performance of one SPM and four IPM machines for an EV traction application using the same distributed-winding stator and rated voltage and current.

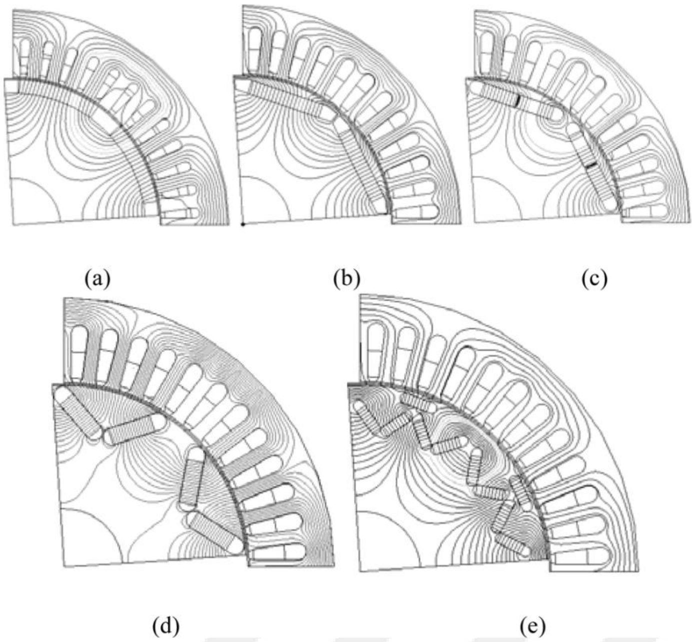


**Figure 1.9 :** Different IPM machine rotor configurations [22].

It was found that the $V$-shape PM rotor has the lowest magnet mass. The $\overline{W}$-shape PM rotor has the largest $d$- and $q$-axis inductances, followed by the $V$-shape PM, and the surface PM rotor has the lowest inductance. The segmented PM motor has a wider range of constant power speed operation than the conventional PM motor since its capacity for flux weakening is increased because of the greater leakage inductance produced by the path between the two permanent magnets. The $\overline{W}$–shape PM machine has excellent flux-weakening performance and has high efficiency over a wide speed range, so it is a good candidate for electric-vehicle applications. By optimizing the shape and position of the PMs in the rotor, the performance of the PMSM has been further improved, making it more suitable for hybrid electric traction applications. On the other hand, some of the commercial traction machines used in the EV applications, are illustrated in Figure 1.10 [40]-[43]. As clearly seen in the figure, the most famous manufacturers prefer IPM machine topologoies. Since the IPM topology is the most favourable topology for EV applications, it has been chosen as to be studied machine topology in the thesis.

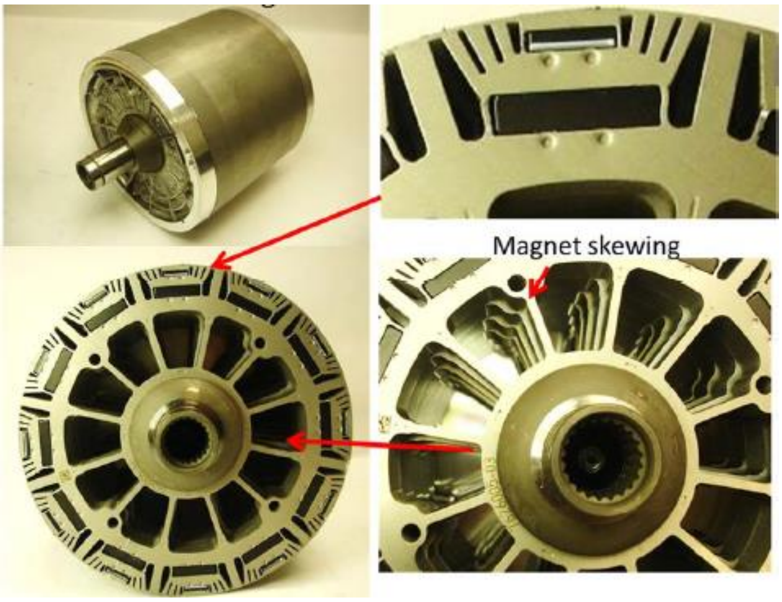


(a) BMW i3 PMaSynR rotor

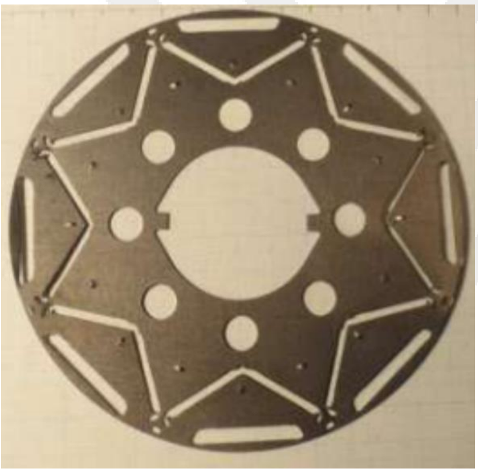

(b) Nissan Leaf IPM rotor

(c) 2016 Chevrolet Volt PMaSynR rotor

(d) 2010 Toyota Prius V-shaped IPM rotor

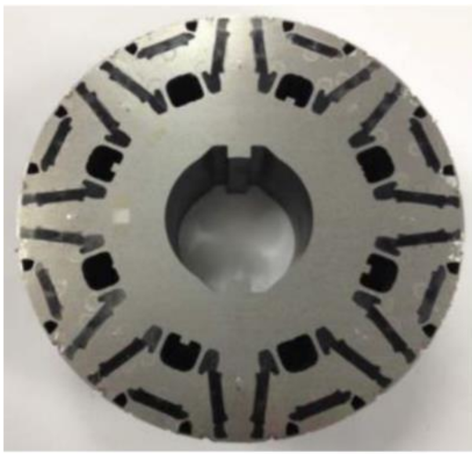

(e) 2017 Toyota Prius double-U IPM rotor

**Figure 1.10 :** Various commercial EV traction machines [40]-[43].

### 1.3 Scope and Contributions of the Thesis

#### 1.3.1 Scope and scientific innovation

As explained in the Introduction Section;

- ✓ Cost-effectiveness;
- ✓ Higher power and/or torque density;
- ✓ Efficient energy consuptions;

are the keys to solve the 21st century global issues on $CO_2$ emmision and hence climate change. Therefore, design of novel electrical machines for EV applications having the above characteristics is of great importance.

In this thesis, the research focuses primarily on developing a novel stator winding for rotating electrical machines used in EV applications having low MMF harmonic content and also short end-winding length in order to increase the torque and/or power density and efficiency, and reduce the cost, simultaneously. The concerned main five topics of the PhD reseach are summarized as follows.

- Investigation of well-known MMF harmonic reduction methods;
- Development of novel windings;
- Investigation of effectiness of proposed windings for different machine tecnologies;
- Systematic desgin optimization;
- Investigation of influence of design parameters on flux-weakening performance characteristics.

The research on the development of novel winding topology is presented in Chapters 2-6 and principally divided into the following steps:

**Step 1**: *Chapter 2*. Investigation of winding MMF harmonic reductuion methods has been examined overy IPM machine having FSCWs. Effect of MMF harmonics on rotor losses has been demonstrated. Influence of five different winding MMF harmonic reduction methods on rotor losses has been reported.

**Step 2**: *Chapter 3.* A novel winding topology comprising semi-overlapped windings (NSWs) has been developed. The key design rules, basic properties, and other merits and demerits of the proposed novel winding topology are justified.

**Step 3**: *Chapter 4.* The compatibleness/effectiveness of the proposed novel semi-overlapping winding (NSW) topology has been investigated by implementing into different synchronous machine technologies, namely interior permanent-magnet machine, synchronous reluctance machine (SynRM), permanent-magnet assisted SynRM, and double salient reluctance machine.

**Step 4**: *Chapter 5.* A systematic approach to achieve optimized design of interior permanent magnet machine (IPM) having novel semi-overlapping windings (NSWs) is conducted. The optimization parameters have been determined individually by performing sensitivity analyses and subsequently a multi-objective global optimization by genetic algorithm (GA) is performed.

**Step 5**: *Chapter 6.* A design and parametric study of IPM machines equipped with NSWs is performed. The influence of the key design parameters on the flux-weakening (FW) performance characteristics are evaluated in detail.

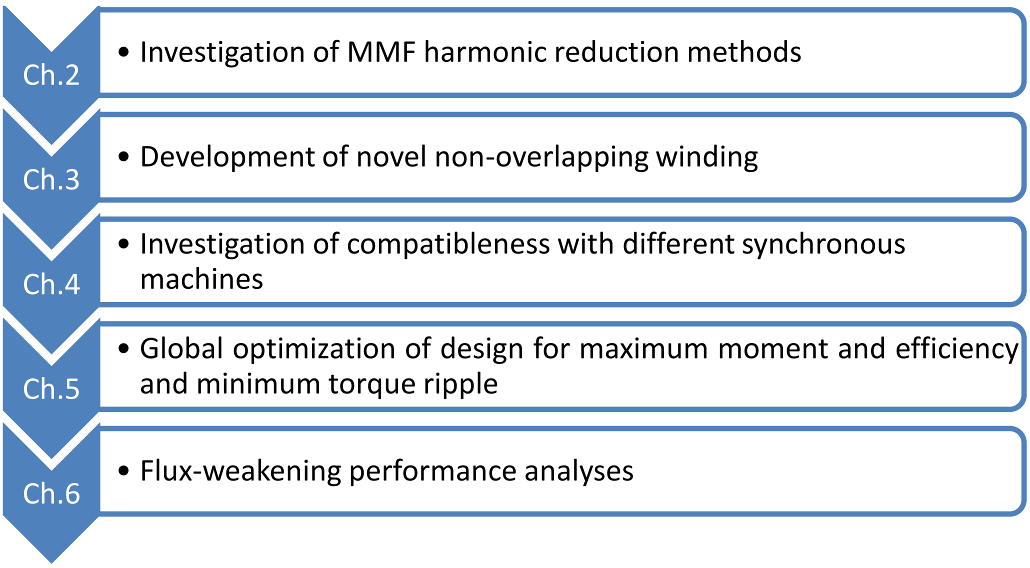


**Figure 1.11 :** Demonstration of research scope, contributions, and the relationshipbetween chapters.

Moreover, the reseach scope, contributions, and the relationship between each chapter have been illustrated as shown in Figure 1.11.

### 1.3.2 The topics covered in the publications derived from the thesis

As demonstrated in Figure 1.11, each chapter of the thesis consists of a journal paper. The topics covered in the publications have been summurized chaperter by chapter as follows.

**Chapter 2**

Since the influence of the MMF harmonic reduction investigated in Chapter 2 is insignificant, the invention of a new winding structure having low MMF harmonics with short end-winding length has resulted. This chapter investigates the implementation of both ISDW (48S/8P) and FSCW (12S/8P) into an IPM machine, designed by using the same geometrical and operational specifications as Toyota Prius 2010 IPM machine in order to reveal the key advantages and disadvantages of FSCW and ISDW topologies. The Toyota Prius's IPM equipped with ISDWs has been considered as a reference machine. Then the geometry of the stator has been adequately modified in other five models to equip FSCWs and adopt different magnetomotive force (MMF) reduction methods. It has been validated that the significantly high level of MMF harmonics causes an increase in the rotor losses. To reduce the effect of these harmonics, different MMF harmonic reduction methods including phase-winding coils with different number of turns, multilayer winding with phase shifting, and stator with flux barriers have been investigated. To reveal the effectiveness of the investigated MMF harmonic reduction methods, the key thermal and electromagnetic performance characteristics including torque, torque ripple, power losses, and efficiency have been numerically calculated by finite element analyses (FEA) and have eventually been compared. The aim of the study presented in this chapter is to reveal the effectiveness of some well-known MMF harmonic reduction methods, particularly for S/P combinations having no sub-harmonics in the MMF waveform.

**Chapter 3**

Since the influences of the MMF harmonic reduction methods investigated in Chapter 2 are insignificant, the invention of a new winding structure having low MMF harmonics with short end-winding length has resulted. A novel winding topology comprising semi-overlapped windings has been proposed in this chapter. The main advantages of such winding over conventional-distributed (overlapping) and fractional-concentrated (non-overlapping) windings are having very short-end winding lengths and significantly low magnetomotive force harmonic content, respectively. The key design rules, basic properties, and other merits and demerits of the proposed novel winding topology are justified. The key performance characteristics of the proposed winding topology are disclosed through an IPM machine. The obtained electromagnetic analysis results are compared with those of other IPM machines having conventional-distributed and fractional-concentrated windings.

**Chapter 4**

This chapter investigates the compatibleness/effectiveness of the proposed novel semi-overlapping winding (NSW) topology by demonstrating its implemention into different synchronous machine technologies, namely IPM, synchronous reluctance machine (SynRM), permanent-magnet assisted SynRM (PMaSynRM), and double salient reluctance machine (DSRM). In order to reveal the merits/demerits of the proposed winding topology, IPM, SynRM, PMaSynRM, and DSRM having 4-poles with conventional windings, i.e. ISDW with 24S/4P, proposed novel windings with 24S/4P, and FSCW with 6S/4P have been designed and the obtained key steady-state (constant torque operating region) electromagnetic performance characteristics including the torque, torque ripple, power losses, efficiency, total axial length, risk of irreversible magnet demagnetisation, etc. have been quantitatively compared.

**Chapter 5**

In this chapter, a systematic approach to achieve optimized design of IPM machine having NSWs is presented. The optimization parameters have been determined individually by performing sensitivity analyses. Multi-objective global optimization is subsequently performed. Genetic algorithm (GA) approach, which is also known as "random search with learning algorithm" and an effective optimization tool used for design optimization of electric machines, is employed. In order to reveal the effectiveness and rapidity of the multiobjective global optimization, a comprehensive electromagnetic performance comparison between the original (with ISDWs), initial and optimal designs (with NSWs) is presented. The aim of this chapter is to propose an advanced state of the art in the multi-objective design optimization of NSW IPM machines by performing sensitivity analyses to reach the optimal solution quickly and to determine the most sensitive design parameters affecting the key performance characteristics.

**Chapter 6**

In order to investigate the influence of design parameters on the flux-weakening (FW) performance characteristics, a design and parametric study of IPM machines equipped with NSWs is performed in this chapter. The influence of the key design parameters including; number of turns per phase, stack length, distance and angle between V-shaped magnets, rotor yoke thickness, magnetic bridge width and thickness, and number of magnet segments on the FW performance characteristics are evaluated in detail. The influence of material of segmentation (material of bridge namely, air or iron) is also considered. A combination of analytical calculation-based program and a time-stepping 2-D finite-element analysis (FEA) based program are employed to evaluate the FW characteristics. The electromagnetic torque, torque ripple, output power and FW capability are investigated by parametric analyses. Moreover, the power losses and efficiency maps together with the FW curves are calculated for the optimal NSW IPM machine. The major objectives of this study are to (*i*) reveal the FW ability of IPM machine designed with proposed NSWs and determine the most dominant parameters on FW capability by explaining the reasons underling; (*ii*) fulfil the gap in literature on the impact of both excitation and geometric design parameters of IPM machines used in EV applications on both low- and high-speed performance characteristics.

**Chapter 7**

This chapter presents the general discossions and findings of the theses and the potential future work for the advancement of IPM machines for EV applications.

### 1.3.3 Thesis contribution to the current state of knowledge

The main contributions are summarised as follows:

- ✓ Reveal the effectiveness of some well-known MMF harmonic reduction methods.

**J1**. *Gundogdu, T. and Komurgoz, G. (2019) Investigation of winding MMF harmonic reduction methods in IPM machines equipped with FSCWs, Int. Trans. Elect. Energy Syst, 29(1), e2688, 1-27.*

- ✓ Advancement of a compact and improved electrical machines for EV applications by developing a semi-overlapping winding topology in order to increase the torque and power densities and efficiency, simultaneously.

**J2**. *Gundogdu, T. and Komurgoz, G. (2020) Design and analysis of interior permanent magnet machines equipped with novel semi-overlapping windings, IET Elect. Power Appl., 14(8), 1446-1457.*

- ✓ To investigate the effectiveness of the proposed NSW compatibleness/ effectiveness of the proposed NSW topology by implementing into different synchronous machine technologies.

**J3**. *Gundogdu, T. and Komurgoz, G. (2020) Comparative study on performance characteristics of pm and reluctance machines equipped with overlapping, semi-overlapping, and non-overlapping windings, IET Elect. Power Appl., 14(6), 991-1001.*

- ✓ To propose an advanced state of the art in the multi-objective design optimization of electrical machines by performing sensitivity analyses to reach the optimal solution quickly and to determine the most sensitive design parameters affecting the key performance characteristics.

**J4**. *Gundogdu, T. and Komurgoz, G. (2021) A systematic design optimization approach for interior permanent magnet machines equipped with novel semi-overlapping windings, Struct. Multidis. Optim., 63(3), 1491-1512.*

- ✓ Reveal the FW ability of IPM machine designed with proposed NSWs and determine the most dominant parameters on FW capability by explaining the reasons underling. Fulfil the gap in literature on the impact of both excitation and geometric design parameters of IPM machines used in EV applications on both low- and high-speed performance characteristics.

**J5**. *Gundogdu, T. and Komurgoz, G. (2020) Influence of design parameters on flux-weakening performance of interior permanent magnet machines with novel semi-overlapping windings, IET Elect. Power Appl., 14(13), 2547-2563.*

# 2. INVESTIGATION OF WINDING MMF HARMONIC REDUCTION METHODS IN IPM MACHINES EQUIPPED WITH FSCWS[1]

In this section, implementation of fractional-slot concentrated windings (FSCWs) into an interior permanent magnet machine (IPM), designed by using the same geometrical and operational specifications as Toyota Prius 2010 IPM machine, has been presented. In detail, the Toyota Prius's IPM equipped with integer-slot distributed windings (ISDWs) has been considered as a reference machine. Then, the geometry of the stator has been adequately modified in other 5 models to equip FSCWs and adopt different MMF reduction methods. It has been validated that the FSCW technique causes a significant increase in the rotor losses due to increase in the rate of the THD of the MMF harmonics. In order to reduce the effect of these harmonics, different MMF harmonic reduction methods, including phase winding coils with different number of turns, multi-layer winding with phase shifting, and stator with flux barriers have been investigated. In order to reveal the effectiveness of the investigated MMF harmonic reduction methods, the key thermal and electromagnetic performance characteristics including torque, torque ripple, power losses, and efficiency have been numerically calculated by finite-element method (FEM) and have eventually been compared.

## 2.1 Introdution

The internal combustion engine has dominated the automotive market over the last century. However, with ever-increasing ecological awareness, such as climate change, air pollution, public health, and the shortage of fossil-fuel resources, the focus on automotive electrification has dramatically increased in the last decade. Nowadays, with more recent improvements in electric machines, battery technology and power electronics it is possible to develop more efficient vehicles, with lower or no fuel consumption without reducing driving comfort and with zero emission [44-54].

[1] This chapter is based on the paper: **Gundogdu, T. and Komurgoz, G.** (2019) Investigation Of Winding MMF Harmonic Reduction Methods in IPM Machines Equipped With FSCWs, *Int. Trans. Elect. Energy Syst*, 29(1), e2688, 1-27.

Permanent magnet (PM) machines, particularly interior-PM (IPM) machines, have been widely adopted as traction electrical machine in the EV applications [44-54]. This is because of their excellent properties, including high torque density and high efficiency over a wide operation range [44, 45, 47].

The FSCWs exhibit many merits such as short end-winding length, high copper packing factor, good field weakening capability owing to relatively large d-axis inductance, better fault tolerant capability due to low mutual inductance, etc. compared to the ISDWs. On the other hand, FSCWs are characterized with highly distorted MMF waveform. The high amplitudes of these space harmonics cause a significant increase in the eddy current losses in the rotor. In addition, these MMF harmonics result in other undesirable effects, including acoustic noise, vibrations, and localized core saturation which tend to reduce reluctance torque. It is shown that the FSCWs can be utilized to increase the *d*-axis inductance and thus improve the field weakening capability of PM machine [55]. The performance of PM machine with FSCWs is compared with PM machines with the ISDWs [56]. It is shown that by using the FSCSW configuration, the copper loss can be reduced considerably owing to both the short end-winding length and the high copper packing factor (if the segmented stator structure is employed). Furthermore, the cogging torque can also be significantly reduced when the least common multiple of the slot number and the pole number increases. However, by employing FSCW configurations in PM machines, the rotor PMs are subjected to a large amount of stator MMF harmonics and consequently incur high eddy current loss [57, 58]. This can further lead to a high rotor temperature particularly at high speeds, and hence the rotor magnets will suffer from a high risk of irreversible demagnetization. On the other hand, compared to the FSCW configurations, the ISDW configurations have lower copper packing factor (slot fill factor), longer end-winding length, higher cogging torque, and less fault tolerant owing to higher mutual inductance and winding overlapping [59-62]. Thus, the FSCW configurations are of potential to be employed in IPMs, given that the lower and higher order space harmonics in the stator MMF can be suppressed to a desirable level. This can increase IPM machines' reluctance torque production, reduce the eddy-current losses in both rotor magnets and rotor iron.

To be able to reduce the MMF harmonics some other studies have been proposed different methods such as adopting asymmetrical windings [63], applying a new vector control schema observing the back-EMF waveform [64], and adopting axial flux modular structure with straight slots and concentrated windings [65]. The importance and effect of MMF harmonics on the performance characteristics of various machines form induction machine to reluctance machine has also been emphasized [66, 67].

In this study, influence of FSCWs on the electromagnetic and thermal performance of an IPM machine, designed by using the same specifications as Toyota Prius 2010 IPM machine, has been investigated. It has been validated that the significantly high level of MMF harmonics causes an increase in the rotor losses. In order to reduce these losses, different MMF harmonic reduction methods, including phase winding coils with different number of turns, multi-layer winding with phase shifting, and stator with flux barriers have been utilized for a 12-slot/8-pole (12S/8P) IPM machine. It has been revealed that the influence of these methods on the MMF harmonic reduction is insignificant.

## 2.2 MMF Harmonic Analysis and Investigated Harmonic Reduction Methods

In this section, the following topics have been covered.

I. Design of Toyota Prius 2010 IPM machine (with ISDW);

II. Determination of slot/pole number (S/P) combination suitable for FSCW technique;

III. Design of IPM machine with FSCW technique [54-61];

IV. Implementation of different number of turns per coil side method [68, 69];

V. Implementation of multi-layer winding with phase shifting method [70-73];

VI. Implementation of flux-barrier method [74-77];

VII. Electromagnetic performance comparison between IPM machines designed with the ISDW technique and the FSCW technique combined with one/some of the utilized methods.

VIII. Thermal analysis by using the total loss distributions of IPMs obtained by electromagnetic analyses.

### 2.2.1 MMF harmonic analysis

The MMF distribution of any 3-phase machine with any feasible slot/pole combination due to unit current, known as the winding function, can be expressed as Fourier series given in (2.1).

$$\begin{cases} n_A(\theta_m) = \sum_h [N_h \cos(h\theta_m + \beta_h)] \\ n_B(\theta_m) = \sum_h [N_h \cos(h\theta_m + \beta_h - h\theta_{\mathrm{phm}})] \\ n_C(\theta_m) = \sum_h [N_h \cos(h\theta_m + \beta_h + h\theta_{\mathrm{phm}})] \end{cases} \tag{2.1}$$

where $h$ indicates the harmonic order, $N_h$, $\beta_h$, $\theta_{\mathrm{phm}}$, and $\theta_m$ are the amplitude of the $h^{\text{th}}$ order harmonic, phase angle of the $h^{\text{th}}$ order harmonic, mechanical angular displacement, and the space angle at a point of interest in the air-gap with respect to $A$-axis as illustrated in Figure 2.1, respectively. Because of the symmetrical distribution of the 3-phase winding, $\theta_{\mathrm{phm}} = 120°$ or $-120°$, depending on the direction of rotation of the MMF working harmonic. Assuming the current amplitudes in all the phases are identical, the phase currents are expressed by (2.2).

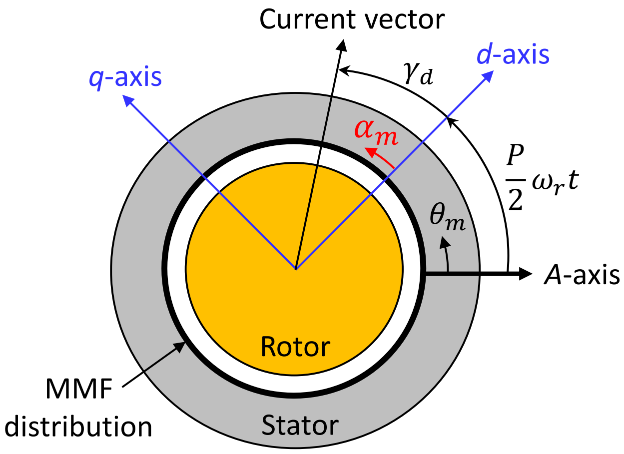


**Figure 2.1 :** Current vector diagram in dq0 and ABC frames.

$$\begin{cases} i_A = I\cos\left(\frac{P}{2}\omega_r t + \gamma_d\right) \\ i_B = I\cos\left(\frac{P}{2}\omega_r t + \gamma_d - 120°\right) \\ i_C = I\cos\left(\frac{P}{2}\omega_r t + \gamma_d + 120°\right) \end{cases} \tag{2.2}$$

where $I$, $P$, $\omega_r$, $t$, and $\gamma_d$ are the current amplitude, the pole number, the rotor angular speed, the time, and the phase angle between the current vector and the rotor $d$-axis as shown in Fıgure 2.1, respectively. The combined MMF of all the 3 phase windings is given in (2.3). The forward and backward rotating MMF harmonics can be derived by substituting (2.1) and (2.2) into (2.3) as given in (2.4) and (2.5), respectively.

$$F_s = n_A i_A + n_B i_B + n_C i_C \tag{2.3}$$

$$\begin{aligned} F_f = \frac{1}{2}\sum_h \{ & N_h I\left[1 + 2\cos\left(h\theta_{\text{ph}m} - 120°\right)\right] \\ & \cdot \cos[h\alpha_m + (h - p)\omega_r t - \gamma_d + \beta_h]\} \end{aligned} \tag{2.4}$$

$$\begin{aligned} F_b = \frac{1}{2}\sum_h \{ & N_h I\left[1 + 2\cos\left(h\theta_{\text{ph}m} + 120°\right)\right] \\ & \cdot \cos[h\alpha_m + (h + p)\omega_r t + \gamma_d + \beta_h]\} \end{aligned} \tag{2.5}$$

where $\alpha_m = \theta_m - \omega_r t$. The periodicity $r$ for an electrical machine having $S$ slots and $P$ poles is subject to the greatest common divider between $S$ and $P$ as expressed in (2.6) [78].

$$r = \text{GCD}\left\{S, \frac{P}{2}\right\} \tag{2.6}$$

The expressions given from (4) to (6), any stator MMF harmonic of a conventional 3-phase winding configuration can be predicted. The magnitude of the $h^{\text{th}}$ order winding function harmonic $N_h$ can be obtained by Fast Fourier Transform (FFT) of the winding function waveform of a given winding configuration. For example, in a double layer winding with even $S/r$ rate, the orders of harmonics for the single phase winding function are odd numbers $(2h - 1)r$ except for the integer multiplies of $S$. This is because the even $S/r$ can form a symmetric pattern with opposite phasors. In addition, since a 3-phase windings are uniformly displaced in space with respect to each other by $120°$ electrical degrees all the triplen MMF harmonics are eliminated. This can also be observed in (2.4) and (2.5), where the terms $\left[1 + 2\cos\left(h\theta_{\text{ph}m} - 120°\right)\right]$ and $\left[1 + 2\cos\left(h\theta_{\text{ph}m} + 120°\right)\right]$ are derived. Furthermore, the orders of MMF harmonics for a double layer 3-phase winding with an even $S/r$ are odd numbers $(2h - 1)r$ except for the triplen multiplies of $r$.

The above technique can be used to analyse the MMF harmonic distributions of any kind of 3-phase winding, including the multi-layer winding configurations with shifted winding coils adopted to reduce the MMF harmonics which will be discussed in the following section.

### 2.2.2 Investigation of MMF harmonic reduction methods

The IPM machine, which has the high-power density and efficiency and the most preferable traction machine by the EV/HEV manufacturers, has been determined as the best candidate to be improved. To be able to improve the electromagnetic performance characteristics, improvement methods are summarized as follows.

- Determination of the best slot number/pole number combination;
- Utilization of FSCW topology;
- Utilization of winding coils with different number of turns (uneven turn numbers);
- Adaptation of the multi-layer winding with phase shifting method;
- Utilization of the stator flux barriers;

As seen above, all these methods are applicable for the stator part. In order to improve the torque density and torque quality, the improvement methods applicable for the rotor part will also be investigated in future study.

#### 2.2.2.1 Winding coils with different number of turns

A 12-slot/10-pole winding configuration with uneven number of turns is developed. The uneven number of turns differ only by one turn from the neighbour coil side $(n_2 = n_1 - 1)$ [74, 75]. Thus, the slot with less turn number should not complete the last turn. The ratio of $n_1$ to $n_2$ determines the MMF harmonic cancellation effect.

This technique restricts the difference in the uneven turn numbers to be only one turn. Therefore, the ability to reduce MMF harmonics by this technique is quite limited when the turn number has to be designed high. On the other hand, it is not practical to have the difference in the number of turns on two sides of a coil being greater than one. Further, uneven Ampere turn distribution in slots lead to less effective utilization of the slot areas and localized saturation in the stator teeth, compromising the electromagnetic performances.

#### 2.2.2.2 Phase shifted multi-layer windings

The multi-layer winding method is proposed to be able to reduce the effect of the MMF harmonics. The concept is to split the phase windings into two sets of windings and shift one set by one or more slots, whilst maintaining the same number of slot for a given number of pole pairs [76-79]. Initially, two layers of windings are created. Then, by splitting all the coils into two, a four-layer winding configuration has been developed. In addition, the number of turns per coil can be adjusted to reduce the most MMF harmonics. The multi-layer winding configurations increases the complexity of the winding structure and results in lower fundamental winding factor and hence low torque generating capability. Moreover, the most detrimental harmonic whose order is close to that of the working harmonic is not significantly reduced.

#### 2.2.2.3 Stator flux barriers

In order to reduce the amplitude of the MMF harmonics flux barriers located at the stator back-iron is proposed [71-77]. The introduced flux barriers significantly increase the reluctance to the 1$^{st}$ order MMF harmonic while the reluctance to other higher order harmonics are less affected. Consequently, the air-gap flux density due to the 1$^{st}$ MMF harmonic is reduced. As will be shown, these flux barriers can be in radial or tangential direction and can be located at the stator back-iron or stator tooth part. In addition, the sizes of these flux barriers can be optimized to obtain the best harmonic cancellation effect. While the concept is simple to be implemented there a number of disadvantages associated with this technique. The harmonic cancellation effects may be compromised at heavy load condition since the saturation in the stator core affects the reluctance in the magnetic circuit. The fundamental winding factor and torque production may be compromised without careful design. In addition the flux linkages generated by permanent-magnets are slightly reduced due to higher reluctances caused by the flux barriers in the stator, and thus the magnetic loading is reduced with the same amount of PMs.

### 2.2.3 Implementation of the MMF harmonic reduction methods

The MMF reduction methods explained above have been implemented by sequence as illustrated in Figure 2.2. Firstly, the original Toyota Prius 2010 IPM machine with ISDW configuration has been designed. Secondly, the FSCW configuration has been utilized. Note that, the same outer diameter, stack length, and operation specifications such as phase voltage, phase current, rated speed, etc. has been used for the design of FSCW IPM machine. Multi-layer winding technique has been utilized as a third step. Finally, flux-barrier method has been adopted. The influence of each method on the performance characteristics of the IPM machine has been investigated in the following section.

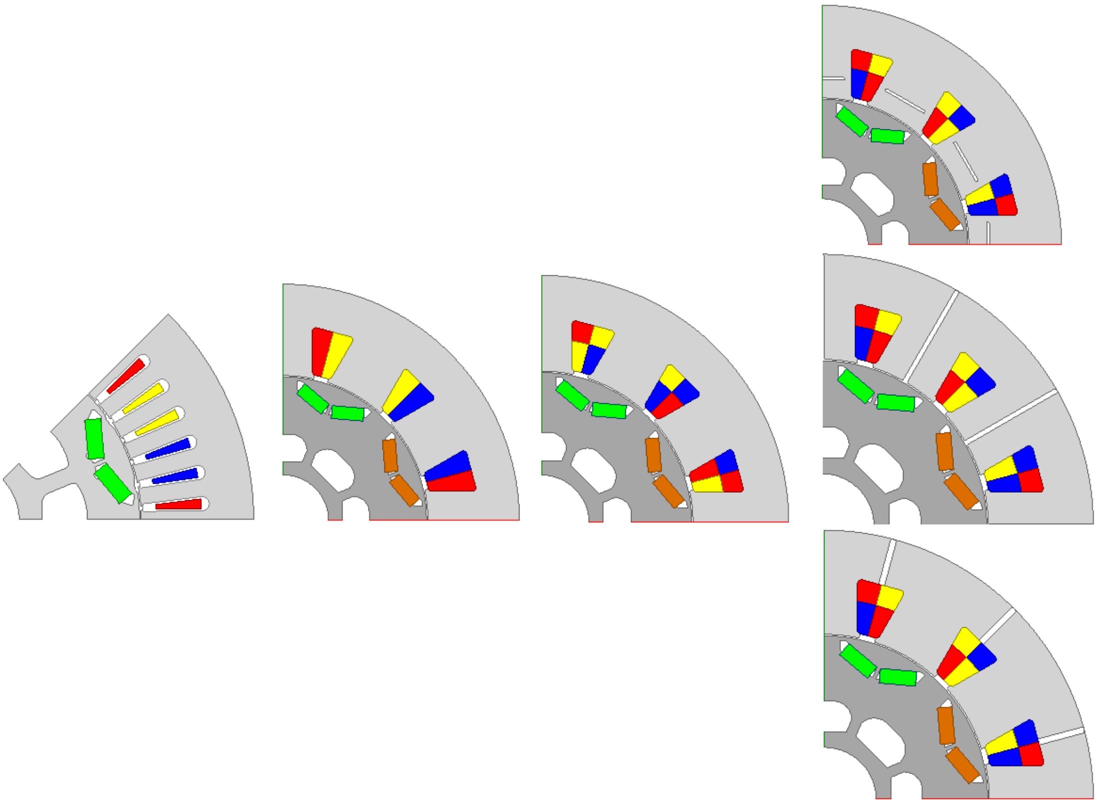

**Figure 2.2 :** Sequence of implementation of the MMF harmonic reduction methods.

#### 2.2.3.1 Determination of slot/pole number combination

In order to determine the proper S/P combination, the winding factor and MMF harmonics are very important parameters which should be taken into consideration. Since the pole number of the original ISDW IPM machine is 8, only the 8-pole combinations have been considered for a fair comparison.

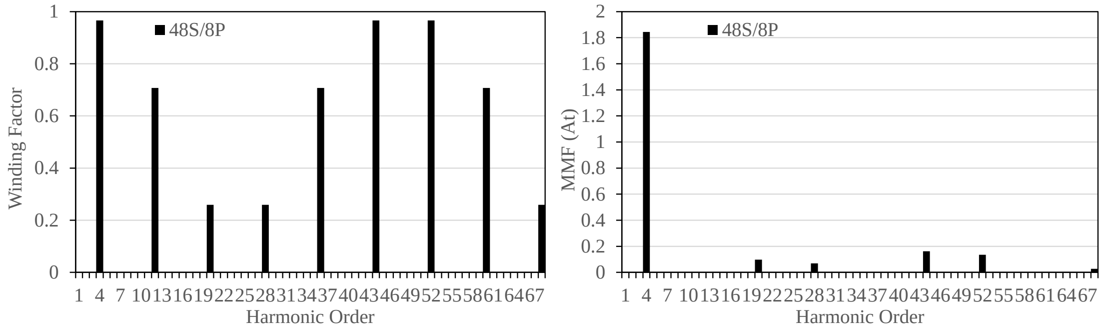


(a) Winding factor harmonics (b) MMF spectrum

**Figure 2.3 :** Winding factor and MMF spectrum of the 48S/8P ISDW configuration.

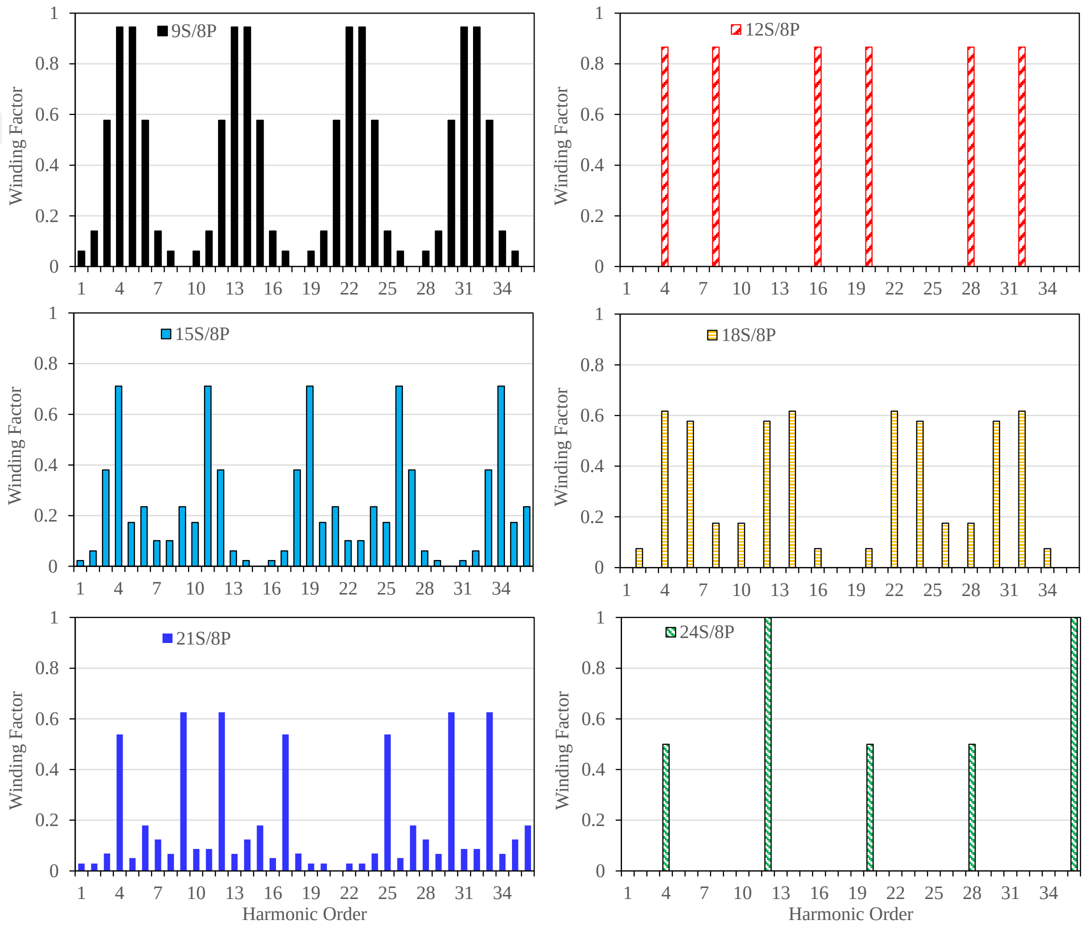


**Figure 2.4 :** Comparison of the winding factors of the various winding figurations with different slot/pole numbers.

The winding factor and MMF harmonics of the 48-slot/8-pole (48S/8P) ISDW IPM machine with single-layer 5-slot pitch winding configuration is shown in Figure 2.3. As seen in the figure, the fundamental winding factor is 0.966 and amplitude of the MMF harmonics (except for the fundamental) are quite low. The winding factor and MMF harmonics of the FSCW IPM machines with 9S/8P, 12S/8P, 15S/8P, 18S/8P, 21S/8P, and 24S/8P combinations with double-layer, 1-slot pitch winding configurations are show in Figure 2.4. It is obvious that although the amplitude of the fundamental winding factors of the FSCW combinations are low, the harmonic contents are quite high when compared to the ISDW configuration. In addition, as seen in the figures, only the 12S/8P and 24S/8P combinations do not include sub-harmonics while others include. MMF harmonic spectrum of the FSCW combinations are illustrated in Figure 2.5. As seen in the figures, the harmonic content of the FSCW combinations are quite high. In addition, all the combinations include sub- and super-harmonics except for the 12S/8P and 24S/8P combinations. In addition, the amplitudes of the fundamental MMF of the FSCWs are quite low when compared to ISDW combination.

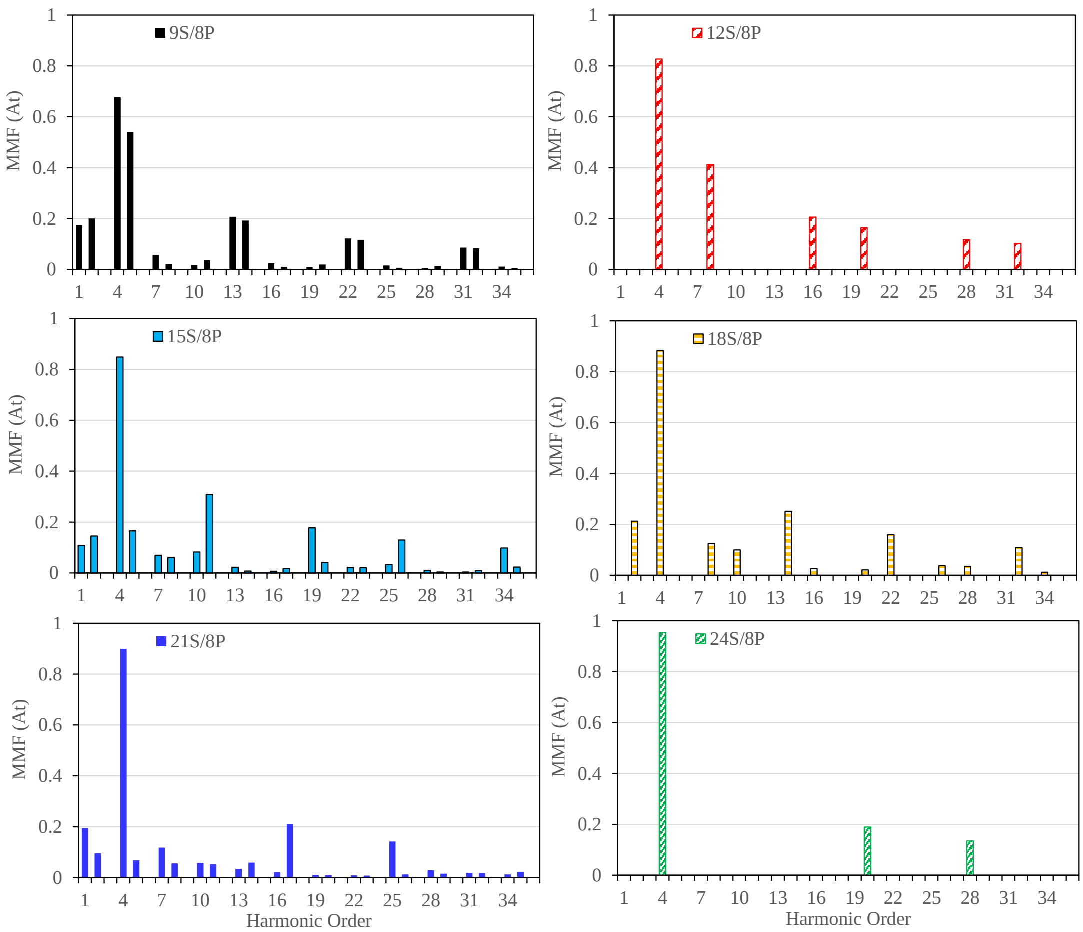


**Figure 2.5 :** Comparison of the MMF spectrum of the various winding figurations with different slot/pole numbers.

The winding specifications of the considered slot/pole combinations are compared in Table 2.1. As seen in the figure, while the 48S/8P combination has the highest fundamental winding factor, fundamental MMF amplitude, and the lowest MMF THD, the 9S/8P has the lowest fundamental MMF amplitude and the highest MMF THD. It can be concluded that since the 12S/8P and 24S/8P combinations do not include any sub-harmonics, they show similar characteristics with the ISDW configurations. Considering the winding analysis results, selecting the 12S/8P combination is reasonable in terms of low harmonic content and relatively high fundamental winding factor.

**Table 2.1 :** Comparison of the winding specifications of the different slot/pole number combinations.

| | $k_{w1}$ | $MMF_1$ (At) | MMF THD (%) | Sub-Harmonic |
|---|---|---|---|---|
| **9S/8P** | 0.945 | 0.677 | 106.951 | + |
| **12S/8P** | 0.866 | 0.827 | 65.888 | — |
| **15S/8P** | 0.711 | 0.848 | 60.35 | + |
| **18S/8P** | 0.617 | 0.883 | 51.006 | + |
| **21S/8P** | 0.538 | 0.9 | 46.64 | + |
| **24S/8P** | 0.5 | 0.954 | 28.776 | — |
| **48S/8P** | 0.966 | 1.844 | 14.56 | — |

### 2.2.3.2 Fractional-slot concentrated winding technique

A 12S/8P FSCW IPM has been designed by using the same geometrical and operational specifications as conventional IPM machine. In order to reveal the basic properties of the FSCW technique, electromagnetic properties of the FSCW IPM machine is compared with that of the ISDW IPM machine as follows. Note that all the geometric, operational, and core material specifications are given in Appendix-A. Flux line and flux density distributions of the IPM machines are illustrated in Figure 2.6 and 2.7. It can be seen that the saturation level of the ISDW IPM machine parts, especially stator tooth body and yoke are higher than that of the FSCW IPM machine. Back-EMF waveforms and their harmonic spectra are shown in Figure 2.8. As seen, the waveforms are heavily distorted. Although the serial number of turns per phase are 88 and 104 for ISDW and FSCW IPM machines, respectively, the fundamental amplitude of the ISDW IPM machine is higher than that of the FSCW IPM machine.

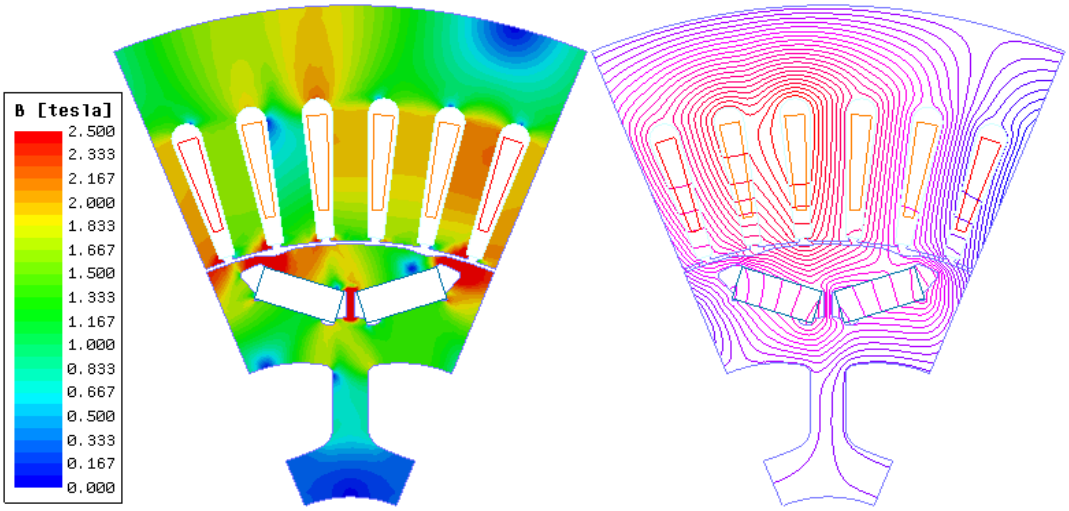


(a) Flux density distribution (b) Flux line distribution

**Figure 2.6 :** Flux density and flux line distribution of the Toyota Prius 2010 IPM machine.

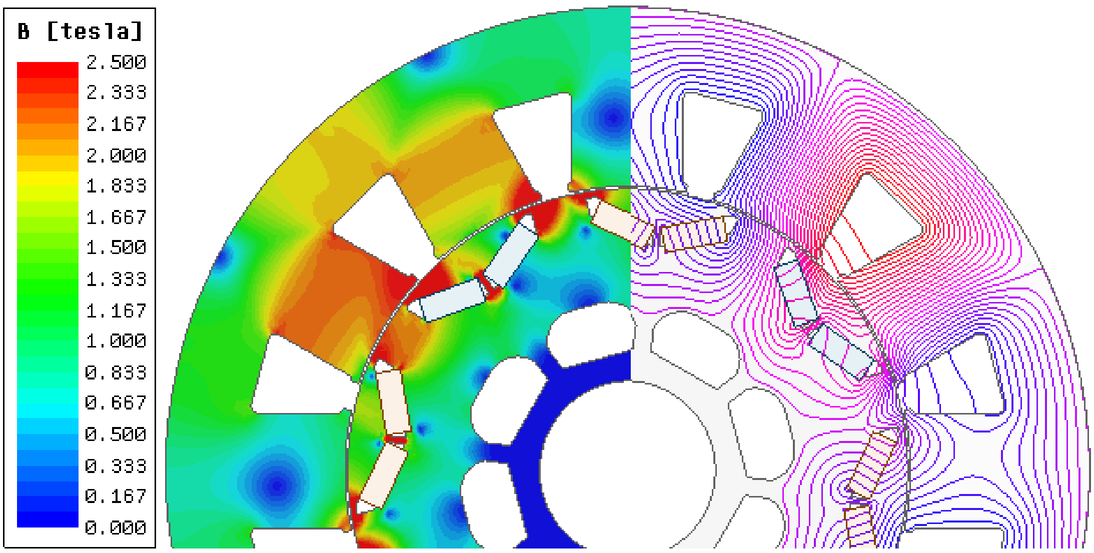


**Figure 2.7 :** Flux density and flux line distribution of the FSCW IPM machine.

This is because of the ~10.5% lower fundamental winding factor of the FSCW IPM machine. As seen in Figure 2.8(b), the back-EMF THD level of the FSCW IPM machine is higher than that of the IPM machine.

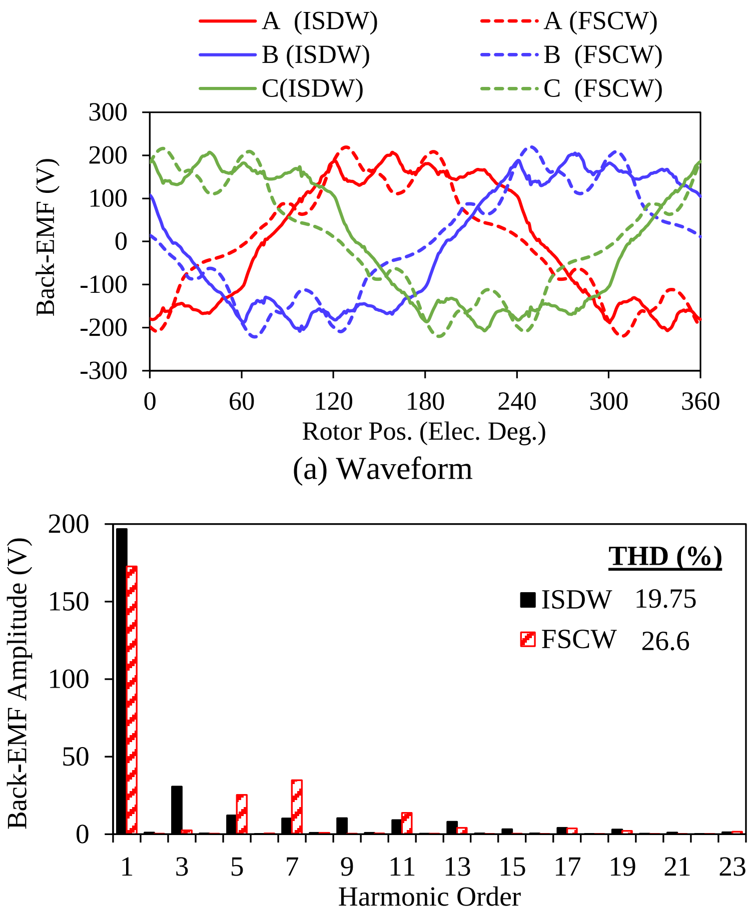


(a) Waveform



(b) Harmonic spectra of back-EMF

**Figure 2.8 :** Comparison of the (a) back-EMF waveforms and (b) their harmonic spectra.

Flux linkage waveforms and their harmonic spectrum are shown in Figure 2.9. As seen in the figure, the flux linkage fundamental amplitude of the FSCW IPM machine is higher than that of the ISDW IPM machine. In addition, its distortion level is lower. On the other hand, as seen in Figure 2.10, the distortion level of the air-gap flux density of the FSCW IPM machine is significantly higher (~2 times) that that of the ISDW IPM machine. Furthermore, the fundamental amplitude of the air-gap flux density of the ISDW IPM machine is slightly higher. The radial component of the flux density on the tooth body is the useful (torque generating) component while the tangential component is the leakage flux component [79]. Variation of these flux densities are illustrated in Figure 2.11. As validated in [80, 81], due to the magnetic saturation of the tooth, the waveform turns in to the flat-tapped shape (non-sinusoidal). Therefore, it can be concluded that the saturation level of the stator of the ISDW IPM machine is higher than that of the FSCW IPM machine.

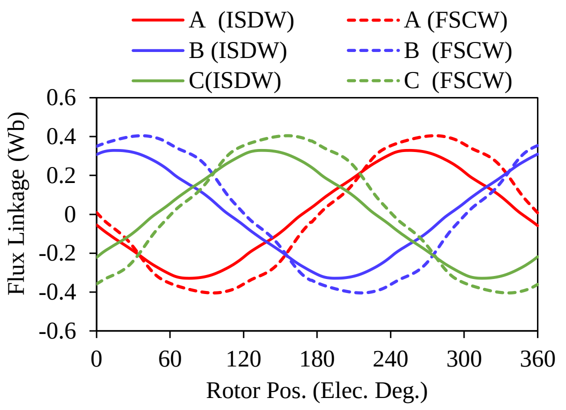


(a)

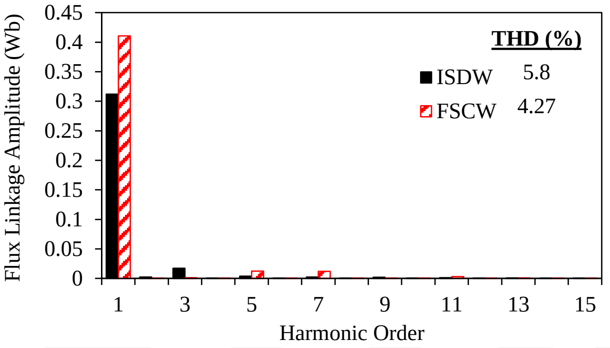


(b)

**Figure 2.9 :** Comparison of the flux linkage waveforms and their harmonic spectra.

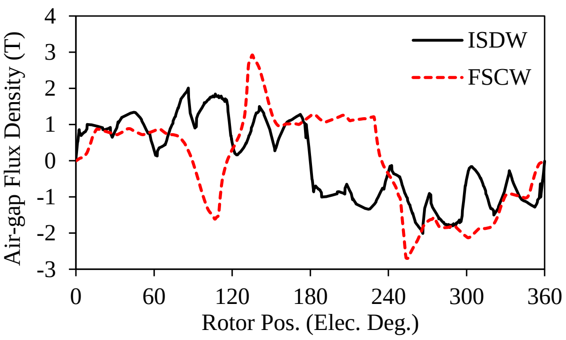


(a)

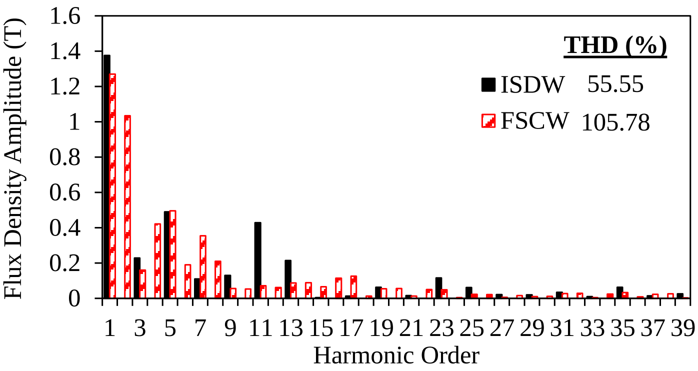


(b)

**Figure 2.10 :** Comparison of the air-gap flux density waveforms and their harmonic spectra.

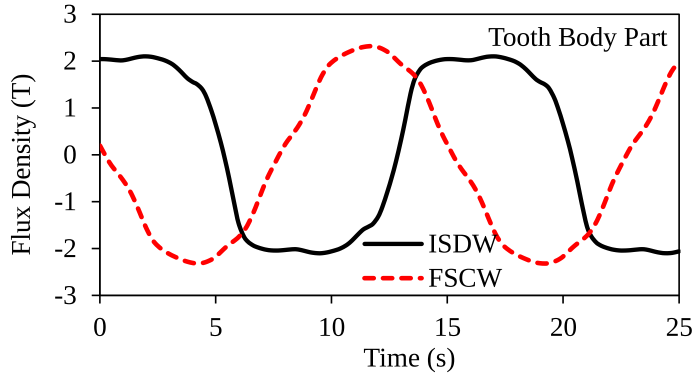

(a) Amplitudes: ISDW 1.8, FSCW 1.62

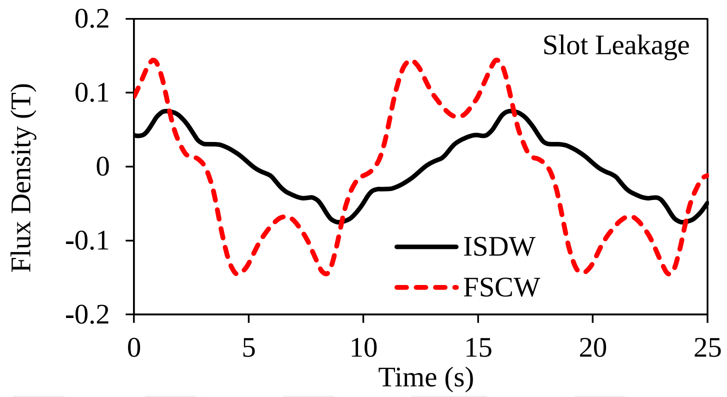

(b) Amplitudes: ISDW 0.044, FSCW 0.094

**Figure 2.11 :** Variation of stator tooth body and stator slot leakage flux densities with respect to time.

However, as seen in the slot leakage waveform, the flux-leakage of the FSCW IPM machine is much higher (more than twice) than that of the ISDW IPM machine. Therefore, under the same operational conditions, the average torque level of the FSCW IPM machine is lower as seen in Figure 2.12. On the other hand, the torque ripple percentage of the FSCW IPM machine is much higher than that of the ISDW IPM machine.

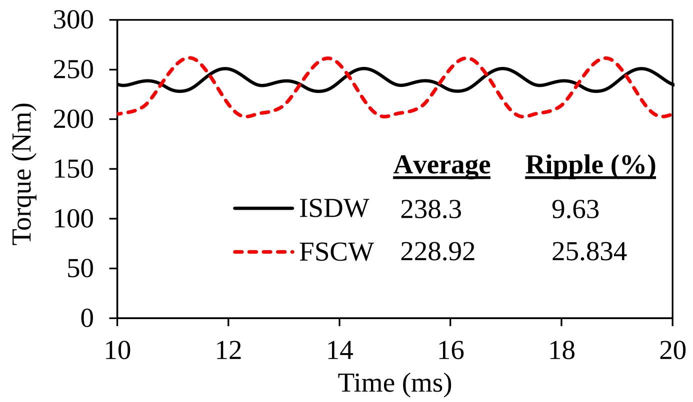

**Figure 2.12 :** Variation of the torque with respect to time.

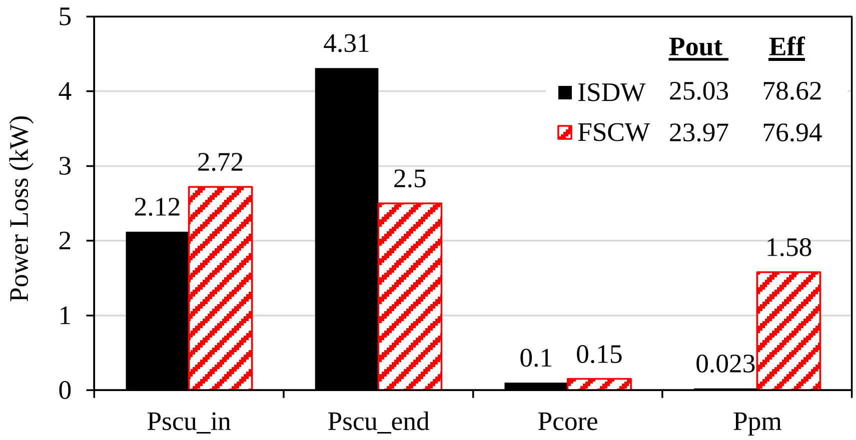


**Figure 2.13 :** Comparison of the power losses, output power, and efficiency.

$$P_{PM} = \frac{1}{S_{pm}} I_{e\_PM}^2 \tag{2.7}$$

$$l_{av\_ISDW} \approx 2l_{stack} + 2.8W + 12 \tag{2.8}$$

$$l_{av\_FSCW} \approx 2l_{stack} + 2.4W + 5 \tag{2.9}$$

Comparison of the power losses, output power, and efficiency is illustrated in Figure 2.13. Stator slot copper loss Pscu_in and end-winding loss Pscu_end are calculated by using the average coil lengths given in (2.8) and (2.9). As seen, the average length $l_{av}$ is calculated separately for FSCWs and ISDWs. Here, $l_{stack}$ is the average stack length and $W$ is the average radial length of the end-winding. The PM loss Ppm is calculated by considering the conductivity of the PM material $S_{pm}$ and the eddy current $I_{e\_PM}$ induced on the PMs as given in (2.7). As seen in Figure 2.13, although, the end-winding loss of the FSCW is lower, the slot copper loss is higher due to the more number of turn requirement of the FSCW IPM machine. On the other hand, because of the higher amount of the eddy current of the FSCW IPM machine, the core and PM losses are higher. It should be noted that the Ppm loss of the FSCW IPM machine is significantly higher than that of the ISDW IPM machine. It can be concluded that although the end-winding length of the FSCW IPM machine is quite low and consequently the total axial length and end-winding copper loss are quite low, the PM loss is significantly high. As previously explained, the reason behind these significantly high PM loss is the high eddy current resulting from the highly distorted MMF waveform of the FSCW configuration. As seen in Figure 2.13, this quite high PM loss cause a remarkable decrease in the efficiency. Therefore, to be able to use the FSCW topology in the EV/HEV applications, in where the power and efficiency are the most critical parameters, the MMF harmonics should be reduced considerably. In the following sections, many MMF reduction methods have been adopted for the FSFW IPM machine.

#### 2.2.3.3 Winding coils with different number of turns

As reported in [74, 75], it is possible to reduce some MMF harmonics by using uneven number of turns $n_t$ per coil. Considering the winding configuration, there is two different winding layouts, namely consequence and conventional winding layouts for this method as shown in Figure 2.14. Influence of these methods on the electromagnetic performance characteristics of the FSCW IPM machine is investigate as follows.

The variation of torque with respect to time is shown in Figure 2.15. As seen, there has been a slightly decrease in the average torque although there has been an increase in the torque ripple percentage in both consequence and conventional cases. The comparison of the power losses, output power, and PM losses are illustrated in Figure 2.16. As seen in the figure, since he total winding of turns is reduced by one number of turns per each coil, the slot and end-winding copper losses are reduced slightly. Moreover, although the output power is reduced due to the reduced average torque, the efficiency is increased slightly because of the reduction in the PM loss.

It has been revealed that thanks to the uneven number of turn method the efficiency can be improved by sacrificing the torque and output power. However, in additional to the torque and power the filling factor is also reduced/sacrificed, this method is not effective.

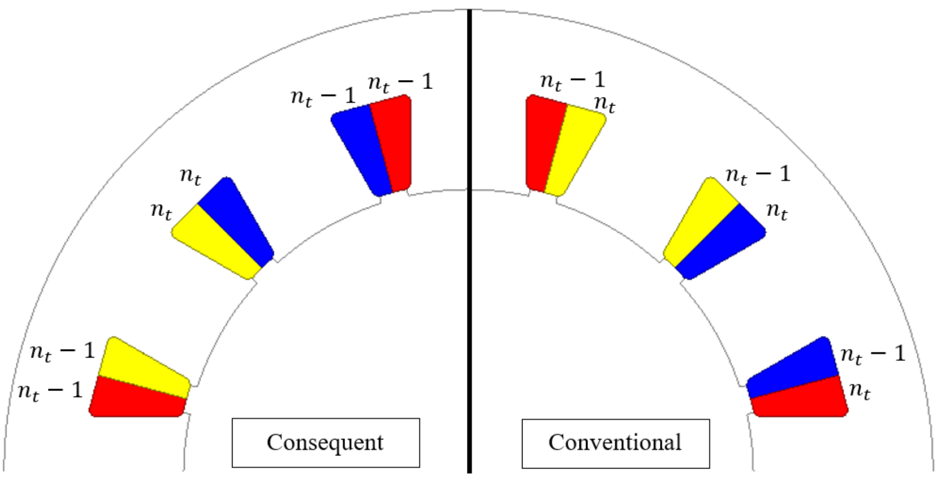


**Figure 2.14 :** Illustration of the uneven number of turns per coil method.

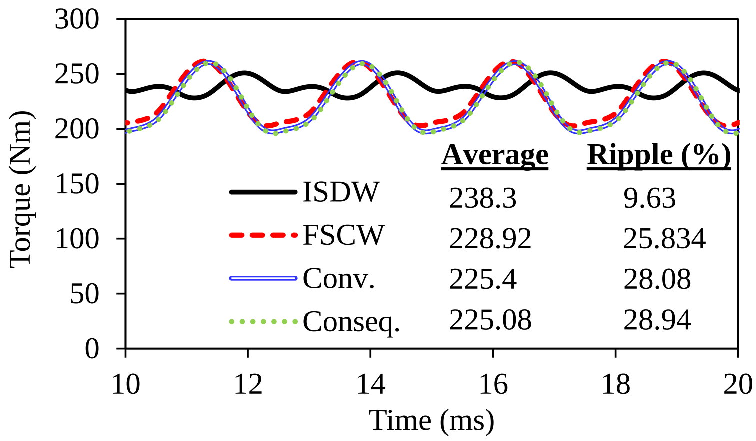


**Figure 2.15 :** Comparison of obtained torque waveforms.

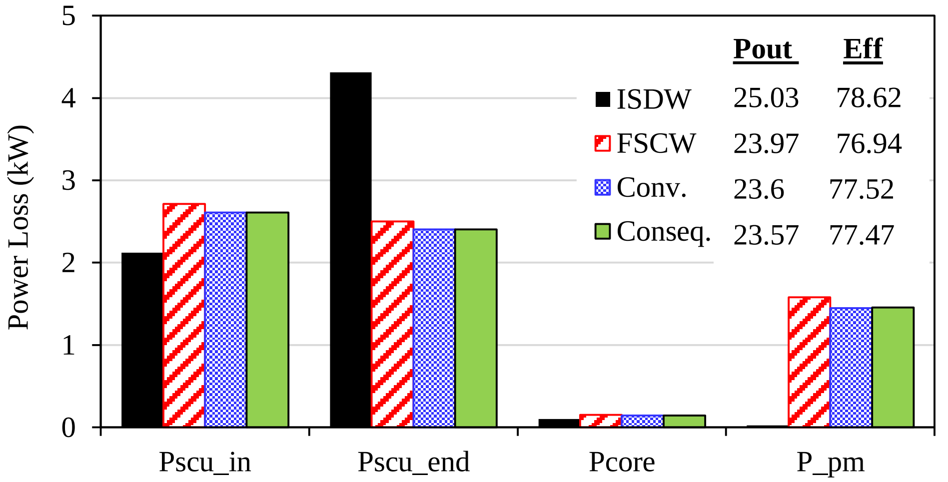


**Figure 2.16 :** Comparison of power losses, output power, and efficiency obtained after the utilization of the uneven number of turns method.

#### 2.2.3.4 Winding coils with different number of turns

The multi-layer winding with phase shifting method is illustrated in Figure 2.17. As seen in the figure, the each coil is separated into 2 coils. Then, the winding groups named gap-layer is shifted by a slot (mechanical deg.) whilst the yoke-layer is fixed all the time. Thus, it is possible to obtain different winding layouts. However, as can be realised, there are only 2 different shift angle available for 12S/8P combination which are 120°e and 240°e. In order to reveal the variation of the winding factor harmonics of the 12S/8P combination, the gap-layer is shifted by 360°m by using this method. Since the positions of the windings have changed by the shifting angle, the amount of the initial winding factor after phase shifting will be changed as expressed in (2.10).

$$k_{wh_{final}} = k_{wh_{initial}} \left|\cos\left(h\frac{\alpha}{2P}\right)\right| \tag{2.10}$$

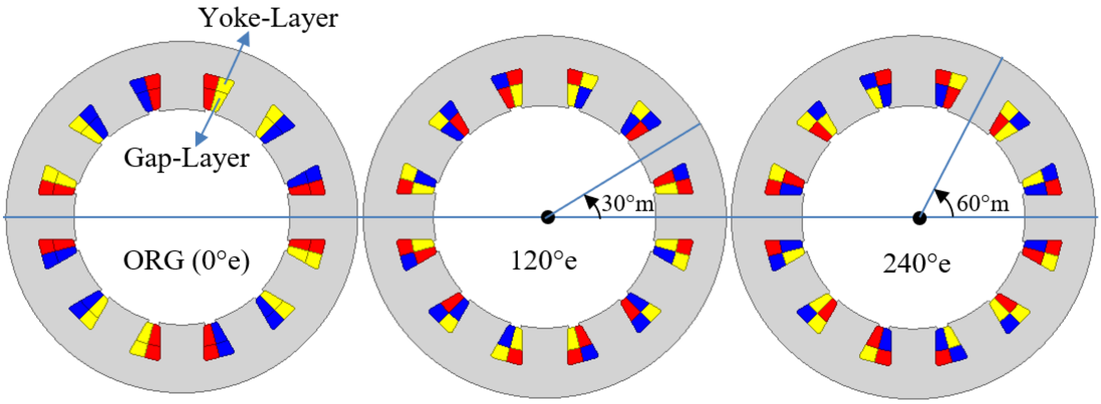


**Figure 2.17 :** Flux density and flux line distribution of the FSCW IPM machine.

where $k_{wh\_final}$ is the new winding factor after phase shifting is applied, $k_{wh\_initial}$ is the initial winding factor, $h$ is the harmonic order, $\alpha$ is the phase shifting angle, $P$ is the pole number. The variation of winding factor according to shifting angle is calculated by using (2.10) and the obtained results for the low-order and high-order winding factor harmonics are illustrated in Figure 2.18(a) and (b), respectively. As seen, the 4$^{th}$, 20$^{th}$, and 28$^{th}$ harmonics have the same trajectory whiles the remains have another trajectory. It is obvious that the fundamental winding factor reduces as between 0-360°e and finally becomes zero at 360°e. On the other hand, the 8$^{th}$, 16$^{th}$, and 32$^{nd}$ harmonics become maximum (0.866) at 360°e. Therefore, it can be concluded that the fundamental winding factor changed from 8-pole to 16-pole at 360°e. That is why it is expected that the average torque becomes zero. In the same manner, variation of the high-order harmonics are shown in Figure 2.18 (b). As seen in the figures, there is no possible shift angle to make reduce the harmonics to minimum. It can be predicted that there will be always a large amount of winding factor for this combination. The variation of the torque for ISDW, FSCW, and FSCW with different shift angles are illustrated in Figure 2.19. As clearly seen, the average torque is reduced considerably since the fundamental winding factor is reduced. Furthermore, the torque ripple is reduced for 120°e while it is increased for 240°e. The flux line and flux density distributions for different shift angles are shown in Figure 2.20. As seen, the saturation level is slightly reduced once the shift angle is assigned as 120°e.

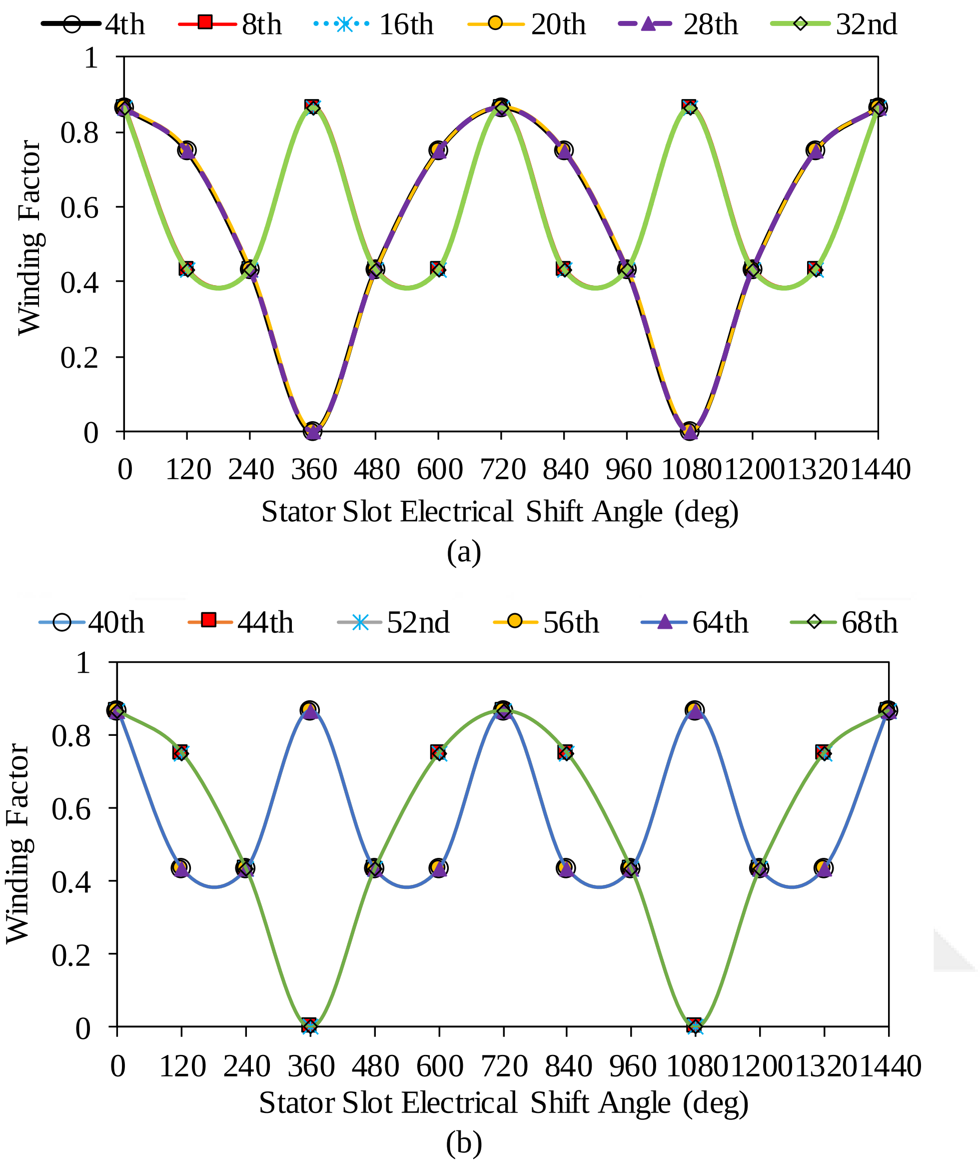


**Figure 2.18 :** Variation of low- and high-order winding harmonics with respect to shift angle.

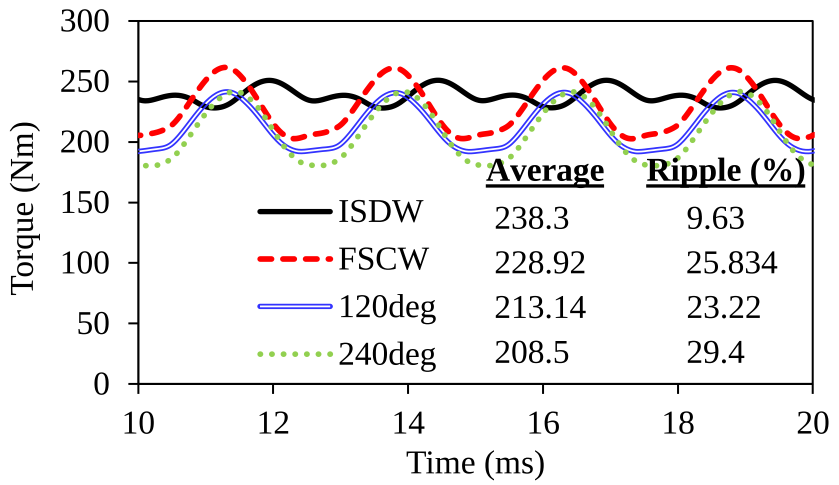


**Figure 2.19 :** Comparison of torque waveforms for different phase shift angles.

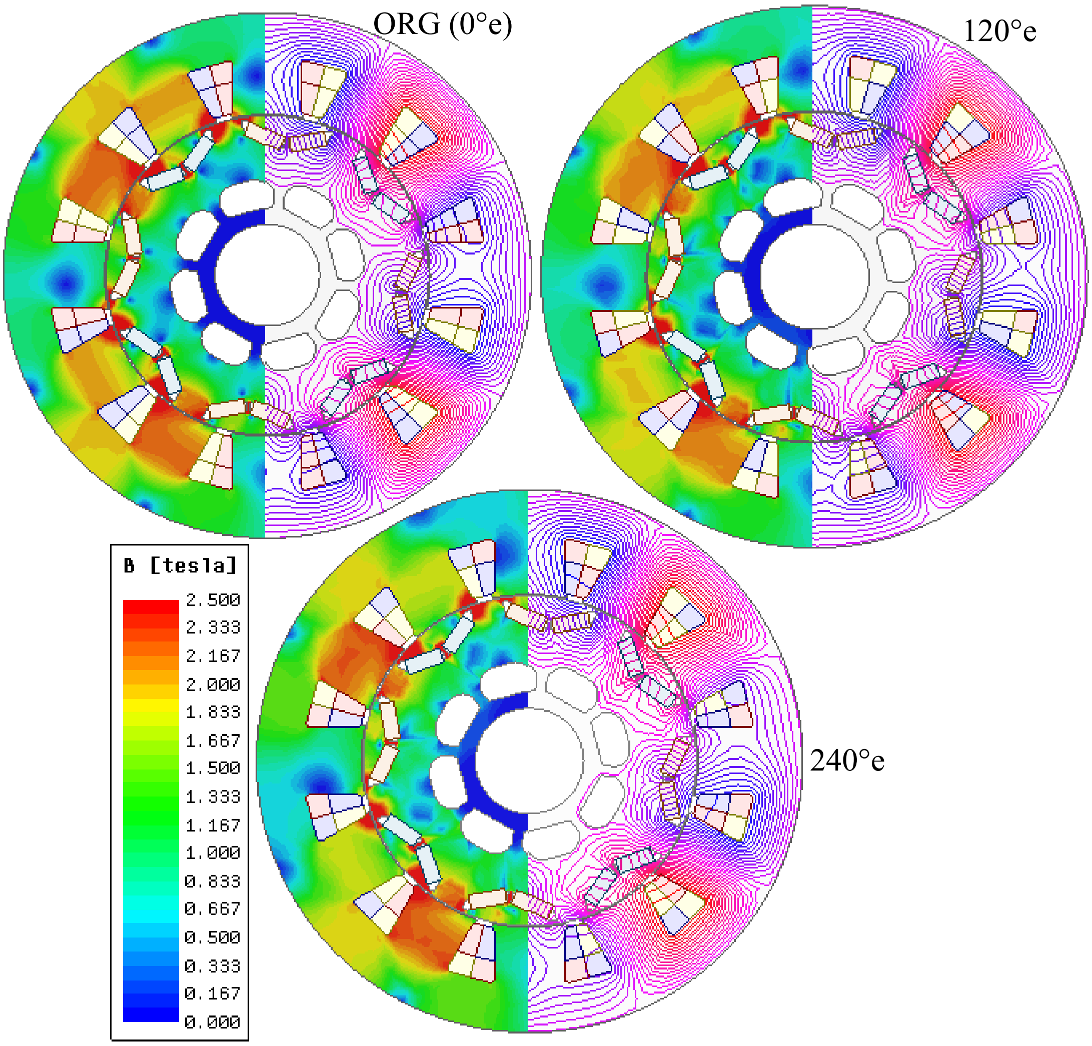


**Figure 2.20 :** Flux density and flux line distributions of the FSCW IPMs with different phase shift angles.

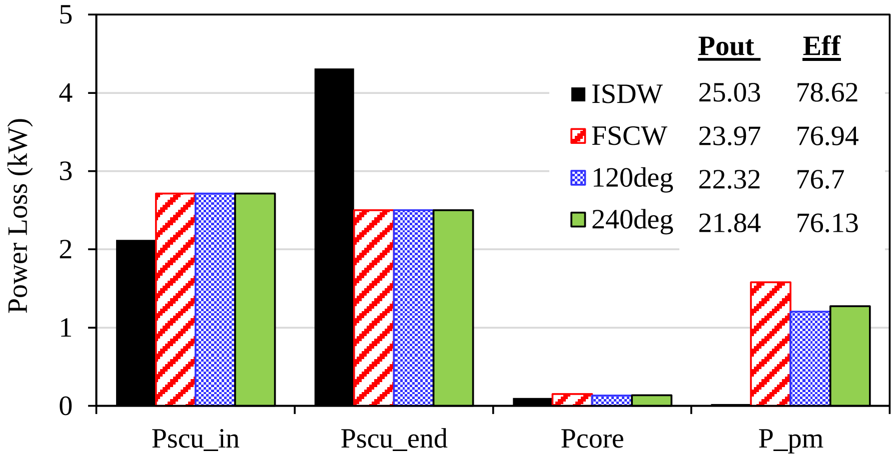


**Figure 2.21 :** Comparison of power losses, output power, and efficiency for different phase shift angles.

Comparison of the power loss, output power, and efficiency is shown in Figure 2.21. As seen in the figure, since the number of turns per coil is not changed, all the FSCW IPM machines have the same copper losses. Since the winding factor harmonics are reduced slightly, the level of the eddy current is reduced consequently. However, since the output power is reduced considerably, the efficiency is reduced consequently.

It can be concluded that although this method helps to reduce some of the winding factor harmonics, since it causes a reduction in the fundamental winding factor as well, the average torque and hence the output power is reduced. Is seems that it is not possible to reduce the MMF harmonics with this method without sacrificing the torque and efficiency.

#### 2.2.3.5 Stator with flux barriers

In order to reduce the MMF harmonics, the flux barriers can be placed to stator parts [74-77]. The possible variations for the place and number of the flux barriers are illustrated in Figure 2.22. As seen in Figure 2.22, the direction (shape) of the flux barrier can be either tangential or radial direction. Furthermore, the location of the flux barrier can be either on the stator slot body or yoke. In addition, it possible to use 1-flux barrier per slot or 1-flux barrier per 2-slots. The influence of flux barrier parameters on the performance of the FSCW IPM machine is investigated for various positions and flux numbers as follows.

The geometrical parameters of the tangential flux barrier on the stator tooth body parts is shown in Figure 2.23. The variation of the performance characteristics of the FSCW with 12-flux barriers (12-B) and 6-flux barriers (6-B) are shown in Figure 2.24 and Figure 2.25. It is obvious from the figure that the average torque reduces whilst the torque ripple increases as the barrier height is increased. Since the 12-B causes more saturation on the stator parts, its average torque variation is more sensitive to the barrier height. The variation of the PM loss and efficiency with respect to barrier height is illustrated in Figure 2.25. As seen, the variation of the PM loss and efficiency reduce slightly between 0-40mm barrier heights. However, after 40mm, PM losses increase significantly and consequently the efficiency reduce remarkably. Since the output power of 6-B FSCW IPM machine is higher than that of the 12-B FSCW IPM machine, its efficiency is higher even if the PM loss is higher.

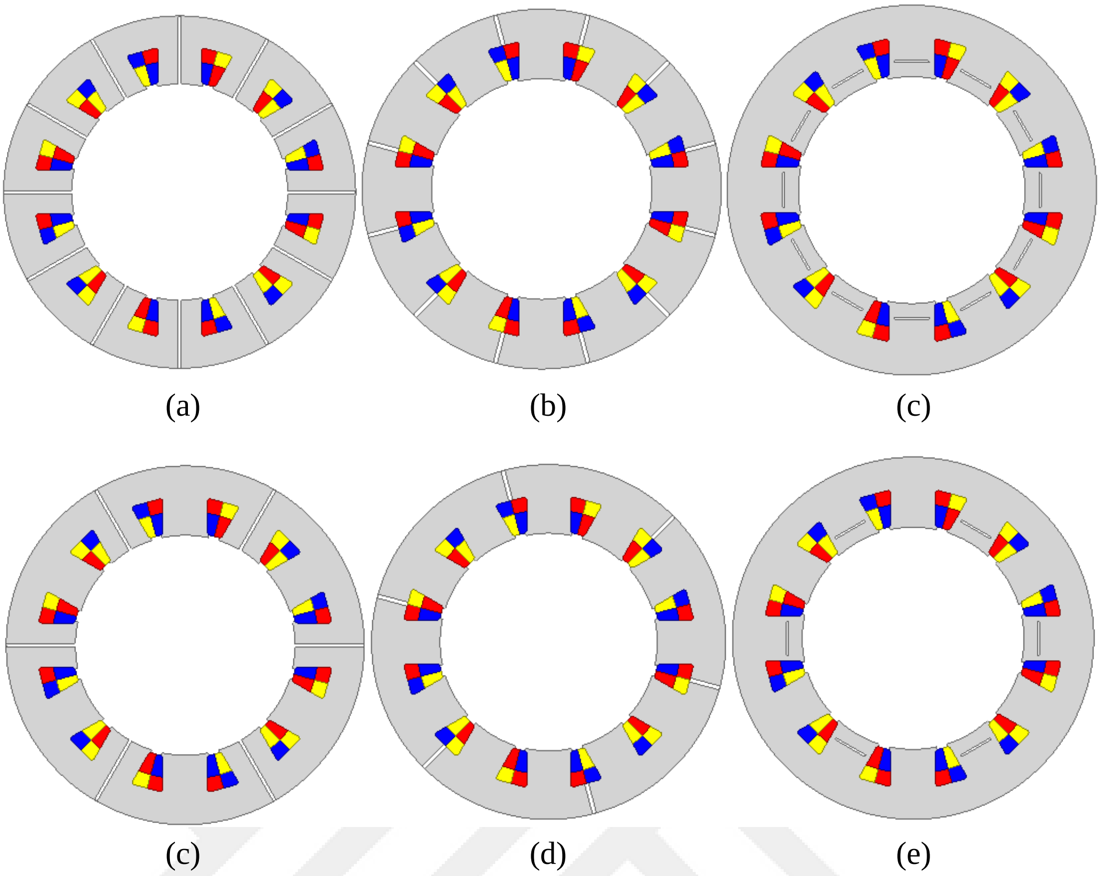


**Figure 2.22 :** Stator slots with radial and tangential flux barriers: 12-barrier versions (a-c) and 6-barrier versions (c-d).

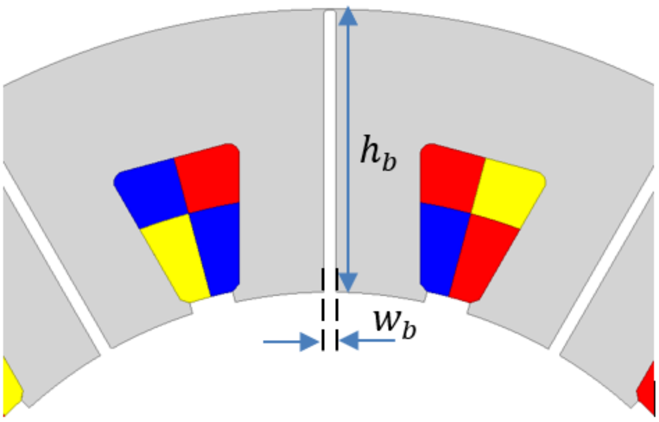


**Figure 2.23 :** Flux density and flux line distribution of the FSCW IPM machine.

Variation of the performance characteristics of the FSCW IPM with 12-B and 6-P with respect to tangential stator tooth flux barrier width are illustrated in Figure 2.26 and 2.27. As the tangential barrier width is increased, the average toque reduces and the torque ripple increases significantly for both 12-B and 6-B FSCW IPM machines. The speed of the torque ripple increase in the 6-B is faster than that of the 12-B as seen in Figure 2.26.

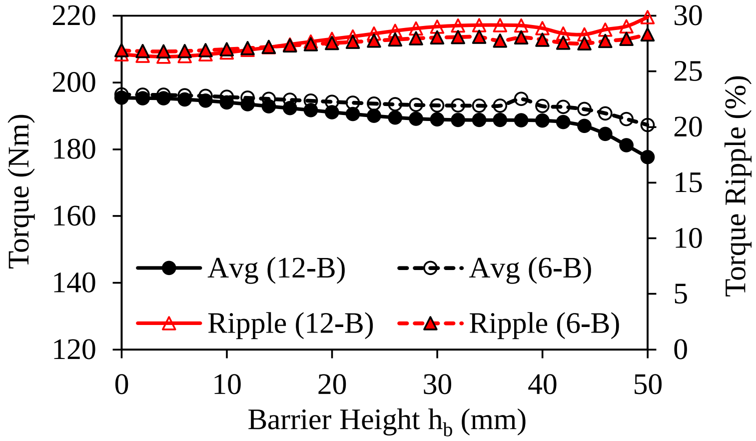


**Figure 2.24 :** Variation of torque and torque ripple with respect to stator tangential flux barrier height.

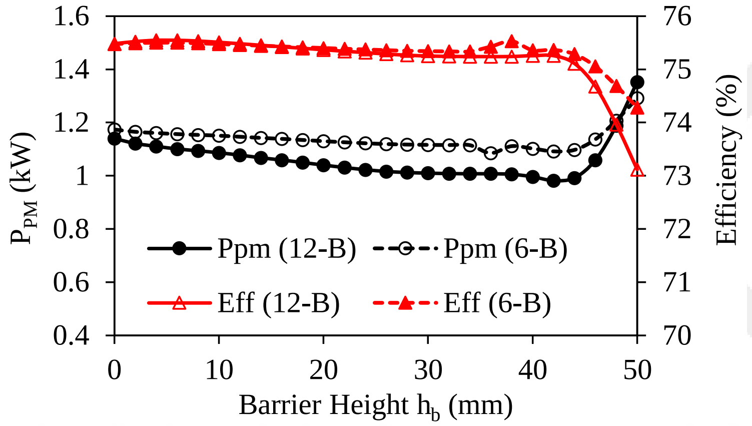


**Figure 2.25 :** Variation of the PM loss and efficiency with respect to stator tooth tangential flux barrier height.

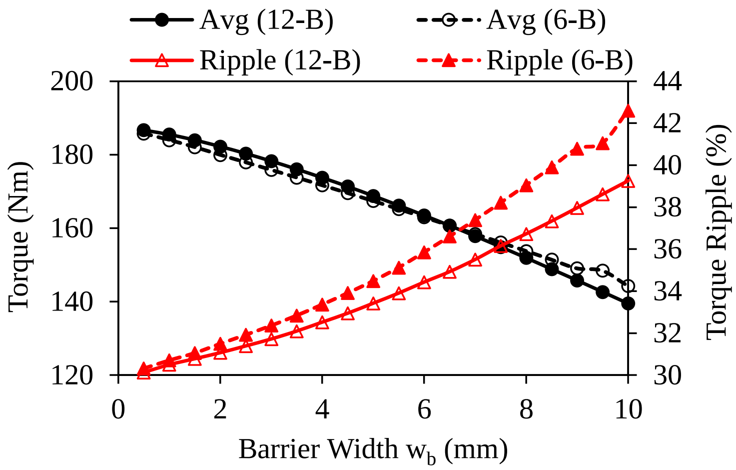


**Figure 2.26 :** Variation of average torque and torque ripple with respect to stator tooth tangential flux barrier width.

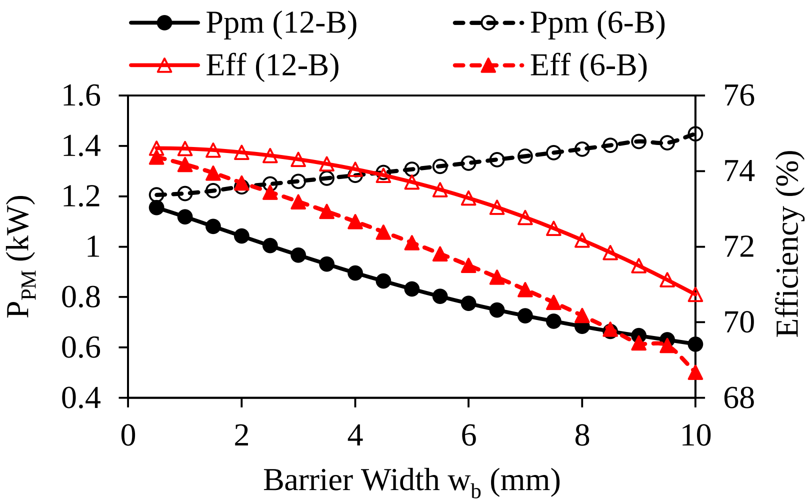


**Figure 2.27 :** Variation of the PM loss and efficiency with respect to stator tooth tangential flux barrier width.

The variation of the Ppm and efficiency with respect to tangential stator slot tooth flux barrier is shown in Figure 2.27. While the Ppm of the 12-B decreases, the Ppm of the 6-B increases as the barrier width is increased. Therefore, it can be deduced that the 1-flux barrier per tooth is more effective for reducing of the MMF harmonics. Moreover, since the torque and consequently the output power is reduced, the efficiency is reduced as the barrier width is increased. This is because of the increase in the level of the saturation of the stator parts.

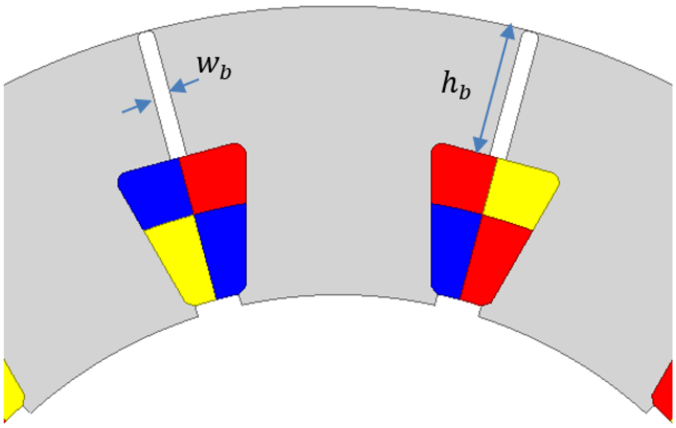


**Figure 2.28 :** Parameters of the tangential stator yoke flux barrier.

The geometrical parameters of the tangential flux barriers on the stator yoke are illustrated in Figure 2.28. As seen, there is only width and height parameters are considered. The variation of the average torque and torque ripple flux barrier width is shown in Figure 2.29. As seen, as the width is increased the average torque and torque ripple decrease consequently. Since the 12-B causes more saturation on the stator yoke parts, its average torque is more sensitive to change in the flux barrier width. The variation of the PM loss and efficiency with respect to width of the yoke flux barrier is shown in Figure 2.30. As seen, whilst the PM loss of the 6-B increases, it reduces in the 12-B. Therefore, efficiency reduction rate of the FSCW IPM machine with the 6-B is much faster than that of the FSCW IPM machine with the 12-B. The variation of the average toque, torque ripple, PM loss, and efficiency with respect to stator yoke tangential flux barrier height are illustrated in Figure 2.31 and Figure 2.32, respectively. As seen in Figure 2.31, as the height is increased, the average torque and torque ripple reduce considerably. In addition, as the barrier height is increased, the Ppm increases for the 6-B whilst it decreases in 12-B design. Therefore, efficiency reduction rate of the 12-B design is much lower than that of the 6-B design when the Ppm loss of the 12-B starts to reduce after 8mm as seen in Figure 2.32.

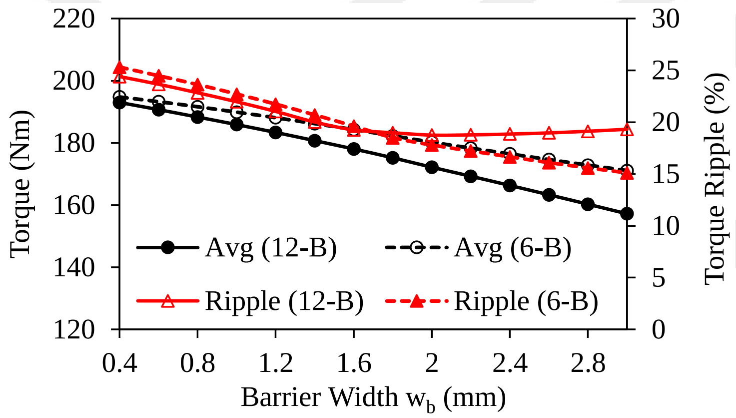


**Figure 2.29 :** Variation of the average torque and torque ripple with respect to stator yoke tangential flux barrier width.

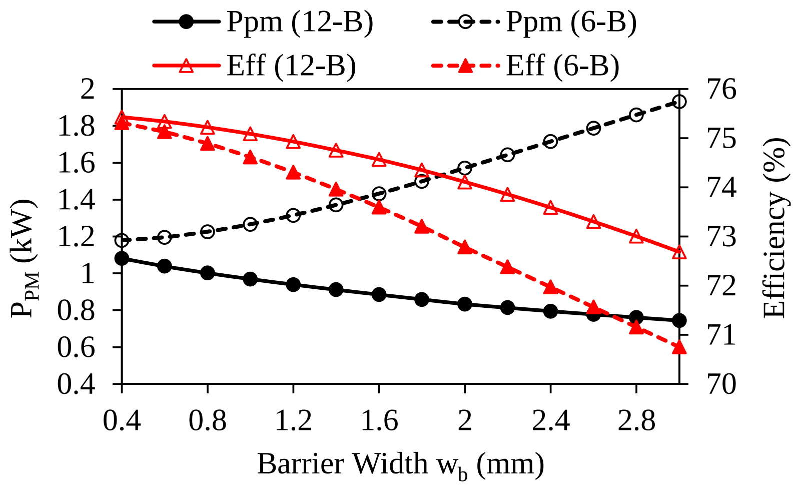


**Figure 2.30 :** Variation of the PM loss and efficiency with respect to stator yoke tangential flux barrier width.

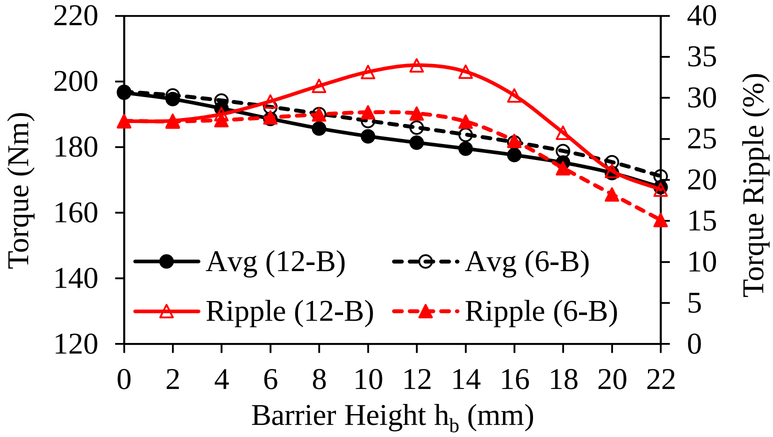


**Figure 2.31 :** Variation of the average torque and torque ripple with respect to stator yoke tangential flux barrier height.

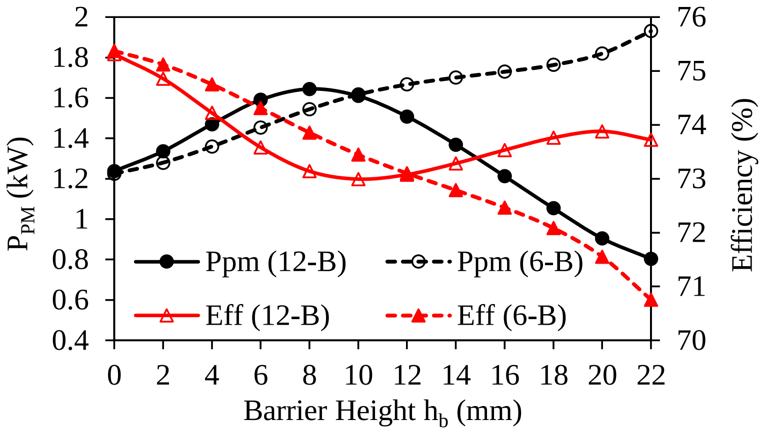


**Figure 2.32 :** Variation of the PM loss and efficiency with respect to stator yoke tangential flux barrier height.

The geometrical parameters of the radial flux barriers on the stator tooth parts are illustrated in Figure 2.33. As seen in the figure, there are 3 parameters, namely barrier width, height, and position height. The variation of the performance characteristics with respect to these geometric parameters are illustrated between Figure 2.34 and 2.39. The variation of the average torque and torque ripple with respect to stator tooth radial flux barrier width is illustrated in Figure 2.34. As the barrier width is increased, the average torque and torque ripple decrease remarkably. Since the saturation factor of the 12-B design is higher, the torque and ripple reduction of the 12-B is much faster than that of the 6-B. The variation of the Ppm and efficiency with respect to stator tooth radial flux barrier width is shown in Figure 2.35. As seen the amount of Ppm and efficiency reduces as the barrier width is increased for both of the IPM machines. However, since the saturation level of the 6-B is much lower than that of the 12-B, the reduction rate of the 6-B is slower.

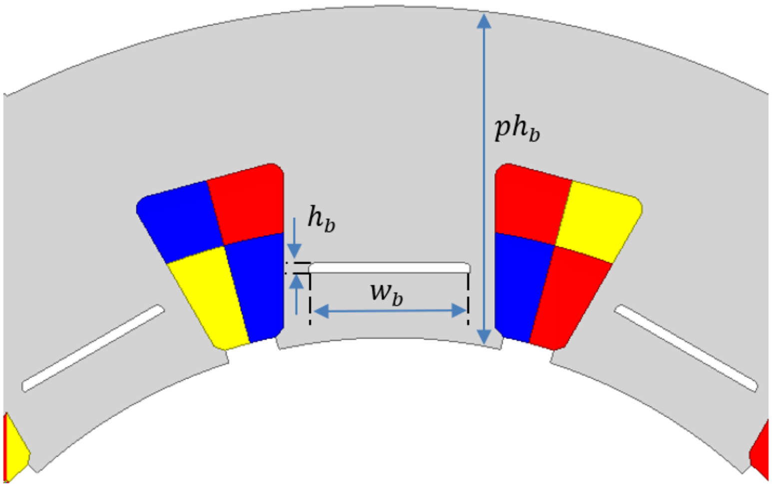


**Figure 2.33 :** Parameters of the stator tooth radial flux barrier.

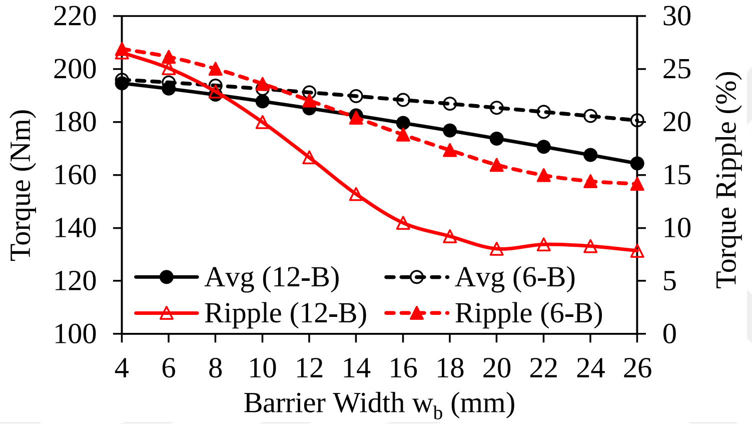


**Figure 2.34 :** Variation of the average torque and torque ripple with respect to stator tooth radial flux barrier width.

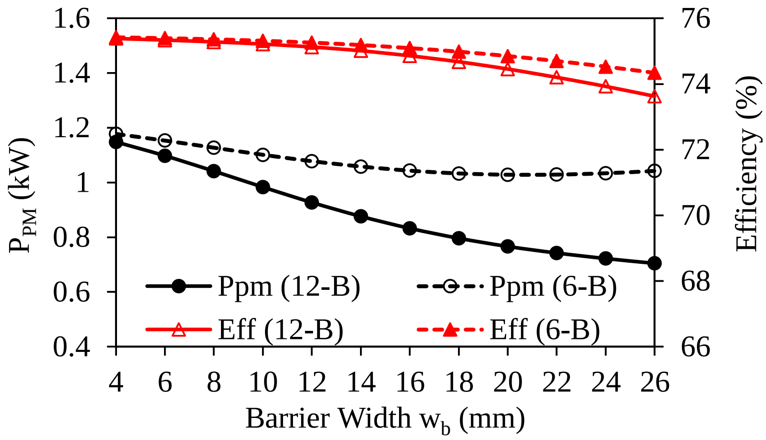


**Figure 2.35 :** Variation of the PM loss and efficiency with respect to stator tooth radial flux barrier width.

The variation of the torque and torque ripple with respect to barrier height is illustrated in Figure 2.36. As seen, the average torque of the both machines reduce as the barrier height is increased. On the other hand, torque ripple of 12-B increases whilst the 6-B decreases as the barrier height is increased. The Ppm and efficiency against the barrier height are shown in Figure 2.37. The $P_{PM}$ of 12-B decreases while the 6-B increases as the barrier height is increased. However, as seen in the figure, since the output power of the 12-B reduces much faster than that of the 6-B, the efficiency of the 6-B is considerably higher.

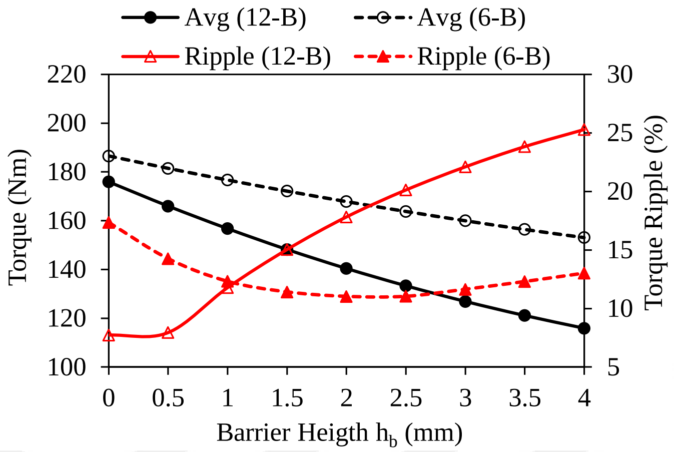


**Figure 2.36 :** Variation of the average torque and torque ripple with respect to stator tooth radial flux barrier height.

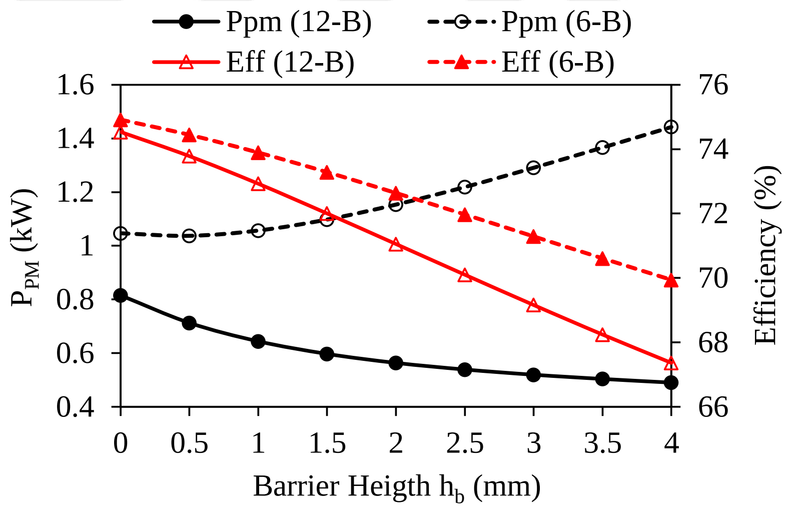


**Figure 2.37 :** Variation of the PM loss and efficiency with respect to stator tooth radial flux barrier height.

The variation of the average torque and torque ripple with respect to position height is shown in Figure 2.38. As seen, as the radial flux barrier is moved away from the stator tooth body, the average torque increases for both 12-B and 6-B. On the other hand, the minimum torque ripple can be obtained once the radial flux barrier around the middle of the stator tooth body. The variation of the PM loss and efficiency with respect to position height is shown in Figure 2.39. As seen in the figure, as the radial flux barrier is getting close to the yoke (moving away from the tooth body towards to the stator yoke), the PM loss (due to the increase in the torque) and efficiency (due to the increase in the output power) increase considerably.

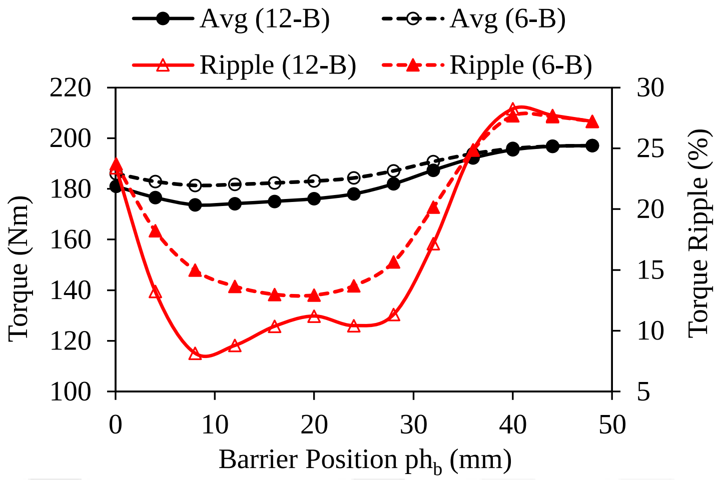


**Figure 2.38 :** Variation of the average torque and torque ripple with respect to position stator tooth radial flux barrier.

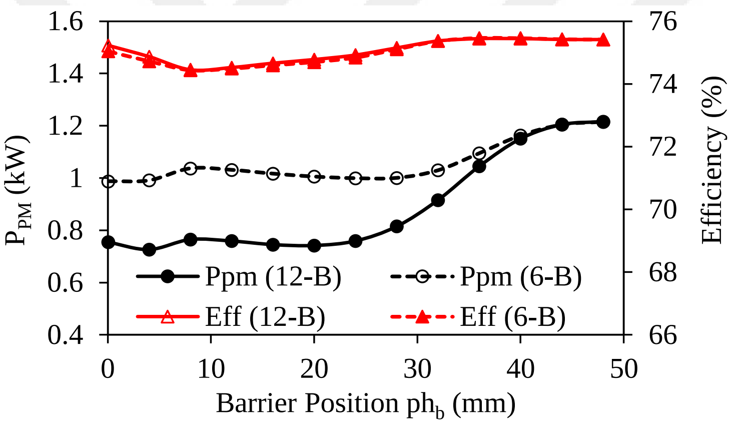


**Figure 2.39 :** Variation of the PM loss and efficiency with respect to position stator tooth radial flux barrier.

Considering figures between Figure 2.24 and 2.39, it can be concluded that it is reasonable to not use flux barriers in the tooth body in terms of torque and efficiency. Because, as seen in the figures, utilizing flux barriers cause to reduce the torque, output power, and efficiency.

Summary on the effectiveness of the proposed methods is given in Table 2.2. It is obvious that any proposed methods cause a decrease in the average torque and consequently output power. For the chosen 12S/8P combination, which does not contain any sub-harmonics, it is not possible to reduce the MMF harmonics without sacrificing the key performance characteristics such as average torque, output power, and efficiency.

**Table 2.2 :** Compariosn of the MMF reduction methods in terms of electromagnetic performance.

<table>
<tr><th colspan="2"></th><th>Average Torque (Nm)</th><th>Output Power (kW)</th><th>Torque Ripple (%)</th><th>Copper Loss (kW)</th><th>PM loss (kW)</th><th>Efficiency (%)</th><th>Total Axial Length (mm)</th></tr>
<tr><td colspan="2">ORG (ISDW)</td><td>238.3</td><td>25.04</td><td>9.63</td><td>6.433</td><td>0.02</td><td>78.62</td><td>112.8</td></tr>
<tr><td colspan="2">Method#1 (FSCW)</td><td>228.92</td><td>23.97</td><td>25.83</td><td>5.216</td><td>1.58</td><td>76.94</td><td>95.02</td></tr>
<tr><td colspan="2">Method#2a (FSCW+Uneven Turn)</td><td>225.08</td><td>23.604</td><td>28.08</td><td>5.015</td><td>1.448</td><td>77.52</td><td>93.22</td></tr>
<tr><td colspan="2">Method#2b (FSCW+120ºe Shift)</td><td>213.92</td><td>22.32</td><td>23.22</td><td rowspan="5">5.126</td><td>1.21</td><td>76.7</td><td rowspan="5">95.02</td></tr>
<tr><td rowspan="2">Method#3 Tooth</td><td>6-B</td><td>196.36</td><td>20.56</td><td>26.82</td><td>1.17</td><td>75.49</td></tr>
<tr><td>12-B</td><td>195.31</td><td>20.45</td><td>23.05</td><td>1.12</td><td>75.52</td></tr>
<tr><td rowspan="2">Method#3 Yoke</td><td>6-B</td><td>195</td><td>20.4</td><td>25.3</td><td>1.18</td><td>75.3</td></tr>
<tr><td>12-B</td><td>193.02</td><td>20.21</td><td>24.41</td><td>1.08</td><td>75.43</td></tr>
</table>

### 2.3 Prediction of Temperature Distribution From Total Loss Distributions

As known, there is a direct correlation between the power losses and electromagnetic loading. The increase of electric loading leads an increase in the amount of the copper loss while the increase of magnetic loading mainly increases the amount of the core losses. In addition, increase of mechanical loading causes to the increase of friction and windage losses. Increase of the power loss is the main reason behind the increase of the temperature rising. Therefore, in order to predict the temperature distribution of IPMs, total loss distributions have been calculated as illustrated in Figure 2.40. Note that end-winding copper loss has not been considered in Figure 2.40. As seen in the figure, because of the very high amplitude of the MMF harmonics, the total core loss amounts of FSCW IPMs are quite higher than that of the ISDW IPM. In the same manner, the PM loss of the FSCW IPMs are higher than that of the ISDW IPM. On the other hand although the (see Figure 2.13) end-winding loss of the FSCW IPMs are lower than that of the ISDW IPM, the in-slot copper loss are higher due to the high number of turns requirement of FSCW IPMs (see Table 2.3). By using the average total losses at the different parts of the machines, the thermal analyses of the ISDW, 2-layer FSCW, and 4-layer FSCW with 120°e phase shifted IPMs are conducted via FEA by assigning the cooling material properties given in Table 2.3. The obtained steady-state temperature of different parts are listed in Table 2.4.

Since the high harmonic content of the FSCWs give a rise to the losses, particularly eddy current losses, the temperature of the PMs are quite higher (more than twice) than that of the ISDW IPM. In addition, since the number of slots of FSCW IPMs are lower, the heat dissipation area of the windings are reduced considerably (see Table 2.4). That is why the slots of the FSCW IPMs have higher temperature in the slots. In addition, it is also shown that the temperature of the magnets have been reduced considerably by using multi-layer phase shifting method. Therefore, it can be concluded that the FSCW IPMs requires more cooling equipment.

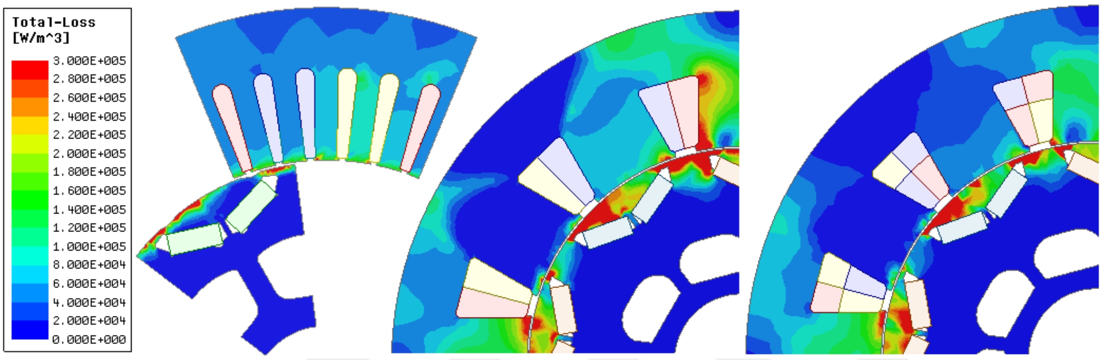


ORG (ISDW) Merhod#1 (FSCW) Merhod#2b (FSCW+120°e Shift)

(a) Core loss distributions

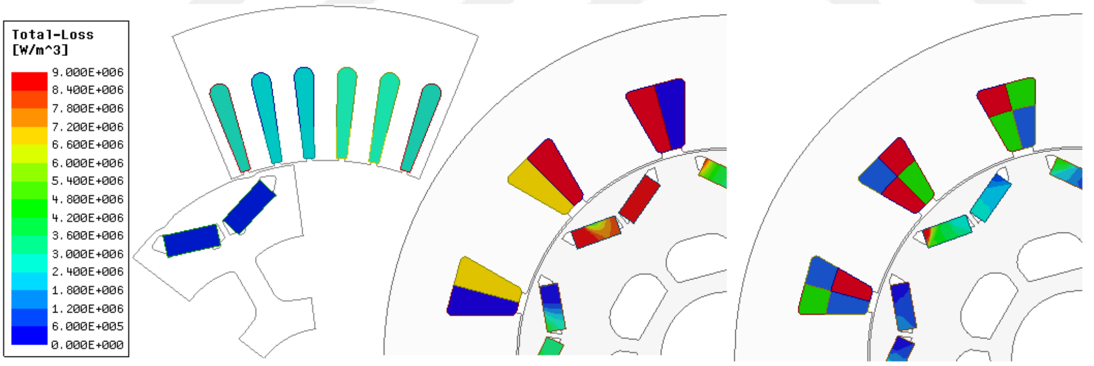


ORG (ISDW) Merhod#1 (FSCW) Merhod#2b (FSCW+120°e Shift)

(b) Excitation loss (copper and PM) distributions

**Figure 2.40 :** Core and excitation source total loss distributions.

**Table 2.3 :** Cooling material and stator winding specifications.

| | ORG (ISDW) | Method#1 (FSCW) | Method#2b (FSCW+120°e Shift) |
|---|---|---|---|
| Cooling system | Housing water jacket (Horizontal) | | |
| Fluid vol. flow rate | 12 | | |
| Inlet temperature (°C) | 40 | | |
| Fluid material | EGW (50/50) | | |
| Lamination stacking factor | 0.97 | | |
| Number of parallel branch | 1 | | |
| Stator slot fill factor | 0.488 | 0.62 | |
| Number of serial turns | 88 | 104 | |
| Number of turns per slot | 11 | 52 | |
| Current Density (A/mm$^2$) | 25.23 | 30.4 | |

**Table 2.4 :** Steady-state average temperature of IPMs in different parts under rated operating through simulation calculation (°C).

| | Temperature (°C) | | |
|---|---|---|---|
| | **ORG (ISDW)** | **Method#1 (FSCW)** | **Method#2b (FSCW+120°e Shift)** |
| Housing | 40.4 | 40.3 | 40.3 |
| Stator yoke | 43.7 | 42.9 | 42.2 |
| Stator tooth body | 55.1 | 48.9 | 48.1 |
| Stator tooth tip | 50.1 | 46.4 | 45.9 |
| Stator in-slot winding | 94.3 | 152.1 | 151.2 |
| Stator end-winding | 97.2 | 157.4 | 155.1 |
| Magnet | 40.1 | 93.3 | 74.7 |
| Rotor core | 40.1 | 57 | 48.2 |
| Shaft centre | 40 | 42 | 40.5 |

### 2.4 Conclusions

This section of the thesis investigates the current state-of-the-art of the MMF harmonic reduction techniques for FSCW configurations in IPM machines, including multi-layer winding with phase shift, different number of turns per coil side (uneven turn numbers per coil side) and stator flux barriers. Merits and demerits of each method have been discussed and verified by numerical analyses by FEM. The milestones of the study may explained as follows.

Firstly, the Toyota Prius 2010 IPM machine with ISDWs is designed and analysed. Secondly, the accurate slot/pole number combination for the FSCW topology is determined and the IPM machine with FSCW technique is designed and analysed. Finally, the MMF cancellation methods given below are adopted for the FSCW IPM machine.

a) The different number of turns per coil side (uneven number of turns per coil side) method;

b) The multi-layer winding with phase shifting method;

c) The flux-barrier method including the parametric analysis of the flux barrier's position and dimensions;

A comprehensive comparative study on the electromagnetic performance characteristics between IPM machines designed with the ISDW technique and the FSCW technique combined with one/some of the utilized methods has been conducted. In addition, thermal analyses have also been conducted by using the total loss distributions of the IPMs. In this study, obtained key findings can be summarized as follows.

- It is validated that very short end-windings and low end-winding copper loss are achieved by adopting the FSCW technique;

- The FSCW technique cause a dramatic increase in the eddy losses including the rotor core and PM losses;

- Since the leakage flux density of the IPM machine designed by utilising the FSCW technique is much higher than that of the IPM machine designed by utilizing the ISDW technique, the obtained average torque of the FSCW IPM machine lower;

- Adopting the multi-layer winding configuration increases the complexity of the winding structure and causes to obtain lower fundamental winding factor and consequently low torque production capability.

- Adopting the uneven number of turns per coil causes a decrease in the average torque and a slightly decrease in PM loss, but it also leads an increase in the efficiency. In addition, it also causes to less effective utilization of the slots;
- Adopting multi-layer and phase shifting method and using flux barriers on the stator is not favourable in terms of average torque, output power, and efficiency;
- It has been shown that the considered MMF reduction methods have very limited effect on the MMF harmonics of the chosen 12S/8P combination which has no sub-harmonics;
- It has been revealed that since the large amount of MMF harmonics of the FSCWs cause a significant increase in the total losses, the temperature of the magnets quite higher under the same operating condition. In addition, it has also shown that reduction of the number of stator slots causes a remarkable reduction at the heat dissipation area of the windings;
- The IPMs equipped with FSCWs require more cooling equipment.

# 3. DESIGN AND ANALYSIS OF INTERIOR PERMANENT MAGNET MACHINES EQUIPPED WITH NOVEL SEMI-OVERLAPPING WINDINGS[2]

A novel winding topology, comprising of semi-overlapped windings has been proposed in this chapter. The main advantages of such winding over conventional-distributed (overlapping) and fractional-concentrated (non-overlapping) windings are having very short-end winding lengths and significantly low MMF harmonic content, respectively. The key design rules, basic properties, and other merits and demerits of the proposed novel winding topology are justified. The key performance characteristics of the proposed winding topology are disclosed through an IPM machine. The obtained electromagnetic analyses results are compared with those of other IPM machines having conventional-distributed and fractional-concentrated windings. It has been demonstrated that the proposed winding topology promises significant superiorities; such as improved efficiency with substantially reduced total axial length, low eddy current losses and low risk of irreversible magnet demagnetization over other winding topologies. The analysis is verified by finite-element analysis results and experiments on a prototype novel semi-overlapping winding IPM machine.

## 3.1 Introduction

With ever-increasing ecological awareness, such as climate change, air pollution, public health, and the shortage of fossil-fuel resources, the focus on automotive and aerospace electrification is intensely increasing each passing day. Because of the superb properties, including high torque density and high efficiency over a wide operation range, permanent magnet (PM) machines, particularly interior-PM (IPM) machines, have been widely adopted as traction electrical machine in the EV applications [82-84]. Considering the demand for electrification of automotive and

---

[2] This chapter is based on the paper: **Gundogdu, T. and Komurgoz, G.** (2020) Design and Analysis of Interior Permanent Magnet Machines Equipped with Novel Semi-overlapping Windings, *IET Elect. Power Appl.*, *14*(8), 1446-1457.

aerospace traction systems, improving the machine performance is of great significance in terms of national economy and efficient use of energy sources. For over a decade, great efforts have been made in research and in performance improvement of the electrical machines [85-117]. Some of these studies have been categorized as follows.

To reduce the length of the end-winding, which has no influence on the air-gap magnetomotive force (MMF) and only performs the connections between the in-slot conductors, is one of the most important and easy way to improve the machine performance, particularly the torque/power density and efficiency. The aim of reducing the end-winding axial length is to decrease the most dominant machine loss, which typically is the stator copper loss, and to decrease the total axial length to reduce the space requirement (promote compactness) of the electrical machines. The most recent performance improvement methods related to electrical machine windings have been listed as follows.

- Multi-layer fractional-slot concentrated windings (FSCWs) and integer slot concentric windings with phase shifted and un-even number of turns per coil side [85-97, 116-119]. In addition, FSCWs having more than 2 layers [87, 89, 94-97, 107-109, 111, 117];
- Conventional short-pitch and short-pitch with different number of turns winding topologies [96-100];
- Stator cage windings [101, 103];
- Combined star-delta windings [103-106];
- Shifted FSCWs with additional sets of windings [107-110];
- Toroidal type windings [111, 112];

However, since limited improvements have been achieved after implementing these methods, it is observed that the performance characteristics of the machines are still not satisfactory. The key problems and restrictions of implementing these methods into the stator windings have been summarized as follows:

- Reduced fundamental winding factor: much greater number of turns is required to tolerate the torque;

- Restricted number of turn ratios: At least two set of windings should be used, and the turn ratio of the winding groups should be equal to a constant number;
- Restricted pole number: Some topologies are suitable for only low pole combinations;
- Increased risk of irreversible magnet demagnetization: Quite high eddy current losses, particularly PM loss;
- Increased cooling equipment size: Quite high eddy current losses, particularly in the rotor part;
- Significantly increased cost: Increased power electronic device usage and increased manufacturing cost;
- Increased parasitic effects; such as torque ripple, acoustic noise, vibration, etc.

It has been shown that by using the FSCW configuration, the copper loss can be reduced considerably owing to both the short end-winding length and the high copper packing factor (if the segmented stator structure is employed). Furthermore, the cogging torque can also be reduced significantly when the least common multiple of the slot number and the pole number increase. However, by employing FSCW configurations in PM machines, the rotor PMs are subjected to a large amount of MMF (space) harmonics and consequently incur high eddy current loss [113, 114]. This can further lead to a high rotor temperature particularly at high speed operating regions, and hence the rotor magnets will suffer from a high risk of irreversible demagnetization. Yet, compared to the FSCW configurations, the integer-slot distributed winding (ISDW) configurations have lower copper packing (fill) factor since prepressed windings with segmented stator structures cannot be used, and have longer end-winding length, higher cogging torque, and less fault tolerant owing to higher mutual inductance and winding overlapping [115, 116]. Consequently, the FSCW configurations are of potential to be employed in IPM machines, once the sub- and super-harmonic contents of the stator MMF can be suppressed to a desirable level. Yet, a recent study [119] has been shown that, even though several different MMF harmonic reduction methods have been applied to an IPM machine with 12S/8P

FSCWs, excessive eddy current losses in PMs are inevitable since the MMF harmonics could not be suppressed sufficiency. Subsequently, the FSCW topology is not suitable for the IPM machines in large power applications. Consequently:

I. A new winding topology with short-end windings and low MMF harmonics should be developed;

II. Alternative machine topologies with no excitation source on rotor suitable for FSCW topology (i.e. synchronous reluctance machines (SRMs)) might be advanced.

This study focuses on the option (I). It is worth noting that the previous basic study [40] introduced a novel winding topology having substantially short-end windings compared to ISDWs and quite low MMF harmonic content compared to FSCWs. Investigation into the influence of some key winding parameters and comparison of electromagnetic performance characteristics with different winding topologies have also been presented for small machine size in [118]. This study extends to show how the proposed winding topology is feasible for large machine size (*LD*). This study also includes saturation and demagnetization analyses and experimental verification of analytical and numerical analyses by manufactured prototype of novel semi-overlapping winding (NSW) IPM machine. Note that direct measurements of eddy current losses in magnetic core and PMs could not be conducted. Nevertheless, their verifications are supported by the experimental verifications of overall efficiency. Moreover, this study demonstrates that thanks to the proposed winding topology, more compact IPM machines or IPM machines with significantly improved electromagnetic performance characteristics can be designed and manufactured.

The major objective of this chapter is to evaluate and validate the merits and demerits of the proposed NSW topology. In Section 3.2, the key design rules are explained and various parametric analyses, including influence the number of layers, number of turns combinations and number of stator slots on the air-gap flux density and torque, are conducted to be able to determine the finest values of the winding parameters. To reveal the pros and cons of the NSW topology, electromagnetic performance characteristics obtained from the IPM machines designed with single- and double-layer ISDWs and FSCW topologies are comprehensively compared with the IPM machine designed by the NSWs in Section 3.3. The magnetic saturation and PM demagnetization issues are also examined together with the influence of the machine size on the dominant machine losses. The prototype machine and its experimental results together with the validation of the 2-D, non-linear, time-stepping finite-element analysis (FEA) predictions are shown in Section 3.4. Finally, the conclusions and future work are drawn in Section 3.5.

### 3.2 Development of Novel Semi-Overlapping Winding Topology

The major objective of developing such a winding is to reduce the axial length of end-windings for achieving more compact machine design and improve the overall performance characteristics such as torque/power density and efficiency.

As presented in the previous section, a great amount of effort has been made to reduce the end-winding both axial and radial lengths with the aim of improving the performance and/or compactness of the electrical machines. In this section, design rules and key properties of the NSW topology are presented. In the existing literature, some similar winding topologies may be found with single phase [96, 97, 109] or semi-filled stator slots [95] or with different number of turns per concentrated coils [98, 99, 108]. Nevertheless, since the fundamental winding factor amplitude is reduced, the number of turns between the winding groups are restricted to a constant rate, and half of the stator slots are not fully filled, the reported electromagnetic performance results are not satisfactory. Thus, this study will be the first study presenting a new winding topology having substantially short-end winding with remarkably high torque density compared to conventional distributed winding and significantly low MMF harmonic content, and relatively high fundamental winding factor amplitude compared to concentrated winding topologies.

With the purpose of utilizing the proposed NWS topology for any integer stator slot $S$ and pole number $P$ combination, the key rules are deducted as follows by considering the winding design rules presented in [120].

1) Determine number of coils $N_c$ by using (1)

2) Determine coil pitch number $y_c$ by using (2)

3) Determine phase pitch number $\alpha_{120}$ by using (3)

4) Determine the number of turns. Note that most convenient coil pitch number is $y_c \leq 6$ for $S \leq 48$ and $y_c \leq 12$ for $S \leq 96$ and so on. Hence, the empirical formulation is derived as follows:

   a. For *2L*: $N_{t1}/N_{t2} = 7x/x$

   b. For *3L*: $N_{t1}/N_{t2}/N_{t3} = 7x/4x/x$

$$N_c = \frac{S}{2m} \tag{3.1}$$

$$y_c = \text{round}\left(\frac{S}{P}\right) \quad \text{if} \quad y_c = \begin{cases} even \rightarrow y_c = y_c - 1 \\ odd \rightarrow y_c = y_c \end{cases} \tag{3.2}$$

$$\alpha_{120} \approx \frac{N_c}{120} \quad \text{if} \quad \begin{cases} \alpha_{120} < 2 \rightarrow +,+,+,+\cdots \\ \alpha_{120} \geq 2 \rightarrow +,-,+,-\cdots \end{cases} \tag{3.3}$$

For the sake of demonstrating the winding layout of the NSW topology, a 24-stator slot and 4-pole ($24S/4P$) combination has been selected. Eventually, $y_c$ is calculated as 6. Furthermore, the number of layers $L_c$ is assessed as 3. After the required calculations presented from (3.1) to (3.3), the achieved winding layout is illustrated in Figure 3.1(a). A fully non-overlapped winding topology can be designed by taking $\alpha_{120} = 1$ for the considered $S/P$ combination. Nevertheless, in that case, the MMF harmonic cancellation/reduction cannot be accomplished effectively. Another key element in the winding design procedure is to consider the winding inductances. With the aim of avoiding additional disturbances such as unbalanced magnetic pull (UMP), torque ripple, acoustic and magnetic noises, etc., the coil distributions of each phase should be symmetrically balanced. Thus, inductance of each phase winding should be identical. As illustrated in Figure 3.1, only the ‘Phase B’ coil is overlapped. Moreover, each coil member in a phase winding has different number of turns as declared previously. Therefore, to create a symmetrical and balanced winding layout, the total number of turns in each slot should be equal. Otherwise, it is impossible the achieve identical inductance per phase. For the sake of simplifying the illustration of the winding layout, Figure 3.1(b) is provided. Hereby, slots of the windings and the semi-overlapped winding group can be seen easily. The distribution of the number of turns per coil sets and semi-overlapped winding structure are illustrated in Figure 3.2. Furthermore, variation of corresponding winding self- and mutual-inductance is illustrated in Figure 3.3. It has been evident from the figure that the same amount of the inductance has been achieved as a result of symmetrically distribution of balanced phase windings over the stator slots.

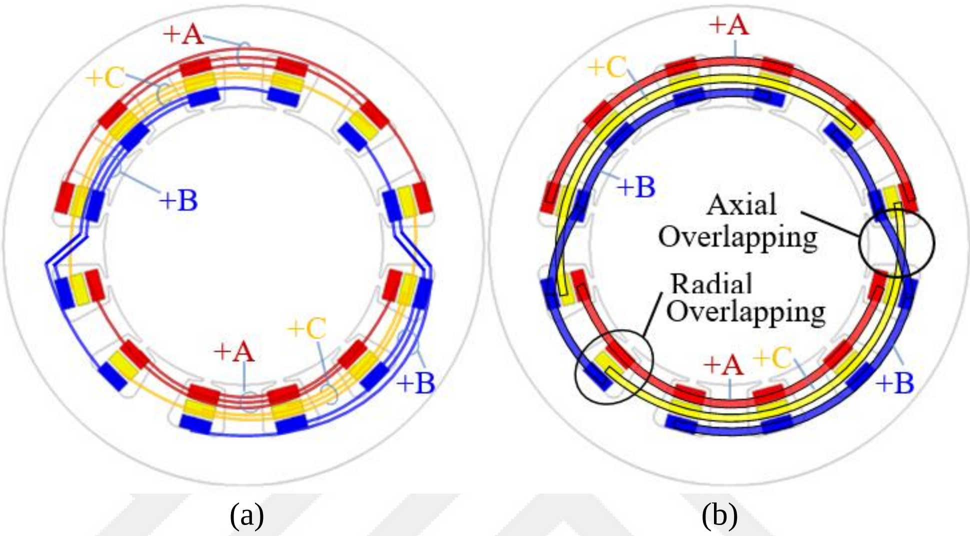


**Figure 3.1 :** Winding layout of NSW topology: (a) Open form illustration of each coil sets, (b) Close form illustration of phase coils (simplified illustration).

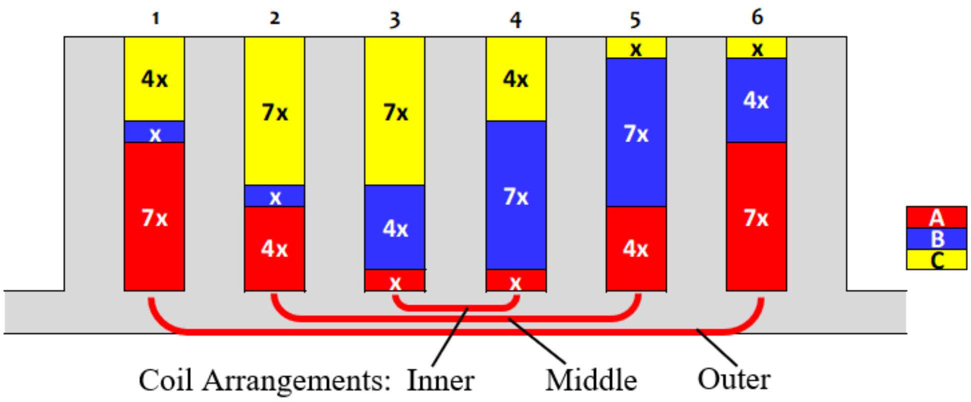


**Figure 3.2 :** Distribution of turn numbers of phase coils per slot.

As shown in Figure 3.2(b), not only the axial overlapping is exist because of the arrangement of the ‘Phase B’ coils over other phases, but also a radial overlapping between the phase coils is exist as a result of using different number of turns per coil arms. This radial overlapping causes an $2x$ unit increase in the total thickness of the end-winding ($14x$ unit instead of $12x$ unit). Since the number of turns of each coil member are different, winding factor calculation approach of the NSW topology is a bit different than that of the conventional calculation approach. The winding factor $k_{wh}$ consists of pitch $k_{ph}$ and distribution $k_{dh}$ factors, where there is no skewing on the stator slots. $k_{wh}$ for FSCW and ISDW are calculated separately by using the expressions given from (3.4) to (3.8) [97, 120].

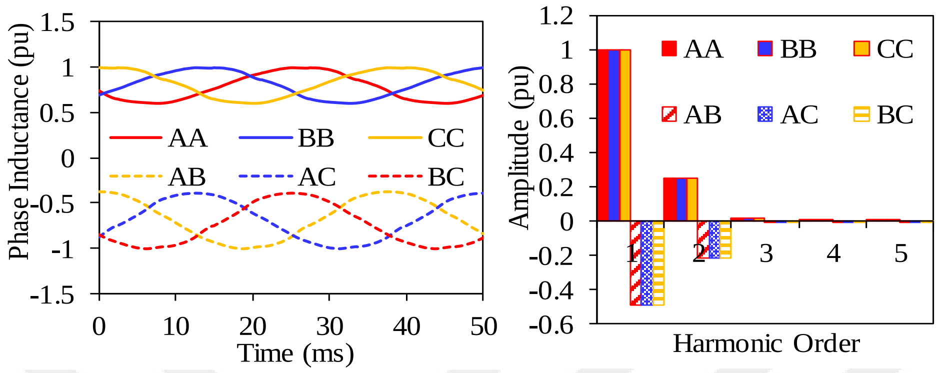


(a) (b)

**Figure 3.3 :** Winding self- and mutual-inductances: (a) waveform, (b) harmonic spectrum.

$$k_{wh} = k_{ph} \cdot k_{dh} \tag{3.4}$$

$$k_{ph\_ISDW} = \sin\left(h \frac{\pi}{S} y_c\right) \tag{3.5}$$

$$k_{ph\_FSCW} = \sin\left(h \frac{\pi}{S}\right) \tag{3.6}$$

$$k_{dh\_ISDW} = \frac{\sin\left(h \frac{\pi}{P \cdot m}\right)}{\frac{S}{P \cdot m} \cdot \sin\left(h \frac{\pi}{S}\right)} \tag{3.7}$$

$$k_{dh\_FSCW} = \frac{\sin\left(h \frac{\pi}{P \cdot m}\right)}{S \cdot \sin\left(h \frac{\pi}{S \cdot P \cdot m}\right)} \tag{3.8}$$

where, $h$ is the harmonic order and $m$ is the phase number. Considering $k_{wh}$ as initial winding factor which is derived from the conventional calculation approach, the new winding factor comprising of *2L* or *3L* winding can be calculated by modifying the phase shifting method reported in [87] and [119] in order to consider the number of turns $N_1$, $N_2$, and $N_3$ and number of coils $N_c$ as expressed in (3.9) and (3.10), respectively.

$$k_{wh\_NSW2} = k_{wh\_ISDW}\, cos\left[h\frac{2N_2}{N_1}\left(N_c + \frac{N_1}{N_2}\right)\right] \tag{3.9}$$

$$k_{wh\_NSW3} = k_{wh\_ISDW}\, cos\left[h\frac{N_2}{N_1 N_3}\left(N_c + \frac{N_1}{N_3}\right)\right] \tag{3.10}$$

The influences of winding parameters such as layer number, turn number combinations, and stator slot number on the air-gap flux density and torque are examined for fixed current density/stator copper loss as follows. Note that the geometric dimensions given in Appendix B, Table B.1 indicated with small dimensions–*SD* has been used for the analyses in this section.

### 3.2.1 Influence of winding layer numbers

The NSW topology can be designed as to has got different number of winding layers $L_c$. Notching that for the NSW topology $L_c$ is a function of $y_c$ and it can be estimated for any $S/P$ combination by using (2.2) as expressed in (2.11).

$$L_c = \text{round}\left(\frac{2y_c - 1}{3}\right) \tag{2.11}$$

It should be clarified that if $y_c = 1$, no NSW topology can be existed. With aim of showing the influence of number of winding layers, the $24S/4P$ combination is examined. From (3.2), the normal $y_c$ is evaluated as 5 and the short $y_c$ may be taken as 3. At this point, the max/min winding layer numbers per slot is calculated as 2 and 3, respectively by using (3.3). The winding-layouts of the *2L* and *3L* combinations are derived by (3.1)-(3.3) and the obtained winding layouts for *2L* and *3L* combinations are shown in Figure 3.4, respectively. The $24S/4P$ IPM machines with 2 and 3 winding layers are designed via FEA and the key characteristics including the air-gap flux density and electromagnetic torque are predicted as shown in Figure 3.5.

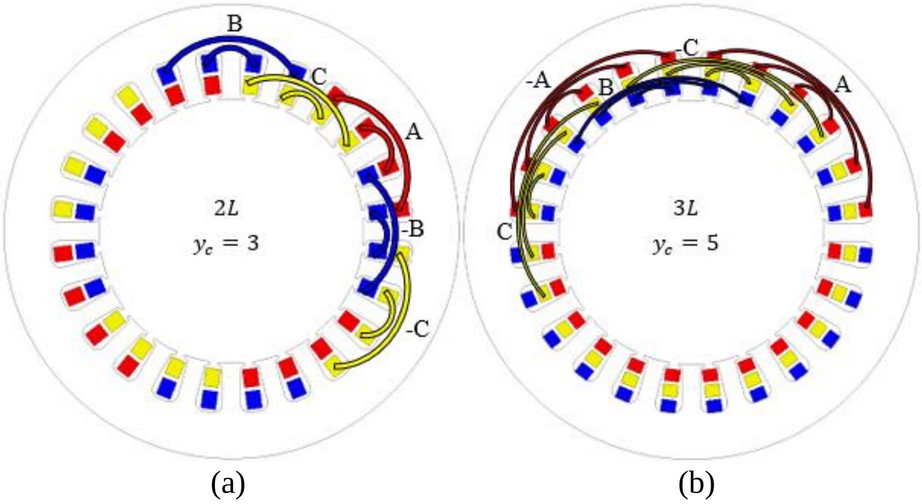


**Figure 3.4 :** Winding layouts of 24S/4P combination with different winding layers: (a) 2L ($y_c$ = 3), (b) 3L ($y_c$ = 5)

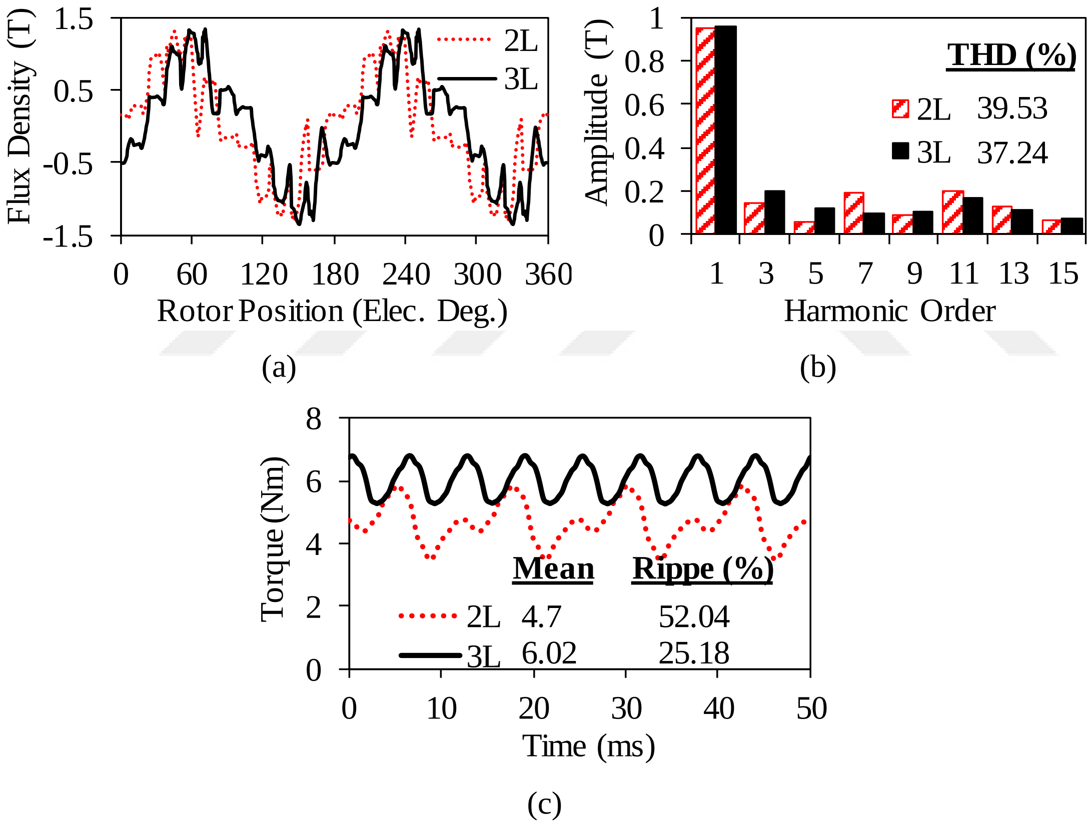


**Figure 3.5 :** Performance characteristics of 24S/4P combination with 2L and 3L topologies: (a) air-gap flux density waveform, (b) harmonic spectra of air-gap flux density, (c) electromagnetic torque waveform.

As illustrated in Figure 3.5(b), the total harmonic distortion (THD) level of the air-gap flux density of the *3L* winding is lower than its *2L* counterpart. As can be realized, the fundamental and triple harmonics of the *3L* topology are higher than its *2L* counterpart. Nevertheless, the THD of the *3L* topology is ~1.8% lower than that of the

*2L* topology. Furthermore, as shown in Figure 3.5(c), the time-averaged torque of the *3L* topology is ~28.1% higher than that of the *2L* topology. Moreover, the torque ripple rate of the *3L* topology is ~51.5% lower than that of the *2L* topology. Consequently, it can be deduced that the higher the number of layers, the higher the air-gap flux density and eventually higher the average torque and the lower the torque ripple rate.

### 3.2.2 Influence of number of turns combinations

For the purpose of establishing the best number of turns combinations by considering the winding layers, the number of turns listed in Table 3.1 have been designated for $4P$ IPM machines with $24S$ and $12S$ combinations. The winding arms with different number of turns have been represented by alphabetic characters as shown in the table. Notice that the total number of turns per slot are kept unchanged for different sets of winding groups. Furthermore, only the FEA results of the $24S/4P$ combinations have been presented in this section. The maximum overlapping degree of the windings are set up as 1/12 of the stator slot whilst the minimum is set up as 7/12 of the stator slot. Consequently, the overlapping degree is limited. Note that the given overlapping rates are determined empirically after conducting several parametric FEAs.

**Table 3.1 :** Number of Turns Combinations.

| | $\boldsymbol{24S/4P}$ | | | | | $\boldsymbol{12S/4P}$ | | | | |
|---|---|---|---|---|---|---|---|---|---|---|
| | *2L* | | *3L* | | | *2L* | | *3L* | | |
| | *Nt1* | *Nt2* | *Nt1* | *Nt2* | *Nt3* | *Nt1* | *Nt2* | *Nt1* | *Nt2* | *Nt3* |
| **a** | 24 | 24 | 16 | 16 | 16 | 48 | 48 | 32 | 32 | 32 |
| **b** | 36 | 12 | 24 | 16 | 8 | 72 | 24 | 48 | 32 | 16 |
| **c** | 42 | 6 | 28 | 16 | 4 | 84 | 12 | 56 | 32 | 8 |

The predicted air-gap flux density and torque are illustrated in Figure 3.6 and 3.7, respectively. It can be comprehended that the fundamental amplitude of the air-gap flux density increases significantly as the number of turns of the 3$^{rd}$ set *Nt3* (c) is decreased. As a consequence, the number of turns of the 1$^{st}$ set *Nt1* (a) is increased. Furthermore, the THD of the air-gap flux density is decreased as the number of turns of the *Nt3* is decreased. These findings are valid for both winding layer combinations. The average torque of the *3L* combinations are higher than that of the *2L* combinations whereas the torque ripple rates are lower as seen in Figure 3.7.

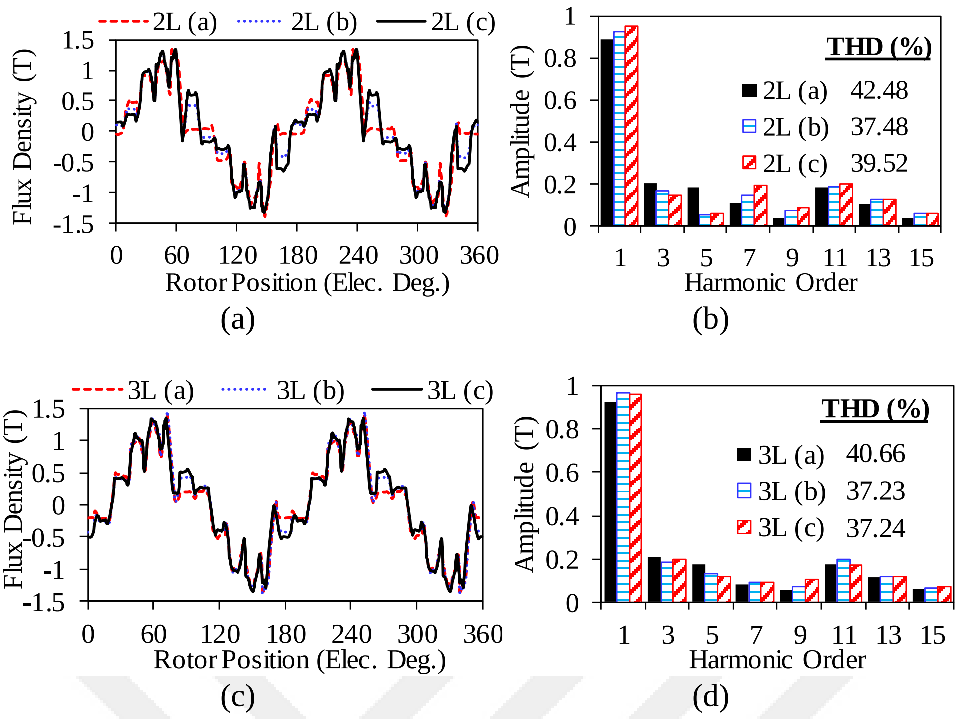


**Figure 3.6 :** Air-gap flux density waveforms and their harmonic spectra for various number of turns and winding layer combinations: (a) Waveform (2L's), (b) Harmonic Spectra (2L's), (c) Waveform (3L's), (d) Harmonic Spectra (3L's).

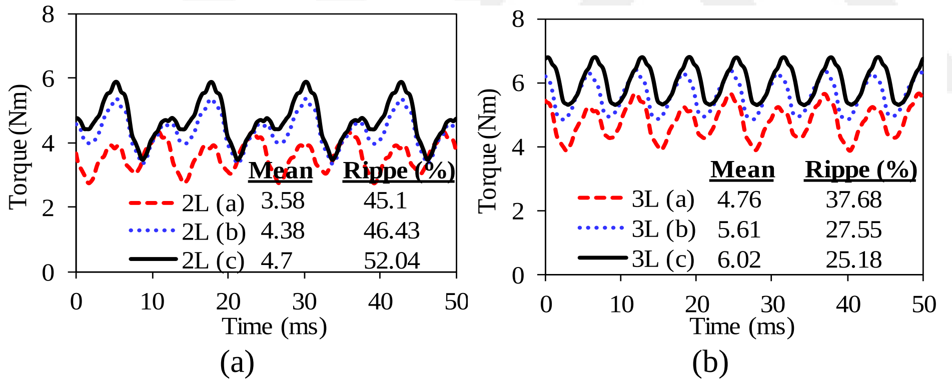


**Figure 3.7 :** Electromagnetic torque waveforms for various number of turns and winding layer combinations: (a) *2L* combinations, (b) *3L* combinations.

Moreover, as the number of turns of the 3$^{rd}$ set of coils are decreased (c), the average torque is increased substantially for both *2L* and *3L* combinations. Therefore, considering the findings it can be concluded that the lower the number of turns of the inner coil, the higher the average torque. Nevertheless, the number of turns of the inner coil cannot be zero (initially set to 1/12 of the slot) owing to an increase in the overlapping proportion.

### 3.2.3 Influence of number of stator slots

The influence of number of stator slots have been investigated by designing $12S/4P$ combination with *2L* and *3L* windings as shown in Figure 3.8. Then, the predicted key electromagnetic characteristics are compared with the results of previously designed $24S/4P$-*2L* and *3L* combinations as shown in Figure 3.9 and Figure 3.10. Note that only the combinations indicated with (c) are examined.

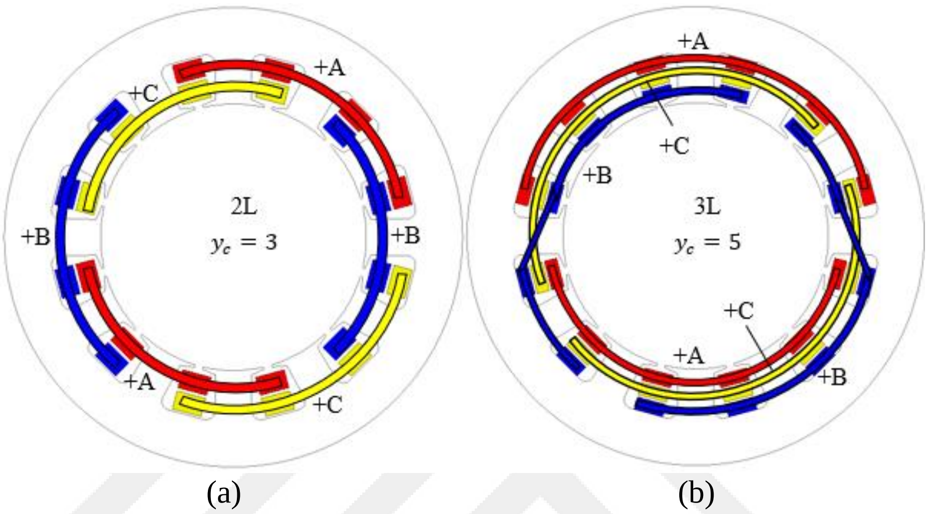


**Figure 3.8 :** Winding layouts of 12S/4P combination with different winding layers and coil pitches: (a) 2L ($y_c = 3$), (b) 3L ($y_c = 5$).

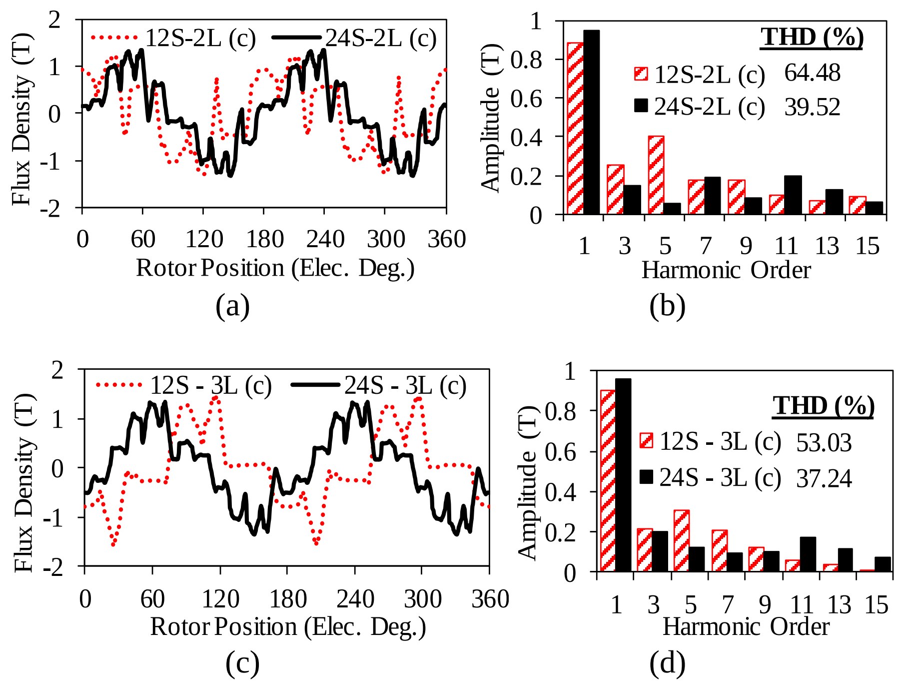


**Figure 3.9 :** Air-gap flux density waveforms and their harmonic spectra for various number of turns and winding layer combinations: (a) Waveform (2L's), (b) Harmonic Spectra (2L's), (c) Waveform (3L's), (d) Harmonic Spectra (3L's).

The fundamental amplitude of the $24S$ combinations are higher than that of the $12S$ combinations. Thanks to the doubled stator slot number, a large amount of air-gap flux density harmonics is cancelled (see Figure 3.9). The $24S$ combinations provide higher average torque than that of the $12S$ combinations as illustrated in Figure 3.10. Furthermore, *3L* combination generates higher torque than *2L* combination. Moreover, combinations with higher stator slot and higher winding layers have lower torque ripple rate. It can be concluded that the higher the slot and winding layer, the higher the average torque and the lower the torque ripple rate.

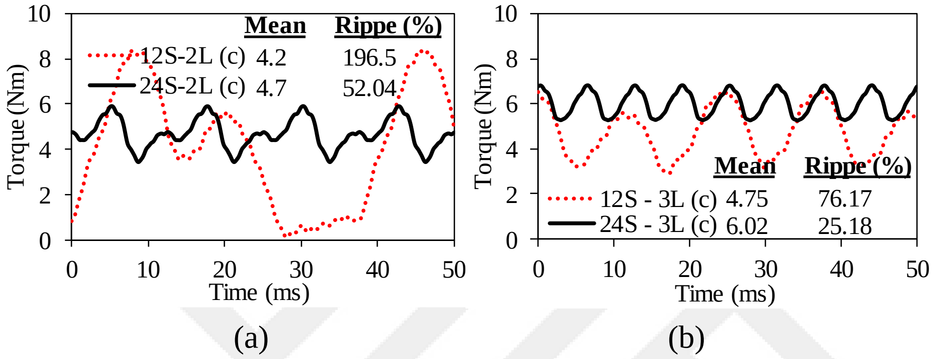


**Figure 3.10 :** Electromagnetic torque waveforms for various number of stator slots and winding layer combinations: (a) *2L* combinations, (b) *3L* combinations.

### 3.3 Performance Comparison with Different Winding Topologies

For the sake of validating the properties of the NSW topology, IPM machines having ISDW, FSCW, and NSW with the same outer diameter, stack length, excitation current, and synchronous speed as Toyota Prius 2010 IPM machine (see Appendix, Table B.1 for the specifications indicated with *LD*) are designed. Notching that the original Toyota Prius 2010 IPM machine has single layer (SL) windings as illustrated in Figure 3.11.

To be able to expose the influence of winding layers, double layer (DL) counterpart of ISDW-SL topology is also designed. The 2-D cross-sectional views, winding layouts and flux line distributions of the designed IPM machines are shown in Figure 3.11. The performance characteristics are predicted by performing 2-D, non-linear, time-stepping FEA under steady state operating with current source supply providing 236Apeak phase current, 1krpm rotor speed, and the current angle delivering the maximum torque (see Appendix A.1 for other specifications). Notice that the IPM machines with ISDW DL, FSCW, and NSW *3L* combinations have been globally optimized by genetic algorithm (GA) for the objectives of average torque $T_{e_{avg}} \geq$ 239Nm, torque ripple $\Delta T \leq 10\%$, and stator copper loss $P_{cu} \leq 6\text{kW}$. Moreover, mechanical limits and manufacturing tolerances such as rotor shaft diameter, outer bridge thickness, etc. are considered during the optimization process. Notching that as for the FSCW topology, the combinations having no sub-harmonics have been considered for a fairer comparison.

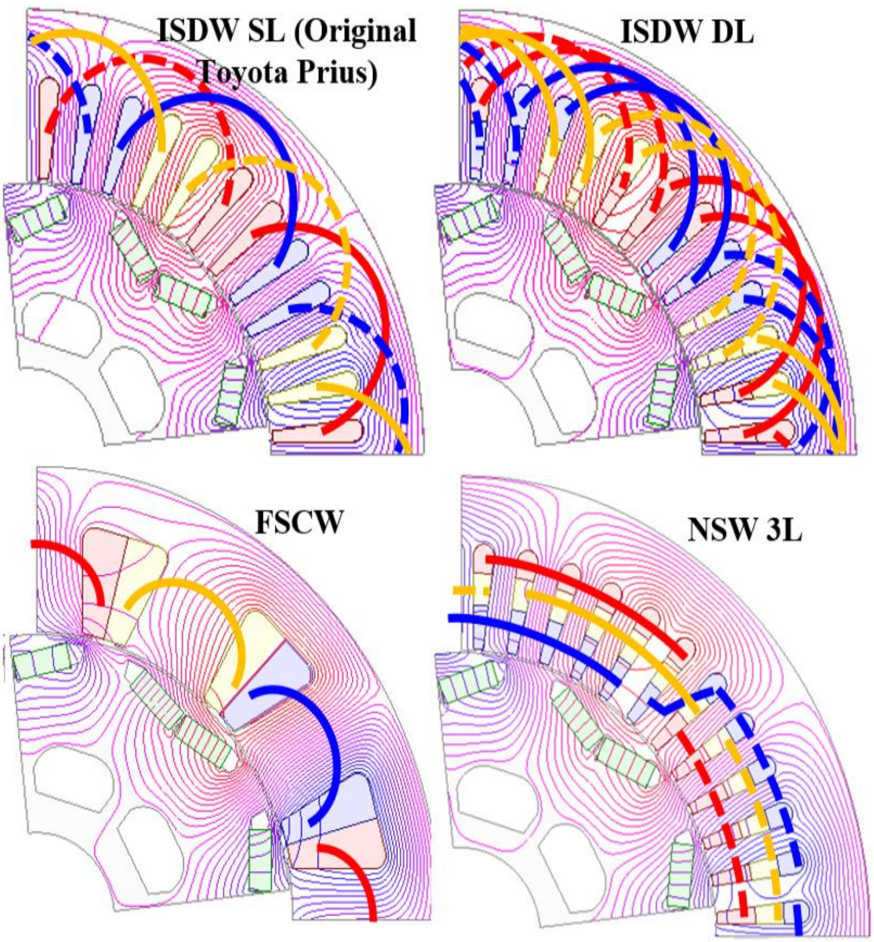


**Figure 3.11 :** Various winding layouts and full-load flux line distributions.
*Red: Phase 'A', Blue: Phase 'B', Orange: Phase 'C'*
*Solid Line: (+) polarity, Dashed Line: (–) polarity.*

### 3.3.1 Winding structure analysis

The winding factor and MMF harmonics of the considered winding topologies having different S/P combinations and winding layers are specified in Table 3.2 and 3.3, respectively. The fundamental winding factor of the ISDW topology is the highest whereas FSCW is the lowest.

**Table 3.2 :** Winding factor.

| # | 48S/8P ISDW *SL* | 48S/8P ISDW *DL* | 48S/8P NSW *3L* | 12S/8P FSCW *DL* | 24S/4P ISDW *DL* | 24S/4P NSW *3L* | 6S/4P FSCW *DL* |
|---|---|---|---|---|---|---|---|
| 1 | 0.966 | 0.933 | 0.869 | 0.866 | 0.933 | 0.869 | 0.866 |
| 2 | 0 | 0 | 0 | 0.866 | 0 | 0 | 0.866 |
| 3 | 0.707 | 0.5 | 0.636 | 0 | 0.5 | 0.636 | 0 |
| 4 | 0 | 0 | 0 | 0.866 | 0 | 0 | 0.866 |
| 5 | 0.259 | 0.067 | 0.233 | 0.866 | 0.067 | 0.233 | 0.866 |
| 6 | 0 | 0 | 0 | 0 | 0 | 0 | 0 |
| 7 | 0.259 | 0.067 | 0.233 | 0.866 | 0.067 | 0.233 | 0.866 |
| 8 | 0 | 0 | 0 | 0.866 | 0 | 0 | 0.866 |
| 9 | 0.707 | 0.5 | 0.636 | 0 | 0.5 | 0.636 | 0 |
| 10 | 0 | 0 | 0 | 0.866 | 0 | 0 | 0.866 |
| 11 | 0.966 | 0.933 | 0.869 | 0.866 | 0.933 | 0.869 | 0.866 |

In addition, the harmonic content of the FSCW is the highest. Thus, it may be predicted that the rotor losses of IPM machines having FSCWs, will be fairly high. Moreover, considering the fundamental amplitude of the MMF, it can be predicted that the FSCW and NSW topologies require a greater number of turns to produce the same amount of torque with ISDW topology. The average winding length, which is required for the estimation of the stator resistance, are approximated for different winding structures as expressed from (3.12) to (3.15) [121, 122].

$$l_{avg_{ISDW\,SL}} \approx 2l_{stack} + \frac{3.2\pi^2 r_w y_c}{S} \tag{3.12}$$

$$l_{avg_{ISDW\,DL}} \approx 2l_{stack} + \frac{6.4\pi r_w}{P} \tag{3.13}$$

$$l_{avg_{FSCW}} \approx 2l_{stack} + \frac{3.72\pi r_w}{S} \tag{3.14}$$

$$l_{avg_{NSW}} \approx 2l_{stack} + \frac{5.44\pi r_w}{S} \tag{3.15}$$

where $r_w$ is the average winding radius which is calculated as the distance from the centre of the shaft to the middle of the stator slot. The total end-winding thickness of the different winding topologies have been calculated using the calculation methods reported in [121, 122, 126]. The end-winding configurations and their parameters are illustrated in Figure 3.12. [79] Note that the quantity $t_e$ and $t_{en}$ represents the air space between two insulated coils. In the most cases, $t_{en}$ is neglegibly low. $b_{cx}$, $\tau_p$, and $\tau_s$ are coil thickness, the pole and slot pitches measured at the middle of the slot.

**Table 3.3 :** Winding MMF (pu).

| # | 48S/8P ISDW *SL* | 48S/8P ISDW *DL* | 48S/8P NSW *3L* | 12S/8P FSCW *DL* | 24S/4P ISDW *DL* | 24S/4P NSW *3L* | 6S/4P FSCW *DL* |
|---|---|---|---|---|---|---|---|
| 1 | 1 | 0.966 | 0.9 | 0.897 | 0.966 | 0.87 | 0.897 |
| 2 | 0 | 0 | 0 | 0.448 | 0 | 0 | 0.448 |
| 3 | 0 | 0 | 0 | 0 | 0 | 0 | 0 |
| 4 | 0 | 0 | 0 | 0.223 | 0 | 0 | 0.224 |
| 5 | 0.053 | 0.014 | 0.048 | 0.178 | 0.014 | 0.012 | 0.179 |
| 6 | 0 | 0 | 0 | 0 | 0 | 0 | 0 |
| 7 | 0.038 | 0.01 | 0.034 | 0.126 | 0.01 | 0.009 | 0.128 |
| 8 | 0 | 0 | 0 | 0.11 | 0 | 0 | 0.112 |
| 9 | 0 | 0 | 0 | 0 | 0 | 0 | 0 |
| 10 | 0 | 0 | 0 | 0.087 | 0 | 0 | 0.089 |
| 11 | 0.088 | 0.085 | 0.079 | 0.079 | 0.087 | 0.078 | 0.081 |
| 12 | 0 | 0 | 0 | 0 | 0 | 0 | 0 |
| 13 | 0.074 | 0.071 | 0.066 | 0.066 | 0.073 | 0.066 | 0.068 |
| 14 | 0 | 0 | 0 | 0.061 | 0 | 0 | 0.063 |
| 15 | 0 | 0 | 0 | 0 | 0 | 0 | 0 |
| 16 | 0 | 0 | 0 | 0.052 | 0 | 0 | 0.055 |
| 17 | 0.015 | 0.004 | 0.013 | 0.049 | 0.004 | 0.004 | 0.052 |
| 18 | 0 | 0 | 0 | 0 | 0 | 0 | 0 |
| 19 | 0.013 | 0.003 | 0.012 | 0.043 | 0.004 | 0.003 | 0.046 |
| 20 | 0 | 0 | 0 | 0.04 | 0 | 0 | 0.044 |
| 21 | 0 | 0 | 0 | 0 | 0 | 0 | 0 |
| 22 | 0 | 0 | 0 | 0.036 | 0 | 0 | 0.039 |
| 23 | 0.038 | 0.036 | 0.034 | 0.034 | 0.041 | 0.036 | 0.038 |
| 24 | 0 | 0 | 0 | 0 | 0 | 0 | 0 |
| 25 | 0.034 | 0.033 | 0.03 | 0.03 | 0.037 | 0.033 | 0.034 |
| **%** | **14.677** | **13.032** | **14.613** | **65.867** | **13.928** | **13.858** | **66.667** |

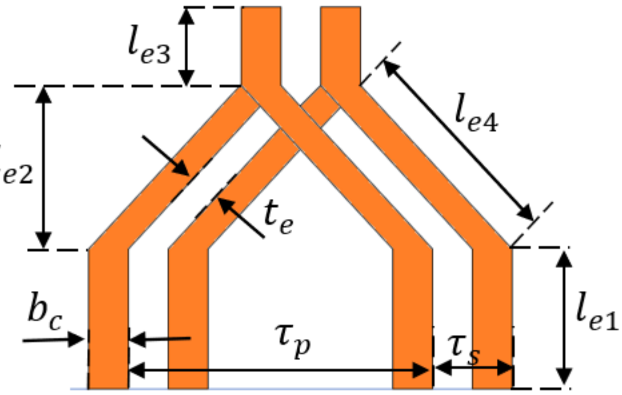


(a)

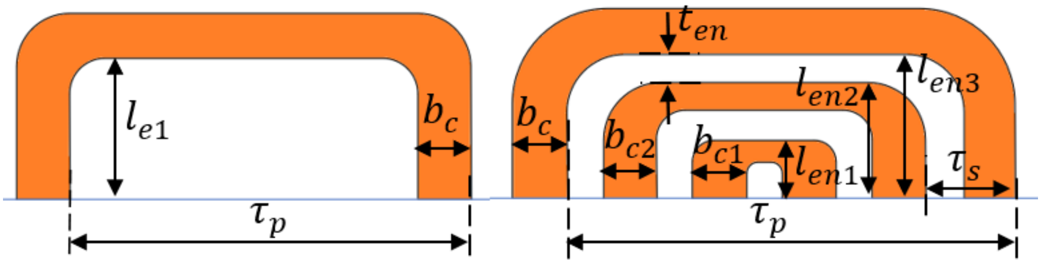


(b) (c)

**Figure 3.12 :** End-winding configurations:(a) ISDW *SL*, (b) FSCW *DL*, (c) NSW *3L*.

$$l_{e2} = \frac{p\tau_p(b_c + t_e)}{2\sqrt{\tau_s^2 - (b_c + t_e)^2}} \tag{3.16}$$

$$l_{e_{ISDW}} \approx l_{e1} + l_{e2} + l_{e3} \tag{3.17}$$

$$l_{e_{FSCW}} \approx l_{e1} + b_c \tag{3.18}$$

$$l_{e_{NSW}} \approx 1.15(l_{en1} + l_{e2} + l_{e3} + b_{c1} + b_{c2} + b_c - 2t_{en}) \tag{3.19}$$

Note also the value of $l_{e1}$ depends upon the voltage and ranges from 10mm to 100mm for a 13.2kV machine [126]. In addition, $l_{e3}$ usually assumed as to be equal to $2b_c$ (max). The total axial length values $l_{avg}$ have been approximated by using the equations given from (3.16) to (3.19). The calculated phase resistances $R_{phase}$ and total axial lengths $l_{avg}$ are listed in Table 3.4 for different stack lengths $l_{stack}$. Since the compactness is chosen as one of the main comparison criteria in this study, to tolerate the average torque and efficiency due to the lower MMF amplitudes of FSCW and NSW designs, the stack lengths have been increased by 7.7mm and 5.2mm, respectively and indicated with (L). Thus, it is possible to compare the key performance characteristics for the same stack length, average torque, and efficiency parameters (see Table 5). As seen in Table 4, even though the stack length is increased slightly to be able to tolerate the average torque and hence output power of the NSW(L) IPM machine, since the end-winding length of the NSW is much shorter than that of ISDW, $l_{avg}$ is 13.66% shorter and the phase resistance is ~18.2% lower.

**Table 3.4 :** Phase resistance and machine lengths.

| | $R_{phase}$ ($\Omega$) @20°C | $R_{phase}$ ($\Omega$) @100°C | $l_{stack}$ (mm) | $l_{avg}$ (mm) |
|---|---|---|---|---|
| **ISDW SL** | 0.077 | 0.101 | 50.8 | 112.88 |
| **ISDW DL** | 0.064 | 0.084 | 50.8 | 101.28 |
| **FSCW** | 0.056 | 0.074 | 50.8 | 81.53 |
| **FSCW(L)** | 0.061 | 0.08 | 58.5 | 89.23 |
| **NSW** | 0.06 | 0.079 | 50.8 | 92.26 |
| **NSW(L)** | 0.063 | 0.083 | 56 | 97.46 |

### 3.3.2 Back-EMF and flux linkage analyses

No-load and full-load back-EMFs are shown in Figure 3.13 and 3.14, respectively. As for the no-load operating condition, due to the slotting effect the obtained back-EMF waveforms are quite distorted for all IPM machines (see Figure 3.13). However, among them the proposed topology has the least distortion.

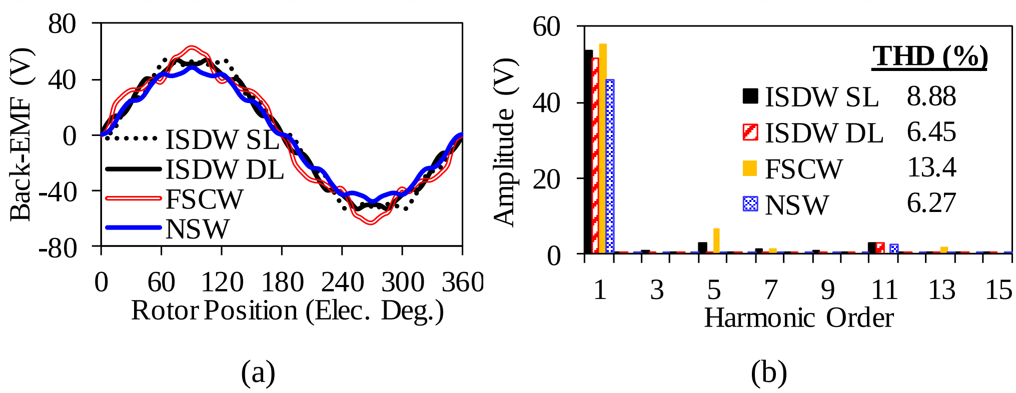


**Figure 3.13 :** No-load Back-EMF: (a) waveform, (b) harmonic spectra.

On the other hand, as a consequence of combined effect of slotting and magnetic saturation, the distortion level of the back-EMF has increased significantly under full-load operating as shown in Figure 3.14. The NSW topology has again the least distortion whilst the FSCW topology has the highest. In addition, as for the ISDWs, it has also been revealed that the DL configuration has lower distortion in both operating conditions. The very same phenomenon can be observed from the flux linkage waveforms (see Figure 3.15). The 3rd and 5th harmonics are dominant harmonics for ISDW and FSCW topologies, respectively.

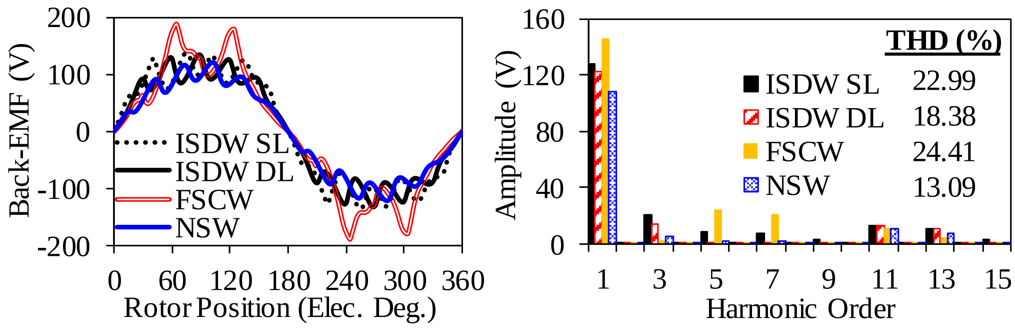


(a) (b)

**Figure 3.14 :** Full-load Back-EMF: (a) waveform, (b) harmonic spectra.

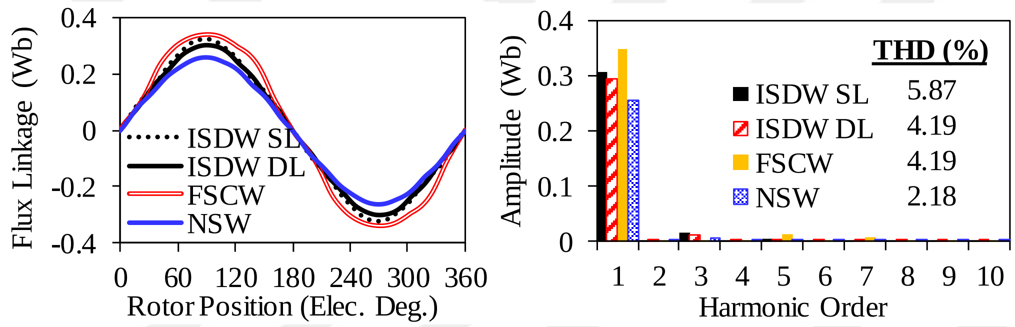


(a) (b)

**Figure 3.15 :** Full-load flux linkage: (a) waveform, (b) harmonic spectra.

### 3.3.3 Air-gap flux density analysis

The radial component of the air-gap flux density is shown in Figure 3.16. Note that since the MMF amplitude of the FSCW is the lowest among the considered topologies, it is number of turns per phase is increased slightly (see Appendix, Table B.1) with the intention of tolerate the average torque. That is why it has the highest back-EMF amplitude. As expected, since the FSCW has the highest MMF distortion, its air-gap flux density waveform is quite distorted when compared to other machines. In addition, the air-gap flux density distortion level of the NSW is ~7% lower than its ISDW DL counterpart and the fundamental air-gap flux density amplitude of the NSW is slightly lower than that of the ISDW.

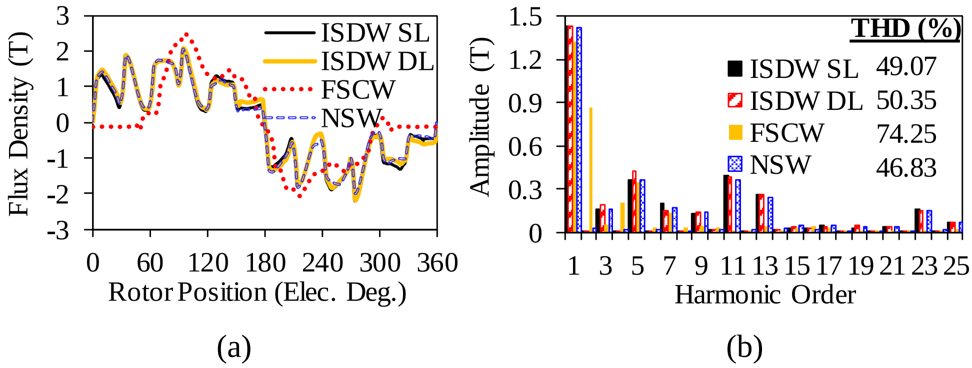


**Figure 3.16 :** Air-gap flux density: (a) waveform, (b) harmonic spectra.

### 3.3.4 Saturation and demagnetization analyses

Since the machines have different MMF harmonic contents as seen in Table 3, which in turn leads to different saturation characteristics of the magnetic circuit and hence loss behaviour. Local magnetic saturation effects have been shown to cause the variation of the $dq$-axis inductances in PM machines. The different local saturation characteristics for the considered IPM machines are shown in Figure 3.17. Owing to the reduced coupling between the phases, higher self- and lower mutual-inductances are desired characteristics for fault tolerance [114]. The winding characteristics coupled with the slotting effect influences the machine inductances. Considering the peak-to-peak variations of $dq$-axis inductances (see Figure 3.18) and flux density distributions (see Figure 3.17), it can be concluded that the FSCW topology has the highest local saturation level. Moreover, its fault tolerance is somewhat better than that of the other topologies. As stated previously, the excessive eddy currents in the rotor part can cause the irreversible demagnetization and it can seriously influence the electromagnetic performances. The irreversible demagnetization of PMs is investigated by operating the considered machines under nominal ($I_{peak}$) and over-load conditions ($2I_{peak}$). During the analyses the temperature of the PMs is held constant at 80°C and the critical flux density of irreversible demagnetization is assumed to be 0T. Figure 3.19 illustrates the detailed flux density distributions in PMs at nominal (N) and overloads (O). Obviously, partial irreversible demagnetization can be observed in ISDW machines when they operate under overload conditions (marked in circles).

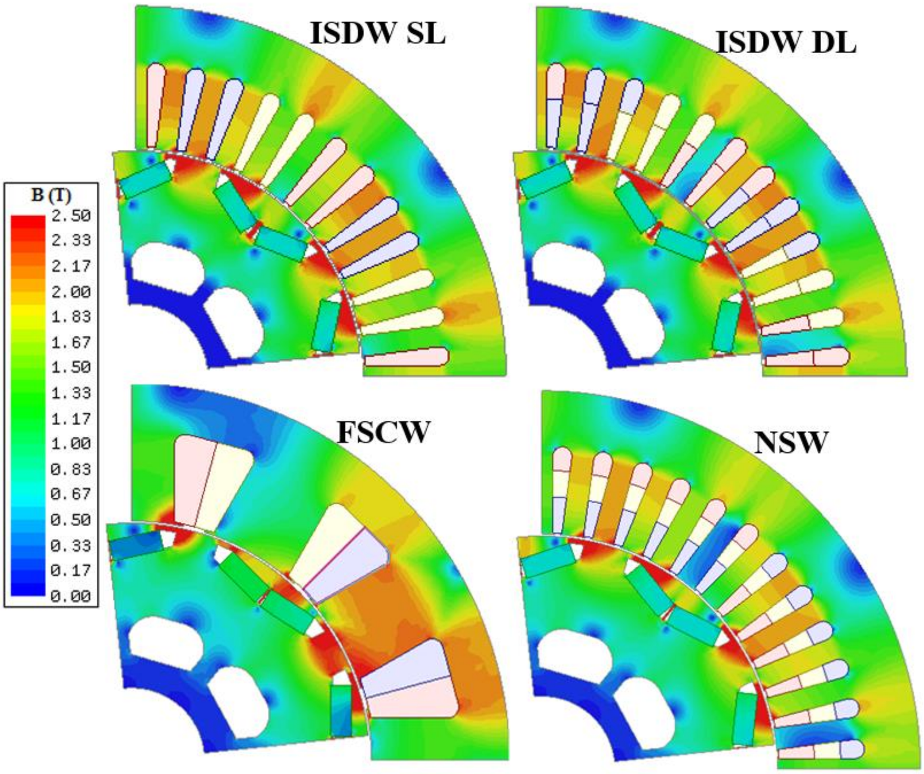


**Figure 3.17 :** Flux density distributions of IPM machines. *(Knee point of the B-H curve of the core material is ~1.48T)

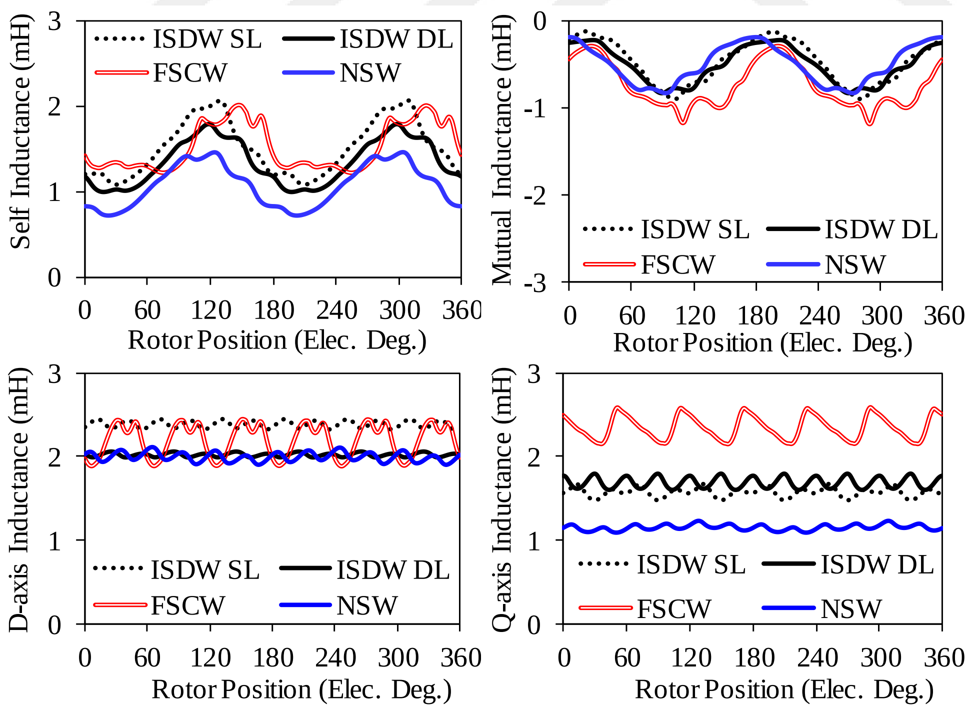


**Figure 3.18 :** Self, mutual, *d*-axis, and *q*-axis inductance variations.

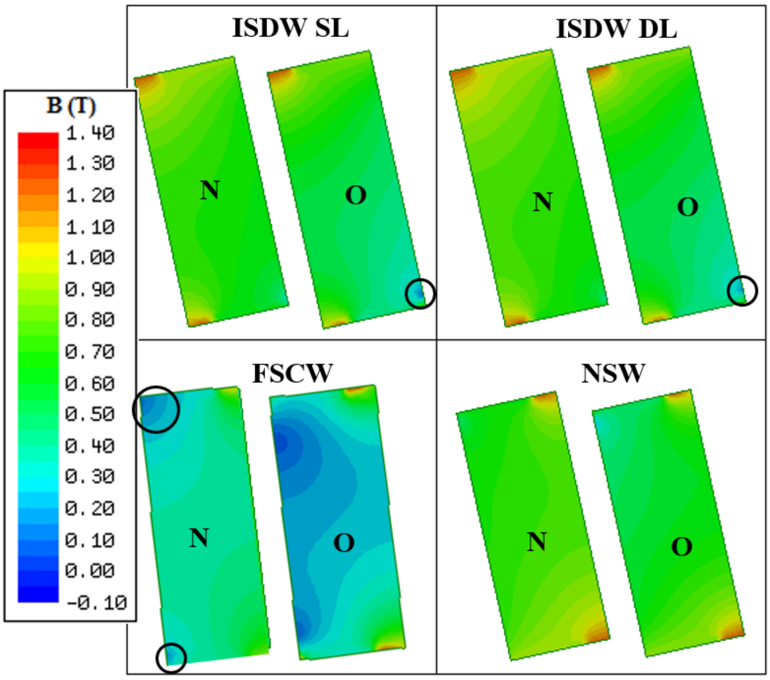


**Figure 3.19 :** Flux density distributions of PMs at the worst demagnetization of IPM machines under nominal load (N) and overload (O) operations.

However, it occurs in FSCW machine under both loading conditions. On the other hand, the NSW machine exhibits superior capability of withstanding irreversible demagnetization as compared to other machines in both operations, which is due to quite lower MMF harmonic content. It is revealed that the demagnetization region only accounts for ~0.2% of the total PM region for ISDW machines. Hence, the influence due to partial demagnetization is quite slight, and the PMs of ISDW and NSW machines are safe when they operate under nominal load and overload. Nevertheless, in order to avoid the partial irreversible demagnetization in FSCW machines, much thicker PMs may be used [123].

### 3.3.5 Electromagnetic torque analysis

Figure 3.20 presents torque waveforms for each machine. The time averaged, torque ripple percentage, and torque per volume (TPV), calculated by (16), are given in the figure.

$$TPV = \frac{4T_{e_{avg}}}{\pi D_{so}^2 l_{avg}} \tag{2.20}$$

As clearly seen, although the fundamental MMF amplitude of the NSW topology is the lowest, very similar torque values has been obtained for the same stack length designs thanks to the global optimization process. On the other hand, if exactly the same geometric parameters as the original Toyota Prius IPM machine (corresponding to ISDW DL) would been used for the NSW design, 216.28Nm averaged torque value (~10% lower than that of the ISDW SL since the fundamental MMF amplitude of the NSW is ~10% lower) had been obtained. In addition, it has been shown that by slightly increasing the stack lengths (<8mm) of the FSCW and NSW machines, corresponding to FSCW(L) and NSW(L), torque and efficiency can be significantly increased for NSW design while the efficiency can be tolerated for FSCW design by keeping the total axial lengths still lower than that of the ISDW SL and DL designs. In addition, since the total axial lengths of FSCW and NSW designs are quite lower than that of ISDW designs, their TPV values are remarkably higher.

The global optimization objective $\Delta T \leq 10\%$ could not be achieved for the FSCW design due to irreducible effect of slotting and slot leakage flux levels (see also $dq$-axis inductances in Figure 3.18). Moreover, it is also revealed that the stack length has an ignorable influence on the torque ripple.

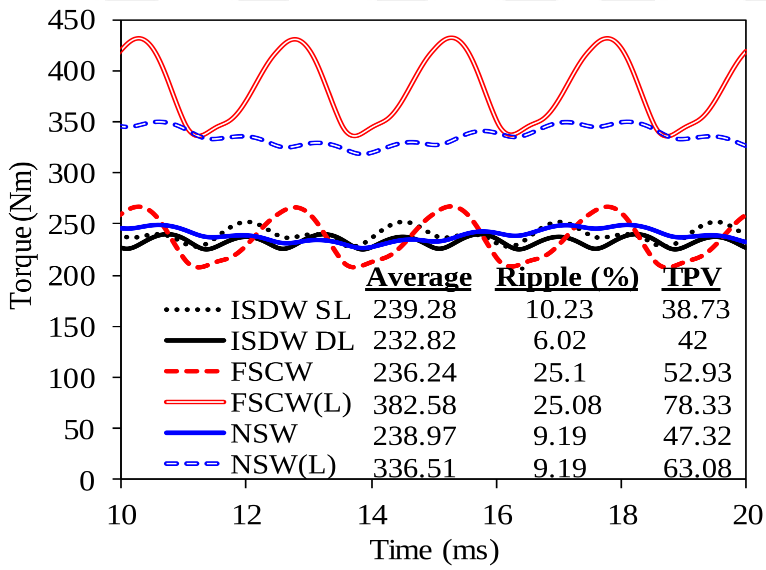


**Figure 3.20 :** Torque waveforms of IPM machines.

### 3.3.6 Power losses and efficiency analyses

As reported in [125], the practical maximum stator slot stacking factor is 0.78 with the hard-pressed windings. In this study, the corresponding calculations have been done with 0.448 fill factor (same as the Toyota Prius IPM machine). Comparison of the power losses and efficiency $\eta$ is listed in Table 5. Stator slot copper loss $Pcu_{Slot}$ and end-winding loss $Pcu_{End}$ are calculated by using the average coil lengths. Note that for more accurate calculation of $P_{cu}$, the additional AC losses due to skin and proximity effects have been partially taken into account by using 3-D approximation coefficients for AC resistance of 2-D models [125]. And the PM loss due to eddy current in PMs is calculated by considering the conductivity of the PM material $\sigma_{PM}$ and the eddy current $I_{e_{PM}}$ induced on the PMs as given in (3.21) [120].

$$P_{PM} = \frac{1}{\sigma_{PM}} I_{e_{PM}}^2 \tag{2.21}$$

To calculate time-varying $I_{e_{PM}}$, eddy current field solver using the FEA to compute the magnetic vector potential $\boldsymbol{A}$ and electric scalar potential ϕ using the relationship given in (3.22) is used [125].

$$\begin{aligned} \nabla \times \frac{1}{\mu_{PM}} (\nabla \times \boldsymbol{A}) &= \left(\sigma_{PM} + \frac{\partial \varepsilon}{\partial t}\right)\left(-\frac{\partial \boldsymbol{A}}{\partial t} - \nabla \phi\right) \\ I_{e_{PM}} &= \int_{\Omega} \left(\sigma_{PM} + \frac{\partial \varepsilon}{\partial t}\right)\left(-\frac{\partial \boldsymbol{A}}{\partial t} - \nabla \phi\right) d\Omega \end{aligned} \tag{2.22}$$

where $\mu_{PM}$, $\varepsilon$ and $\Omega$ are the magnetic permeability, absolute permittivity, and volume of the PMs, respectively. Note that in transient eddy current calculations time-varying quantity of $\boldsymbol{A}$, which is $\boldsymbol{A} = \boldsymbol{A_m} \cos(\omega_s t + \theta)$, is employed.

**Table 3.5 :** Power losses and efficiency comparison (Prius 2010 dimension–*LD*).

| *Parameter* | ISDW SL | ISDW DL | FSCW | FSCW (L) | NSW | NSW (L) |
|---|---|---|---|---|---|---|
| $\boldsymbol{P_{cu_{Slot}}}$ (kW) | 2.12 | 2.12 | 2.402 | 2.766 | 2.12 | 2.337 |
| $\boldsymbol{P_{cu_{End}}}$ (kW) | 4.288 | 3.224 | 2.293 | 2.293 | 2.928 | 2.928 |
| $\boldsymbol{P_{core}}$ (kW) | 0.102 | 0.103 | 0.121 | 0.196 | 0.088 | 0.124 |
| $\boldsymbol{P_{PM}}$ (kW) | 0.018 | 0.009 | 2.101 | 3.402 | 0.021 | 0.03 |
| $\boldsymbol{P_{out}}$ (kW) | 25.057 | 24.381 | 24.739 | 40.064 | 25.025 | 35.239 |
| $\boldsymbol{L_d/L_q}$ | 1.51 | 1.19 | 0.93 | 1.18 | 1.73 | 1.82 |
| $\boldsymbol{\cos\varphi}$ | 0.82 | 0.78 | 0.73 | 0.95 | 0.89 | 0.97 |
| $\boldsymbol{\eta}$ (%) | 78.706 | 81.051 | 77.544 | 81.562 | 82.231 | 85.927 |

**Table 3.6 :** Axial length and efficiency comparison.

| | *Same Stack Length* | | *Same Total Axial Length* | |
|---|---|---|---|---|
| | $l_{axial}$ (%) | $\eta$ (%) | $P_{out}$ (%) | $\eta$ (%) |
| **ISDW SL** | -18.3 | +4.478 | +40.635 | +9.175 |
| **ISDW DL** | -8.9 | +1.456 | +44.534 | +6.016 |

Since all machines have the same numbers of turn per phase, the in-slot copper losses are the same, and the end-winding copper loss of the NSW design is between the ISDW and FSCW designs. Note that the eddy current loss, arising from the induced eddy currents in the end-windings, is negligibly low at the rated operating speeds. Because of high MMF harmonic content of the FSCW topology, excessive eddy currents are induced in the rotor part resulting in inevitably huge core and PM losses. That is why the FSCW designs' $\eta$ is quite low even though the copper losses are lower than that of the other machines. On the other hand, the NSW has slightly high PM loss than that of ISDW DL is because the NSW has slightly higher MMF harmonic content as shown in Table 3. Note that 1% of output power [76] is considered as additional power losses for the sake of obtaining more accurate efficiency percentage.

$$\cos\varphi = \frac{P_{out}}{3(E_0 + I_s R_{phase} + I_c R_c) I_s \eta} \tag{2.23}$$

The power factor $\cos\varphi$ of the designed machines have been calculated by using the expression given in (3.23), where $E_0$ is the back-EMF fundamental amplitude, $I_s$ is the rms stator current, $R_c$ is the equivalent iron core loss resistance, and $I_c$ is the core loss current. Considering Table 3.4, 3.5 and (3.23), it can be deduced that the larger and longer machines have better $\cos\varphi$ as a consequence of having higher output power with lower resistance and back-EMF amplitude. In addition, it has been reported in [120], that a higher inductance ratio $(L_d/L_q)$ leads to a small current angle, and thus to a small load angle and a better $\cos\varphi$. This finding is verified in Table 3.5 and 3.7. It can also be observed from Table 3.5 that the longer the stack length, the higher the $L_d/L_q$ ratio and consequently the higher the $\cos\varphi$. Table 3.6 summarize the effectiveness of the proposed winding topology. The DL and SL versions of the ISDW topology has been compared with the NSW topology for the same stack length and the same average torque (NSW(L)) designs. It has been revealed that thanks to the proposed NSW topology, IPM machines having much higher efficiency can be designed producing the same output power as its ISDW counterpart with still shorter total axial length.

### 3.3.7 Influence of machine size

Small power (0.2kW) IPM machines with the dimensions given in Appendix B (*SD*'s) have also been designed to figure out the effect of machine sizes on the performance characteristics, particularly dominant rotor losses. The 2-D views, flux line, and flux density distributions of $4P$, $24S$ ISDW, $6S$ FSCW, and $24S$ NSW IPM machines are illustrated in Figure 3.21. Note that the winding factor and MMF harmonics of these machines are also given in Table 3.2 and 3.3.

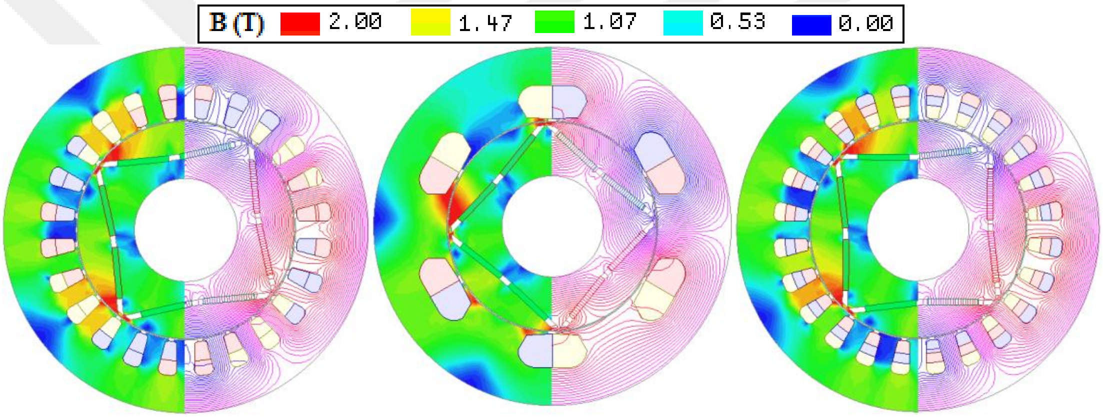


(a) (b) (c)

**Figure 3.21 :** Flux density and flux line distributions of 4P IPM machines designed with small dimensions–*SD*: (a) ISDW *DL*, (b) FSCW, (c) NSW *3L*.

The key design parameters and performance characteristics of IPM machines having different winding structures and smaller dimensions than that of the Toyota Prius 2010 IPM machine are compared in Table 3.7. Once Table 3.5 and 3.7 is compared, it can be realized that the PM loss is not one of the dominant loss components anymore for the FSCW designs with smaller dimensions. In addition, it can be deduced that the NSW topology ensures higher efficiency with much shorter axial length independently of the power rate. Furthermore, due to the higher resistance versus lower output power and lower $L_d/L_q$ ratio of machines with *SD*s, their cos $\varphi$ are considerably poorer than their *LD* counterparts. It has also been revealed that for small power application of the IPM machines, it might me be more reasonable to use FSCW topology because of the moderate output power with high efficiency. Nevertheless, for large power application, since a large amount of the cooling equipment might be required because of the large eddy current induced in the rotor part and sacrificed efficiency, it is not reasonable to use FSCW topology. Furthermore, the excessive eddy currents can further lead to a higher rotor temperature particularly at high speed operating regions, and hence the PMs will suffer from a high risk of irreversible demagnetization [113-116]. In contrast, since the NSW topology has fairly lower MMF harmonic contents and consequently low eddy current losses, it does not require additional cooling equipment and it has an ignorable risk of irreversible demagnetization.

**Table 3.7 :** Design parameter and performance comparison (for *SD*).

| ***Parameter*** | **ISDW DL** | **FSCW** | **NSW** |
|---|---|---|---|
| $\boldsymbol{R_{phase}}$ @20°C (Ω) | 0.128 | 0.0808 | 0.103 |
| $\boldsymbol{R_{phase}}$ @100°C (Ω) | 0.1682 | 0.1062 | 0.1354 |
| $\boldsymbol{l_{end\_1}}$ (mm) | 25.54 | 12.133 | 16.11 |
| $\boldsymbol{T_{e_{avg}}}$ (Nm) | 5.15 | 4.71 | 4.65 |
| $\boldsymbol{T_{ripple}}$ (%) | 9.367 | 12.945 | 10.8 |
| $\boldsymbol{P_{cu_{Slot}}}$ (kW) | 0.0274 | 0.0274 | 0.0274 |
| $\boldsymbol{P_{cu_{End}}}$ (kW) | 0.0363 | 0.0156 | 0.0248 |
| $\boldsymbol{P_{core}}$ (kW) | 0.001 | 0.001 | 0.001 |
| $\boldsymbol{P_{PM}}$ (kW) | 2.11e-05 | 2.28e-03 | 1.8e-05 |
| $\boldsymbol{P_{out}}$ (kW) | 0.216 | 0.197 | 0.195 |
| $\boldsymbol{L_d/L_q}$ | 0.65 | 0.83 | 0.67 |
| $\boldsymbol{\cos\varphi}$ | 0.67 | 0.69 | 0.68 |
| $\boldsymbol{\eta}$ (%) | 74.814 | 81.895 | 78.008 |

## 3.4 Conclusion

The studies conducted in this chapter can be divided into three main sections. Firstly, a novel winding topology having significantly short end-windings compared to ISDWs and substantially low MMF harmonics compared to FSCWs is developed. Secondly, for the purpose of establishing the best values of the winding parameters, including the winding layer number, turn number combinations, and $S/P$ combinations, their influences on air-gap flux density and torque have been investigated parametrically. Finally, the proposed winding topology has been implemented into IPM machine in large and small power applications and the key performance characteristics have been comprehensively compared with other IPM machines designed with ISDWs and FSCWs. In this study, obtained key findings can be specified as follows.

- The numerical studies on developing more compact IPMs with improved performance have been successfully verified by the experiments;
- It has been validated that thanks to the proposed NSW topology, the end-winding lengths can be successfully shortened without increasing the MMF harmonic content;
- The proposed NSWs do not require a special stator slot geometry. They can be implemented into the stator of any existing electrical machine with ISDWs;
- The MMF distortion level of the proposed NSW is ~80% lower than that of the FSCW;
- The main drawback of the NSW topology is that because of the semi-overlapping windings it is not very suitable for automated manufacturing with today's technology;
- Another disadvantage is that high winding layer (*3L*) structure of NSW causes a reduction in the copper fill factor due to the increase in the additional insulation between layers of different phase windings.
- Under the same output power operating, the NSW IPM machine have 4.27% higher efficiency and ~18.7% shorter axial length than its ISDW DL counterpart;
- The torque ripple level of the IPM machine with NSWs is the same as its ISDW counterpart;
- It has been revealed that for IPM rotor, the FSCW topology is not feasible for large power application because of its quite large amount of PM loss component.
- The poor power factor of electrical machines can be significantly improved with extended stack length.

The feasibility analyses of implementing proposed NSW topology into the other machine technologies and flux-weakening performance analyses and will be presented in Chapter 4, and Chapter 6, respectively.

# 4. COMPARISION OF PERFORMANCE CHARACTERISTICS OF PM AND RELUCTANCE MACHINES EQUIPPED WITH OVERLAPPING, SEMI-OVERLAPPING, AND NON-OVERLAPPING WINDINGS[3]

In this chapter, the compatibleness/effectiveness of the proposed novel semi-overlapping winding (NSW) topology has been investigated by implementing into different synchronous machine technologies, namely interior permanent-magnet machine (IPM), synchronous reluctance machine (SynRM), permanent-magnet assisted synchronous machine (PMaSynRM), and double-salient reluctance machine (DSRM). All considered machines have also been designed with different winding topologies; i.e. integer-slot distributed winding (ISDW), fractional-slot concentrated winding (FSCW) in order to reveal the merits/demerits of the proposed NSWs. A comprehensive electromagnetic performance comparison has been presented. It has been validated that the proposed winding topology promises significant advantages; such as improved efficiency with substantially reduced total axial length, low eddy PM loss and low risk of irreversible magnet demagnetization over conventional winding topologies. It has also been revealed that the implementation of proposed NSWs into the reluctance machines results with higher torque and power output than that of FSCWs.

## 4.1 Introduction

Efficient energy consumption is the key to solving the 21$^{st}$ century global issues on climate change. Since over 65% of the electrical energy is consumed by electric motors in different industry applications [127], improvements in the efficiency of motors make significant imprints on reduction of its consumption and make a substantial contribution to the economic prosperity of countries. The most dominant power loss component of electric motors is copper loss, particularly constant torque operating area

[3] This chapter is based on the paper: **Gundogdu, T. and Komurgoz, G.** (2020) Comparative Study on Performance Characteristics of PM and Reluctance Machines Equipped with Overlapping, Semi-overlapping, and Non-overlapping Windings, *IET Elect. Power Appl.*, *14*(6), 991-1001.

of variable speed applications. Therefore, reduction of copper loss can be achieved by optimizing the design for maximum efficiency (very limited improvement), implying various MMF reduction methods, such as flux-barriers, different number of turns per phase, phase shifting, etc. [119] or introducing a new winding topology having very short-end windings with very low MMF harmonic content. In [118], a new winding topology, called novel semi-overlapped winding (NSW), has been introduced by presenting the influence of winding parameters on the performance characteristics and merits/demerits of the proposed winding by comparing the electromagnetic performance characteristics of the interior permanent-magnet machines (IPMs) having different winding topologies.

In this chapter, the proposed winding topology in [118] has been implemented into different machine topologies; including IPM, synchronous reluctance machine (SynRM), permanent-magnet assisted synchronous machine (PMaSynRM), and double-salient reluctance machine (DSRM). Thus, it is intended to reveal the compatibleness of the proposed winding topology for other machine topologies.

In the existing literature, several different studies on reviewing/comparing the electromagnetic performance characteristics of different machine technologies can be found [111, 128-145]. Different electric machine topologies have been compared and it is concluded that the PM machines, particularly having IPM topologies, are one of the best rotor topologies suitable for the EV/HEV and aerospace applications [128, 129]. In addition, it has also been shown that the PMaSynRMs has also comparable performance characteristics with IPMs, particularly when the cost becomes more important criteria [128-130]. The influence of winding structure, magnet shape optimization, using much cheaper rare-earth magnets; such as ferrite, different rotor topologies, flux barrier geometry optimization, etc. on the performance characteristics have also been investigated [130-142]. It has also shown that the switched reluctance machines namely DSRMs has also potential to be used in the aerospace applications [143-145]. Most of the studies performed for the DSRM is to increase the reluctance torque component by redesigning the rotor geometry [144, 145].

Furthermore, recently published performance comparison studies on electrical machine and winding topologies, considering

a) the usage of low-cost ferrite PMs in PMaSynRMs;

b) variable speed operations: traction electrical machine in EV/HEV applications;

c) fault-tolerance;

d) overlapping (inter-slot distributed winding: ISDW) and non-overlapping winding (fractional-slot distributed winding: FSCW) configurations,

can be found in the existing literature [131-154].

In [118], it has been shown that although very high PM loss originated from the high MMF harmonics, the FSCW topology may still be used in IPMs designed for small power (<0.3 kW) applications with relatively high efficiency. Because of great advantages of FSCW topology such has very short end-winding, fault-tolerance, relatively high winding factor, etc., an extensive research on reduction of MMF harmonics has been conducted. In [119], several different MMF harmonic reduction methods have been implemented into an IPM with FSCW and a very limited improvement has been achieved. It has been shown that the FSCW topology is not suitable for the IPMs used in large power applications, and particularly variable speed applications. Therefore, this study has the feature of answering the following questions given below.

a) Is it possible to develop a new winding topology with short-end windings and low MMF harmonics? → (introduced in [118]);

b) Might the new winding topology show better performance once implemented into different machine topologies? → (presented in this chapter);

c) Alternative machine topologies (with no excitation source on rotor) suitable for FSCW topology (i.e. SRM – in order to cancel the rotor excitation losses originated from the high MMF harmonic contents of the FSCWs) → (presented in this chapter).

Furthermore, in this chapter, combinations of different rotor and stator winding topologies are studied. A comprehensive performance comparison finding is presented. In order to reveal the merits/demerits of the proposed winding topology, IPM, SynRM, PMaSynRM, and DSRM having 4-poles with conventional windings i.e.; integer-slot distributed winding (24S/4P ISDW), proposed novel windings (24S/4P NSW), and 6-slot/4-pole fractional-slot concentrated winding (6S/4P FSCW) have been designed and the obtained key steady-state (constant torque operating region) electromagnetic performance characteristics including the torque, torque ripple, power losses, efficiency, total axial length, etc. have been quantitatively compared. It has been revealed that the proposed winding topology can work perfectly with any machine technology, particularly for SynRM and PMaSynRM, and thanks to the proposed method much more compact machines can be designed with significantly increased torque and power density and overall efficiency.

The crucial contributions can be summarized in the form of main titles as follows.

1. Design and analysis of different machine topologies summarized in Table 4.1. Implementation of NSW topology into different machine topologies including IPM, SynRM, PMaSynRM, and DSRM;
2. Comprehensive comparison of electromagnetic performance characteristics of different machine topologies with ISDWs, FSCWs, and NSWs;
3. Determination of effectiveness/compatibility of NSW topologies for various machine technologies.

**Table 4.1 :** Winding and electrical machine technology combinations.

| | **IPM** | **SynRM** | **PMaSynRM** | **DSRM** |
|---|---|---|---|---|
| **ISDW** | √ | √ | √ | √ |
| **FSCW** | √ | √ | √ | √ |
| **NSW** | √ | √ | √ | √ |

### 4.2 Classification of Winding Topologies

The winding of an electrical machine is one of the key components producing the electromagnetic torque. In essence, only the parts of windings inside the stator slots, called as in-slot windings, contribute the air-gap flux density and hence torque generation. The other parts, called as end-windings, do not contribute the torque generation, they only perform the connections between the in-slot conductors. The total axial length of the machine and amount of copper loss are determined by length of the end-windings. The windings for a radial air-gap field, inner rotor and slotted stator machines are classified into two common categories as overlapping and non-overlapping windings. Apart from these well-known winding types, different unconventional winding topologies are presented and a novel non-overlapping type of winding having quite low MMF harmonics is proposed in [111]. On the other hand, a new class of winding topology, called as semi-overlapping winding, consists of not totally but partly overlapped windings, is introduced in [118]. The key features of these winding configurations will be presented in the following sub-sections.

### 4.2.1 Overlapping windings

Mostly known as conventional or inter-slot distributed windings (ISDWs). The number of stator slots per pole per phase and coil pitch are larger than unity ($q \geq 1$ and $y_c > 1$, respectively). Therefore, the phase windings overlap each other as illustrated in Figure 4.1(a). The most distinct feature of this class of windings are these: (a) have long end-windings and hence higher copper loss; (b) have low MMF harmonics and hence lower rotor losses, particularly low eddy current and PM losses; (c) commonly have higher fundamental winding factor and hence requires lower number of turns per phase in order to product the same amount of torque. Other key features of overlapping windings are listed and compared with non-overlapping windings in Table 4.2.

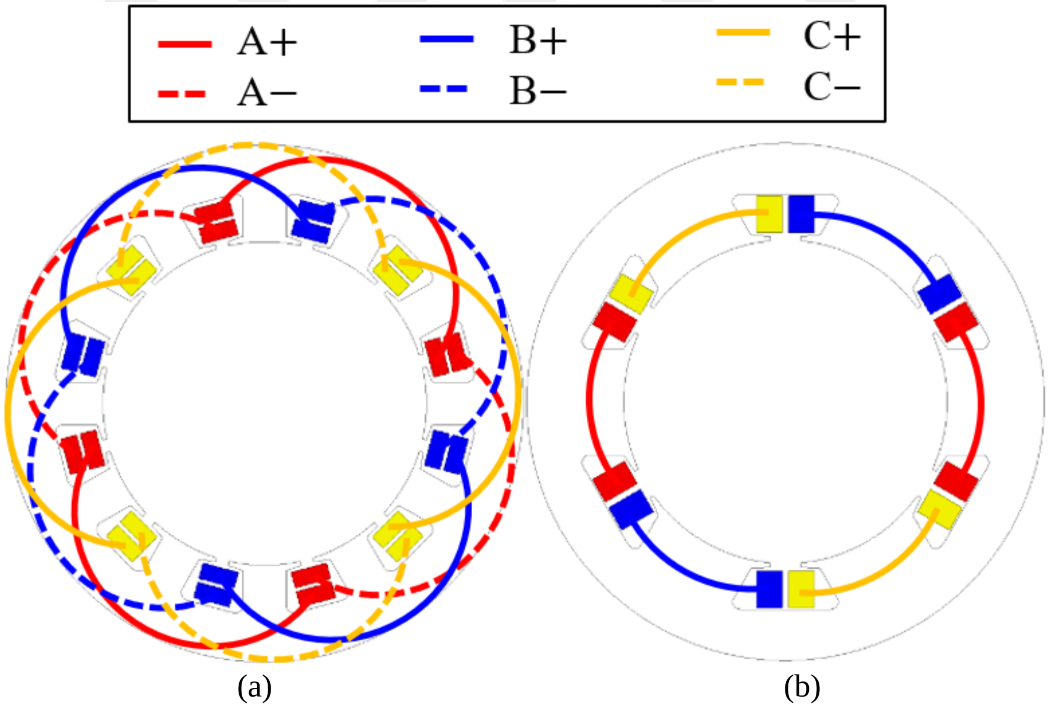


**Figure 4.1 :** Double-layer 4-pole winding layouts: (a) Overlapping winding, (b) Non-overlapping winding.

**Table 4.2 :** Comparison of winding topologies .

| | ***Overlapping*** | ***Semi-Overlapping*** | ***Non-Overlapping*** |
|---|---|---|---|
| Winding factor | $= 1$ or $< 1$ | Usually $< 1$ | Usually $< 1$ |
| End-winding | Long | Short | Very short |
| Slot fill factor | Low | Moderate | High |
| Space distribution of stator MMF | Very close to sine-wave | Very close to sine-wave | Square-wave |
| MMF harmonics | Low | Low | High |
| Rotor losses | Low | Low | High |
| Winding inductance | Low | Low | High |
| Fault tolerance | No | Partly | Yes |
| Cogging torque | Usually high | Usually Moderate | Usually low |
| Flux-weakening capability | Depends on electrical machine type | Depends on electrical machine type | Usually High |
| Manufacture | Difficult | Difficult | Easy |

### 4.2.2 Non-overlapping windings

Mostly known as concentrated or fractional-slot concentrated windings (FSCWs). The number of stator slots per pole per phase is lower than unity and coil pitch is one ($q < 1$ and $y_c = 1$, respectively). Therefore, the phase windings do not overlap each other and concentrated on only one stator tooth as illustrated in Figure 4.1(b). The most distinct feature of this class of windings are exactly the vice versa of the features of overlapping windings presented in Section 4.2.1. Some other important features of this class of windings are listed in Table 4.2.

### 4.2.3 Semi-overlapping windings

The semi-overlapping winding, consists of windings having different number of turns per coil arms which are not completely overlapped but only some phase coils are overlapped, is introduced in [118] (see Figure 4.2). As seen in Figure 4.2, the winding layout of the proposed NSW is similar to a kind of conventional winding, known as *concentric winding CW*. The main difference between the CWs and NSWs are: (i) only a very limited number of coils of NSW are overlapped, (ii) NSW has different number of turns per coil arms.  In [118], the general properties and influence of some design parameters such as number of layers, number of turns combinations, and number of stator slots on the electromagnetic performance characteristics has been investigated and the specifications delivering the maximum torque with minimum PM loss have been determined. For the sake of completeness, some key properties of the proposed winding topology are summarized as follows.

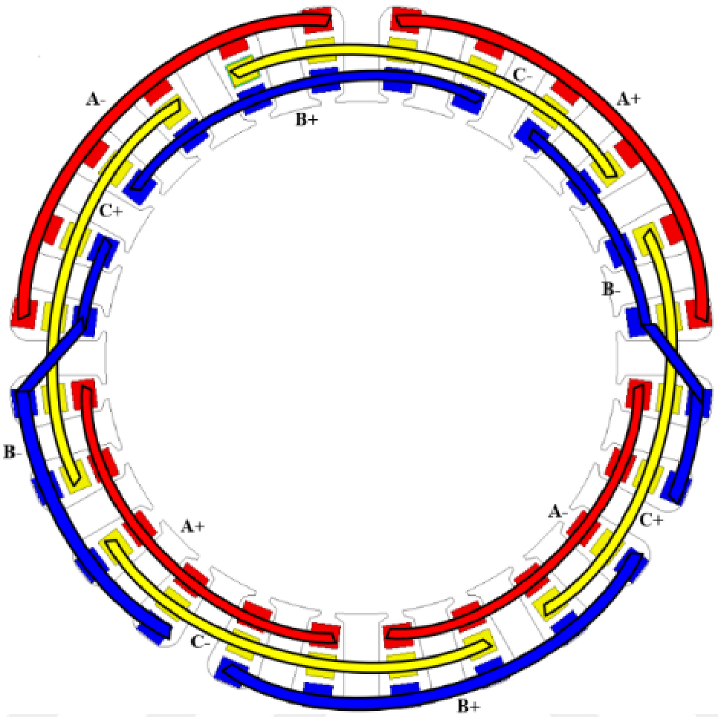


(a)

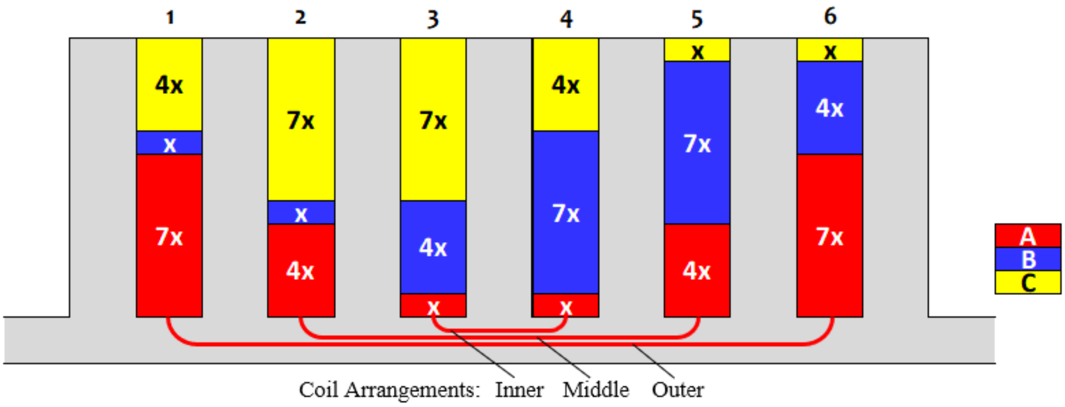


(b)

**Figure 4.2 :** Novel semi-overlapped winding topology: (a) simplified illustration, (b) distribution of number of turns per slot.

In the existing literature, some similar winding topologies can be found with single phase [97, 110, 155] or semi-filled stator slots [156]. However, since the fundamental winding factor amplitude has been reduced, and the number of turns between the winding sets are restricted to a constant rate, and half of the stator slots have not been fully filled, the obtained results are not satisfactory in these studies. Therefore, a new compact winding topology having high quality of MMF waveform is proposed in this chapter.

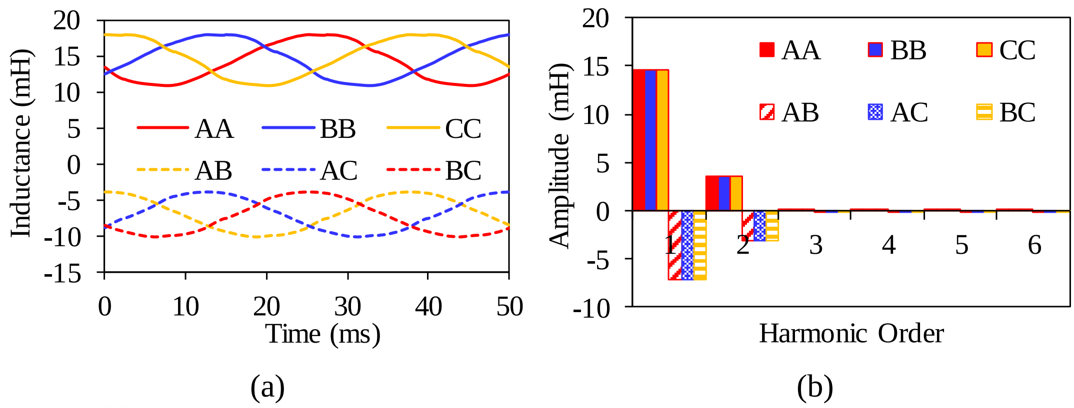


**Figure 4.3 :** Winding self- and mutual-inductance: (a) variations, (b) harmonic spectra.

As illustrated in Figure 4.2(a), one of the key points of the winding topology is that only the 'Phase B' winding is overlapped and each coil arms in a phase coil have different number of turns. Note that Figure 4.2(a) illustrates the simplified winding layout, the open (full) schema of each coil can be seen in Figure 4.7. Therefore, in order to create a symmetrical and balanced winding, the total number of turns in each slot should be equal. Otherwise, the inductance of the phases cannot be identical. The corresponding winding self- and mutual-inductance variation of such winding topology is shown in Figure 4.3. As clearly seen in the figure, since the balanced phase windings have been symmetrically distributed over the slots, the same amount of the inductances have been obtained. As illustrated in Figure 4.2(b), except for the axial overlapping of the 'Phase B', there is a radial overlapping between the phase windings because of the different number of turns of coil groups. This radial overlapping causes an increase in the total thickness of the end-winding. Total thickness of the end-winding will be $14x$ instead of $12x$. Therefore, in order to avoid additional sag of the end-winding, only $2x$ bending is required for winding sets close to the stator yoke side. This circumstance should be considered in the manufacturing progress of the windings.

### 4.2.4 Comparison of winding properties

The key properties of the considered winding topologies are compared in Table 4.2. As indicated in table, the proposed NSW topology have the advantage of both winding topologies. The key advantages of the proposed NSW topology are: (i) shorter end-winding than that of ISDW; (ii) lower end-winding copper loss than that of ISDW; (iii) lower space requirement than that of ISDW; (iv) depending on the machine type, usually comparable or lower torque ripple rate than those of ISDW and FSCW; (v) higher efficiency than that of ISDW. On the other hand, the main disadvantages of the proposed NSW topology are relatively low winding factor and manufacturing difficulty. As will be shown in Section 4.4.6, even though the winding factor of the NSW is lower than those of ISDW and FSCW, since its reluctance torque component is considerably higher than that of FSCW, it usually has higher torque and output power than that of FSCW. In addition, even though the NSW has lower fundamental winding factor amplitude and consequently has lower torque and output power than that of ISDW, it is efficiency is higher as a consequence of having shorter end-winding length and consequently lower copper loss (see Section 4.4.7). Commonly, there are two winding configurations for overlapped and non-overlapped windings: multi- and single-layer windings. The multi-layer windings have the advantage of lower MMF harmonics and hence lower rotor losses while the single-layer windings have the advantage of high winding factor and better fault tolerance.

### 4.2.5 Winding structure analysis

In this section, the winding factor harmonics and the winding MMF harmonics of the ISDW, FSCW, and the proposed NSW have been investigated. In addition, average axial end-winding lengths of the machines have been calculated and the total axial lengths of the machines have been compared. Winding factor harmonics of the considered topologies are illustrated in Figure 4.4 As clearly seen, the fundamental winding factor of the ISDW topology is the highest whilst NSW is the lowest. In addition, the harmonic content of the FSCW is the highest. Therefore, it can be predicted that the rotor losses, including the PM and core, will be quite high for the FSCW topology. The MMF harmonics have also been given in Figure 4.5. As seen, the fundamental MMF amplitude of the ISDW is the highest while it is the lowest for NSW. Therefore, it can be predicted that the NSW topology requires a greater number of turns in order to produce the same amount of torque as the ISDW topology.

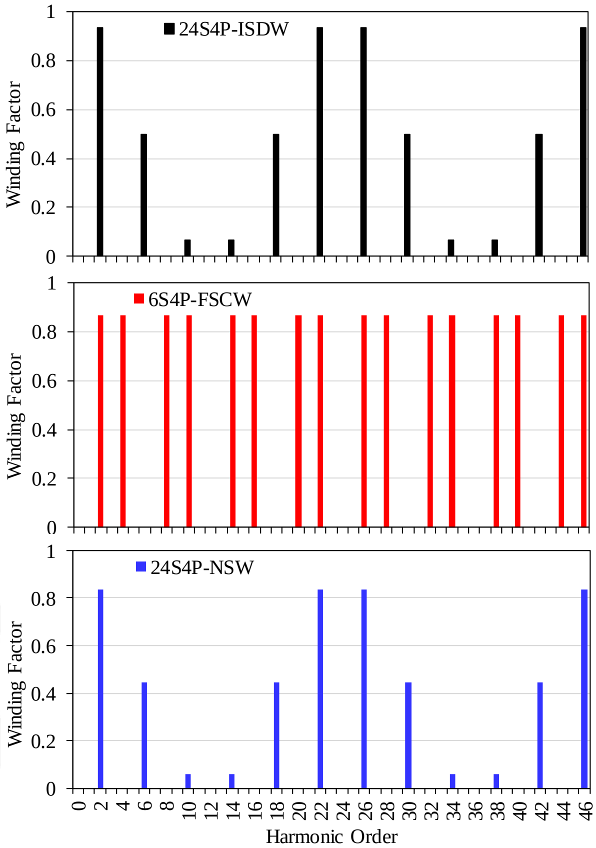


**Figure 4.4 :** Winding factor harmonics of different winding topologies.

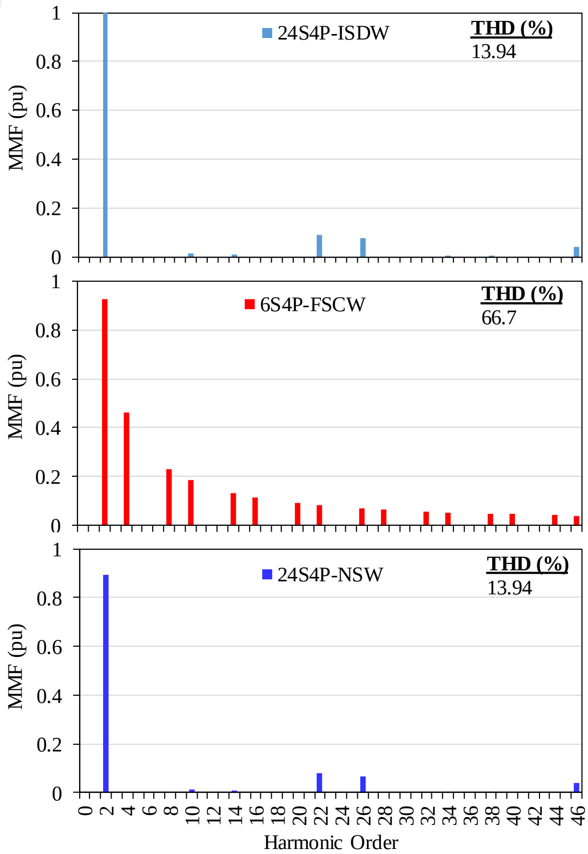


**Figure 4.5 :** MMF harmonics and THD percentages for different winding topologies.

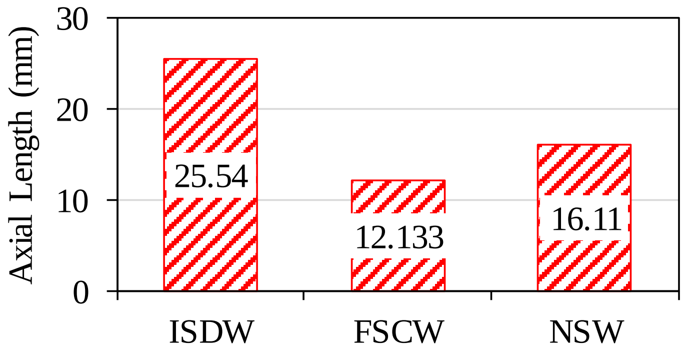


**Figure 4.6 :** Comparison of one-side end-winding axial lengths.

The average end-winding lengths are calculated by using the approximation given in [122] as follows.

$$l_{end\_ISDW} \approx \frac{2\pi^2 r_w y_c}{S} \tag{4.1}$$

$$l_{end\_FSCW} \approx \frac{3.72\pi r_w}{S} \tag{4.2}$$

$$l_{end\_NSW} \approx \frac{5.44\pi r_w}{S} \tag{4.3}$$

where $y_c$ is the coil pitch number, $r_w$ is the average winding radius, calculating as the distance from the centre of the machine to the middle of the slot, and $S$ is the stator slot number. The stack length is determined as 50mm and the calculated axial end-winding length of one coil side is illustrated in Figure 4.6 for each topology. As seen in the figure, the FSCW has the shortest end-winding length while the ISDW is the highest because of the overlapping winding structure. The one-side axial end-winding length of the NSW is 36.92% shorter than that of the ISDW. Consequently, two different aspects can be raised as given below:

1. The stack lengths of the machines having NSWs can be increased up to 18.86mm (as to become having the same total axial length) → Thus, the output power and efficiency can be improved significantly.
2. The stack lengths of the machines having NSWs can be changed as to become having the same average torque and hence output power → Thus, the efficiency can be improved significantly without sacrificing the compactness.

## 4.3 Design of PM and Reluctance Machines

In order to show the merits/demerits and compatibility of the proposed winding topology, interior PM machine (IPM), synchronous reluctance machine (SnyRM), PM assisted synchronous reluctance machine (PMaSynRM), and double-salient reluctance machine (DSRM) having integer-slot distributed windings (ISDW), fractional-slot concentrated windings (FSCW), and proposed novel semi-overlapping windings (NSW) having the same outer diameter, stack length, excitation current, number of turns per phase, slot fill factor, and synchronous speed have been designed. The considered machines are designed for HEV/EV traction applications. Note that the same amount of PM is used for IPM and PMaSynRM machines. The electromagnetic performance characteristics of all machines with different winding topologies have comprehensively been compared. In addition, each topology has been globally optimized for nominal operating conditions by genetic algorithm for the objectives of the average torque $T_{e_{avg}} \geq 5\text{Nm}$, torque ripple $\Delta T_{e_{avg}} \leq 0.5$, and stator copper loss $P_{cu} \leq 52\text{W}$. Furthermore, mechanical limits and manufacturing tolerances such as rotor shaft diameter, outer bridge thickness, etc. has also been considered during the optimization process. Consequently, the number of flux barrier and number of magnets in PMaSynRM designs may vary according to winding configuration. However, for the fair comparison purpose, the total weight of PMs is kept constant for all PM machine topologies.

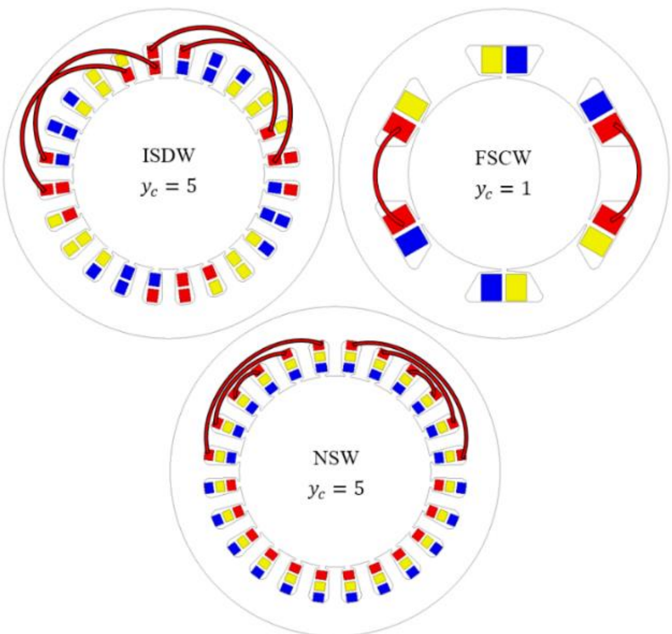


**Figure 4.7 :** Considered stators and winding topologies.

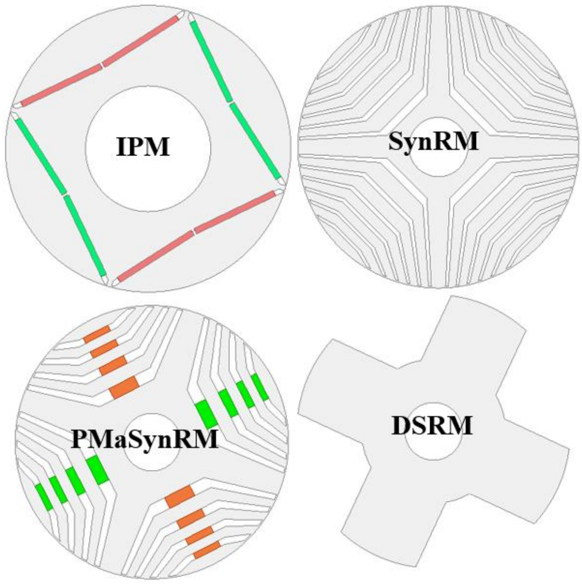


**Figure 4.8 :** Considered rotor topologies.

The winding layouts and some key winding specifications of the considered winding topologies have been shown in Figure 4.7. As seen in the figure, the design with ISDWs has 24-stator slot (24S), 5 pitch of coil pitch ($y_c = 5$), and 2-layer of windings (*2L*). The FSCW design has 6S, $y_c = 1$, and *2L* winding. Note that as for the FSCW topology, 12S10P combination, which has significantly high fundamental winding amplitude, can be chosen. However, it would be not fair because: (i) 12S10P contains both sub and super MMF and winding factor harmonics, yet, the considered combinations contain only super-harmonics; (ii) not reasonable and fair to make a comparison between the combinations having different pole numbers. In addition, the NSW design has 24S, $y_c = 5$, and *3L* winding. Note that the serial turn per phase are the same for all the machines and all machines have 4-poles. The structure of the V-type IPM rotor, reluctance rotor with U-type flux barriers, and spoke-type salient pole are illustrated in Figure 4.8. All machines are globally optimized using genetic algorithm for maximum torque under the fixed constraints of the identical: (a) number of turns; (b) copper loss; (c) stator outer diameter; (d) air-gap length; (e) stack length; and (f) PM volume. The key specifications of the optimized machines including all the geometric, operational, and material specifications are listed in Appendix Table B.1. The electromagnetic performance analyses are investigated by performing 2-D, non-linear, time-stepping FEM under steady state operation condition with 26Apeak phase current, $13.\bar{3}$Hz synchronous frequency, and 400rpm rated rotor speed.

## 4.4 Comprehensive Comparison of Design and Electromagnetic Performance Characteristics

In this section, the key performance characteristics of electrical machines at rated speed, consists of the combination of Figure 4.7 and 4.8 (see Table 4.1), including dq-axis inductances, back-EMF and air-gap flux density waveforms, irreversible demagnetization, electromagnetic torque, torque ripple, power losses, efficiency, etc. have been investigated in depth and all obtained results have been compared in order to reveal the merits/demerits of the proposed winding topology and figure out how compatible with different rotor topologies. Note that in order to reveal the combined effect of the stator MMF and rotor excitation, the electromagnetic performance waveforms and their harmonic spectra are grouped according to rotor type and winding topology.

### 4.4.1 Inductance

Since the winding configurations have different MMF harmonics, loss behaviour and saturation characteristics of the magnetic circuits are different. In [40], it has been shown that local magnetic saturation causes the variation of the dq-axis inductances in PM machines.

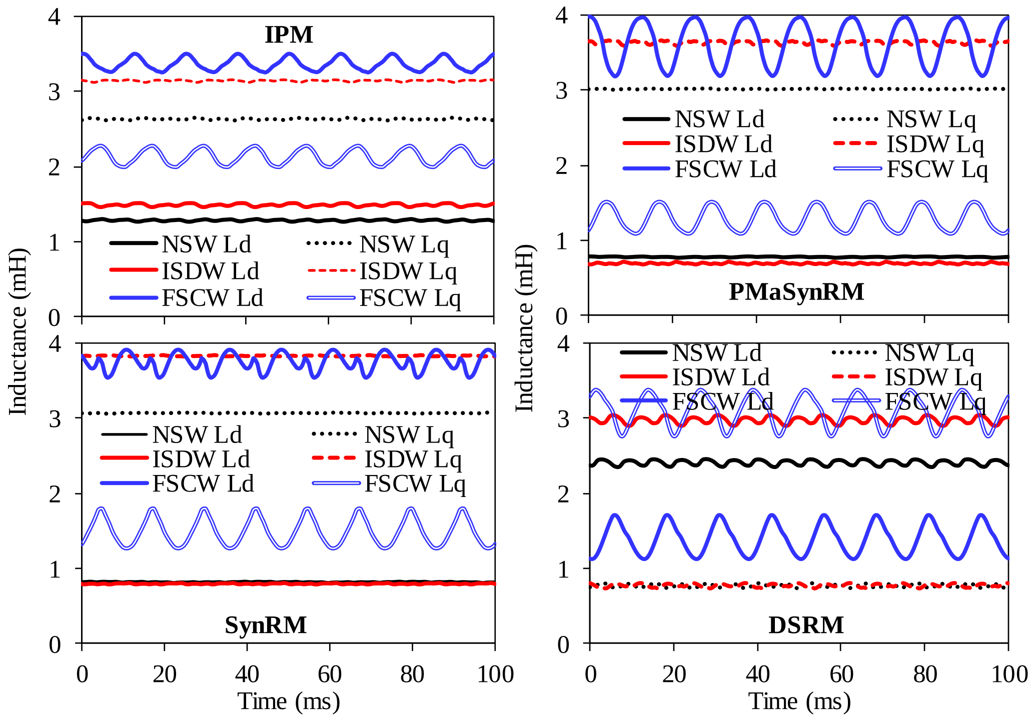


**Figure 4.9 :** Variation of *dq*-axis inductances.

The local saturation characteristics for the machines are shown in Figure 3.14. Therefore, considering Figure 3.14 and Figure 3.9, it can be concluded that the higher the local saturation level, the larger the variation *dq*-axis inductances. Consequently, the FSCW topologies have the highest saturation and hence *dq*-axis inductance variations. It is interesting that the *d*-axis inductance of the FSCW topologies are the highest for IPM, SynRM, and PMaSynRM topologies, but then *q*-axis inductance is the highest for DSRM topology. This is due to the huge reluctance variation between *d*- and *q*-axes of DSRM topology.

### 4.4.2 Back-EMF and induced voltage

The back-EMF and induced voltage waveforms and their harmonic spectra are illustrated in Figure 4.10 and 4.11, respectively. As seen, although the same number of turns per phase have been assigned for all machines, the fundamental amplitudes of the NSW topologies are the lowest due to its lower fundamental winding factor (except for the PMaSynRM and this difference is owing to an increase in the influence of slotting effect). It can be seen from Figure 4.11 that the back-EMF THD level of the FSCW topologies are the highest while it is the lowest for NSW topologies. It has been revealed that the minimum THD levels have been achieved for SynRM topologies while the highest levels have been obtained from the DSRM topologies.

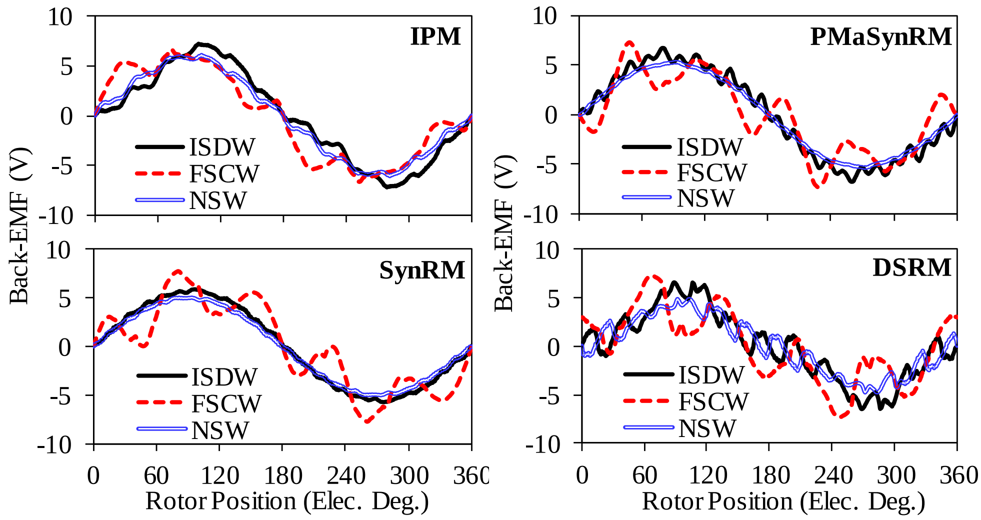


**Figure 4.10 :** Back-EMF (for PM machines) and induced voltage (for Reluctance machines) waveforms.

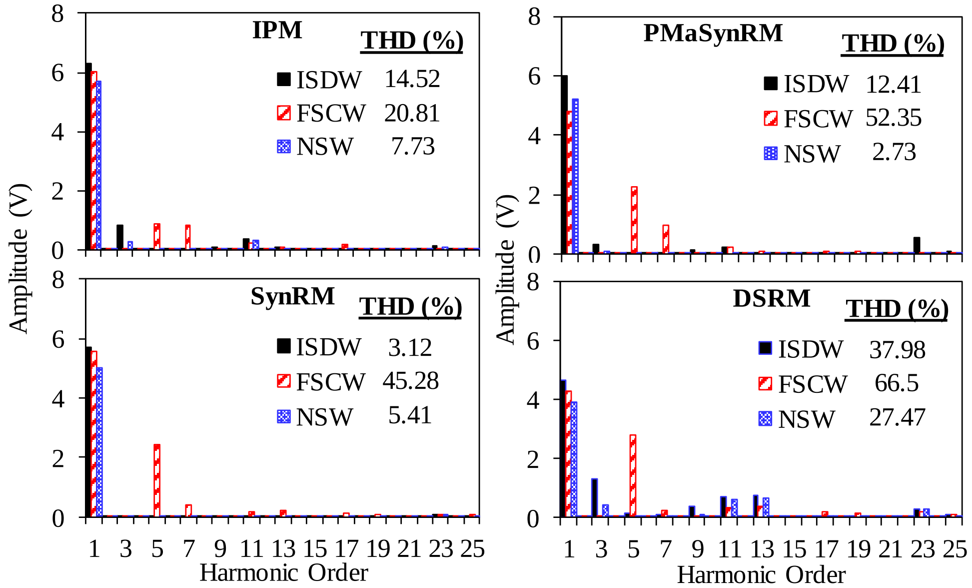


**Figure 4.11 :** Back-EMF and induced voltage harmonic spectra.

### 4.4.3 Air-gap flux density

Investigation of air-gap flux density is quite important for determining the combined effect of winding MMF harmonics, slotting effect, and rotor excitation. The air-gap flux density waveforms and their harmonic spectra are shown in Figure 4.12 and 4.13, respectively. It is possible to investigate the air-gap flux density in terms of winding and rotor topology, separately. As for the winding topology, the machines having FSCWs have the highest MMF distortion level, so, their air-gap flux density waveforms are quite distorted when compared to other machines having ISDWs and NSWs. As for the rotor technology, machines with DSRM rotor have the highest air-gap flux density distortion level and quite low air-gap flux density fundamental amplitude. Therefore, it can be predicted that the machines having DSRM rotors will have the lowest average torque amplitude. In addition, the air-gap flux density distortion levels of the NSW machines are lower than their ISDW counterparts and the fundamental air-gap flux density amplitude of the NSW machines are slightly lower than those of the ISDW machines.

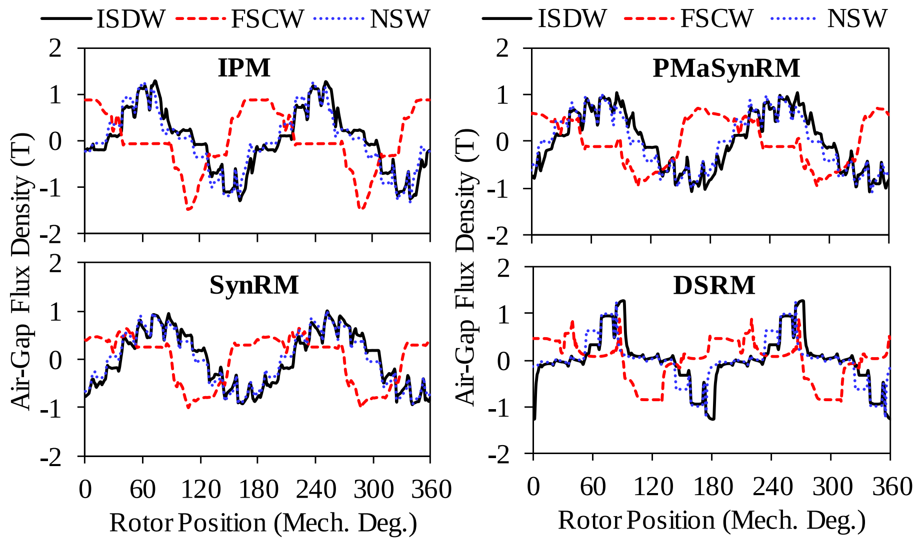


**Figure 4.12 :** Air-gap flux density waveforms.

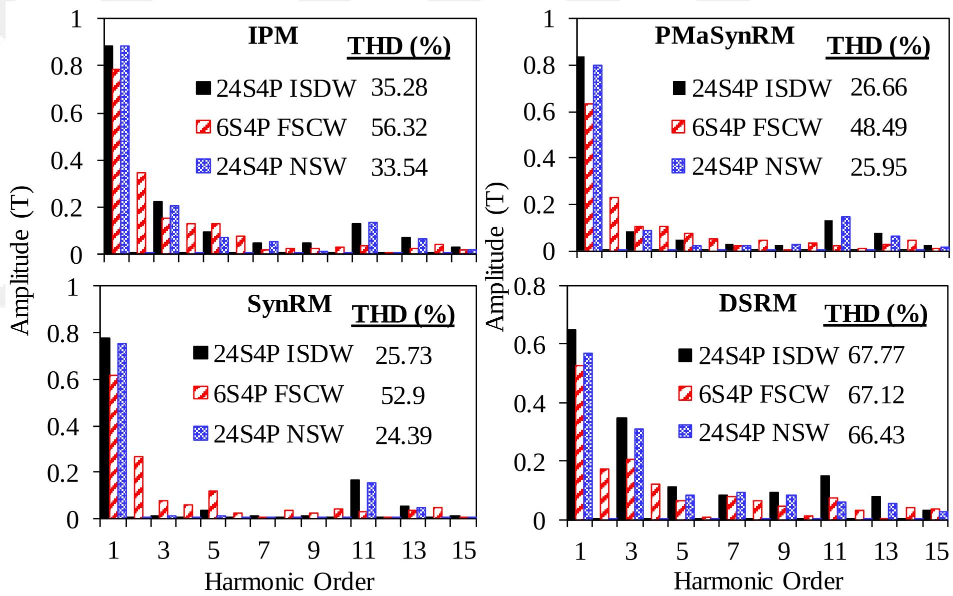


**Figure 4.13 :** Air-gap flux density harmonic spectra.

### 4.4.4 Flux line and density distributions

Magnetic flux density and flux line distributions of the machines are in Figure 4.14. It can be observed that there are some local saturated parts in the stator and rotor parts, particularly in the stator tooth parts. In addition, overall averaged flux densities of the machines are similar. Moreover, it can be observed that the local saturation level of machines having FSCWs are higher than those of the ISDW and NSW machines. This is due to the combined effect of the slotting effect and MMF harmonics.

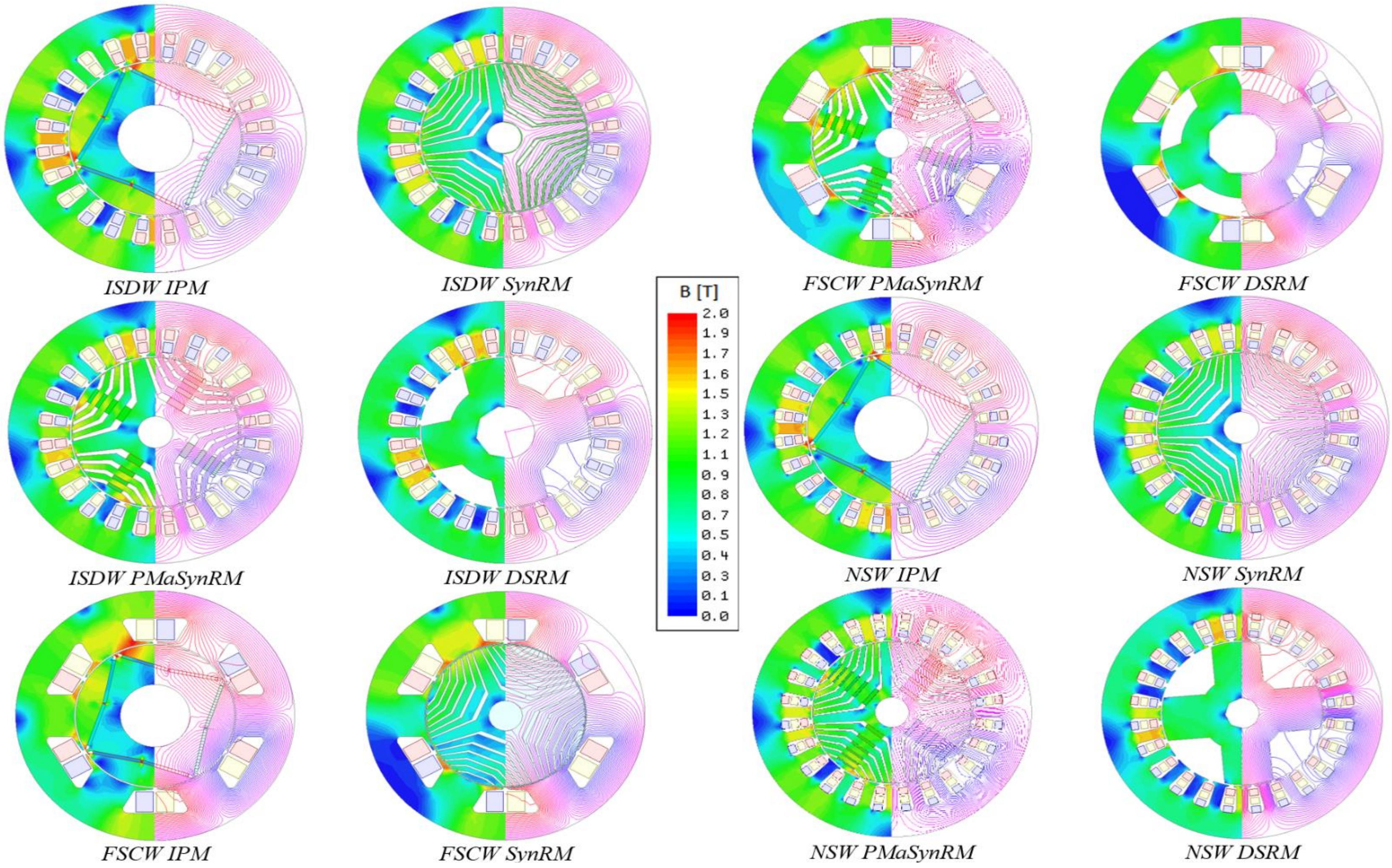


**Figure 4.14 :** Flux density and flux line distributions of considered machines having different winding topologies.

### 4.4.5 Irreversible demagnetization

Since, the irreversible demagnetization may seriously influence the electromagnetic performance, it is quite essential to investigate it. In order to investigate the irreversible demagnetization of PMs, IPMs and PMaSynRMs are operated under overload representing twice the nominal current $(2I_s)$ and the temperature of the PMs is assigned as 80°C. The critical flux density of irreversible demagnetization is assumed to be 0T. Figure 4.15 illustrates the detailed flux density distributions in PMs of IPMs and PMaSynRMs having ISDW, FSCW, and NSW at overloads to observe the partial demagnetization regions.

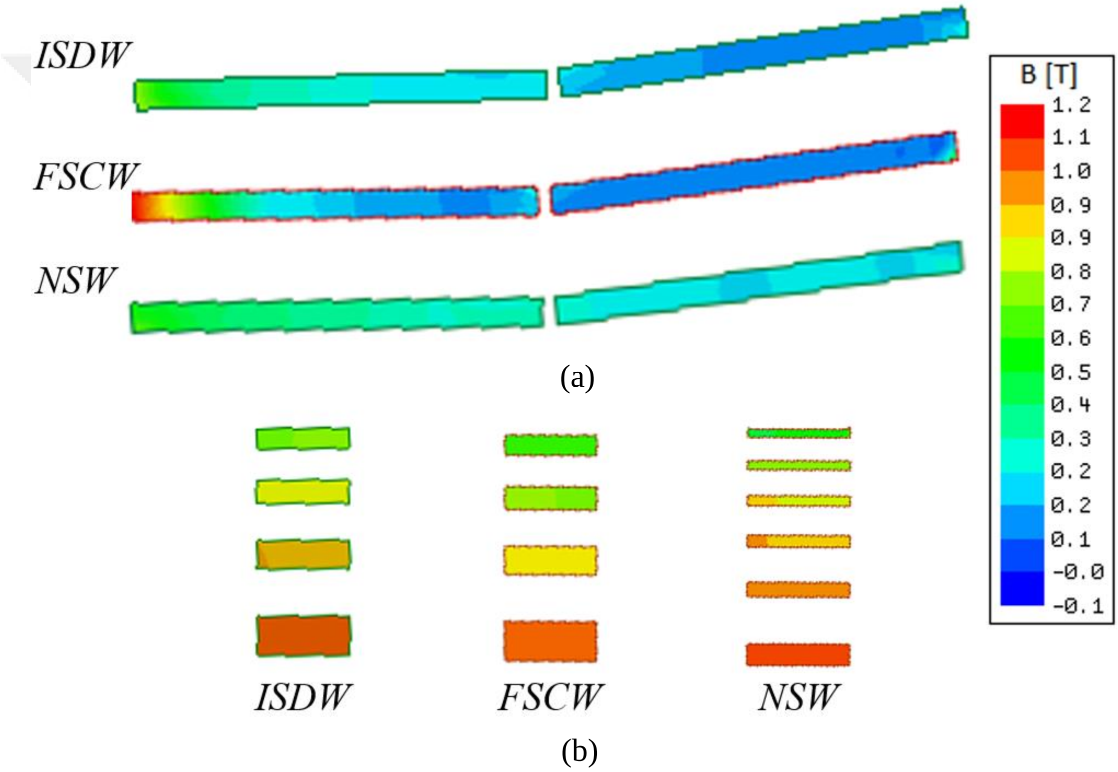


**Figure 4.15 :** Flux density distributions of one pole PMs at overload operating condition for (a) IPMs, (b) PMaSynRMs.

As clearly seen in Figure 4.15, the demagnetization risk of IPMs are higher than those of PMaSynRMs. It is observed that even though the PMaSynRMs have thinner magnets, no demagnetization occurs. As expected, the worst demagnetization occurs in the IPM with FSCW, once it operates at twofold overload. As explained before, this is due to the fact that the FSCWs have significant MMF harmonics causes a significant increase in the level of eddy currents in rotor. In addition, the machines with NSWs exhibit superior capability of withstanding irreversible demagnetization. Yet, it can be observed that partially demagnetized regions of IPM with FSCW are quite narrow (less than ~0.05% of total PM section). Hence, it can be concluded that partial demagnetization is very slight which can be ignored.

### 4.4.6 Electromagnetic torque

The variations of the electromagnetic torque are shown Figure 4.16. As for IPMs, under the same load current and number of turns operating condition, the time averaged torque of the ISDW design is the highest whilst the NSW is the lowest. This is because of the lower fundamental winding factor of the NSW design. As shown in Figure 4.4, the fundamental winding factor of the NSW is ~10.6% lower than that of the ISDW. Consequently, the averaged torque of the NSW design is also ~10% lower than that of the ISDW design, since all the operating and geometric parameters, including phase current and number of turns per phase, have been kept constant for all the machines for a fair comparison (see Table A). The torque ripple levels of the of the machines are similar.

As for the SynRM designs, since the high content of the MMF harmonics causes a significant increase in the level local saturations [157] (see Figure 4.14), the average torque of the FSCW design is the lowest as a consequence of considerable reduction in the amplitude of *reluctance torque* component $T_{rel}$.Therefore, in order to verify this phenomenon, the electromagnetic torque $T_e$ has been separated into its components, which are *alignment* or *PM torque* $T_{pm}$ and $T_{rel}$ by using the combination of frozen permeability and the numerical method presented in [154] and [155], respectively in consideration of (4.4).

$$T_e = T_{pm} + T_{rel} = \frac{3P}{4}\left\{\left[\left(L_d - L_q\right)i_d i_q\right]_s + \left[\lambda_{pm} i_q\right]_s\right\}$$

$$\begin{cases} T_{pm} = \dfrac{3P}{4}\left(\lambda_{pm_d} i_q - \lambda_{pm_q} i_d\right) \\ T_{rel} = \dfrac{3P}{4}\left[\left(L_d - L_q\right)i_d i_q + \left(i_q^2 - i_d^2\right)L_{dq}\right] \end{cases} \tag{4.4}$$

$T_{pm}$ is due to the interaction between the PMs $\lambda_{pm}$ dq-axis components and stator q-axis current $i_q$ and $T_{rel}$ is due to the rotor saliency $\left(L_d - L_q\right)$ and mutual inductance $L_{dq}$. After required calculations, $T_{pm}$ and $T_{rel}$ have been obtained as illustrated in Figure 4.17. Notching that the ratio shown in the figures indicates that how much percentage of $T_e$ is contributed by $T_{pm}$ or $T_{rel}$. Also note that the SynRM and DSRM has no $T_{pm}$ component which mean is that their $T_{rem}$ ratio is 100%. As clearly seen in Figure 4.16 and 4.17, the $T_{rel}$ component of the NSW is considerably higher than that of FSCW. It has also been revealed that the ratio of $T_{rel}$ contribution to $T_e$ of PMaSynRM is more than 2 times higher than that of IPM. Moreover, due to the increased combined effect of the slotting and MMF harmonics as a consequence of the chosen slot/pole combination, the torque ripple level of the FSCW design is the highest. As for the PMaSynRM topology, again the FSCW design has the lowest torque as expected and the highest torque ripple rate. On the other hand, as for the DSRM topology, all designs show similar characteristics: quite low torque and very high torque ripple rate. It can be deduced that the NSW topology is compatible for any motor technology. In addition, among the considered machine technologies, IPM and PMaSynRM topologies show promising results in terms of torque density (see Figure 4.16 and Table 4.3). In terms of torque ripple rate, the SynRM topology provides quite low torque ripple rate once it is combined with ISDW or NSW winding topologies.

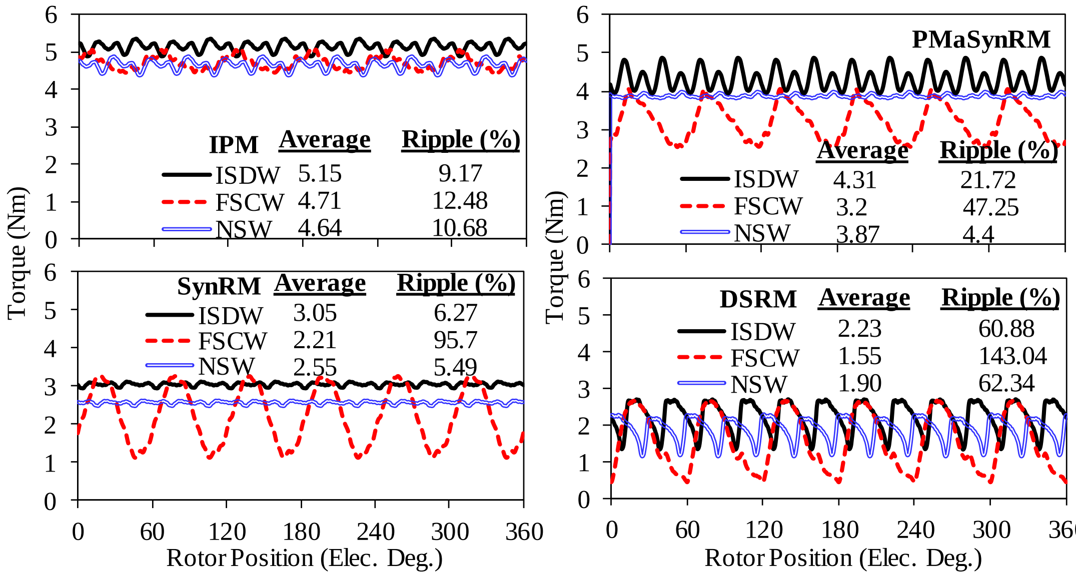


**Figure 4.16 :** Variation of torque $T_e$ with respect to time.

Another important point in this analysis is that the reason behind the lower electromagnetic torque of the PMaSynRM (even though the same amount of PM volume is used). The reason behind this phenomenon can be explaining by examining $T_e$ given in (4.4). The variation of all related inductances of the IPM and PMaSynRM are illustrated in Figure 4.18. As seen from (4.4), the lower the difference between $L_d$ and $L_q$, the higher the average electromagnetic torque, since the sign is negative. As clearly seen in Figure 4.18, the difference between the inductances of PMaSynRM is almost 3 times of the IPM. As a consequence of significantly reduction of reluctance torque component, the total torque of the PMaSynRM is reduced considerably. Therefore, even though the same amount of PM material is used, the average torque of the PMaSynRM will always be lower than that of the IPM under the same design specifications and operating conditions.

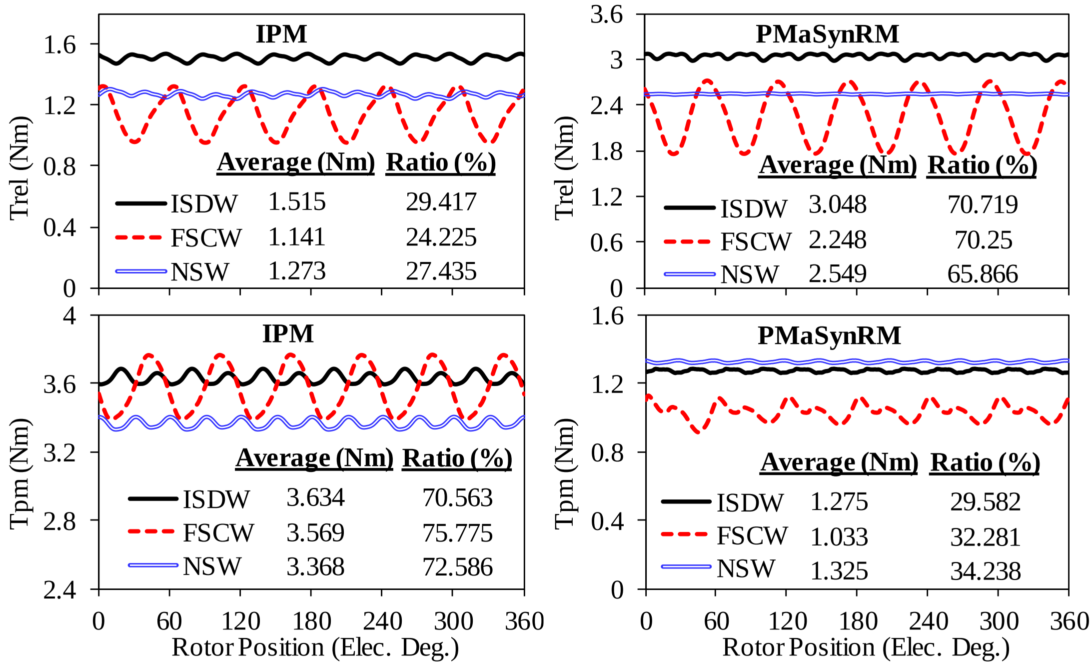


**Figure 4.17 :** Variation of torque components $T_{rel}$ and $T_{pm}$ of IPMs and PMaSynRMs with respect to time.

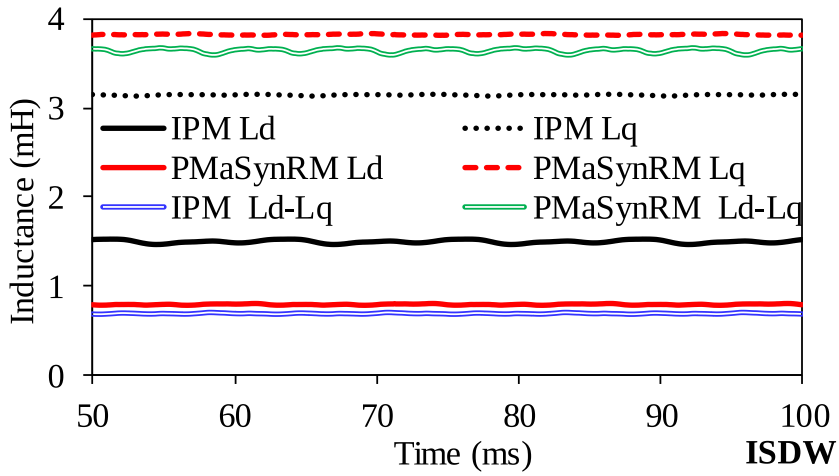


**Figure 4.18 :** Variation of *dq*-axis inductances of IPM and PMaSynRM having ISDWs.

Torque density (torque per volume) $TPV$ is one of the important parameters that should be considered while comparing the features of the different winding topologies. The TPVs have been calculated by using (4.5) for each machine and obtained results listed in Table 4.3.

$$TPV = \frac{4T_{e_{avg}}}{\pi D_{so}^2 l_{axial}} \tag{4.5}$$

where $T_{e_{avg}}$, $D_{so}$, and $l_{axial}$ are average electromagnetic torque, stator outer diameter, and total axial length (see Figure 4.6). As clearly seen, the IPMs have the highest torque density while the DSRMs have the lowest. Table 4.3 shows also that the torque density of NSW is comparable to other topologies, even the highest once combined with PMaSynRM.

**Table 4.3 :** Torque density TPV (kNm/m$^3$) comparison.

| | **IPM** | **SynRM** | **PMaSynRM** | **DSRM** |
|---|---|---|---|---|
| **ISDW** | 4.22 | 2.5 | 3.53 | 1.83 |
| **FSCW** | 5.25 | 2.47 | 3.57 | 1.73 |
| **NSW** | 4.67 | 2.57 | 3.9 | 1.91 |

### 4.4.7 Power losses and efficiency

The slot filling factor is the most important parameter for the accurate calculation of the stator phase resistance and hence efficiency. The variation of the phase resistance and stator copper loss with respect to slot fill factor is illustrated in Figure 4.19. Note that the stator and windings of the ISDW deign have been used for the calculation of the phase resistance and stator copper loss.  It is obvious that the higher the stator slot fill factor, the lower the phase resistance and lower the copper loss. As shown in [155], the practical maximum filling factor is 0.78 with the pressed windings. And the corresponding calculations have been done with 0.51 fill factor.

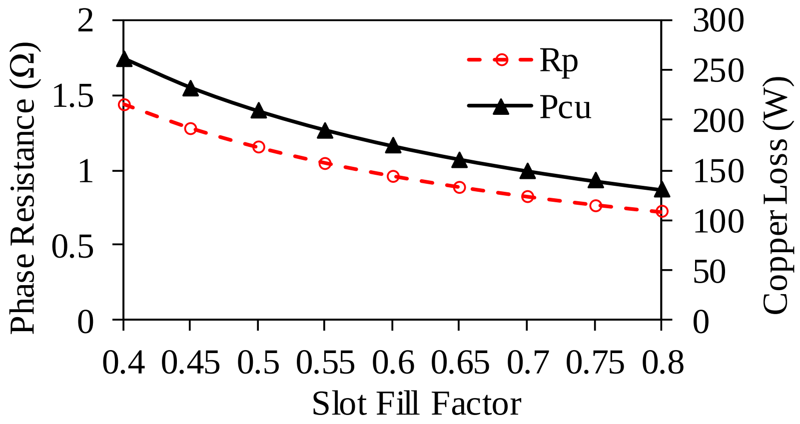


**Figure 4.19 :** Variation of phase resistance *Rp* and copper loss *Pcu* with respect to slot fill factor.

Comparison of the copper, core, and PM losses and efficiency at a number of different speeds under rated power $P_{out}$ (see Table 4.4) are given in Table 4.5. Stator slot copper loss $Pscu_{in}$ and end-winding loss $Pscu_{end}$ are calculated by using the average coil lengths given between (4.1)-(4.3) and (4.7)-(4.10), where $V_n$ accounts for the insulation of the winding in V, resistivity of copper $\rho_{cu}$, number of turns per slot $N_t$, number of coils per phase $N_c$, cross-sectional slot area $A_c$, slot fill factor $k_f$, and average coil length $l_{av\_winding}$ [123].

$$P_{PM} = \frac{1}{\sigma_{PM}} I_{ePM}^2 \tag{4.6}$$

$$l_{av\_ISDW} \approx 2l_{stack} + \frac{2\pi r_w y_c}{S} + 4y_c \cdot V_n 10^{-5} \tag{4.7}$$

$$l_{av\_FSCW} \approx 2l_{stack} + \frac{3.72\pi r_w}{S} + 4y_c \cdot V_n 10^{-5} \tag{4.8}$$

$$l_{av\_NSW} \approx 2l_{stack} + \frac{5.44\pi r_w}{S} + 4y_c \cdot V_n 10^{-5} \tag{4.9}$$

$$P_{core} = k_h f B_m^2 + k_c (f B_m)^2 + k_e (f B_m)^{1.5} \tag{4.10}$$

$$P_{cu} = 3 I_s^2 \rho_{cu} N_t^2 N_c \frac{l_{av\_winding}}{A_c k_f} \tag{4.11}$$

$$P_{out} = T_e \omega_r \tag{4.12}$$

$$\eta = 100 \frac{P_{out}}{P_{out} + P_{cu} + P_{PM} + P_{core} + P_{add}} \tag{4.13}$$

As seen in Table 4.5, since the same number of turns and slot fill factor is assigned for the machines, the slot-winding copper losses are the same. However, since the end-winding lengths of the machines are different, the ISDW has the highest end-winding copper loss while the FSCW has the lowest. As expected, the end-winding copper loss of the proposed NSW design is between the ISDW and FSCW designs. The PM loss $P_{pm}$ calculated by considering the conductivity of the PM material $\sigma_{pm}$ and the eddy current induced on the PMs $I_{e_{pm}}$ as expressed in (4.6) and the core loss $P_{core}$ calculated by considering the core loss coefficients; hysteresis, eddy-current, and excessive $k_h$, $k_c$, and $k_e$, respectively, working frequency $f$, and the amplitude of the AC flux component $B_m$ as expressed in (4.11) are illustrated in Table 4.5 for each machine. Because of the very high MMF harmonics and consequently eddy current of the FSCW design, particularly in the rotor part, the total core and PM losses of the FSCW IPM and PMaSynRM are quite higher than those of the ISDW and NSW counter parts. Comparison of rated output power $P_{out}$, expressed in (4.12) where $T_e$ electromagnetic torque and $\omega_r$ angular speed, for each machine topology is given in Table 4.4. Moreover, the efficiency $\eta$, calculated as expressed in (4.13), is shown in Table 4.5. Note that 1% of output power is considered as additional power losses $P_{add}$ in order to obtain more accurate efficiency rate [157]. As clearly seen in the Table 4.4, since there is a direct correlation between the fundamental winding factor and output power (in the case of same number of turns, current excitation, stator outer diameter, and stack length), the average output powers of the machines are proportional to their fundamental winding factor. The highest torque is achieved for the IPM with ISDW and the highest efficiency is achieved for the IPM with FSCW. Furthermore, Table 4.5 reveals also these findings from low to high speed: (i) dominant loss component changed from copper to core; (ii) combination of FSCW and PMaSynRM results with excessively high $P_{pm}$. Considering the $T_e$ or $TPV$, the IPM and PMaSynRM machines show promising results for the electric vehicle and aerospace applications.

**Table 4.4 :** Comparison of rated $P_{out}$ (W)

| | **IPM** | **SynRM** | **PMaSynRM** | **DSRM** |
|---|---|---|---|---|
| **ISDW** | 216 | 128 | 181 | 93.33 |
| **FSCW** | 197.25 | 93 | 134.25 | 65 |
| **NSW** | 194 | 107 | 162.21 | 79.43 |

**Table 4.5 :** Comparison of losses at a number of different speeds under rated power.

| | | $n_r$ | $Pscu_{i.n}$ | $Pscu_{end}$ | $P_{core}$ | $P_{pm}$ | $\eta$ | | | $n_r$ | $Pscu_{i.n}$ | $Pscu_{end}$ | $P_{core}$ | $P_{pm}$ | $\eta$ |
|---|---|---|---|---|---|---|---|---|---|---|---|---|---|---|---|
| IPM | ISDW | 400 | 27.38 | 36.3 | 1.57 | 0.02 | 76.19 | PMaSynRM | ISDW | 400 | 27.38 | 36.3 | 1.6 | 0.17 | 72.86 |
| | | 1000 | 5.26 | 6.98 | 3.32 | 0.05 | 92.4 | | | 1000 | 8.12 | 10.77 | 2.4 | 0.62 | 88.38 |
| | | 2000 | 1.48 | 1.96 | 6.76 | 0.12 | 94.54 | | | 2000 | 2.28 | 3.02 | 4.85 | 1.21 | 93.22 |
| | | 3000 | 0.65 | 0.86 | 10.7 | 0.09 | 93.6 | | | 3000 | 1 | 1.33 | 8.98 | 0.96 | 92.78 |
| | FSCW | 400 | 27.38 | 15.6 | 1.83 | 1.9 | 80.21 | | FSCW | 400 | 27.38 | 15.6 | 1.47 | 1.17 | 74.09 |
| | | 1000 | 5.26 | 3 | 3.27 | 0.2 | 93.68 | | | 1000 | 7.16 | 4.08 | 2.55 | 2.37 | 88.52 |
| | | 2000 | 1.46 | 0.83 | 5.92 | 0.23 | 95.09 | | | 2000 | 1.98 | 1.13 | 4.62 | 2.71 | 91.91 |
| | | 3000 | 0.65 | 0.37 | 9.35 | 0.25 | 94.06 | | | 3000 | 0.88 | 0.5 | 7.29 | 2.9 | 91.21 |
| | NSW | 400 | 27.38 | 24.77 | 1.52 | 0.02 | 77.75 | | NSW | 400 | 27.38 | 24.77 | 1.37 | 0.12 | 74.59 |
| | | 1000 | 5.26 | 4.76 | 3.25 | 0.06 | 92.73 | | | 1000 | 7.96 | 7.2 | 2.02 | 0.37 | 89.36 |
| | | 2000 | 1.48 | 1.34 | 6.75 | 0.12 | 94.38 | | | 2000 | 2.23 | 2.02 | 4.2 | 0.76 | 93.73 |
| | | 3000 | 0.65 | 0.59 | 10.62 | 0.08 | 93.26 | | | 3000 | 0.98 | 0.89 | 7.27 | 0.54 | 93.48 |
| SynRM | ISDW | 400 | 27.38 | 36.3 | 1.43 | 0 | 65.77 | DSRM | ISDW | 400 | 27.38 | 36.3 | 1.11 | 0 | 58.68 |
| | | 1000 | 10.37 | 13.75 | 2.16 | 0 | 82.35 | | | 1000 | 10.37 | 13.75 | 1.67 | 0 | 77.79 |
| | | 2000 | 2.91 | 3.86 | 4.41 | 0 | 91.13 | | | 2000 | 2.91 | 3.86 | 3.4 | 0 | 89.33 |
| | | 3000 | 1.28 | 1.69 | 8.56 | 0 | 90.9 | | | 3000 | 1.28 | 1.69 | 6.62 | 0 | 89.84 |
| | FSCW | 400 | 27.38 | 15.6 | 1.54 | 0 | 67.11 | | FSCW | 400 | 27.38 | 15.6 | 1.01 | 0 | 59.25 |
| | | 1000 | 9.11 | 5.19 | 2.62 | 0 | 83.83 | | | 1000 | 10.5 | 5.98 | 1.82 | 0 | 77.43 |
| | | 2000 | 2.56 | 1.46 | 4.85 | 0 | 90.47 | | | 2000 | 2.91 | 1.66 | 3.38 | 0 | 88.33 |
| | | 3000 | 1.12 | 0.64 | 8.56 | 0 | 89.2 | | | 3000 | 1.29 | 0.74 | 5.96 | 0 | 88.26 |
| | NSW | 400 | 27.38 | 24.77 | 1.33 | 0 | 66.2 | | NSW | 400 | 27.38 | 24.77 | 1 | 0 | 59.56 |
| | | 1000 | 10.63 | 9.62 | 1.91 | 0 | 82.4 | | | 1000 | 10.39 | 9.4 | 1.48 | 0 | 78.18 |
| | | 2000 | 2.98 | 2.7 | 3.97 | 0 | 90.89 | | | 2000 | 2.92 | 2.64 | 3.07 | 0 | 89.34 |
| | | 3000 | 0.51 | 1.18 | 8.24 | 0 | 90.68 | | | 3000 | 1.28 | 1.16 | 6.38 | 0 | 89.16 |

**Units—$n_r$:rpm; Losses: W; $\eta$:%.*

On the other hand, considering that the usage of the same amount of PM, since the IPM topologies have higher torque/power densities than those of the PMaSynRM topologies, it is cost effective to choose IPM topology. However, it is also very important to know the flux-weakening performance characteristics before choosing the best candidate. Considering Figure 4.6 and 4.20, it can be concluded that if the proposed NSW topology is utilized instead of ISDW topology, ~18.7% shorter total axial length can be achieved with ~2.05% increased efficiency but with ~10.2% reduced output power (for IPM) under rated speed. Therefore, it can be predicted that thanks to the proposed NSW topology, much higher efficiency IPM machines can be designed generating the same output power as its ISDW counterpart with still shorter total axial length. It has also been revealed that for small power applications, it might me be more reasonable to use FSCW topology because of the moderate output power with high efficiency. However, as shown in [118] and [119] for large power application, since large amount of the cooling equipment might be required because of the large eddy current induced in the rotor part. In addition, excessive eddy currents can further lead to a high rotor temperature particularly at high speeds, and hence the rotor magnets will suffer from a high risk of irreversible demagnetization [57, 59, 115, 117]. On the other hand, since the proposed winding topology has quite low MMF harmonics and consequently low eddy current losses, it does not require additional cooling for the rotor part and has low risk of irreversible demagnetization. Consequently, more compact and high efficiency IPMs can be designed for particularly EV/HEV applications by utilizing the proposed NSWs.

### 4.5 Conclusion

In order to investigate the combability of the proposed winding topology for different machine technologies, IPM, SnyRM, PMaSynRM, and DSRM have been designed and analysed. Then, in order to reveal the merits/demerits of the proposed winding topology, the ISDW and FSCW topologies have been utilized for the considered machine technologies and obtained electromagnetic performance results have been compared comprehensively. In this paper, the obtained key findings can be summarized as follows.

- It is validated that the electromagnetic performance characteristics of the IPM, SynRM, PMaSynRM, and DSRM with the proposed NSW topology are comparable to design with ISDW and FSCW topologies;
- Implementation of NSWs into the considered machine technologies results with:
  - ✓ Significantly improved efficiency over ISDWs;
  - ✓ Substantially shortened end-winding axial and radial lengths over ISDWs;
  - ✓ Lower rotor losses, particularly PM losses over ISDWs and FSCWs;
  - ✓ Lower risk of irreversible demagnetization of PMs over ISDWs and FSCWs;
  - ✓ Higher torque density over ISDWs and FSCW for all reluctance machines;
  - ✓ Higher output power over FSCWs for all reluctance machines.
- The main disadvantages of NSW topology are relatively low winding factor and manufacturing difficulty;
- Since the lower winding factor is compensated by higher reluctance torque component of NSWs, it does not require more number of turns compared to FSCWs;
- The highest torque/power density can be achieved by utilizing IPM rotor.

The flux-weakening (FW) calculations of the IPM machine designed by utilizing the proposed NSWs will be presented in Chapter 6. On the other hand, influence of design parameters such as stack length, number of turns, etc. on performance characteristics will also be investigated for the sake of completeness and reviving of the merits of the proposed NSW topology in Chapter 6. In addition, the details of the optimization procedure for the best machine topology, which is determined as IPM technology in this study, will also be presented in Chapter 5.

# 5. SYSTEMATIC DESIGN OPTIMIZATION APPROACH FOR INTERIOR PERMANENT MAGNET MACHINES EQUIPPED WITH NOVEL SEMI-OVERLAPPING WINDINGS[4]

In this chapter, a systematic approach to achieve optimized design of IPM having NSWs is presented. The optimization parameters have been determined individually by performing sensitivity analyses. Multi-objective global optimization is subsequently performed. Genetic Algorithm (GA) approach, which is also known as "random search with learning algorithm" and an effective optimization tool used for design optimization of electric machines, is employed. IPMs equipped with ISDW and NSW are initially designed by using the geometric and operating parameters of Toyota Prius 2010 IPM. Subsequently a time-stepping 2-D FEA based program is employed to perform the optimization and quickly evaluate the optimal solution among the thousands of design candidates thanks to the sensitivity analyses. In order to reveal the effectiveness and rapidity of the multi-objective global optimization, a comprehensive electromagnetic performance comparison between the original (with ISDWs), initial and optimal designs (with NSWs) is presented. Finally, a small IPM prototype globally optimized by using the proposed procedure is manufactured and the FEA results have been validated by measurements. The goal of this study is to advance the state-of-the-art in the multi-objective design optimization of NSW IPMs by performing sensitivity analyses to reach the optimal solution quickly and to determine the most sensitive design parameters affecting the key performance characteristics.

## 5.1 Introduction

In recent years, there has been a growing need for high-performance electrical machines. Electrical machines with PMs are excessively employed in various applications due to their superior output characteristics, such as high efficiency, high

[4] This chapter is based on the paper: **Gundogdu, T. and Komurgoz, G.** (2021) A systematic design optimization approach for interior permanent magnet machines equipped with novel semi-overlapping windings, *Struct. Multidisc. Optim.*, *63*, 1491-1512.

torque and power densities, etc. It is necessary to develop an optimal design technique to meet the demand for high-performance electrical machines. In literature, papers on the optimization of IPMs by various optimization algorithms with different objectives have been extensively presented. In addition, comprehensive review studies on recent developments in electrical machine design optimization methods can also be found (26). Extensively used optimization algorithms for the design optimization of PM machines have been summarized as follows.

1) Genetic algorithms (GAs) [158-168];
2) Differential evolution (DE) [169-177];
3) Particle swarm optimization (PSO) [178-180];
4) Response surface (RS) [164, 181, 182]. rapidity

As can be realized, the GA and the DE are the most preferred optimization algorithms because, both algorithms provide fast and accurate solutions for multi-objective problems and they can be run without any need for experimental data. Typical objectives for the design optimization of any kind of PM machine, such as highest available torque and efficiency, minimum torque ripple, lowest cost, and minimum weight of active materials, can be individually (single-objective) or simultaneously (multi-objective) met by a process in which the electromagnetic problem is solved with consideration of the mechanical, thermal, and material aspects. The designers, engineers, or researchers, dealing with the PM machine design, mostly determined the following objectives for different industry applications.

a) Performance improvement via various optimization algorithms [159-164, 167, 172-177, 182-185, 187-190];
b) Back-EMF characteristic improvement [165, 180, 191];
c) Torque ripple reduction [162, 165, 169, 175-178, 182, 184, 186];
d) Cost and/or weight reduction [160, 169, 167, 175-177];
e) Performance improvement by considering the flux-weakening capability [163, 166, 168, 170, 174, 176, 181];
f) Performance improvement by considering the driving cycle [170, 171];

Multi-objective design optimization methods to find the global optimum solution by considering a number of design parameters; such as split ratio, stator slot and slot opening dimensions, magnet and flux barrier position and dimensions, etc. for achieving maximum torque and output power, minimum machine losses or maximum efficiency, maximum back-EMF (for generator operating), and minimum torque ripple and cogging torque have been extensively studied for IPMs [159-164, 167, 172, 175, 177, 182, 185, 187-191]. In addition, different winding topologies; i.e. ISDWs, fractional-slot concentrated windings (FSCWs), etc. and PM rotor topologies; i.e. embedded surface PM and IPM have also been considered for multi-objective design optimization [173].

In literature, magnet shape and flux barrier optimization studies can also be found extensively [165, 169, 178, 184, 186, 190]. In [190], a rotor shape optimization method for IPM to reduce the harmonic iron losses at high rotating speed under flux-weakening control is introduced. [178] proposed a PSO method with the aim of determining the best flux barrier shape for an IPM with the objective of achieving a smooth and high torque. [184] introduced an optimization approach based on a phase field method using an Allen-Cahn equation to be able to obtain a sinusoidal air-gap flux density for low torque ripple and cogging torque. [182] optimized the anisotropic ferrite magnet shape and magnetization direction to achieve maximum back-EMF amplitude and minimum torque ripple by GA. [169] presented a rotor optimization method, consisting of rotor segmentation and arrangement, to improve the utilization of rare earth PM materials and reduce the torque ripple. [186] proposed to tackle the combined shape and topology optimization problem by solving an adjoint formulation by a sequential gradient-based convex programming approach to minimize the torque ripple of an IPM.

Various optimization methods by considering the flux-weakening capability (achieving wide operating range) by mainly maximizing the characteristics current [166, 168, 170, 171, 174, 176, 181, 190], driving cycle and efficiency map [170, 171], material cost under wide operating range [174, 176], saturation effect [181], rotor shaping for achieving wide operating range and reducing harmonic losses at high speed [190] are also available in the literature. Furthermore, [185] suggested a set of general rules for optimizing the saliency ratio of an IPM with fractional slot concentrated windings (FSCWs).

In the design stage of IPMs, finding the global optimal solution effectively and quickly is very challenging task due to the existence of a large number of design parameters and interdependence of these parameters (see Figure 5.1). Therefore, determining the design parameters which have a considerable effect on the key performance characteristics, such as torque, torque ripple, power losses, material weight, efficiency, etc. is of great importance. In this study, we propose an unconventional multi-objective design optimization approach for IPM with NSWs to obtain maximum electromagnetic torque with minimum torque ripple and high efficiency. The proposed unconventional optimization approach consists of two stages. The first stage is the individual optimization which is a vital procedure to determine the most dominant optimization parameters and their constraints. And the second stage is the global optimization which offers insight on cross-correlation between different parameters and can be achieved very quickly thanks to the first stage. Therefore, this is the first study presenting a comprehensive optimization procedure for the quick global optimization of IPMs with NSWs. The proposed optimization procedure has been conducted for large (original Toyota Prius 2010 IPM) and small (prototype) machine dimensions in order to examine the reliability. The variation of optimization parameters and cost with respect to evaluation number are shown. The pareto front in average torque, torque ripple, and efficiency graphs has also been illustrated. Furthermore, a comprehensive design and electromagnetic performance characteristics comparison between original Toyota Prius 2010 IPM with integer-slot distributed windings (ISDWs) and initial and optimized IPMs with NSWs are presented. We are of the opinion that this paper will serve as a reliable guideline for the readers dealing with the design optimization of IPMs.

The paper is organized as follows. The structure and key properties of the NSW are introduced in Section 5.2. In Section 5.3, sensitivity analyses, conducted for the determination of the dominant optimization parameters and their constraints, are presented. Section 5.4 deals with the and justification of objectives and multi-objective global optimization of IPMs having large dimensions. The electromagnetic performance characteristics of globally optimized IPMs having ISDWs and NSWs are compared comprehensively in Section 5.5. Design optimization procedure for the prototyped machine and validation of experimental test results are presented in Section 5.6 and 5.7, respectively.

## 5.2 Individual Optimization of Large NSW IPMs

The aim of design optimization for electrical machines is to adjust the geometric parameters in order to make the most of them to achieve the highest torque, power, efficiency, etc. or the lowest ripple torque, weight, cost, etc. In general, electrical machines can be optimized by either individual or global approaches. Note that the individual optimization approach does not offer insight on cross-correlation between different parameters. However, it does offer insight on sensitivity of electromagnetic performance characteristics, such as torque, torque ripple, power losses, etc. on each considered parameter. Therefore, it is very practical to determine the sensitive optimization parameters and their constraints among a large number of geometry parameters seen in Figure 5.1. After this step, individually optimized multiple geometry parameters, can be globally optimized by using a global optimization approach, such as genetic algorithm (GA). In this way a global optimum can be found very quickly.

In order to implement the individual optimization, the sequence of design parameters should follow their sensitivity [192]. Particularly, the most sensitive parameter, which has the dominant effect on the objective, should be optimized first. Afterwards, the second and so on the most sensitive parameters should be optimized accordingly. The numerical analysis of IPMs in this study is based on FEA. The governing equation of a magnetic system hereby be described as follows.

$$\nabla \times v\mathbf{B} = \mathbf{J} + \nabla \times v\mathbf{B}_r \tag{5.1}$$

$$\mathbf{B} = \nabla \times \mathbf{A} \tag{5.2}$$

where $v$, $\mathbf{B}$, $\mathbf{B}_r$, $\mathbf{J}$, and $\mathbf{A}$ are the magnetic reluctivity, the flux density, the remanent flux density, the load current density, and the vector potential, respectively.

### 5.2.1 Determination of optimization parameters

A two-dimensional IPM with 3-phase winding, 8 magnetic poles and 48 stator slots is considered. The design parameters are indicated in Figure 5.1 for 1/8$^{th}$ segment model of the IPM. The same geometric parameters have been optimized separately for both IPMs having conventional (original-ISDW) and NSWs. Other specifications, not directly participating with the optimization procedure, such as number of turns per phase, stack and air-gap length, stator outer diameter, stator slot and pole number combinations, etc. are kept constant at their initial values (see Table 5.1) which are same as the original Toyota Prius 2010 IPM. The definitions of the optimization parameters and the individual optimization sequence are listed in Table 5.2.

Before initiating the individual optimization, the excitation source should be chosen and fixed during the optimization process. The excitation source (or constant) can be chosen as phase current, stator current density, or stator copper loss. All these excitation constants have been investigated in the following sub-sections. As for the following individual optimizations, the phase current is chosen as excitation constant as expressed in (5.3), where $k_c$, $A_s$, and $N_t$ denote the copper loss coefficient, slot area, and number of turns per coil.

$$I_s = \frac{k_c\sqrt{A_s}}{N_t} \tag{5.3}$$

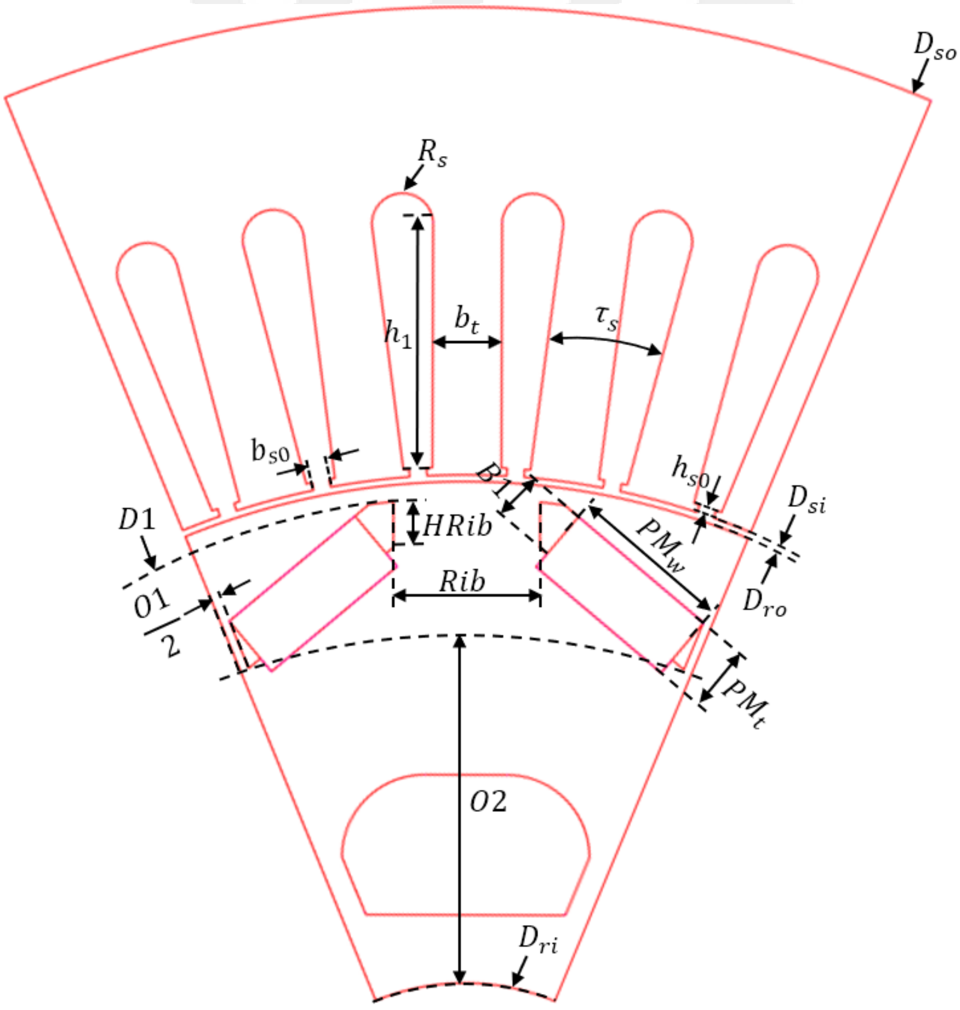


**Figure 5.1 :** Design variables of the IPM.

As can be predicted, time and effort consumption of the optimization process depends on the number of optimization parameters and their constraints. Keeping the number of optimization parameters as low as possible is of great importance. Therefore, the optimization parameters, having the most significant effect on the optimization objective(s), should be chosen carefully.

### 5.2.2 Optimization with restriction of maximum inverter current

In this subsection, the individual optimization of the geometric parameters given in Table 5.2 is presented. The sensitivities of time averaged torque, torque ripple, and stator copper loss to the considered parameters are investigated. the excitation constant as the maximum inverter current, which is determined by (5.4) has been chosen.

$$I_{s_{max}} = \sqrt{i_d^2 + i_q^2} \tag{5.4}$$

In addition, the current angles delivering the maximum electromagnetic torque is parametrically determined for each values of geometric parameters. Variation of average torque, torque ripple, phase peak current, and copper loss with respect to tooth width ratio $b_s$ is illustrated in Figure 5.2.

**Table 5.1 :** Initial parameters.

| Parameter | Value | Parameter | Value |
|---|---|---|---|
| Phase current, $I_s$, $A$peak | 236 | $R_s$ | 2 |
| Current density, $J_s$, $A/mm^2$ | 27.5 | $h_1$ | 26.75 |
| Slot fill factor, $k_f$ | 0.448 | $h_{s0}$ | 0.5 |
| Rated speed, rpm | 1000 | $b_t$ | 7.55 |
| Pole number, $P$ | 8 | $b_{s0}$ | 2 |
| Active stack length, $\ell_a$ | 50.8 | $D_1$ | 156.84 |
| Stator slot number, $S$ | 48 | $O_1$ | 1.86 |
| Outer diameter of stator, $D_{so}$ | 264 | $O_2$ | 118.04 |
| Inner diameter of stator, $D_{si}$ | 161.9 | $B_1$ | 5.3 |
| Stator slot pitch, $\tau_s$ | 12.46 | $HR_{ib}$ | 5 |
| Outer diameter of rotor, $D_{ro}$ | 160.44 | $R_{ib}$ | 16 |
| Inner diameter of rotor, $D_{ri}$ | 51 | $PM_w$ | 17.88 |
| Air-gap length, $g$ | 0.73 | $PM_t$ | 7.16 |

As clearly seen, as the stator tooth ratio is increased, average torque, torque ripple, and stator copper loss linearly increase. Since the excitation constant is chosen as phase current, it kept constant. Enlarging the tooth width is result in lower saturation level in tooth bodies, which causes an increase in torque level. On the other hand, since the slot area is narrowed, namely the diameter of conductor is reduced, the copper loss eventually increases.

**Table 5.2 :** Definitions of geometric parameters.

| # | ***Explanation*** | ***Equation*** |
|---|---|---|
| **1** | Stator split ratio | $\lambda_s = \dfrac{D_{si}}{D_{so}}$ |
| **2** | Stator tooth width ratio | $b_s = \dfrac{b_t}{\tau_s}$ |
| **3** | Stator slot height | $h_1$ |
| **4** | Rotor outer bridge width between flux barriers | $R_{ib}$ |
| **5** | Rotor inner bridge radius | $O_2$ |
| **6** | Flux barrier thickness | $B_1$ |
| **7** | Rotor inner bridge width between flux barriers | $O_1$ |
| **8** | Rotor outer bridge radius | $D_1$ |
| **9** | Height of flux barriers | $HR_{ib}$ |
| **10** | Magnet width | $PM_w$ |
| **11** | Magnet thickness | $PM_t$ |
| **12** | Stator slot opening height ratio | $h_0 = \dfrac{h_{s0}}{h_{s0} + h_1}$ |
| **13** | Stator slot opening width ratio | $b_o = \dfrac{b_{s0}}{\tau_s}$ |

Variation of torque and torque ripple with respect to spit ratio $\lambda_s$ is shown in Figure 5.2(a). As indicated, the maximum average torque is achieved at 0.622 with relatively low torque ripple. Therefore, 0.622 value of $\lambda_s$ is chosen as individual optimal. Note that since the variation of slot height $h_1$ has a significant effect on the $\lambda_s$ and eventually yoke thickness, it has been kept constant during the analyses. Influence of flux barrier thickness $B_1$ on the average torque and torque ripple are shown in Figure 5.3(b). The possible largest value of $B_1$ delivers the maximum torque with lower torque ripple.

Figure 5.4(a) illustrates the influence of rotor outer bridge width between flux barriers $R_{ib}$ on the average torque and torque ripple. The average torque is exponentially increased as the $R_{ib}$ is increased. The minimum torque ripple is achieved at ~9mm of $R_{ib}$ and the maximum torque is achieved at 16mm of $R_{ib}$. Therefore, it can be deduced that the higher the $R_{ib}$ length, the higher the torque amount. On the other hand, the lowest value of flux barrier height $HR_{ib}$ delivers the maximum torque with lower torque ripple (see Figure 5.4(b)). The variations of average torque and torque ripple with respect to rotor inner bridge width between flux barriers $O_1$ and rotor inner bridge radius $O_2$ are illustrated in Figure 5.5. As clearly seen, both rotor parameters have a substantial effect on torque and torque ripple. Since the lowest value of $O_1$ delivers the maximum torque with lower torque ripple it can be chosen as individual optimal whilst it is 122mm for $O_2$ parameter

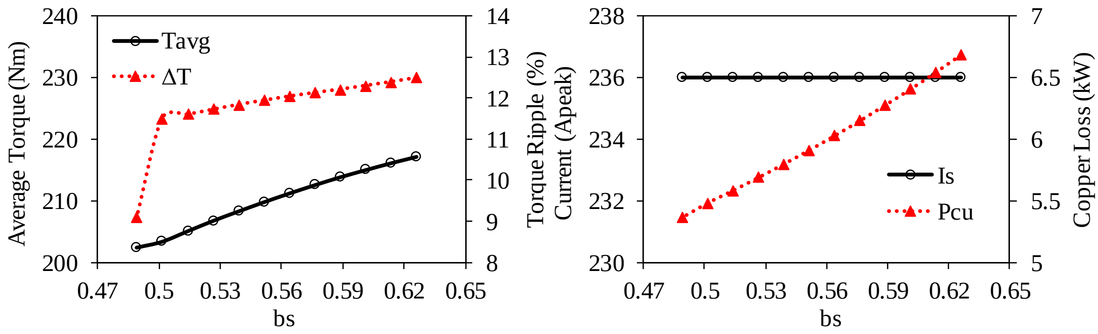


(a) (b)

**Figure 5.2 :** Influence of $b_s$ on performance characteristics with the restriction of maximum inverter current: (a) Torque and torque ripple, (b) Current and copper loss.

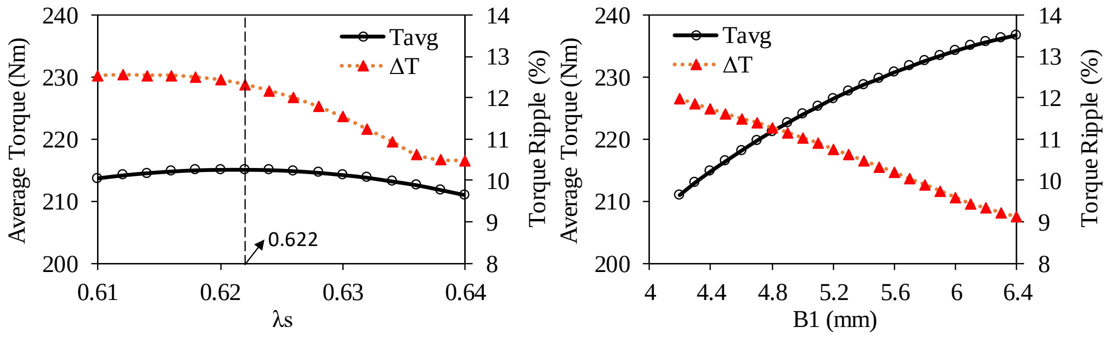


(a) (b)

**Figure 5.3 :** Variation of torque and torque ripple: **(a)** with $\lambda_s$, **(b)** with $B_1$.

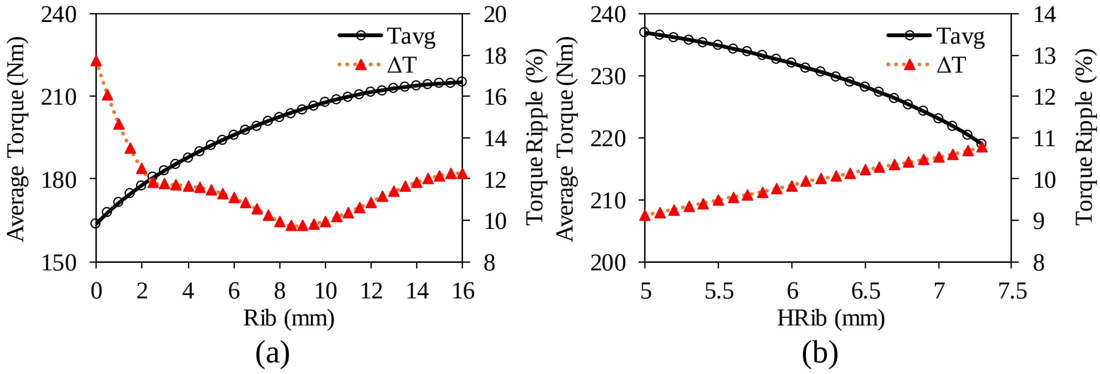


**Figure 5.4 :** Variation of torque and torque ripple: **(a)** with $R_{ib}$, **(b)** with $HR_{ib}$.

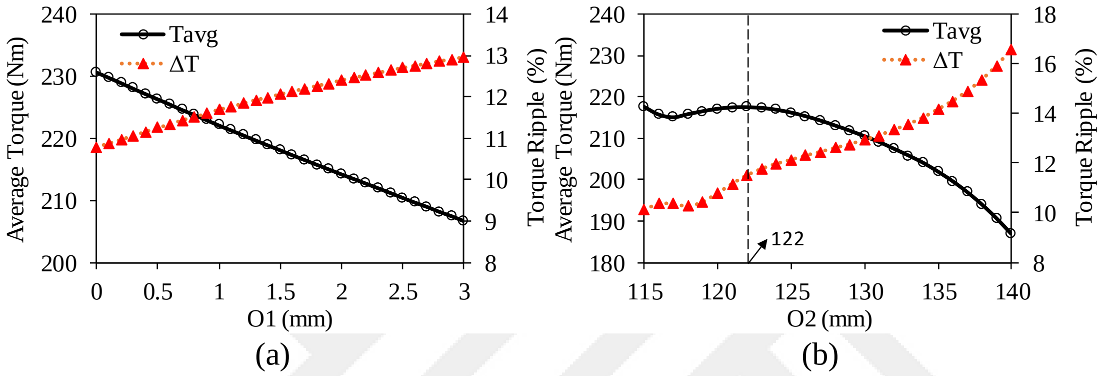


**Figure 5.5 :** Variation of torque and torque ripple: **(a)** with $O_1$, **(b)** with $O_2$.

The influence of magnet width $PM_w$ and thickness $PM_t$ on torque performance, provided that the total volume of magnets is kept constant, is presented in Figure 5.6. It has been revealed that the design with thin and tall magnets can increase the average torque and reduce the torque ripple considerably. However, the mechanical limits should be considered for higher speed operations since the PMs are quite brittle.

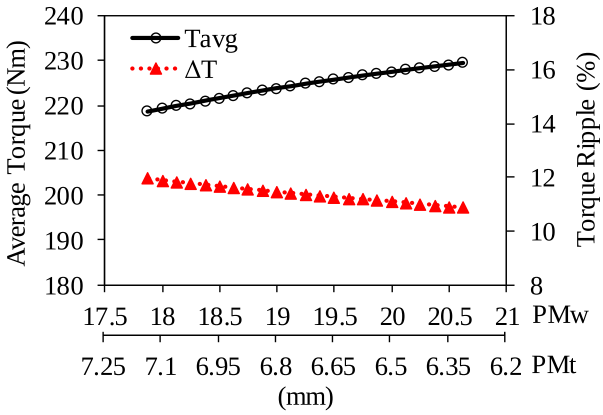


**Figure 5.6 :** Variation of torque and torque ripple with $PM_w \cdot PM_t$.

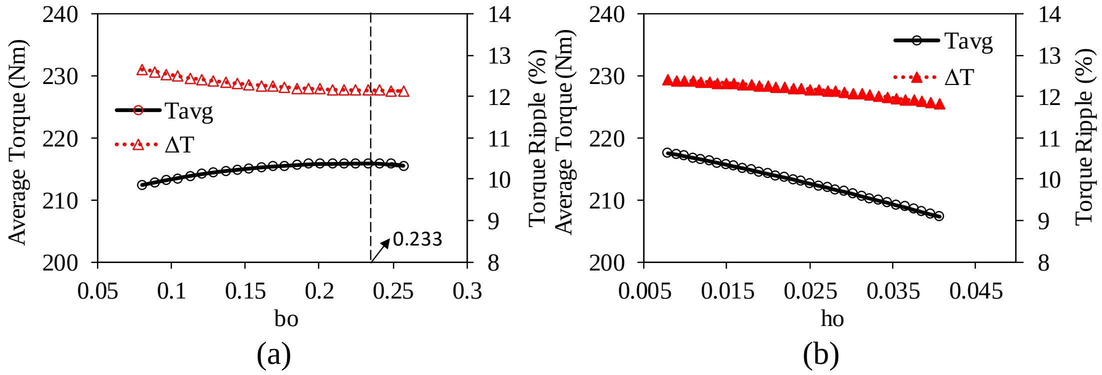


**Figure 5.7 :** Variation of torque and torque ripple: **(a)** with $b_0$, **(b)** with $h_0$.

Note that $D_1$ parameter has a significant effect on the optimization objectives. However, as can be predicted, the lower values of $D_1$ will cause a remarkable decrease in the torque and power levels because of the increasing short-circuited flux. Therefore, considering the mechanical issues, it is kept constant (not included as optimization parameter). Influences of slot opening width $b_0$ and height $h_0$ ratios on the torque performance are shown in Figure 5.7. It is found that the shorter the $h_0$, the higher the torque. On the other hand, there is an optimum value for $b_0$ as indicated in Figure 5.7(a).

### 5.2.3 Optimization with restriction of current density

As stated previously, one of the excitation constants can be assigned as stator current density. For the following analyses, the current density is fixed at 27.5 A/mm$^2$ which is same as the original Toyota Prius 2010 IPM. Then, the amount of current and slot area has been changed according to (5.5). The current angle delivering the maximum electromagnetic torque is chosen for each value of $b_s$. As mentioned previously, the tooth width ratio $b_s$ is responsible from the stator slot area $A_s$. Hence, investigation of $b_s$ variation is also investigation of $A_s$ by implication.

$$J_s = \frac{I_s}{A_s} = \frac{k_c}{\sqrt{A_s}} \tag{5.5}$$

Under these setup conditions, the variations of torque, torque ripple, phase current, and copper loss are illustrated in Figure 5.8. As indicated in Figure 5.8(a), the maximum average torque is obtained at 0.402 of $b_s$ ratio with quite low torque ripple rate. However, as illustrated in Figure 5.8(b), selection of $b_s$ ratio delivering the maximum torque results with quite high copper loss. Another important phenomenon is that continuously increasing the current level does not lead to a continuous increase in the torque level because of increasing saturation level of stator tooth bodies. On the other hand, high excitation current requires high cost due to the requirement of large capacity power switches of inverters. Consequently, we have not chosen the constant current density excitation constant as optimization parameter in this study.

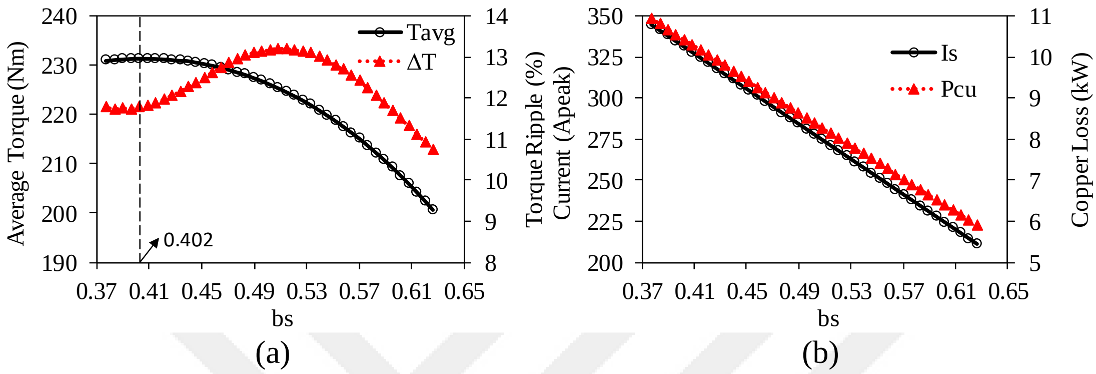


**Figure 5.8 :** Influence of $b_s$ on performance characteristics with the restriction of current density: **(a)** Torque and torque ripple, **(b)** Current and copper loss.

### 5.2.4 Optimization with restriction of copper loss

The last excitation constant for individual optimization is stator copper loss. The stator copper loss can be kept constant by considering a stator copper loss coefficient $k_c$ as expressed in (5.6), where $r_w$ is the average winding radius, calculating as the distance from the centre of the machine to the middle of the slot, $S$ is the stator slot number, $\ell_a$ is the active stack length, $I_s$, $R_{phase}$, $J_s$, $N_t$, $a$, $k_f$, $N_c$, $A_s$, and $\rho_{cu}$ denote the phase current, phase resistance, stator current density, number of turns per coil, parallel brunch number, slot fill factor, number of coils, slot area, and resistivity of the copper, respectively. The influence of $k_c$ on the average torque is shown in Figure 5.10. As clearly seen, the higher the $k_c$, the higher the average torque. With the slot fill factor $k_f = 0.488$, the copper loss of ~6.41kW @20°C, which is equivalent to $k_c \cong 220$, is assumed during the individual optimization.

$$P_{cu} = 3\frac{I_s^2}{a^2}R_{phase} = \frac{6k_c^2N_t^2}{a^2k_f}N_c\rho_{cu}\left[\ell_a + \frac{5.44\pi r_w}{2S}\right] \quad (5.6)$$

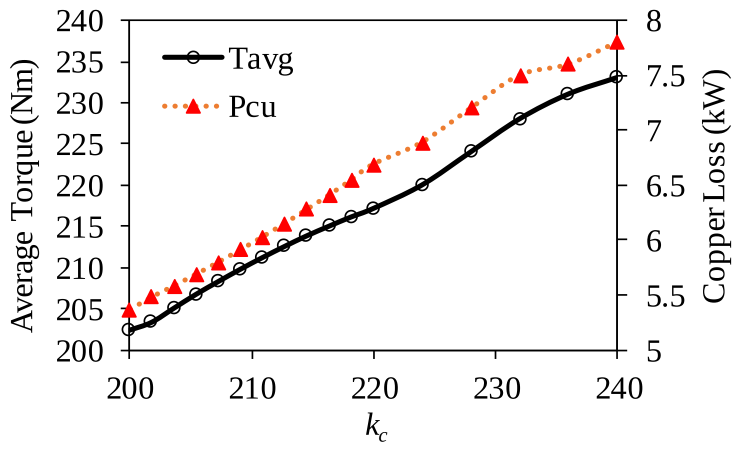


**Figure 5.9 :** Variation of average torque with copper loss coefficient $k_c$.

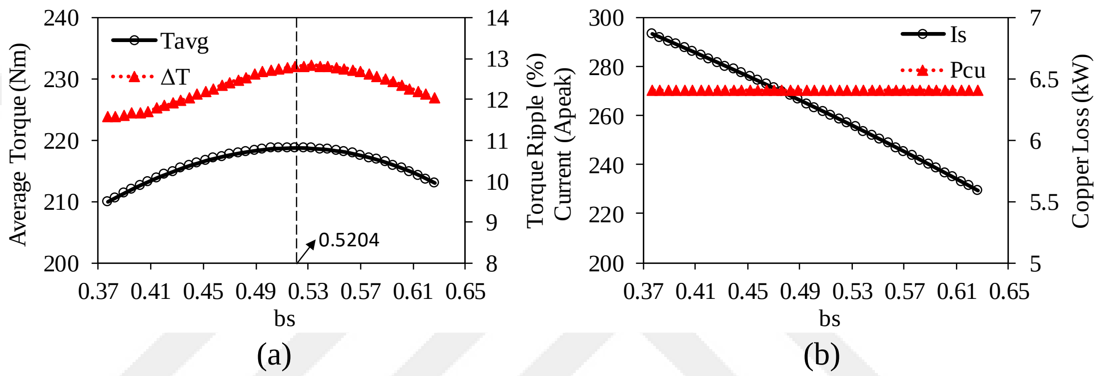


**Figure 5.10 :** Influence of $b_s$ on performance characteristics with the restriction of stator copper loss: **(a)** Torque and torque ripple, **(b)** Current and copper loss.

As for the restriction of stator copper loss excitation constant analyses, the obtained results are illustrated in Figure 5.10. $b_s$ ratio delivering the maximum torque under the copper loss restriction is determined as 0.5204. If this excitation constant is chosen as optimization parameter, the level of inverter current should be increased as seen in Figure 5.10(b). Since this will be resulted as an increase in the inverter cost/size, this parameter has also not been chosen as optimization parameter.

### 5.2.5 Determined optimization parameters

Individual optimization results have been obtained and compared with the initial values as listed in Table 5.3. It can be concluded that wider stator tooth width, larger split ratio and hence thinner yoke thickness, wider slot opening, thicker flux barriers, no inner bridge, thinner and taller magnet shape are preferred to produce higher torque for the given specifications.

**Table 5.3 :** Initial and individual optimized variables.

| # | Parameters | Initial value | Individual Optimized |
|---|---|---|---|
| 1 | $\lambda_s$ | 0.6132 | 0.622 |
| 2 | $b_s$ | 0.6014 | 0.6263 |
| 3 | $h_1$ | 26.75 | 26.75 |
| 4 | $R_{ib}$ | 16 | 16 |
| 5 | $O_2$ | 118.04 | 122 |
| 6 | $B_1$ | 5.3 | 6.4 |
| 7 | $O_1$ | 1.86 | 0 |
| 8 | $D_1$ | 156.84 | 156.84 |
| 9 | $HR_{ib}$ | 5 | 5 |
| 10 | $PM_w$ | 17.88 | 20.625 |
| 11 | $PM_t$ | 7.16 | 6.228 |
| 12 | $h_0$ | 0.01 | 0.008 |
| 13 | $b_0$ | 0.1606 | 0.233 |

### 5.3 Multi-Objective Global Optimization of Large NSW IPMs

The GA, which is known as the one of the effective numerical optimization methods, has been extensively used for exploring the optimized solution of electrical machines. The GA is a random search procedure, which explores the solution space using mechanisms that emulates natural selection including next generations and mutilations for optimization analysis. Some new individuals (Children) are created and the grown population participates in a natural-selection process that consecutively reduces the size of the population to a desired level (Next Generation) in each generation.

The settings of multi-objective global optimization are as follows: parent size (population size), mating pool size, children size, Pareto Front size (number of survivors), population size of next generation, roulette selection, crossover probability, and mutation probability size are 30, 30, 30, 10, 30, 10, 1, and 2 respectively. Maximum number of generations (iteration number) is chosen as 1000.

The multi-objective optimization approach is concerned with optimizing numerous objectives simultaneously. As for the multi-objective optimization, a set of solutions known as Pareto Front, which incorporates the optimal solution of each individual objective and also the solutions representing the best compromise satisfying all objectives, is presented. For the multi-objective optimization, the objective functions create a multi-dimensional space in addition to the natural decision variable space. In this study, we have chosen time averaged torque, torque ripple, and stator copper loss as objectives to be optimized.

### 5.3.1 Determination of objectives and goals

The most charming objectives for a given specific stack length and outer diameter are to maximize the feasibly available torque and efficiency (or to minimize the dominant machines losses such as copper loss, core loss, PM loss, etc.). In this study, it is intended to optimize the IPM with NSW for the constant torque operating region. Therefore, since the core loss quite low at low-frequency operating region, it is not chosen as an objective. On the other hand, the level of MMF harmonics and hence PM loss are quite low as presented in the first chapter, only the most dominant loss component at constant torque region, which is copper loss, is chosen as optimization objective among the other loss components. In addition, since the NSW IPM is intended to use for electrical vehicle application, the torque ripple level is of great importance. Therefore, torque ripple is chosen as the last optimization objective. In summary, the determined objectives have been listed as follows;

- Maximized torque (feasibly available);
- Minimized copper loss (with the restriction of 27.5 A/mm$^2$ current density);
- Minimized torque ripple (with the restriction of the average torque not being low than 230 Nm).

### 5.3.2 Justification of objectives and weights

The optimization objectives of NSW IPM have been justified by considering the experimentally measured parameters of the original Toyota Prius 2010 IPM. The time averaged output torque of original Toyota Prius 2010 IPM is ~239 Nm @ 1krpm [193]. The total stator copper (including the end-winding copper as well) is ~6.41 kW @ 20°C.

However, the since the end-winding length of the proposed NSW topology is significantly short, its end-winding copper loss is also significantly low. In the initial designs, it has been calculated as ~5.1 kW @ 20°C. In addition, the torque ripple level of original Toyota Prius 2010 IPM is ~8% corresponding to ~20 Nm. The weights of the objectives show that how important the related objective is. Which mean is that if the total weights of all objectives is equal to 1, $0.\overline{3}$ per weights shows that all the objectives are equivalently important. In this study, since the proposed IPM is designed for EV/HEV applications, both the torque and efficiency are vitally important parameters. Therefore, their weights are a bit higher than that of torque ripple as listed in Table 5.4.

**Table 5.4 :** Justified objectives and weights.

| Variable | Condition | Weight |
|---|---|---|
| Average torque (Nm) | $\geq 239$ | 0.39 |
| Torque Ripple (Nm) | $\leq 20$ | 0.26 |
| Average copper loss (kW) | $\leq 5$ | 0.35 |

### 5.3.3 Cost Function

The cost function is determined as weighted sum of the sub-goal errors. Each sub-goal gives rise to an error value that represents the divergence between the simulated reaction and the goal value constrain. If the simulation response satisfies the goal limit, the cost value becomes zero. Alternatively, the error value depends on the differences between the simulated response and the specific goal constrain. Therefore, the cost function is defined as expressed in (5.7), where $G$, $w_j$, $N_j$, $e_i$ are the number of sub-goals, the weight factor related with the $j^{th}$ sub-goal, the number of frequencies for the $j^{th}$ sub-goal, and the error contribution from the $j^{th}$ sub-goal at the $i^{th}$ frequency, respectively. Here, the value of $e_i$ is determined by the band characteristics, target value, and the simulated response value.

$$Cost = \sum_{j=1}^{G} \frac{w_j}{N_j} \sum_{i=1}^{N_j} e_i \tag{5.7}$$

### 5.3.4 Multi-objective global optimization procedure

After 420 iteration, the optimal solutions are achieved as shown in Table 5.5, Figure 5.11 and 5.12. The variations of some important optimization parameters and cost by GA show that after the 300$^{th}$ iteration, the largest average cost is achieved as 4.36 (4.95% of initial cost). The minimum cost, which is 2.27, is achieved at 406$^{th}$ iteration.

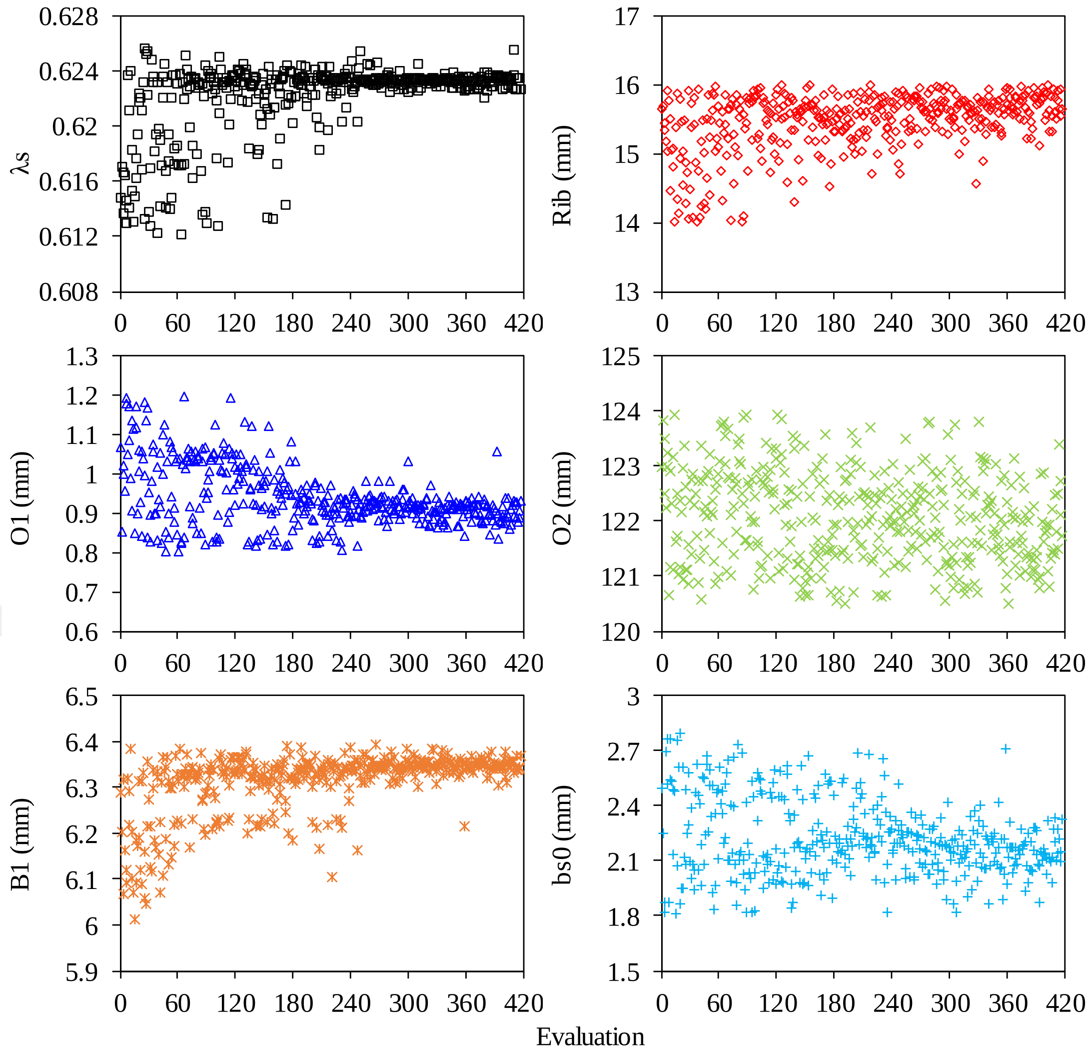


**Figure 5.11 :** Variation of optimization parameters with respect to number of evaluations.

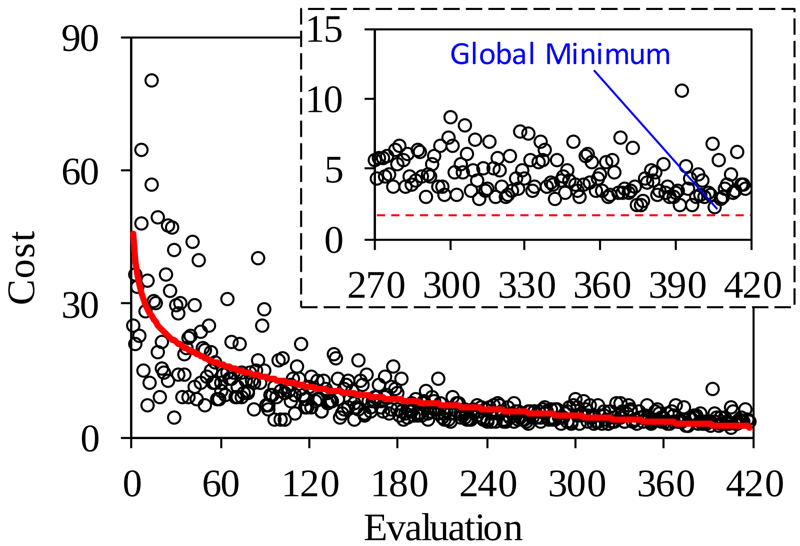


**Figure 5.12 :** Variation of the cost function with respect to evaluation number.

**Table 5.5 :** Constraints of optimization parameters.

| Parameter | Initial value | Individual Optimized | Constraints | Globally Optimized |
|---|---|---|---|---|
| $\lambda_s$ | 0.6132 | 0.622 | [0.612:0.626] | 0.6234 |
| $b_s$ | 0.6014 | 0.6263 | [0.59:0.64] | 0.602 |
| $R_{ib}$ | 16 | 16 | [14:16] | 15.834 |
| $O_2$ | 118.04 | 122 | [120.5:124] | 121.322 |
| $B_1$ | 5.3 | 6.4 | [6:6.4] | 6.3524 |
| $O_1$ | 1.86 | 0 | [0.8:1.2] | 0.8617 |
| $PM_w$ | 17.88 | 20.625 | [18.5:20.625] | 19 |
| $PM_t$ | 7.16 | 6.228 | [6.228: 6.924] | 6.747 |
| $h_0$ | 0.01 | 0.008 | [0.004:0.012] | 0.0089 |
| $b_0$ | 0.1606 | 0.233 | [0.144:0.24] | 0.195 |

The dominant optimization parameters can also be determined from their variation with respect to evaluation number. As seen in Figure 5.11, $\lambda_s$, $O_1$, $B_1$, and $R_{ib}$ are the most dominant (having a significant effect on the justified objectives) optimization parameters since they have reached a fixed value range on the contrary of $O_2$ and $b_{s0}$ parameters. The plots of the objective function whose nondominant vectors are in the Pareto optimal set, known as the Pareto front, are shown in Figure 5.13 for the average torque vs torque ripple, and average torque vs efficiency.

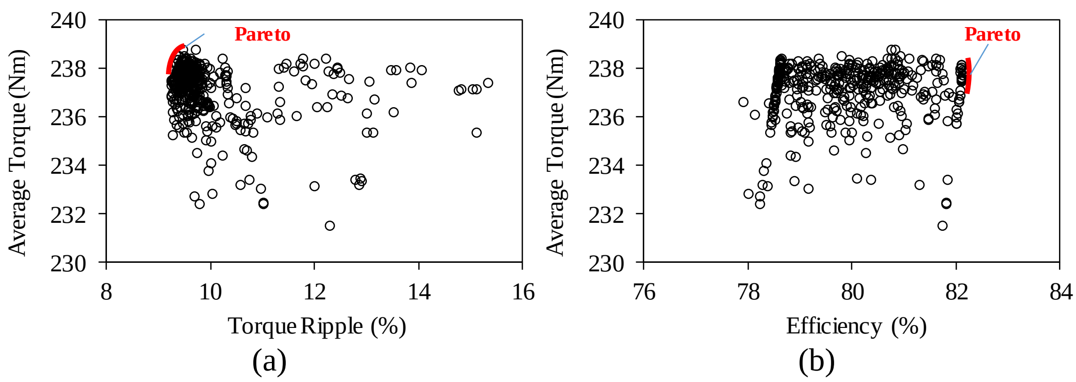


**Figure 5.13 :** Pareto-front graphs: (a) in torque ripple, (b) in efficiency.

### 5.3.5 Conventional multi-objective global optimization procedure

To be able to validate the rapidity and effectiveness of the proposed multi-objective optimization method, a conventional optimization method by GA is employed. The key difference of this optimization method is that there is no sensitivity analysis for any of the design parameter is conducted. In other words, physically available minimum and maximum constraints are assigned for each parameter as given in Table 5.6.

**Table 5.6 :** Constraints of conventional optimization parameters.

| Parameter | Initial value | Constraints (Min-Max) | Globally Optimized |
|---|---|---|---|
| $\lambda_s$ | 0.6132 | [0.5:0.75] | 0.6234 |
| $b_s$ | 0.6014 | [0.3:0.75] | 0.602 |
| $R_{ib}$ | 16 | [0.1:16] | 15.834 |
| $O_2$ | 118.04 | [110:140] | 121.322 |
| $B_1$ | 5.3 | 4:6.4] | 6.3524 |
| $O_1$ | 1.86 | [0.1:3] | 0.8617 |
| $PM_w$ | 17.88 | [17.5:21] | 19 |
| $PM_t$ | 7.16 | [6.2: 7.25] | 6.747 |
| $h_0$ | 0.01 | [0.004:0.05] | 0.0089 |
| $b_0$ | 0.1606 | [0.05:0.3] | 0.195 |

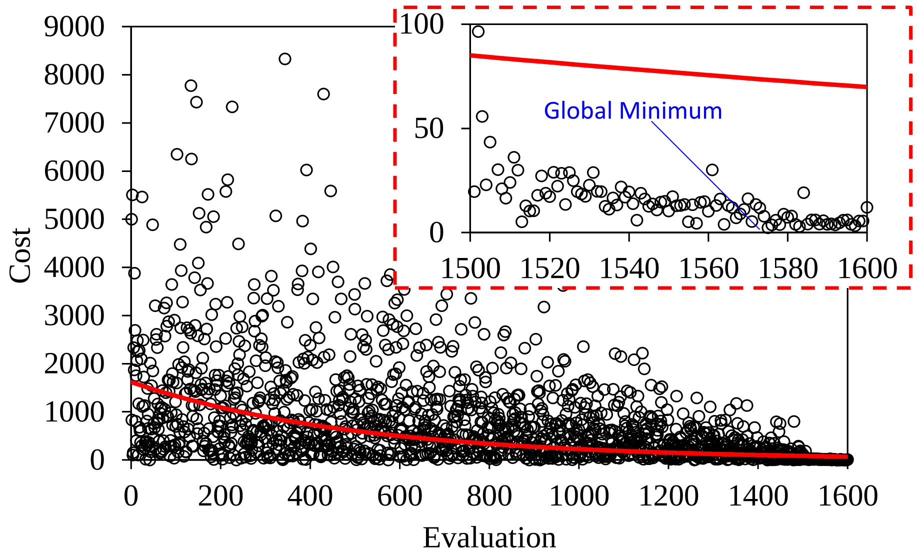


**Figure 5.14 :** Variation of the cost function with respect to evaluation number for conventional multi-objective global optimization method.

For a fair comparison, the same number of design parameters and the same objectives given in Table 5.5 and 5.4, respectively, are used. Under these circumstances, the optimal solution is achieved after 1600 iteration as seen in Figure 5.14. After 1500$^{th}$ evaluation, the largest average cost is achieved as 16.787 (1.93% of initial cost). The minimum cost, which is exactly same as being in proposed optimization method (2.27), is achieved at 1575$^{th}$ iteration. Consequently, considering Figure 5.12 and 5.14, it can be concluded that the optimal solution can be reached almost 4 times faster thanks to the proposed multi-objective optimization method.

### 5.4 Steady-State Performance Results

In this section, the electromagnetic performance characteristics of the original (Toyota Prius 2010 IPM with conventional ISDWs), initial design of IPM with proposed NSWs, and globally optimized IPM with NSW have comprehensively been compared. The cross-sectional views and winding configurations of the original, initial and optimized IPMs are shown in Figure 5.15.

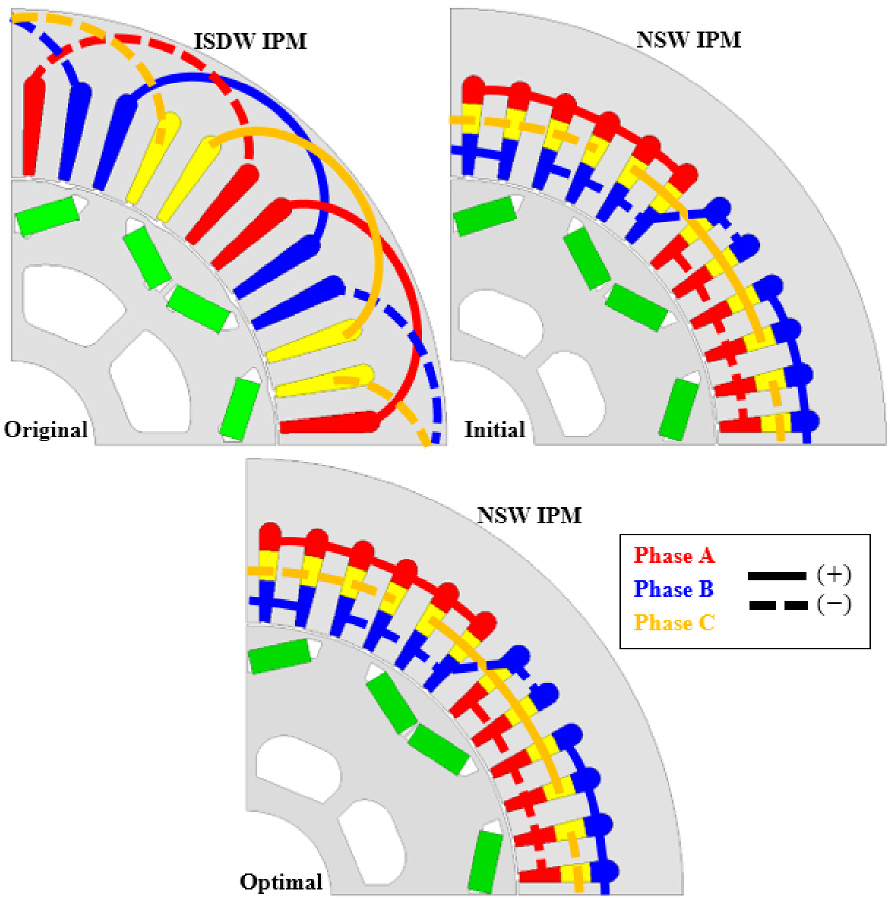


**Figure 5.15 :** Example figure in chapter 5.

The original IPM has 48S/8P with 5-slot pitch single layer winding configuration. Alternatively, the initial and optimal IPMs have 48/8P with 5-slot pitch 3-layer semi-overlapping winding configuration. More information about the winding properties, such as comparison of winding and MMF harmonics, end-winding lengths, ease of manufacturing, etc. of ISDW and proposed NSW can be found in Chapter 3.

### 5.4.1 Axial length, weight and cost

The machine masses and the costs for each machine are evaluated by using the expression given in (5.8), where $D_{W330}$, $A_{Score}$, $A_{Rcore}$, $D_{Cu_S}$, $N_c$, $N_{PM}$, and $A_{S_{coil}}$ are mass density of steel material, surface area of stator core, surface area of the rotor core, mass density of stator winding copper, number of coils, number of magnets, and surface area of the stator slot area with fill factor, respectively. In addition, the average length of winding coil is calculated by using the expression by $\ell_{aw}$ in (5.8). The cost of the copper and steel materials are evaluated by using the data provided by the London Metal Exchange (LME) [194] whereas the PM is evaluated by using the data provided by International Magnaproducts, Inc. [195] as given in (5.8). Note that the housing, heat exchanger, bearings, gears, etc. have not been included in the calculations. Only the active material weights and costs have been calculated by considering following specifications.

- Copper: 5.985 \$/kg – mass density: 8933 (kg/m$^3$);
- Steel: 0.518 \$/kg – mass density: 7650 (kg/m$^3$);
- Magnet: 75 \$/kg – mass density: 7500 (kg/m$^3$);

Calculated axial lengths, weights, and costs are compared in Table 5.7. As seen, thanks to the combined effect of the proposed NSW topology and optimization by GA, the total axial length of the IPM is reduced by 18.3% according to original design. On the other hand, the mass and weight levels are quite similar. The only difference is that since the total amount of the copper mass is reduced due to the short end-windings, a 4.3% reduction in total cost is achieved with optimized IPM having NSWs.

$$M_{Total} = D_{W330}\left(A_{S_{core}} + A_{R_{core}}\right)\ell_a + \underbrace{2\left[\ell_a + \frac{5.44\pi r_w}{2S}\right]}_{\ell_{aw}} D_{cu} N_c A_{s_{coil}} + N_{PM} D_{PM} (A_{PM})\ell_a \tag{5.8}$$

**Table 5.7 :** Comparison of calculated total axial length, cost and weight.

| | *Original* | *Initial* | *Optimized* |
|---|---|---|---|
| **Total Axial Length (mm)** | 112.88 | 93.12 | 92.26 |
| **Stator Core Mass (kg)** | 11.07 | 11.06 | 10.79 |
| **Rotor Core Mass (kg)** | 5.93 | 6.82 | 7.15 |
| **Copper Mass (kg)** | 4.93 | 4.027 | 4.025 |
| **PM Mass (kg)** | 0.773 | 0.773 | 0.773 |
| **Total Mass (kg)** | 22.7 | 22.69 | 22.74 |
| **Total Cost (US $)** | 95.91 | 91.78 | 91.78 |

### 5.4.2 Back-EMF analysis

The no- and full-load back-EMF waveforms have also been compared as illustrated in Figure 5.16. As seen in Figure 5.16, the optimal design has the minimum back-EMF distortion level.

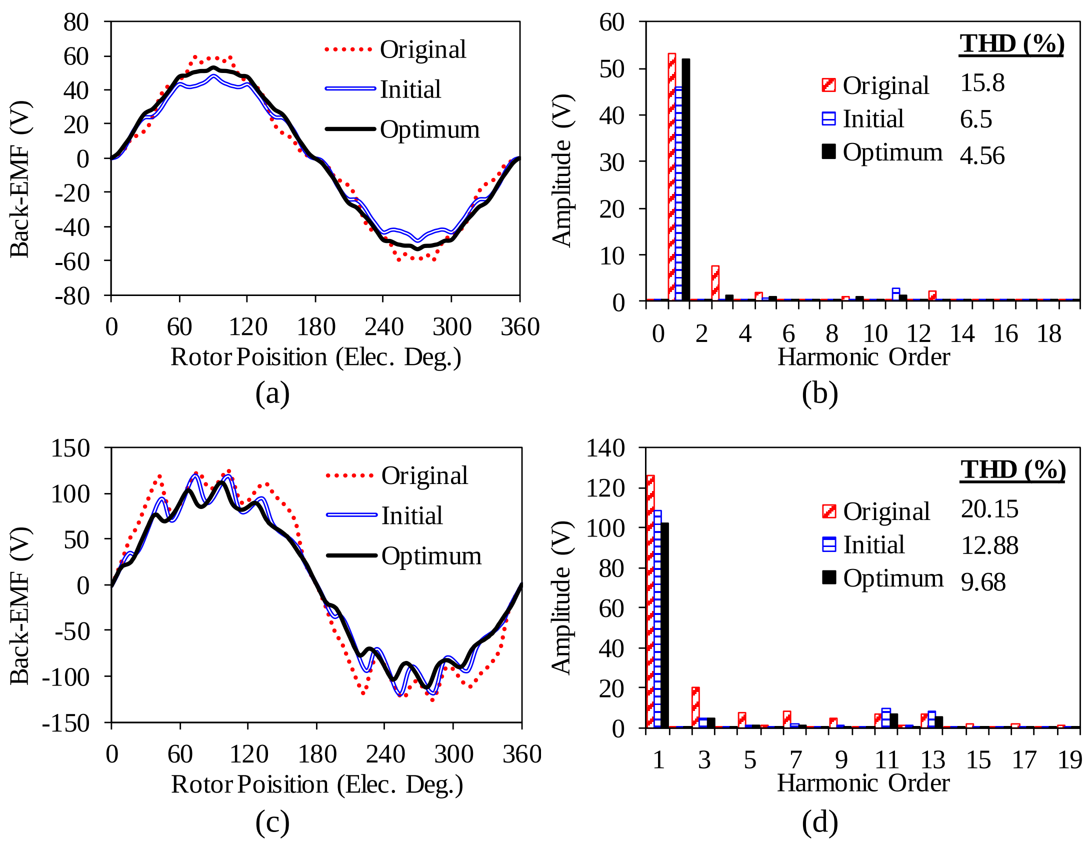


**Figure 5.16 :** Back-EMF at no- and full-load operating condition: (a) waveform at no-load, (b) harmonic spectra of (a), (c) waveform at full-load, (d) harmonic spectra of (c).

Considering the full-load operating condition, the increase in the waveform distortion level can be figured out. This is due to the increased effect of the combination of slotting and magnetic saturation. Considering Figure 5.16(b), it can be expected that the fundamental amplitude of optimal design's back-EMF should be higher than that of the initial design in full-load operating condition as well. However, as seen in Figure 5.16(d), it is lower than that of the initial design. This result shows that the optimal design is much more sensitive the increase of the combining effect of slotting and magnetic saturation that that of the other designs. It can also be deduced that the proposed winding offers much lower winding MMF harmonics. Thus, lower rotor loss components, particularly PM loss, can be expected from the IPM having NSWs.

### 5.4.3 Flux-linkage analysis

Flux-linkage waveforms and their harmonic spectra are shown in Figure 5.17. Since the fundamental winding factor of the original design is a bit higher than those of the initial and optimal designs, lower fundamental flux-linkage amplitudes have been obtained. On the other hand, due to the lower MMF harmonic content of the NSW topology, lower flux linkage THD levels are obtained. Since the optimization parameters effecting the torque ripple; such as $b_0$, $h_0$, $R_{ib}$, $O_2$, etc. have also been optimized as to be delivered the minimum torque ripple, a remarkable decrease in the level of waveform distortions have been achieved. The same phenomenon is also valid for the back-EMF waveforms.

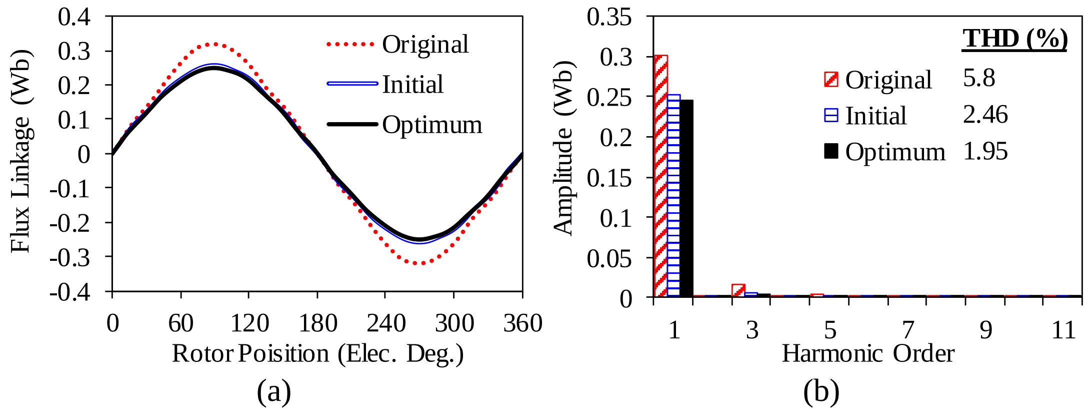


**Figure 5.17 :** Flux-linkage: (a) waveform, (b) harmonic spectra and THD.

### 5.4.4 Inductance analysis

The self-, mutual-, *d*-, and *q*-axis inductances of the IPMs are compared as illustrated in Figure 5.18. As presented in Chapter 3, ISDW and NSW have different MMF harmonics, which in turns leads to different saturation characteristics of the magnetic circuit and loss behaviour. As shown in [196], local magnetic saturation causes the variation of the dq-axis inductances in PM machines.

The local saturation characteristics for the machines are shown in Figure 5.20. Considering the variations of the inductances, it can be predicted that the saturation level of the IPMs having NSWs are somewhat lower than that of the original design. Therefore, considering Figure 5.18 and 5.20, it can be concluded that the higher the local saturation level, the larger the variation *dq*-axis inductances. It is worth notching that due to the reduced coupling between the phase windings, the higher self-inductance and lower mutual-inductances are desired characteristics for fault tolerance. Consequently, in terms of fault tolerance, both winding topologies show similar characteristics.

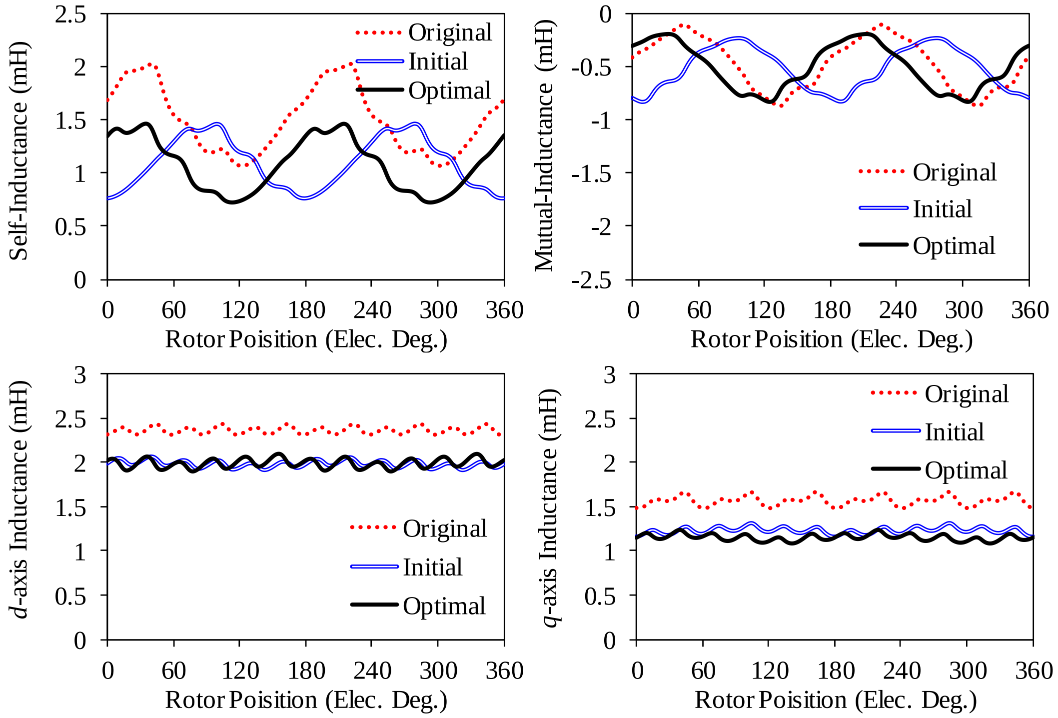


**Figure 5.18 :** Variation of machine inductances with respect to rotor position.

### 5.4.5 Air-gap flux density analysis

Radial component of the air-gap flux density is calculated and its variation with respect to rotor position is shown in Figure 5.19(a). Due to the combined effect of winding MMF, slotting, and magnetic circuit saturation, the waveforms are quite distorted. On the other hand, their harmonic distortion levels are quite similar (see Figure 5.20(b)).

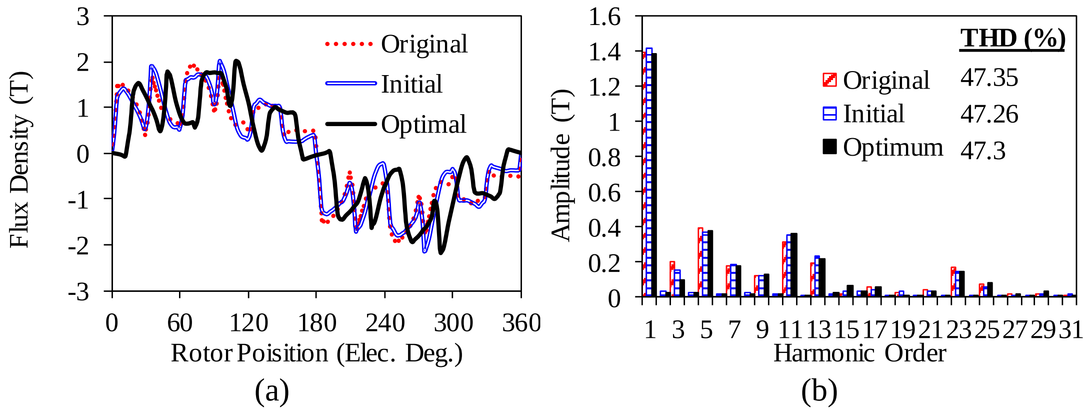


**Figure 5.19 :** Variation of machine inductances with respect to rotor position.

### 5.4.6 Electromagnetic field analysis

Magnetic flux line and flux density distributions of the IPMs are illustrated in Figure 5.20. In order to reduce both the analysis time and effort without affecting the accuracy, the number of total mesh elements have been reduced by employing the model periodicities $P_m$ determined according to winding configuration by using (5.9).

As can be seen from Figure 5.15, the number of symmetrically distributed coils $n_c$ in the original machine is 1 while its 2 in other machines. Therefore, as illustrated in Figure 5.20, $P_m$s are calculated as 8 (1/8 of whole model) and 4 (1/4 of whole model) for initial and other machines, respectively. However, in order to conduct a fair FEA and hence to obtain accurate electromagnetic performance results, similar mesh size and mesh density have been assigned for all models by considering their model periodicity.

From Figure 5.20, it can be observed that there are some local saturated parts in the stator and rotor parts, particularly in the rotor outer bridge regions and stator tooth body parts. Overall averaged flux density of the IPM with ISDWs is relatively higher than the IPMs with NSWs.

$$P_m = \frac{P}{n_c} \tag{5.9}$$

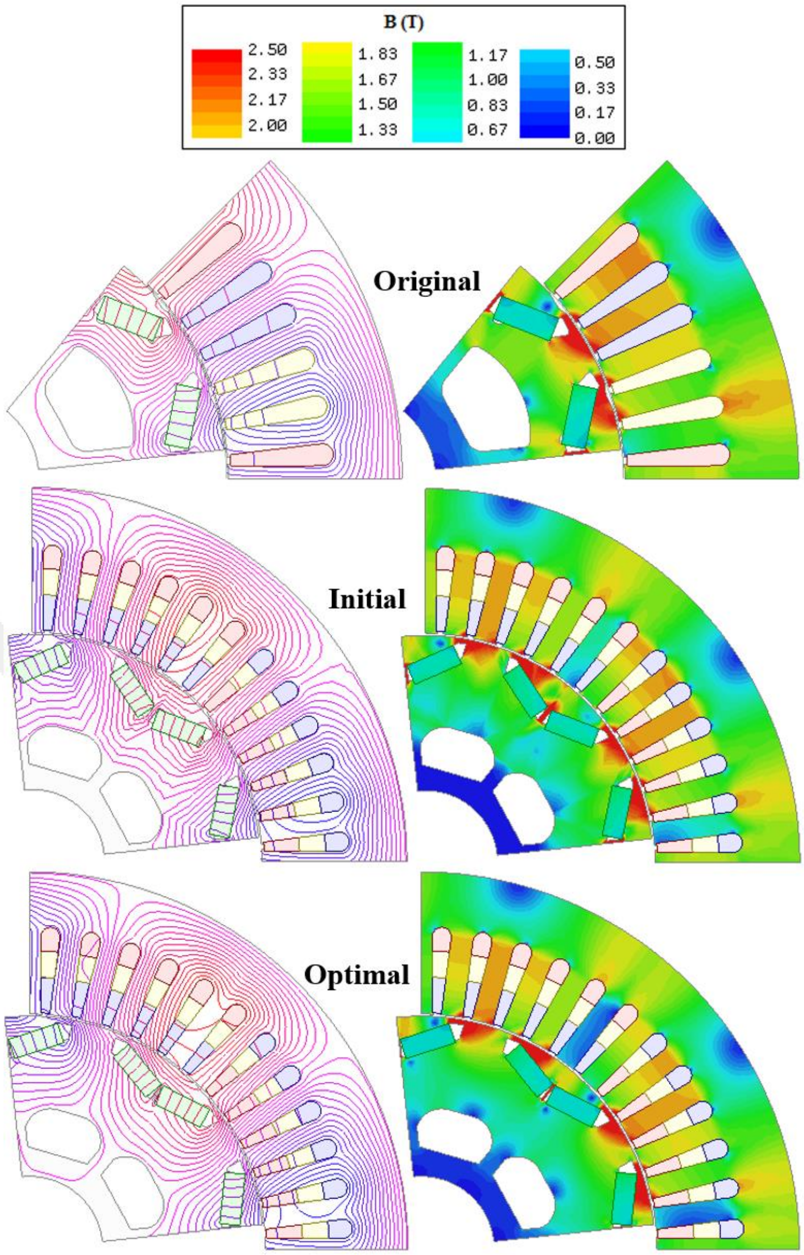


**Figure 5.20 :** Flux line (left-side) and flux density (right-side) distributions.

### 5.4.7 Torque analysis

In PM machines, the cogging torque contributes to the torque ripple due to the PM leakage flux. The variation of cogging torque with respect to rotor position is shown in Figure 5.21(a). As seen, the peak to peak value of the cogging torque of the original design a bit higher than those of other designs. Thus, it can be expected that the averaged torque ripple of the optimized design may be higher than those of original and initial designs. However, as seen in Figure 5.21(b), it is higher than that of the original but lower than that of the initial design. Consequently, the cogging torque component of torque ripple of the optimal design is tolerated by other torque ripple components such as lower PM leakage flux, lower slot leakage flux, etc. Under the same current level and number of turns operating condition, the time averaged torque of the original and optimal designs is quite similar whilst the initial design has the lowest torque (see Figure 5.21(b)). Consequently, according to initial design, thanks to multi-objective global optimization by GA, the average torque is increased by 8.7% and the torque ripple percentage is decreased by 21.32%.

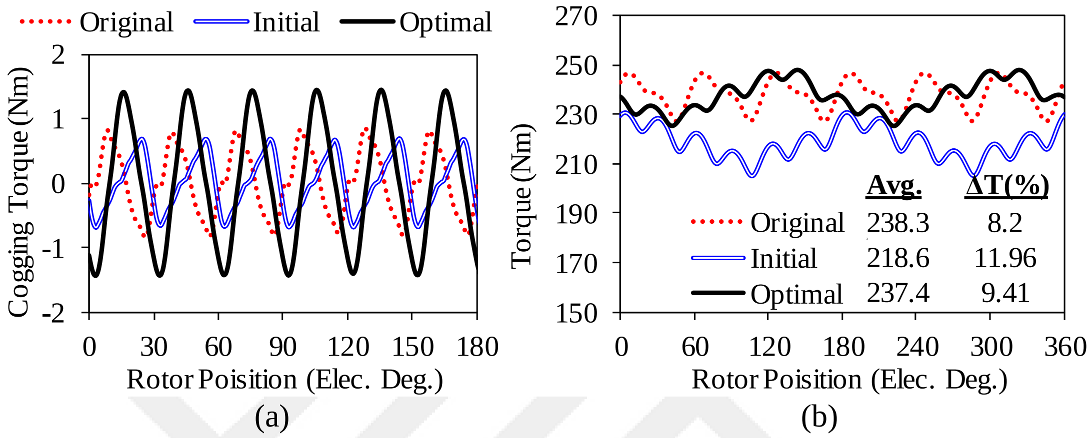


**Figure 5.21 :** Torque waveforms: (a) Cogging torque, (b) Electromagnetic torque.

### 5.4.8 Power losses and efficiency analysis

Comparison of the power losses, output power, and efficiency are given in Table 5.8. In the table, $P_{cu_{slot}}$, $P_{cu_{end}}$, $P_{core}$, $P_{PM}$, $P_{add}$, $P_{out}$, and $\eta$ denote the slot copper loss, end winding copper loss, magnet loss, additional loss, which is considered as the 1% of the output power, output power, and efficiency, respectively. Since the same slot fill factor, wire diameter, and number of turns per phase is used for all IPMs, $P_{cu_{slot}}$ values are the same. On the other hand, since the proposed winding topology provides quite shorter end-winding lengths, $P_{cu_{end}}$ is reduced by 31.7%. Due to the lower MMF harmonic content of the proposed winding topology, and reduced rotor notches (close to shaft), which in turn lead to lower eddy current hence saturation level, the lower $P_{core}$ is achieved for IPMs having NSWs. As expected, $P_{PM}$ level of the initial design with NSWs is lower than that of the original design due to the lower harmonic content of the winding MMF. However, contrary to expectations, $P_{PM}$ level of the original design is higher than that of the original design. This is because of the increased PM leakage flux level due to increased $O_2$ parameter of the optimized design. To increase $O_2$ parameter results with increased harmonic content of the PM flux. Because, as shown in Figure 5.19 the air-gap flux density contains highly distorted flux density components (a large number of harmonics). Those harmonics influence the PM flux harmonics as well. Therefore, the longer the $O_2$, the lower the flux density harmonics in the rotor part. As seen in Table 8, quite similar output power is achieved thanks to the global optimization.

**Table 5.8 :** Comparison of output power, losses, and efficiency.

| | $P_{cu_{slot}}$ (kW) | $P_{cu_{end}}$ (kW) | $P_{core}$ (kW) | $P_{PM}$ (kW) | $P_{add}$ (kW) | $P_{out}$ (kW) | $\eta$ (%) |
|---|---|---|---|---|---|---|---|
| **Original** | 2.12 | 4.29 | 0.1 | 0.0162 | 0.25 | 25.057 | 78.72 |
| **Initial** | 2.12 | 2.94 | 0.09 | 0.0145 | 0.023 | 22.89 | 80.96 |
| **Optimal** | 2.12 | 2.93 | 0.09 | 0.0216 | 0.025 | 24.86 | 82.13 |

As a consequence of utilization of NSW instead of conventional ISDWs, the efficiency can be increased by 2.85%. With the help of multi-objective global optimization by GA, an 1.45% further increase in the efficiency can be obtained. Therefore, as a result of the combined effect of global optimization and shorth end-windings, $\eta$ is increased by 4.33%. This achievement is very important when an 18.3% reduction in the total axial length is considered. It can be concluded that more compact IPMs with improved efficiency can be designed thanks to the proposed NSW topology and global optimization.

### 5.5 Design Optimization of Small NSW IPMs

In order to validate the proposed winding topology and optimization procedure, a small dimension version of the NSW IPM (see Table 5.9 for geometric dimensions and operating specifications) is designed and optimized by using the same optimization method. The designed small NSW IPM has 24-slot and 4-pole combination with 3-layer NSWs. The optimization procedure is given as follows. The optimization objectives and their weights are given in Table 5.10. Note that these objectives have been determined by using the empirical equations and initial electromagnetic analysis results of the FEA. Average copper loss consists of the summation of the inner-slot and end-winding copper loss. Initial and globally optimized parameters have been given in Table 5.11.

**Table 5.9 :** Comparison of output power, losses, and efficiency.

| Parameter | Value | Parameter | Value |
|---|---|---|---|
| Phase current, $I_s$, $A$peak | 26 | $R_s$ | 2 |
| Current density, $J_s$, $A/mm^2$ | 6 | $h_1$ | 9.6 |
| Slot fill factor, $k_f$ | 0.448 | $h_{s0}$ | 0.7 |
| Rated speed, rpm | 400 | $b_t$ | 4.968 |
| Pole number, $P$ | 4 | $b_{s0}$ | 2 |
| Active stack length, $\ell_a$ | 50 | $D_1$ | 70.284 |
| Stator slot number, $S$ | 24 | $O_1$ | 3.89 |
| Outer diameter of stator, $D_{so}$ | 124 | $O_2$ | 45.16 |
| Inner diameter of stator, $D_{si}$ | 47.806 | $B_1$ | 1.3 |
| Stator slot pitch, $\tau_s$ | 11.293 | $HR_{ib}$ | 0.1 |
| Outer diameter of rotor, $D_{ro}$ | 46.806 | $R_{ib}$ | 0.5 |
| Inner diameter of rotor, $D_{ri}$ | 35 | $PM_w$ | 38.88 |
| Air-gap length, $g$ | 0.5 | $PM_t$ | 1.8 |

*All dimensions are in mm.

Note that exactly the same GA setup parameters including random seeds as the large IPM have been used for the achieving the globally optimal parameters. In addition, constant current excitation source is also assigned as being in the optimization of the large IPM. Figire 5.22 illustrates the variation of cost function according to evaluation number. As shown, the global minimum cost is achieved at 565$^{th}$ evaluation. When comparing the optimization with IPM having larger dimensions, achieving the optimal solution took a bit long time because of the more severe objectives. However, the optimal solution can be achieved quicker by employing different random seeds for GA. The cross-sectional views and flux line and flux density distributions of the initial and optimal designs are shown in Figure 5.23.

As seen in the Figure 5.23, the saturation level of the stator tooth parts of the initial design a bit higher than that of the optimal design. The performance characteristics comparison between the initial and optimal designs are given in Table 5.12. Since the slot dimensions of the initial design are larger than that of the optimal design, its copper loss is lower. Therefore, although the torque and hence output power of the initial design is lower than that of the optimal design, its efficiency percentage is greater than that of the optimal design.

**Table 5.10 :** Justified objectives and weights.

| Variable | Condition | Weight |
|---|---|---|
| Average torque (Nm) | $\geq 5$ | 0.39 |
| Torque Ripple (Nm) | $\leq 0.5$ | 0.26 |
| Average copper loss (W) | $\leq 80$ | 0.35 |

**Table 5.11 :** Constraints of optimization parameters.

| Par. | Initial value | Individual Optimized | Constraints | Globally Optimized |
|---|---|---|---|---|
| $\lambda_s$ | 0.591 | 0.6 | [0.585:0.608] | 0.60206 |
| $b_s$ | 0.43 | 0.456 | [0.39:0.5] | 0.475 |
| $R_{ib}$ | 0.5 | 0.5 | [0.4:0.6] | 0.5 |
| $O_2$ | 45.16 | 51.36 | [43:54] | 48.102 |
| $B_1$ | 1.3 | 1.9 | [1:2.1] | 1.7 |
| $O_1$ | 3.89 | 4.1 | [3.2:5] | 4.033 |
| $PM_w$ | 38.88 | 33.33 | [30:40] | 35 |
| $PM_t$ | 1.8 | 2.1 | [1.5:2.5] | 2 |
| $h_0$ | 0.005 | 0.009 | [0.002:0.011] | 0.007 |
| $b_0$ | 0.16 | 0.228 | [0.12:0.24] | 0.18 |

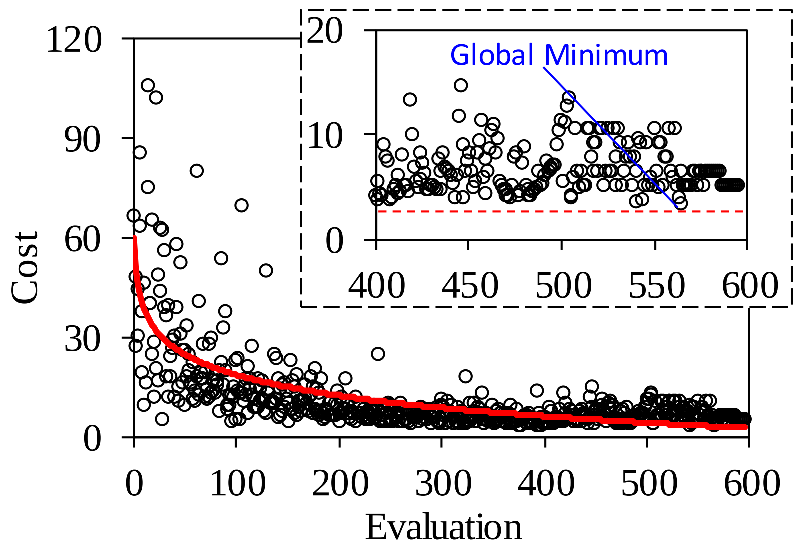


**Figure 5.22 :** Variation of the cost with evaluation number for small NSW IPM.

However, due to the position and dimensions of the PMs, slot opening width and height parameters, split ratio, and etc., the parasitic effects; such MMF harmonics, eddy current loss, torque ripple, etc. of the initial design are more dominant than that of the optimal design. More importantly, even if the output power and efficiency levels are satisfactory, 34.1% torque ripple is not acceptable for the EV applications. As shown in Table 5.12, the torque level is increased by 2.34%. Thanks to the global optimization of the small NSW IPM, the torque ripple level is decreased by 68.33%. However, the efficiency percentage is decreased by 3.17%.

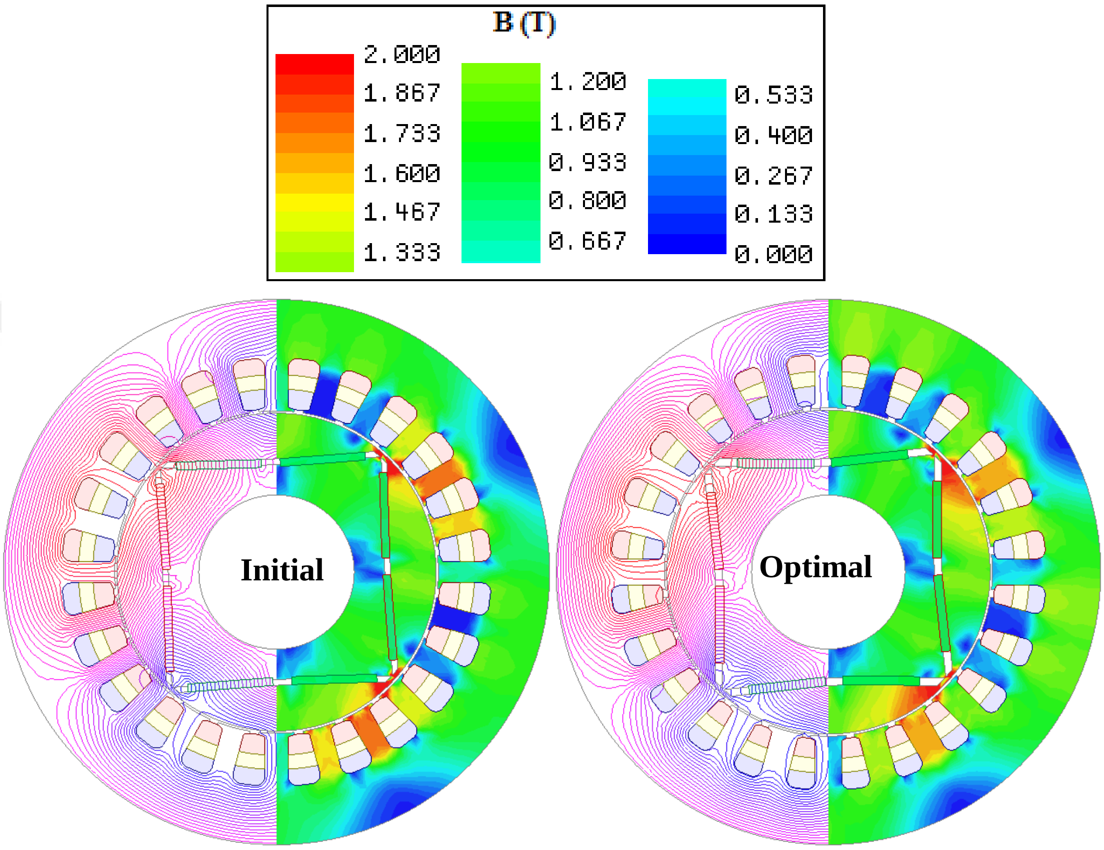


**Figure 5.23 :** 2-D views and flux line and flux density distributions of initial and optimal designs.

**Table 5.12 :** Comparison of key performance characteristics of for Small NSW IPMs (@400rpm).

| *Parameter* | *Initial* | *Optimal* | *Parameter* | *Initial* | *Optimal* |
|---|---|---|---|---|---|
| $P_{cu_{slot}}$ (W) | 28.74 | 33.485 | $P_{out}$ (W) | 189.83 | 194.28 |
| $P_{cu_{end}}$ (W) | 36.67 | 42.73 | $T_e$ (Nm) | 4.532 | 4.638 |
| $P_{core}$ (W) | 1.37 | 0.8725 | $\Delta T_e$ (%) | 34.1 | 10.8 |
| $P_{PM}$ (W) | 0.07 | 0.0148 | $\eta$ (%) | 73.41 | 71.08 |

### 5.6 Replication of Results

In this section, information on how repeatable the results obtained by the GA (random search algorithm) is provided to help the reproduction of results following the guidelines of [197].

**Table 5.13 :** Constraints of optimization parameters.

| **Advanced GA Optimizer Options** | | **Init.** | **R1** | **R2** |
|---|---|---|---|---|
| **Stopping Criteria** | ***Maximum number of generations*** | 1k | 0.7k | 1.5k |
| **Individuals at Start** | ***Parents*** | 30 | 40 | 20 |
| | ***Roulette selections*** | 10 | 12 | 8 |
| **Mating Pool** | ***Number of individuals*** | 30 | 50 | 15 |
| | ***Reproduction setup*** | | | |
| | ➢ **Crossover setup** | | | |
| | • Crossover type* | A | B | C |
| | • Individual crossover probab. | 1 | 1 | 2 |
| | • Variable crossover probab. | 1 | 2 | 2 |
| | • Variable exchange probab. | 0 | 1 | 0 |
| | • Mu | 1 | 0 | 1 |
| | ➢ **Mutation setup** | | | |
| | Mutation type§ | D | E | F |
| | Uniform mutation probab. | 0 | 1 | 2 |
| | Individual mutation probab. | 1 | 1 | 0 |
| | Variable mutation probab. | 2 | 1 | 3 |
| | Standard deviation | 0.05 | 0.07 | 0.03 |
| **Children** | ***Number of Individuals*** | 30 | 40 | 20 |
| **Pareto Front** | ***Number of survivors*** | 10 | 15 | 6 |
| **Next Generation** | ***Number of individuals*** | 30 | 50 | 24 |
| | ***Roulette pressure*** | 10 | 20 | 8 |

*A: Simulated Binary Crossover; B: Uniform; C: Two Point
§D: Polynomial Mutation; E: Gauss Distribution; F: Uniform Distribution

It is intended to obtain the global optimum solution for small NSW IPM (prototype) by repeating the GA for two times with different random seeds listed in Table 5.13 as run 1 (R1) and run 2 (R2). The initial seeds used for the optimization procedure in Section 5.4 are also listed in Table 5.13 for comparison purposes. After running the

GA with these seeds and the optimization constraint given in Table 5.11, the obtained cost function vs evaluation characteristics are illustrated in Figure 5.24. The exactly the same global minimum cost with initial run, which is ~3, is obtained at 358th and 608th evaluations for R1 and R2, respectively. Consequently, the same globally optimized parameters given in Table 5.11 are achieved after repeating the optimization algorithm with different seeds. Thus, the same global minimum is repeatedly discovered from different starting points. Table 5.13 and Figure 5.24 revel also that it is possible to obtain globally optimal solution much quicker by selecting larger starting parents and next generation individuals and Gaussian distribution for mutation type.

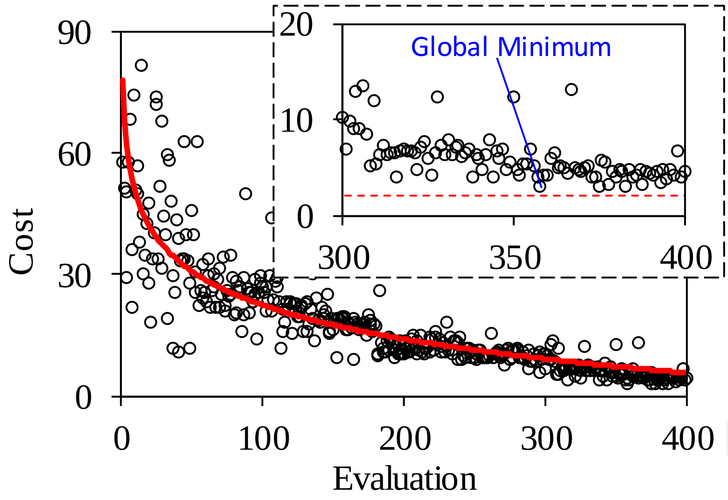


(a)

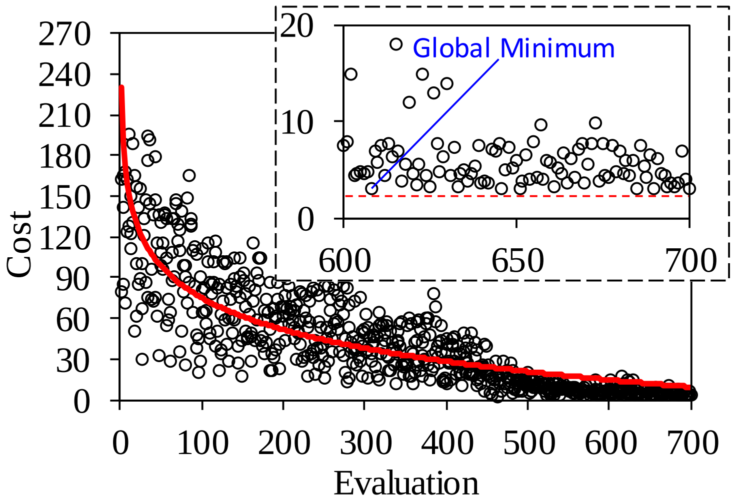


(b)

**Figure 5.24 :** Variations of the cost functions with respect to evaluation number for small NSW IPM optimized with GA having different seeds: (a) R1, (b) R2.

## 5.7 Conclusion

In this study, we developed a systematic optimization method for IPM with NSWs having large and small dimensions. In order to determine the optimization parameters and constrains for reaching the optimal solution very quickly, an individual optimization procedure and sensitivity analysis have been conducted. Following the general framework of sensitivity analyses conducted so far, geometrical design parameter sensitivity is achieved. The most dominant parameters effecting the electromagnetic torque, copper loss, and torque ripple have been determined. Influence of different excitation sources (current, current density, or copper loss restrictions) has also been investigated. Furthermore, optimization parameters and objectives and their weights have been justified for multi-objective global optimization of NSW IPM. Moreover, a comprehensive electromagnetic performance comparison between original (Toyota Prius 2010 IPM having ISDWs), initial (having NSWs), and globally optimized (having NSW) designs have been presented. The key findings obtained successfully within our framework are summarized as follows.

- It has been revealed that among a large number of design parameters, split ratio $\lambda_s$, stator tooth width ratio $b_s$, stator slot height $h_1$, rotor outer bridge width between flux barriers $R_{ib}$, rotor inner bridge radius $O_2$, flux barrier thickness $B_1$, rotor inner bridge width between flux barriers $O_1$, height of flux barriers $HR_{ib}$, magnet width $PM_w$, and magnet thickness $PM_t$ have been determined as the most dominant geometric parameters effecting the average torque.
- Stator slot opening width ratio $b_0$, stator slot opening height ratio $h_0$, rotor outer bridge width between flux barriers $R_{ib}$, and rotor inner bridge radius $O_2$ parameters have been determined as the most dominant geometric parameters effecting the torque ripple rate.
- Thanks to the global optimization, time averaged torque and output power are increased by 8.6%, torque ripple is decreased by 21.32%, and the efficiency is increased by 1.45% according to initial design.
- The reliability and effectiveness of the proposed optimization approach is validated over large and small IPMs.

Considering the rapidity and effectiveness of the proposed multi-objective optimization method, it can be deduced that the proposed optimization method can successfully be applied for the finding the global optimal solution of structures having a large number of geometrical and topological variables, such as wind and hydroelectric turbines, skeletal, runflat, and composite structures, Negative Poisson's Ratio (NPR) structures, etc.

# 6. INFLUENCE OF DESIGN PARAMETERS ON FLUX-WEAKENING PERFORMANCE OF INTERIOR PERMANENT MAGNET MACHINES WITH NOVEL SEMI-OVERLAPPING WINDINGS[5]

In this chapter, a design and parametric study of IPM machines equipped with NSWs is performed. The influence of the key design parameters including; number of turns per phase, stack length, distance and angle between V-shaped magnets, rotor yoke thickness, magnetic bridge width and thickness, and number of magnet segments on the flux-weakening (FW) performance characteristics are evaluated in detail. The influence of material of segmentation (material of bridge namely, air or iron) is also considered. A combination of analytical calculation-based program and a time-stepping 2-D FEA based program are employed to evaluate the FW characteristics. The accuracy of the FW calculations, particularly the performance at high-speed regions, is verified over changes in torque components; namely reluctance and PM, inductance components, PM flux coefficient and inverse saliency ratio due to the change in considered design parameter. The electromagnetic torque, torque ripple, output power and FW capability are investigated by parametric analyses. Moreover, the power losses and efficiency maps together FW curves are calculated for the optimal NSW IPM machine. The experimental measurements, taken from manufactured prototype, verify that the performed analyses and methods described in this paper are accurate and reliable.

## 6.1 Practical Application of This Study

The rapid growth of the automotive industry and the drastic rise in the number of vehicles with internal combustion engine (ICE) consuming fuel derived from natural resources have brought tremendous comfort to human life but have also raised significant problems such as oil shortage and environmental pollution [198]. Electric

---

[5] This chapter is based on the paper: **Gundogdu, T. and Komurgoz, G.** (2020) Influence of design parameters on flux-weakening performance of interior permanent magnet machines with novel semi-overlapping windings, *IET Elect. Power Appl.*, *14*(13), 2547-2563.

vehicles (EVs), on the other hand, are considered as ultimate solution to mitigate these concerns due to their merits of zero transportation emission and zero fossil fuel consumption thanks to generated electrical energy from renewable sources.

As the most important component in the traction system of EVs, electric machines should be designed to have high torque density to provide the required acceleration capability in the low-speed region, and high flux-weakening (FW) capability to expand the constant-power speed range in the high-speed region. In other words, the ability to operate at constant-power over a wide range of speeds, good overload performance and high efficiency are essential for EV applications [6, 45, 82, 199-202]. These features

1. enable the EV to achieve desirable driving quality;
2. allow minimization of the size and weight of the electrical machine drive;
3. allow the best utilization of the limited battery capacity.

The permanent-magnet synchronous machines (PMSMs) are extensively used for EV applications since they precisely ensure the above essentials [6, 45, 82, 200-202]. Therefore, many automobile manufacturers have used PMSMs in their models, such as Toyota Prius, Nissan Leaf, Tesla Model 3, Audi TFSI e Models, BMW i3, Citroen C-Zero, Ford Fusion Electric, etc. Among the different types of PMSMs, the interior permanent-magnet (IPM) machines are getting more attention since they have better PM utilization and wider constant-power speed range [6, 45, 199, 203]. The steady-state and FW performance characteristics of IPM machines are primarily affected by magnetic design, depending on stator/rotor topology and excitation, and sophisticated FW control techniques. From magnetic design point of view, extensively employed performance improvement methods, particularly for FW operation, are classified as follows.

- Winding topologies [60, 90, 185, 204-207];
- PM layer number, shape, and position [5, 48, 208-212];
- Flux barrier configuration and position [213-218];
- PM segmentation [210, 219-224];
- PM Skewing [225-228];

- Novel rotor topology [229-231];
- Rotor shape optimization [169, 232-234];
- Other techniques, such as excitation, axial lamination, damper bars, etc. [220, 235-237].

The key objectives of these studies are to achieve wider constant-power speed range, higher torque density, improved overall FW ability and efficiency, lower torque ripple and cogging torque, improved reliability, etc. In recent literature, many novel IPM machine topologies for EV applications have been reported; nevertheless, the systematic analysis on the impact of key design parameters on the FW ability has rarely been evaluated.

The magnetic design and consequently the FW ability are subjected to excitation and geometric parameters of IPM machine. There exists a high degree of freedom when selecting these parameters for achieving desired FW characteristics and some FW characteristics can be improved by optimizing some geometric parameters [169, 232-234]. It is reported that the FW ability can be improved remarkably by using segmented PMs with optimized iron bridges between PMs [221, 222]. However, the influence of PM segmentation without iron bridges on FW characteristics have not been investigated. Reference [211] presents an optimal design for IPM machine having V-shape PMs but only three design variables, which are angle between one pole magnets, distance between shaft and one pole magnets (rotor yoke depth), and ratio of magnet length to barrier length, are considered and FW ability in high-speed region is not investigated. Moreover, a comprehensive study on influence of only rotor geometric parameters on the FW ability, including both low- and high-speed regions, has been presented in [5]. However, other vital design parameters, such as excitation; i.e. number of turns per phase and stack length and PM segmentation with iron bridge, have not been investigated and a conventional winding topology is employed for analyses. As evidenced by comprehensive literature review presented in this paper, a limited number of papers analyse the effect of excitation and geometric parameters on both low- and high-speed performances.

Apart from the FW ability, particularly wide constant-power speed range, high efficiency and compactness are also extremely critical for IPM machines in EV applications. In the Chapter 3, to be able to reduce the end-winding length and hence increase the efficiency without sacrificing the output torque, a new winding technique, named as NSW, is introduced. Moreover, a comprehensive performance comparison between PM and reluctance machines equipped with overlapping, semi-overlapping, and non-overlapping windings is presented and remarkably improved steady-state performance characteristics for NSW IPM machine are reported in the Chapter 4. In this study, FW ability of IPM machine equipped with NSWs is investigated by considering the impact of number of turns, stack length together with the sole and combined effect with number of turns, distance between one pole PMs, rotor yoke depth, radius between one pole PMs, width of main magnetic bridge, magnet segmentation with air (without bridge) and iron (with iron bridge) for the first time. As evidenced in literature and will be shown in Section 4, the chosen parameters have a significant effect on electromagnetic characteristics, particularly dq-axis inductance and reluctance torque component. The influence of these design parameters on the FW characteristics have been calculated by using a method consisting of the combination of numeric and analytical methods. In addition, in order to reveal the underlying causes of change in FW performance, apart from the dq-axis inductance variations, variations of (i) PM flux coefficient; (ii) inverse saliency ratio; and (iii) flux density distributions showing the magnetic saturation level are analysed. Flux linkage, inductance, and power loss coefficients have been calculated parametrically by employing 2-D, non-linear, time-stepping FEA. These data are used as input data of analytical FW calculation program based on hybrid FW control technique. Comprehensive performance analyses of each parameter are conducted for both low- and high-speed operating regions. Moreover, for variation of each parameter, the level of constant-power speed range is verified over PM flux coefficient and saliency ratio calculated at rated operating point.

The major objectives of this study are to (i) reveal the FW ability of IPM machine designed with proposed NSWs and determine the most dominant parameters on FW capability by explaining the reasons underling; (ii) fulfil the gap in literature on the impact of both excitation and geometric design parameters of IPM machines used in EV applications on both low- and high-speed performance characteristics. The analysis method and FW calculation algorithm are presented in Section 6.2. In Section 6.3, the influence of design parameters on the FW ability is investigated. Finally, the conclusions and future work are drawn in Section 6.4.

### 6.2 Flux-Weakening Mechanism

One of the primary limiting factors of IPM drives is the limited excitation. In constant-torque region, the back-EMF of the IPM machine rises with rotor speed increasing until the voltage limit $u_{max}$ of the inverter reached (see (6.1)). The IPM motor then enters the FW operation. Since the voltage is limited by the rating of the inverter, the current is also limited ($i_{max}$) by rating of the machine (see (6.2)). Normally, $d$-axis current $i_d$ works as weakening current when $i_s$ has a phase advance angle in comparison with $q$-axis [222]. In other words, the IPM machine is controlled by maximum torque-per-ampere (MTPA) mode below corner speed $n_b$ (see (6.5)) and FW control mode above $n_b$ [5]. The relationship between electromagnetic torque $T_e$ and current angle (the angle between current vector and $q$-axis) $\gamma$ is expressed by (6.6). The first term in (6.6) represents the PM torque and the second term represents the reluctance torque. It is reported that there is a significant phase advance in IPM machines to obtain higher reluctance torque and the constant-power speed range can be expanded by using a phase advance technique [5, 201, 222, 238].

$$V_d^2 + V_q^2 \leq u_{max}^2 \tag{6.1}$$

$$i_d^2 + i_q^2 \leq i_{max}^2 \tag{6.2}$$

$$V_d = R_s i_d - \omega_s L_q i_q \tag{6.3}$$

$$V_q = R_s i_q + \omega_s \left(L_d i_d + \lambda_{pm}\right) \tag{6.4}$$

$$n_b = \frac{120}{2\pi P} \frac{u_{max}}{\sqrt{\left(\lambda_{pm} - L_d i_d\right)^2 + \left(L_q i_q\right)^2}} \tag{6.5}$$

$$T_e = 0.5P\left[\lambda_{pm} i_s \cos\gamma + 0.5\left(L_d - L_q\right) i_s^2 \sin 2\gamma\right] \tag{6.6}$$

in which, $V_d$, $V_q$, $i_d$, $i_q$, $L_d$, and $L_q$ are voltage, current, and inductance of $d$- and $q$-axes, respectively and $R_s$, $i_s$, $\omega_s$, $\lambda_{pm}$, and $P$ are stator phase resistance, stator current vector, angular speed, PMs flux linkage, and pole number, respectively.

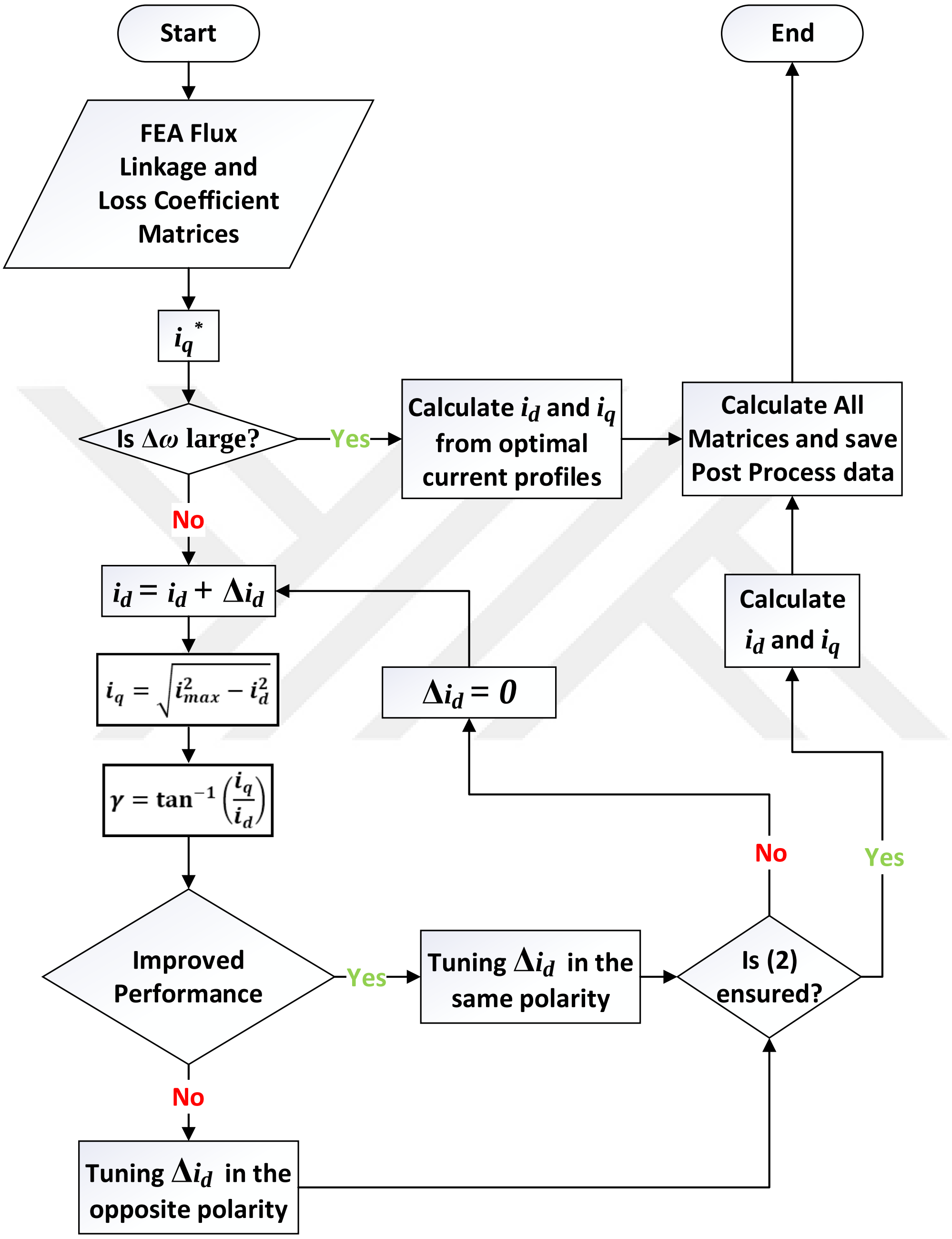


**Figure 6.1 :** Flow chart of employed FW algorithm.

In this study, FW performance characteristics are calculated by using the $dq$-axis equivalent circuit of IPM machine, expressions between (6.1)-(6.6), and the flow chart depicted in Figure 6.1, which employs "hybrid FW control technique" [238]. As can be seen, the employed FW algorithm consists of the combination of numerical and analytical calculations. At the stage of FEA, a $[i_d]_{10x10}$ and $[i_q]_{10x10}$ matrices are injected to phase windings of NSW IPM for evaluating $[\lambda_d]_{10x10}$ and $[\lambda_q]_{10x10}$ flux linkage and $[P_{loss}]_{10x10}$ constraints/coefficient matrices. Subsequently, the obtained matrices are used as inputs of the MATLAB® code developed in this study (see Figure 6.1), calculating the output matrices, including torque- and power-speed, power losses and efficiency maps. $\Delta\omega$ in Figure 6.1 indicates the motor relative speed between reference and actual output speeds. In the [Is $\Delta\omega$ large?] loop, for each reference speed, the program calculates the voltage matrix and determine the corner speed $n_b$ by considering (6.1)-(6.5). If calculated voltage is less than $u_{max}$, the temporary voltage index is changed to 1. When the actual speed has changed substantially, the control algorithm adjusts the $dq$-axis stator currents for maximum power operation based on the optimum current profiles by determining the best $\gamma$. The previous $dq$-axis currents are used as initial values when the motor returns to constant-torque operation, while $i_s$, $q$-axis current error and $\omega_s$ are used as optimization goals to optimize FW control. If one of the above parameters change, the $\Delta i_d$ tuning will ensure maximum inherent power capacity, limited by (6.1) and (6.2), and thus improve the motor efficiency, and the $\Delta i_d$ tuning will continue in the same direction until the condition given in (6.2) is reached. Otherwise, the polarity of $\Delta i_d$ needs to be changed. Thus, MTPA and FW controls are ensured in constant-torque and constant-power regions, respectively.

In most popular approaches, the FW capability of IPM machines is evaluated by considering the PM flux coefficient $k_{FW}$ and the inverse saliency ratio $\xi$, also known as reluctance torque ability, given as follows [239, 240].

$$k_{FW} = \frac{\lambda_{PM}}{\lambda_{PM} - L_d i_{max}} \tag{6.7}$$

$$\xi = \frac{L_q}{L_d} \tag{6.8}$$

In order to achieve a wider constant-power region, the electrical machines should be designed as to have higher $k_{FW}$ and $\xi$ rates as much as possible. Because, it has been reported that $k_{FW}$ is an indicator for the extended PM magnetic field weakened by $i_d$ and $\xi$, which is the inverse of more traditional definition of the saliency ratio for conventional machines, indicates the reluctance torque ability [5, 239, 240].

### 6.3 Influences of Design Parameters on FW Performance of NSW IPM

In this section, the influence of some key design parameters, including:

a) Stator: Number of turns per phase: $N_s$

b) Stator and Rotor: Stack length: $l_s$

c) Rotor: Five parameters shown in Figure 6.2: $O_1$, $O_2$, $R_{ib}$, $B_1$, and $N_{PMs}$ (segmentation with both air and iron)

on performance of V-shape IPM machine both in low- and high-speed operating regions are investigated in detail. As seen in Figure 6.2, a high degree of freedom exists when designing a rotor for IPM machines with V-shaped PMs. Investigated design parameters are chosen as a result of experience gained through numerous investigations and comprehensive literature [5, 48, 60, 82, 90, 169, 185, 202-237]. On the other hand, other key parameters; such as stator outer diameter, stator slot geometry, shaft diameter, air-gap length, $D_2$, $HR_{ib}$, and $w_s$ have not been considered in this paper because of these reasons:

I. their predicted obvious and/or insignificant effects (particularly due to the leakage flux);

II. limited effects as a consequence of existing of mechanical constrains;

III. their very limited range;

IV. not reasonable or possible to investigate its individual effect.

As one of the selected design parameters varies, others are fixed at their optimal values, namely, individual effect of each parameter is investigated. However, only for the analyses of influence of stack length, the number of turns per phase is also varied with stack length in order to keep the torque fixed at constant-torque region. Note that for each analysis, the current angle delivering the maximum torque is determined parametrically and the results are presented accordingly. Moreover, all analyses have been conducted within the current and voltage limit of the inverter. The distance between the segmented magnets, namely bridge width, is another critical design parameter. In order to restore balance between magnet leakage flux and effectiveness of the bridges, an empirical formula expressed in (6.9) [221] is employed to optimal values of the bridge width $w_s$.

$$w_s = \frac{k_{sm}\lambda_{max}P}{(N_{PM} - 1)l_s B_{sat} N_s k_{w_1}} \tag{6.9}$$

where $k_{sm}$, $\lambda_{max}$, $N_{PM}$, $P$, $l_s$, $B_{sat}$, and $k_{w1}$ are the ratio of bridge flux linkage to magnet flux linkage, the allowable maximum flux linkage, the number of segmented magnets, number of poles, the stack length, the saturation flux density in the iron bridges, and the fundamental winding factor, respectively. The performance characteristics are predicted via $dq$ model of NSW IPM by performing 2-D, non-linear, time-stepping FEA under steady state operating with current source supply providing 26Apeak phase current, 0.4krpm rotor speed, and the current angle delivering the maximum torque.

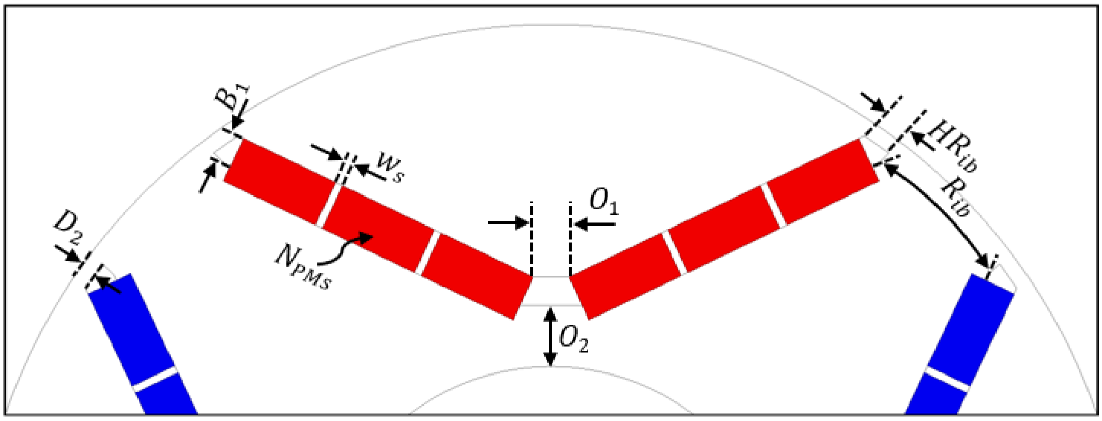


**Figure 6.2 :** Key design variables of the V-shape IPM rotor.

### 6.3.1 Number of turns per phase $N_s$

The influence of number of turns per phase $N_s$ on FW characteristics is investigated for various $N_s$s varying from 8 to 32 by neglecting the level of current density. During analyses, all other parameters are fixed at their optimal values. Furthermore, it is ensured that the number of turns per phase matches the current and voltage limit. The obtained electromagnetic torque and power versus speed characteristics at the limited current and voltage defined in (6.1) and (6.2), respectively are illustrated in Figure 6.3. It has been revealed that the lower the $N_s$,

a) the better the FW ability;

b) the lower the torque level at constant-torque region;

c) the higher the power level at constant-power region.

The reason behind this phenomenon can be explained by using (6.7) and (6.8). The FW capability indicators, $k_{FW}$ and ξ, are calculated for constant-torque region and variation of these parameters with respect to $N_s$ is illustrated in Figure 6.4. Figure 6.4 indicates that as the $N_s$ is increased, the PM magnetic field weakened by $d$-axis current is narrowed and also the reluctance torque ability is weakened.

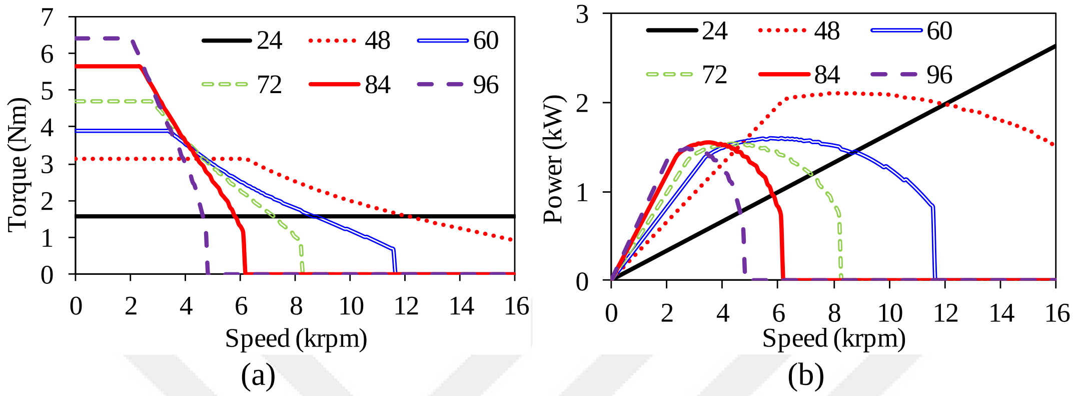


**Figure 6.3 :** Variation of FW characteristics with $N_s$: (a) Torque/speed, (b) Power/speed.

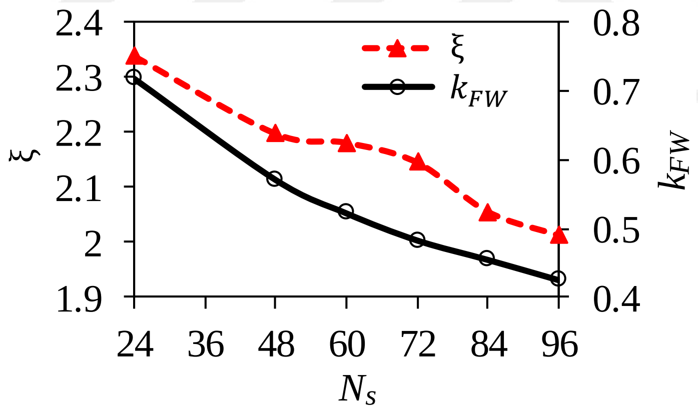


**Figure 6.4 :** Variation of $\xi$ and $k_{FW}$ with respect to $N_s$.

Figure 6.4 reveals also that the FW capability of a previously manufactured IPM machine can be changed easily by changing $N_s$ without changing anything else. For instance, the constant-power region can be significantly widened by reducing $N_s$ if sacrifice of torque level at constant-torque region is tolerable. Alternatively, additional power electronic circuit with controller can be designed for changing $N_s$ as reported in [241-243].

### 6.3.2 Stack length $l_s$

The influence of the stack length parameter $l_s$ on the FW performance is carried out for two different cases as:

<u>*Case#1*</u>: only $l_s$ is varied in order to reveal the individual (sole) impact;

<u>*Case#2*</u>: both $l_s$ and $N_s$ are varied in order to keep the torque fixed at the constant-torque region.

For the first case, $N_s$ is fixed at 96 and the obtained FW performance characteristics are illustrated in Figure 6.5. As $l_s$ is increased linearly whilst $N_s$ is fixed, (***i***) the corner speed (CS) of the IPM is getting smaller; (***ii***) constant-torque region is fixed; and (***iii***) the constant-power region is getting larger. It can be deduced that the FW capability does not change for the Case#1. Because, as illustrated in Figure 6.7 with ($l_s$), the PM magnetic field weakened by *d*-axis current and the reluctance torque ability do not change with $l_s$.

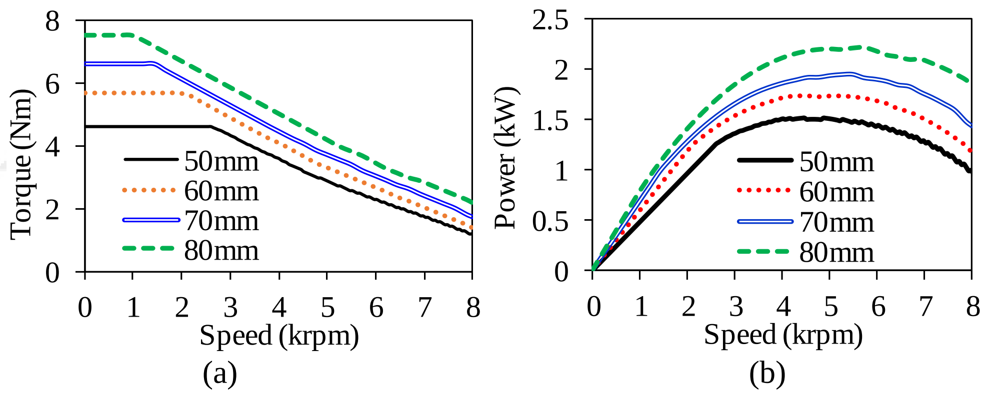


**Figure 6.5 :** Influence of $l_s$ on FW characteristics for Case#1(a) Torque/speed, (b) Power/speed.

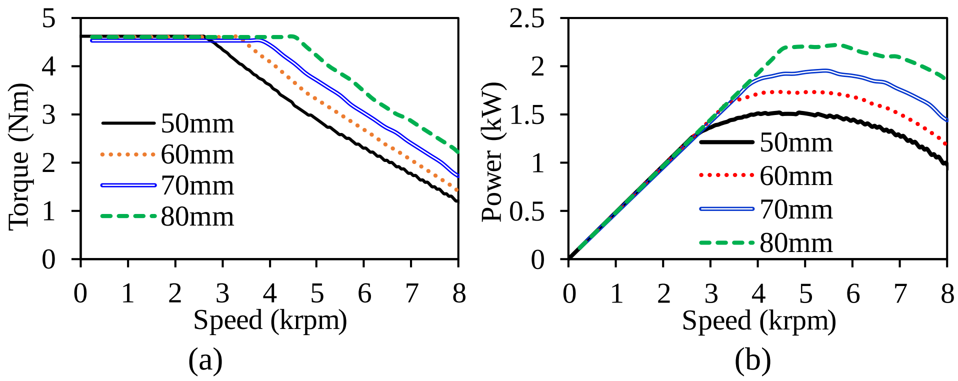


**Figure 6.6 :** Influence of combined effect of $l_s$ and $N_s$ on FW characteristics for Case#2 (a) Torque/speed, (b) Power/speed.

As for the second case, in order to keep the torque fixed at constant-torque region, there exists an inverse (negative) correlation between $N_s$ and $l_s$. $N_s$ is changed from 96 to 78 with 6 turns per phase for 50mm to 80mm. In that case, both of the constant-torque and power regions and the CS are increased remarkably as seen in Figure 6.6. It can be concluded that there is a direct correlation between $(l_s, N_s)$ and FW capability. This correlation can also be observed from Figure 6.7, where the graphs indicated with $(l_s, N_s)$.

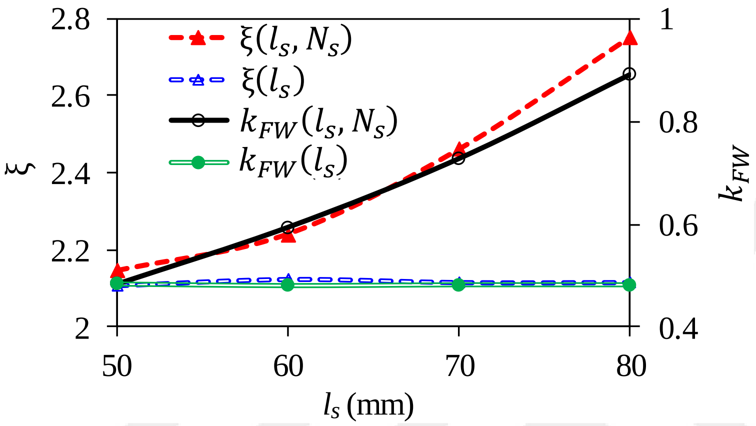


**Figure 6.7 :** Variation of $\xi$ and $k_{FW}$ with $l_s$ for both cases.

### 6.3.3 Distance between V-shape PMs $O_1$

As seen in Figure 6.4, to be able to limit the PM flux leakage to a minimum, there exists no magnetic bridge between V-shaped PMs. Although there is no magnetic bridge, $O_1$ parameter can still restrict the flux leakage slightly by making the flux saturated in rotor as illustrated in Figure 6.8.

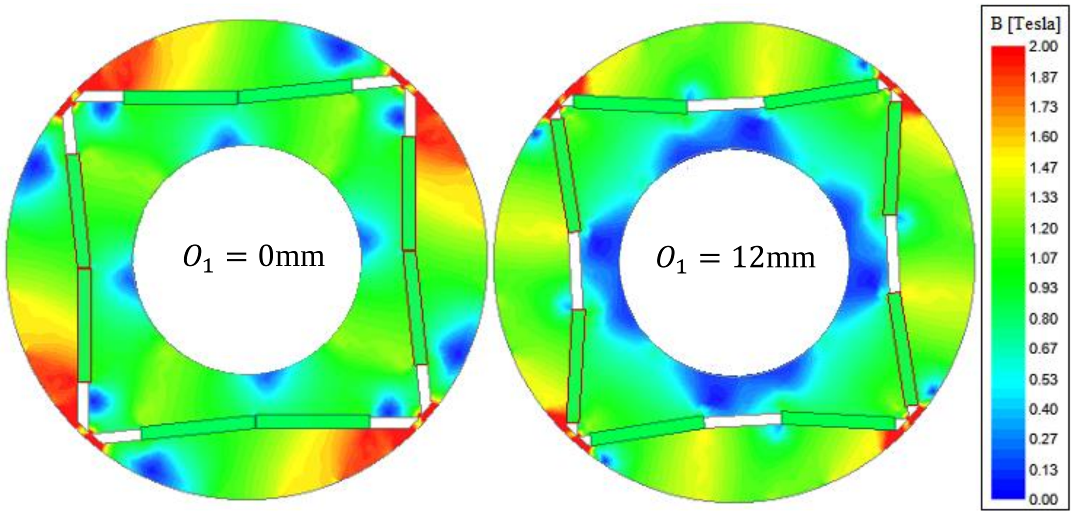


**Figure 6.8 :** Magnetic flux density distributions in rotor for different values of $O_1$ parameter.

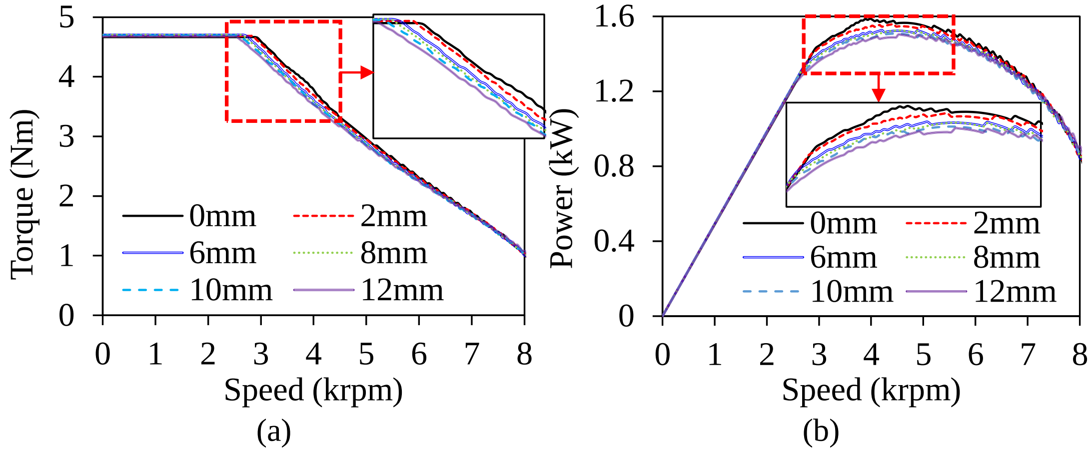


**Figure 6.9 :** Influence of $O_1$ on FW characteristics: (a) Torque/speed, (b) Power/speed.

As seen in Figure 6.9, $O_1$ has a slight impact on the FW ability of IPM. Particularly, it has an impact on the region between constant-torque and deep FW. As can be observed, with $O_1$ increasing, constant-power region decreases. This is because of the fact that the with $O_1$ increasing, the reluctance of leakage magnetic circuit increases, and the flux leakage decreases. Nevertheless, since the different current angle at base speed are adopted to obtain maximum torque with $O_1$ increasing, the average torque does not increase.

### 6.3.4 Distance between shaft and V PMs - $O_2$

The distance between shaft and V PMs, indicated with $O_2$ as shown in Figure 6.2, is one of the key parameters. It has a substantial effect on leakage flux, flux concentrating effect, and effective magnetic energy.

The FW performance, including torque and power versus speed, at limited current and voltage are illustrated in Figure 6.10. For constant-torque region, there is an optimum $O_2$ value, delivering the maximum torque, which is 8mm for the considered IPM. On the other hand, as for the constant-power region, the maximum power is achieved when $O_2$ equals to 1mm. As can be seen, there is no direct correlation between $O_2$ and FW ability. In order to reveal the relationship between FW ability and $O_2$ parameter, variation of electromagnetic torque ($T_e$) components, namely reluctance ($T_{rel}$) and PM ($T_{pm}$), and inductance components are investigated together with $k_{FW}$ and $\xi$ ratios as follows. The FW ability can also be predicted by considering the reluctance torque component. It is well known that the higher the $T_{rel}$ component, the better the FW performance. $T_{rel}$ component is calculated for base speed by using (6.10) and the variations of time averaged torque components with $O_2$ are depicted in Figure 6.11.

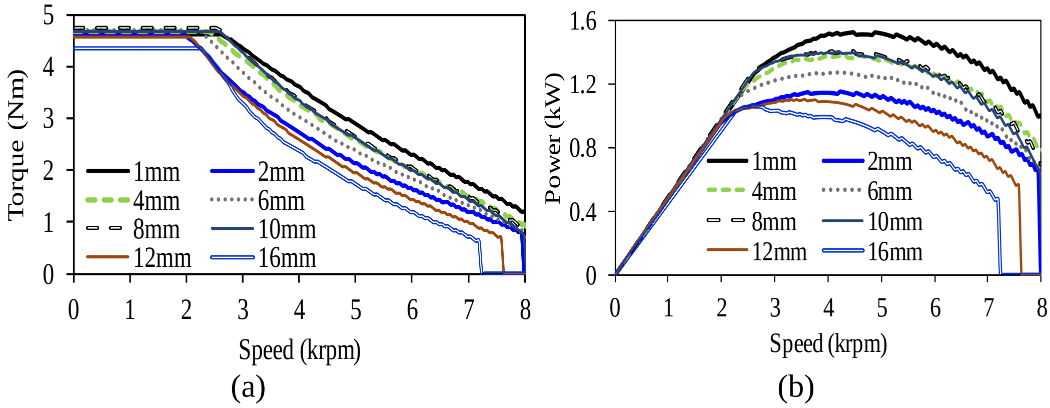


**Figure 6.10 :** Influence of $O_2$ on FW characteristics: (a) Torque/speed, (b) Power/speed.

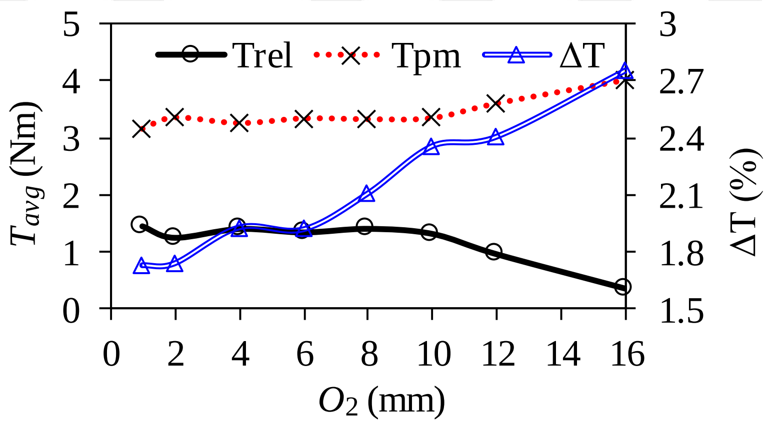


**Figure 6.11 :** Influence of $O_2$ on torque characteristics.

$$T_e = T_{pm} + T_{rel} = \frac{3P}{4}\left\{\left[(L_d - L_q)i_d i_q\right]_s + \left[\lambda_{pm} i_q\right]_s\right\}$$

$$\begin{cases} T_{pm} = \dfrac{3P}{4}\left(\lambda_{pm_d} i_q - \lambda_{pm_q} i_d\right) \\ T_{rel} = \dfrac{3P}{4}\left[(L_d - L_q)i_d i_q + (i_q^2 - i_d^2)L_{dq}\right] \end{cases} \tag{6.10}$$

where $T_{pm}$ is due to the interaction between the PMs flux linkage ($\lambda_{pm}$) dq-axis components and stator dq-axis currents $i_q$ and $i_d$ and $T_{rel}$ is due to the rotor saliency $(L_d - L_q)$, mutual inductance $L_{dq}$ and dq-axis currents. As can be observed, $T_{rel}$ decreases with $O_2$ increasing while $T_{pm}$ increases as a consequence of increasing effective magnetic energy. In addition, the higher values of $O_2$ can restrict the flux leakage slightly by reducing the level of saturated flux as illustrated in Figure 6.12. Moreover, Figure 6.11 reveals that the higher the $O_2$, the higher the torque ripple percentage ΔT.

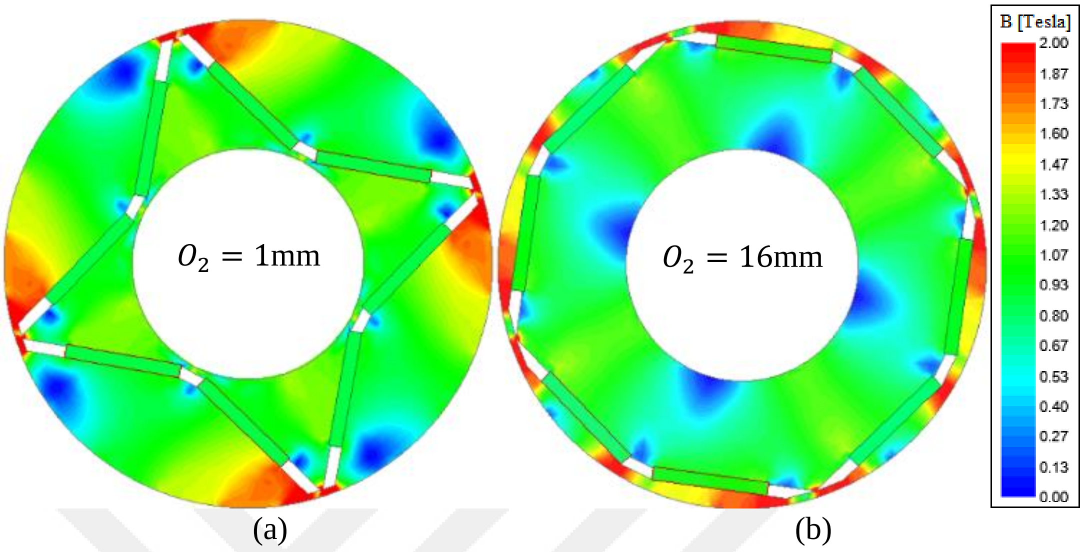


**Figure 6.12 :** Magnetic flux density distributions in rotor for different values of $O_2$ parameter.

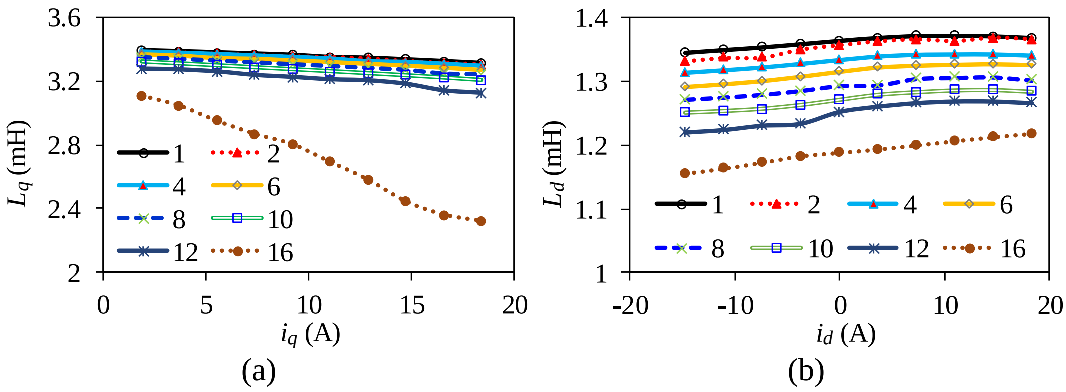


**Figure 6.13 :** Variation of inductance versus current characteristics for various $O_2$ parameters: (a) $L_q$ vs $i_q$, (b) $L_d$ vs $i_d$.

The characteristics of dq-axis inductances against dq-axis currents for various values of $O_2$ are depicted in Figure 6.13. Note that since the flux bridges are located in the d-axis flux direction, a $-i_d$ has the effect of reducing flux density of the saturation. In other words, $-i_d$ allows for some of the magnet fluxes in the flux bridges to be canalized. Therefore, in order to further reduce the air-gap flux, $-i_d$ is employed as shown in Figure 6.13. As can be seen, $L_q$ decreases with $O_2$ and $i_q$ increasing while $L_d$ decreases with $O_2$ increasing while it increases with $i_d$ increasing. Once $O_2$ has its highest value, the inductance components, particularly $L_q$, become more sensitive to the dq-axis current. As a consequence, considering the giving findings between Figures 6.13 and 6.15 it can be deduced that the better FW ability can be achieved for lower values of $O_2$. Because, as $O_2$ increases, $\lambda_{pm}$ increases and $L_d$ decreases, so the torque and power decreases at high speed, which is consistent with the results of FW performance indicators in Figure 6.14. Moreover, it can also be observed that because of the same reason the CS decreases with $O_2$ increasing.

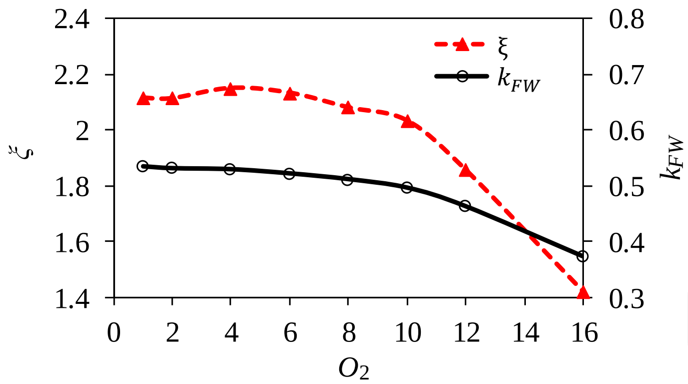


**Figure 6.14 :** Variation of $\xi$ and $k_{FW}$ with respect to $O_2$.

### 6.3.5 Radius Between Λ PMs - $R_{ib}$

Influence of the radius between two adjacent PMs on the FW characteristics at limited current and voltage operating condition is illustrated in Figure 6.15. As can be seen, with $R_{ib}$ increasing, the level of torque at constant-torque region decreases while the level of torque at constant-power region increases (as indicated with arrows in Figure 6.15 (a)). In order to reveal the underlying causes of achieving such FW characteristics, torque components, dq-axis inductances, saturation levels, and the FW performance indicators ($k_{FW}$ and $\xi$) are investigated as follows. As illustrated in Figure 6.16, with $R_{ib}$ increasing, $L_d$ decreases while $L_q$ increases. In the same way, with increasing $i_d$ and $i_q$, $L_d$ increases while $L_q$ decreases. Moreover, as clearly seen in Figure 6.17, the $d$-axis magnetic circuit becomes more effective with $R_{ib}$ increasing. This phenomenon causes a decrease in the level of flux leakage by reducing magnetic saturation in rotor (see Figure 6.17) and hence an increase in the effective magnetic energy (see Figure 6.18 the increase of $T_{pm}$). As can be observed from Figure 6.18, $R_{ib}$ has a significant effect on ΔT. The minimum ΔT is achieved at 10mm while the maximum is achieved at 4mm.

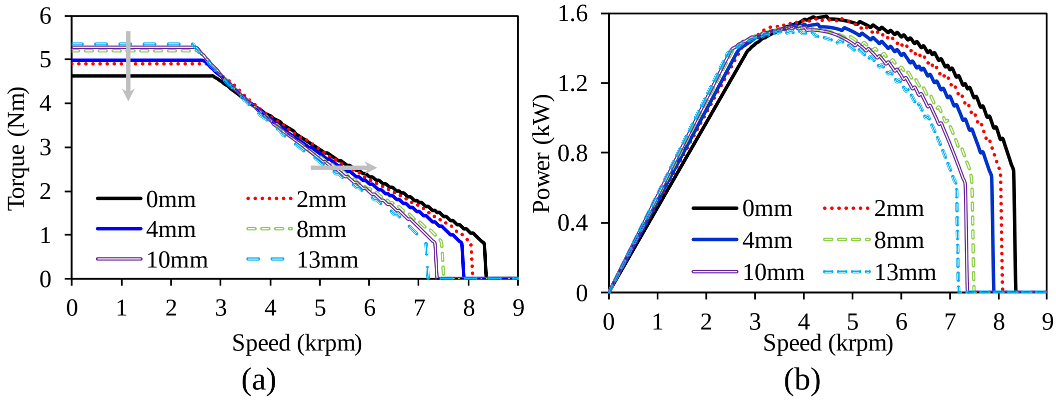


**Figure 6.15 :** Influence of $R_{ib}$ on FW characteristics: (a) Torque/speed, (b) Power/speed.

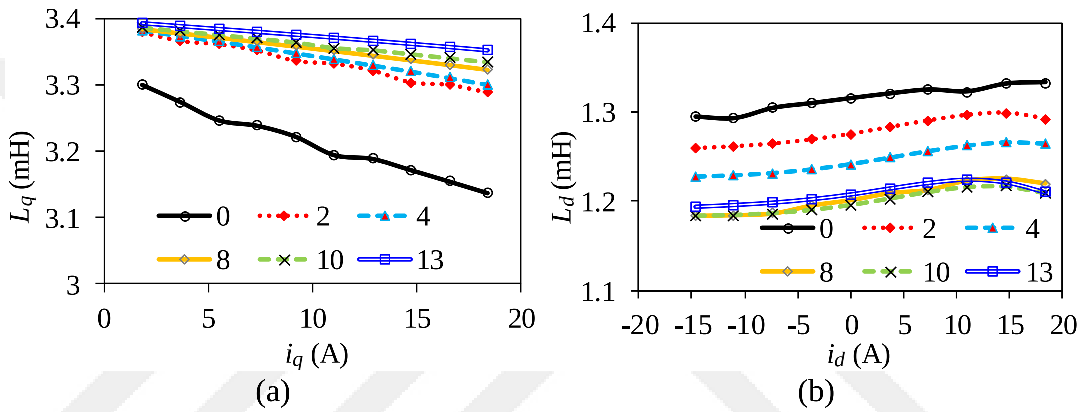


**Figure 6.16 :** Variation of inductance versus current characteristics for various $R_{ib}$ parameters: (a) $L_q$ vs $i_q$, (b) $L_d$ vs $i_d$.

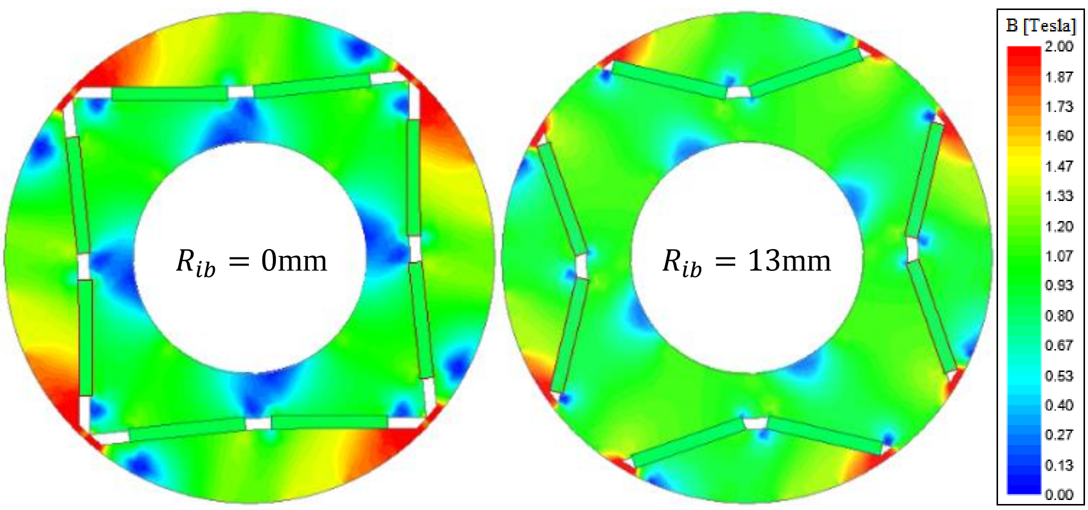


**Figure 6.17 :** Magnetic flux density distributions in rotor for different values of $R_{ib}$ parameter.

The variation of FW characteristics with respect to $R_{ib}$ is also validated with the FW performance indicators depicted in Figure 6.19, which are calculated at base speed with rated operating conditions. As explained previously, the reduction in both $k_{FW}$ and $\xi$ ratios are an indicator for poorer FW performance. Consequently, the practically minimum values of $R_{ib}$ leads to achieve a better FW performance characteristic, particularly at high-speed operating region.

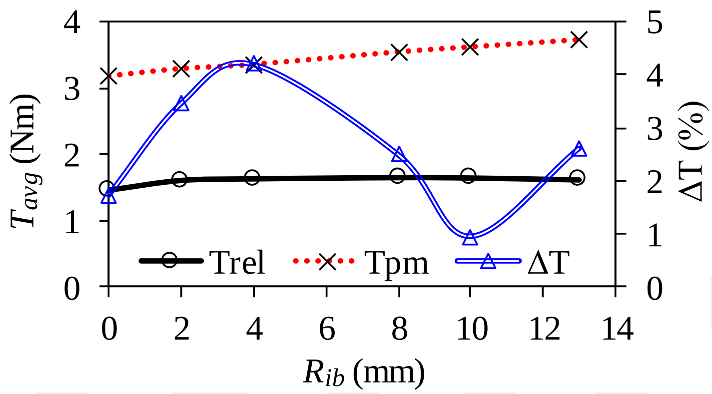


**Figure 6.18 :** Influence of $R_{ib}$ on torque characteristics.

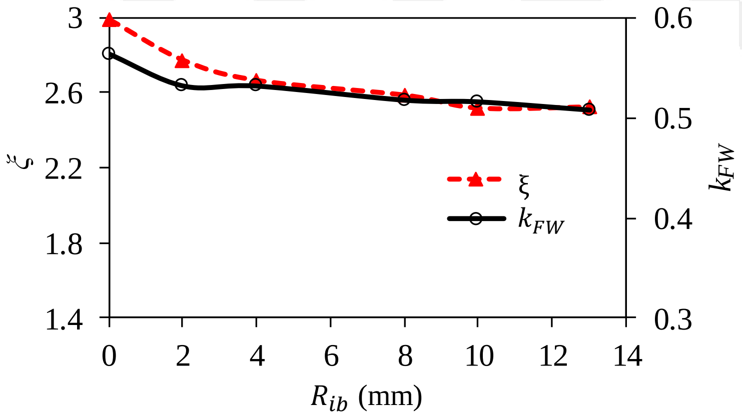


**Figure 6.19 :** Variation of $\xi$ and $k_{FW}$ with respect to $R_{ib}$.

### 6.3.6 Width of main magnetic bridge - $B_1$

Magnetic bridge in IPM machines is one of the key parameters. By saturating the flux at air-gap sites of magnetic bridges, it can limit the flux leakage as shown in Figure 6.20. In addition, as can be seen in Figure 6.21, $B_1$ parameter has a substantial influence on the FW performance. With $B_1$ increasing, the constant-torque speed region increases while the constant-power speed region decreases. At constant-torque region, although the different current angles delivering the maximum average torque at base speed is employed, the maximum average torque increases with $B_1$ increasing.

This is due to the fact that with $B_1$ increasing, the reluctance of leakage magnetic circuit increases, flux leakage decreases, and the effective magnetic energy increases.

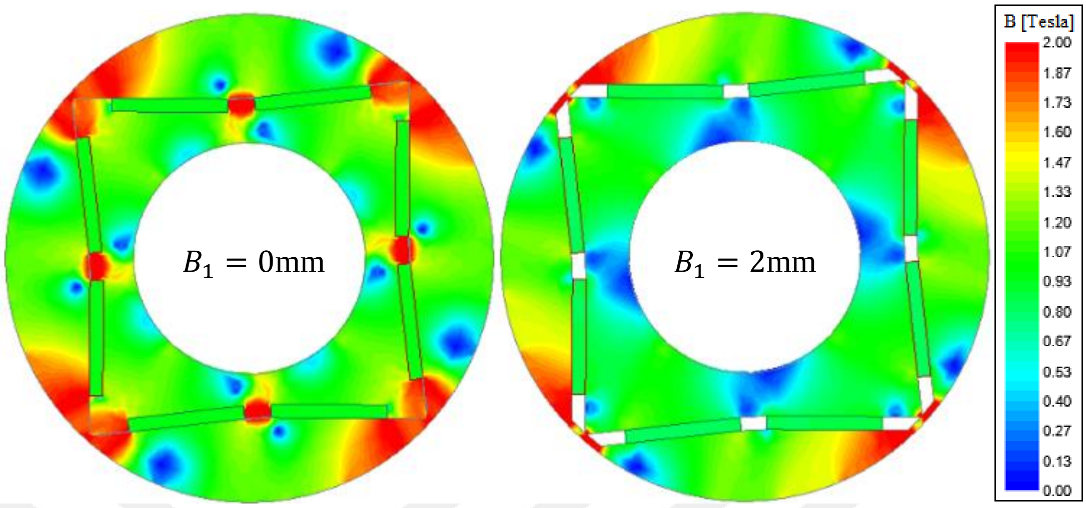


**Figure 6.20 :** Magnetic flux density distributions in rotor for different values of $B_1$ parameter.

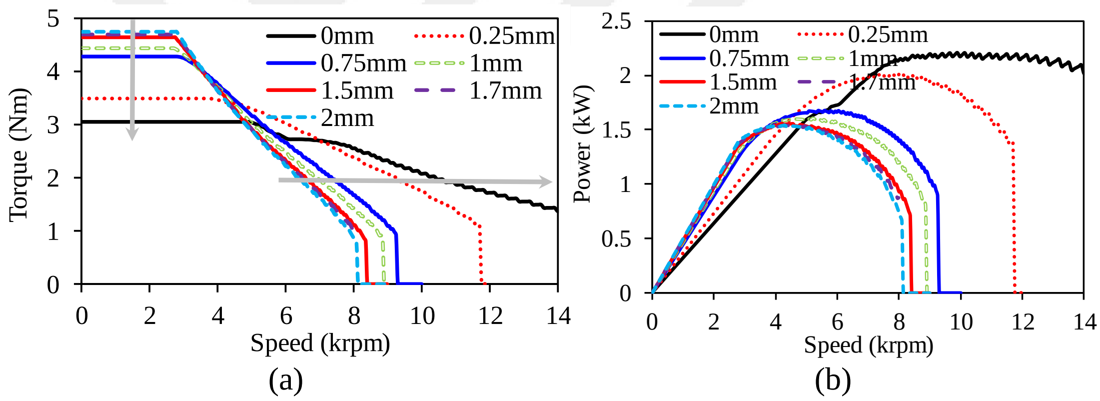


**Figure 6.21 :** Influence of $B_1$ on FW characteristics: (a) Torque/speed, (b) Power/speed.

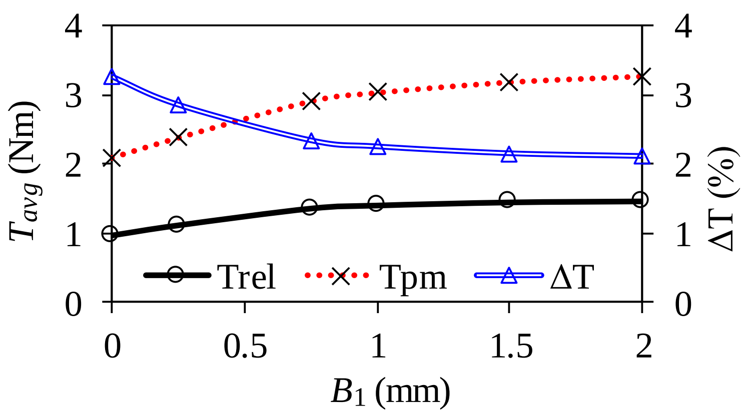


**Figure 6.22 :** Influence of $B_1$ on torque characteristics.

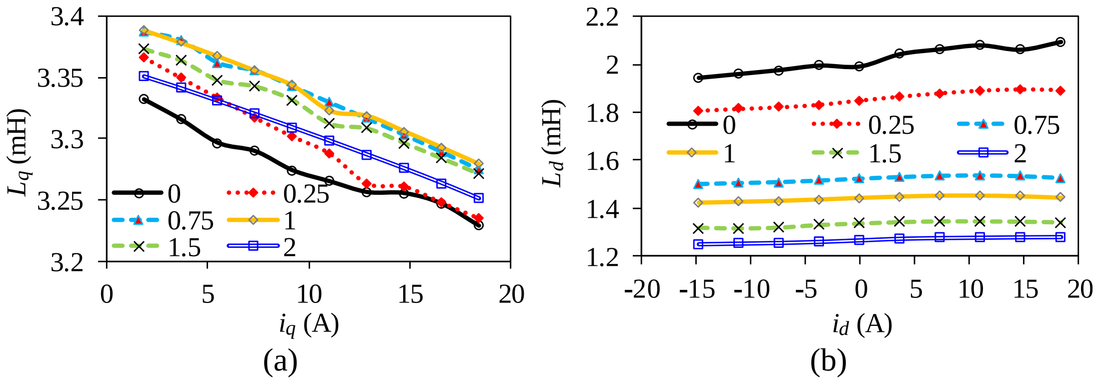


**Figure 6.23 :** Variation of inductance versus current characteristics for various $B_1$ parameters: (a) $L_q$ vs $i_a$, (b) $L_d$ vs $i_d$.

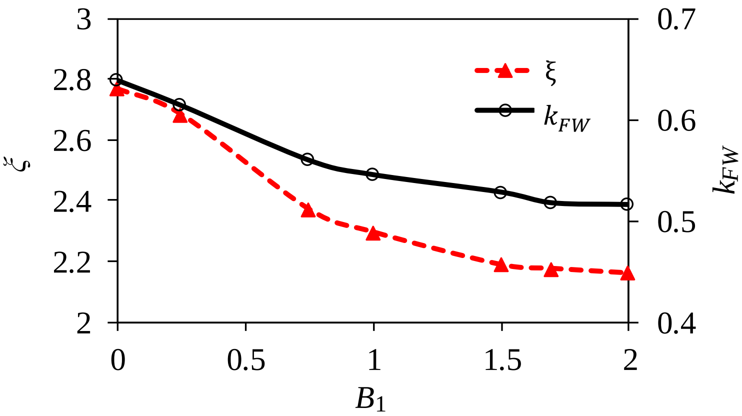


**Figure 6.24 :** Variation of $\xi$ and $k_{FW}$ with respect to $B_1$.

As a consequence, the reluctance and PM torque components increase with $B_1$ increasing, as illustrated in Figure 6.22. It can also be seen that $B_1$ has a slight effect on ΔT percentage. As for the constant-power region, since $\xi$ and $k_{FW}$ ratios decrease with $B_1$ increases (see Figure 6.24), torque and hence power regions decrease with speed increases. In addition, the CS decreases, and the reason is similar to that of $O_2$ in Section 4.4. The influences of $B_1$ on $L_q$ vs $i_q$ and on $L_d$ vs $i_d$ are depicted in Figure 6.23. As can be observed, with $B_1$ increasing, $L_q$ increases while $L_d$ decreases considerably.

### 6.3.7 PM Segmentation with Air - $N_{PMs}$

It is reported in [5] and [221] that the FW capability of IPM machines can be improved by employing segmentation of PMs with the help of iron bridges between PM segments. In this study, the FW performance of NSW IPM machine with and without iron bridges between segmented PMs are investigated. In order to maintain a fair/accurate analysis, the total volume of PMs is kept fixed during the segmentation procedure. In addition, the optimal width of the bridges, usually determined by considering the flux leakage amount and mechanical strength of flux bridges to ensure the machine operated safely on high-speed region, is analytically calculated by using (6.9) for each segment number.

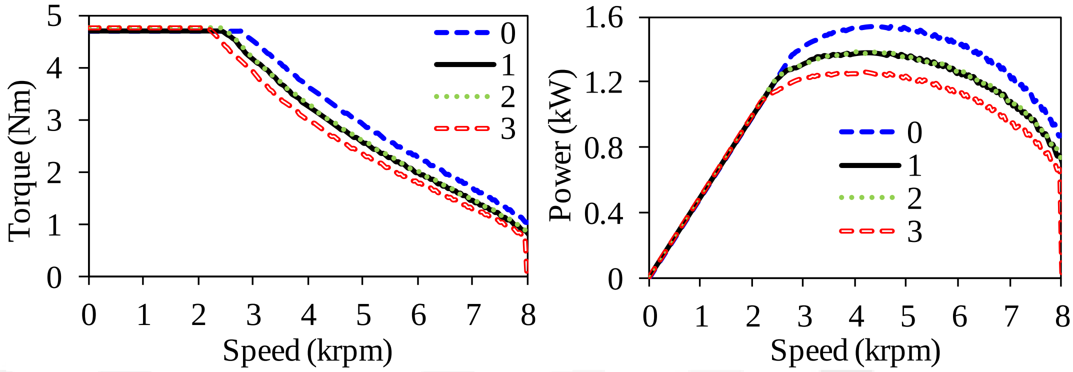


(a) (b)

**Figure 6.25 :** Influence of $N_{PMs}$ on FW characteristics: (a) Torque/speed, (b) Power/speed.

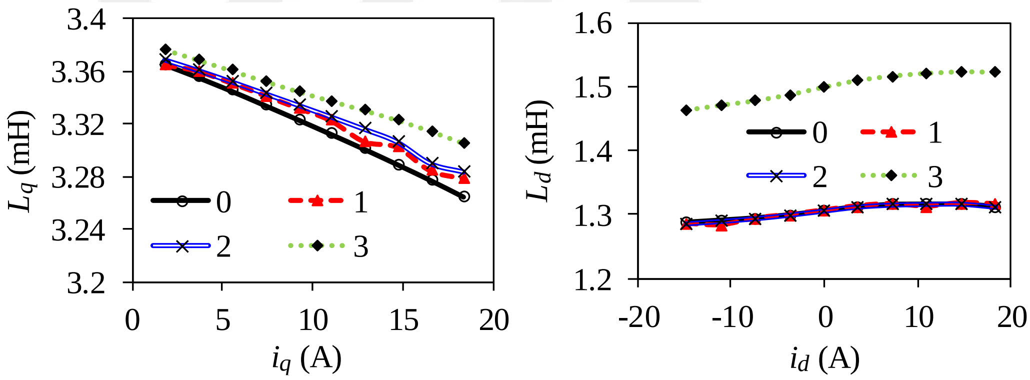


(a) (b)

**Figure 6.26 :** Variation of inductance versus current characteristics for various $B_1$ parameters: (a) $L_q$ vs $i_a$, (b) $L_d$ vs $i_d$.

The FW performance results in case of segmentation with air is illustrated in Figure 6.25. It can be observed that the CS decreases with $N_{PM}$ increasing. In addition, the similar FW characteristics are observed for segment numbers of 1 and 2.

The constant-power speed range decreases with $N_{PM}$ increasing. Because, the PM flux linkage and hence PM torque component (see Figure 6.28) and $\mathrm{L_d}$ increases (see Figure 6.26(b)). Moreover, as illustrated in Figure 6.30(a), both $\xi$ and $k_{FW}$ ratios decrease as $N_{PM}$ increasing. Therefore, it can be concluded that the magnet segmentation with air results with poorer FW performance characteristics.

### 6.3.8 PM Segmentation with Iron - $N_{PMs}$

Once the segmentation is made with iron instead of air, a part of the magnetic flux passes through the magnetic intervals, reducing the *d*-axis reluctance.

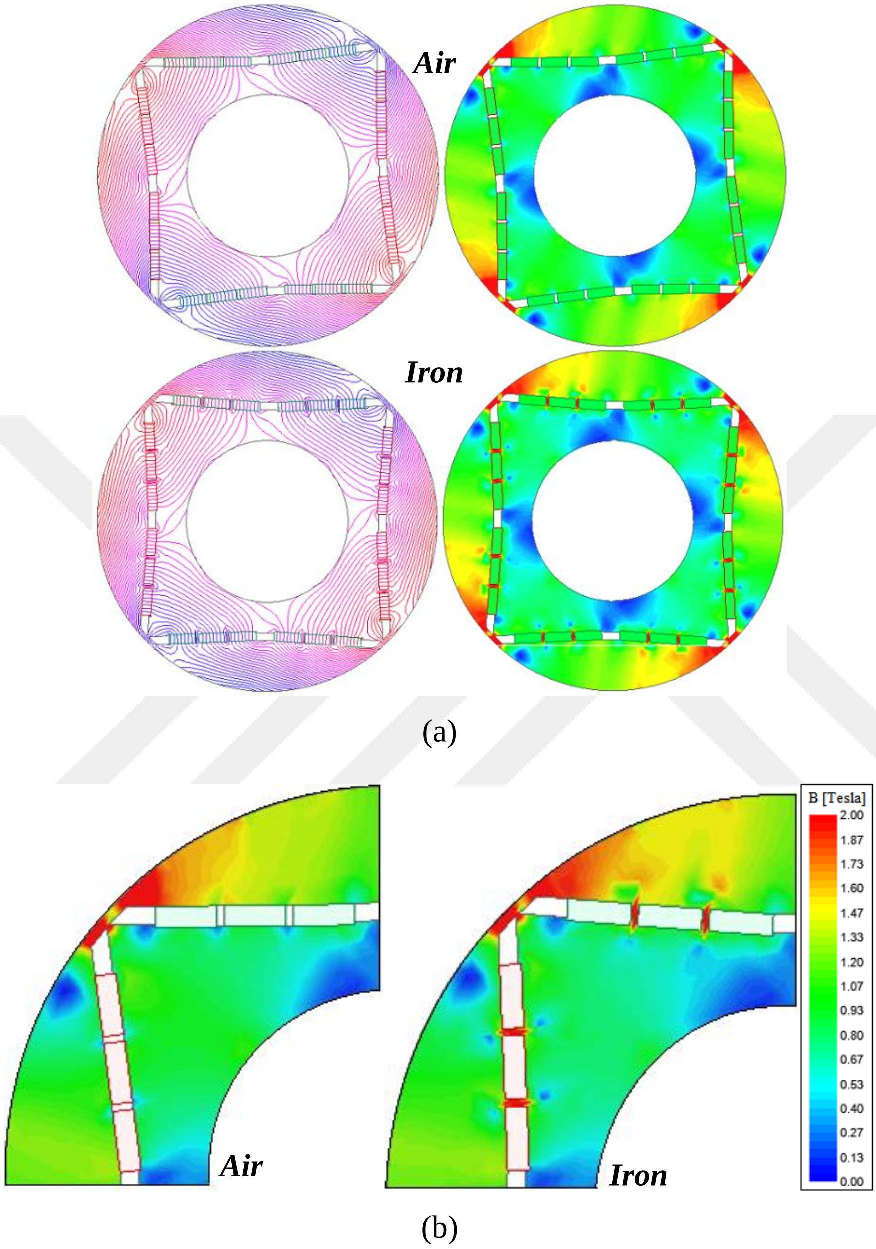


**Figure 6.27 :** Flux line and flux density distributions for rotor for both segmentation type: (a) Whole distributions, (b) Rotor core only flux density distributions.

In addition, as depicted in Figure 6.27, flux lines occurs on the segmentation bridges leading to an increase in flux leakage and a decrease in effective magnetic energy and consequently a decrease in PM torque component (see Figure 6.28(b)). Therefore, better FW performance characteristics can be achieved thanks to magnet segmentation with iron as shown in Figure 6.29. The variation of $\xi$ and $k_{FW}$, illustrated in Figure

6.30, verify that the magnet segmentation with air has a negative effect on FW ability while segmentation with iron has a positive effect. It is also revealed that with $N_{PM}$ increasing, $L_q$ increases (see Figure 6.31). However, $L_d$ increases until $N_{PM}$ becomes 2 and then it decreases back to its minimum once $N_{PM}$ becomes 3. Considering Figure 6.30, it can be deduced that the higher the $N_{PM}$, the lower the torque ripple percentage for both segmentation with air and iron.

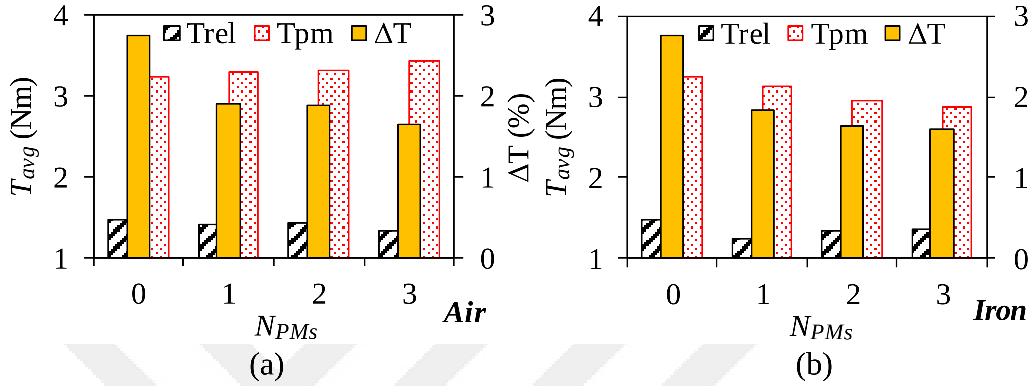


**Figure 6.28 :** Influence of $N_{PMs}$ on torque characteristics: (a) Air, (b) Iron.

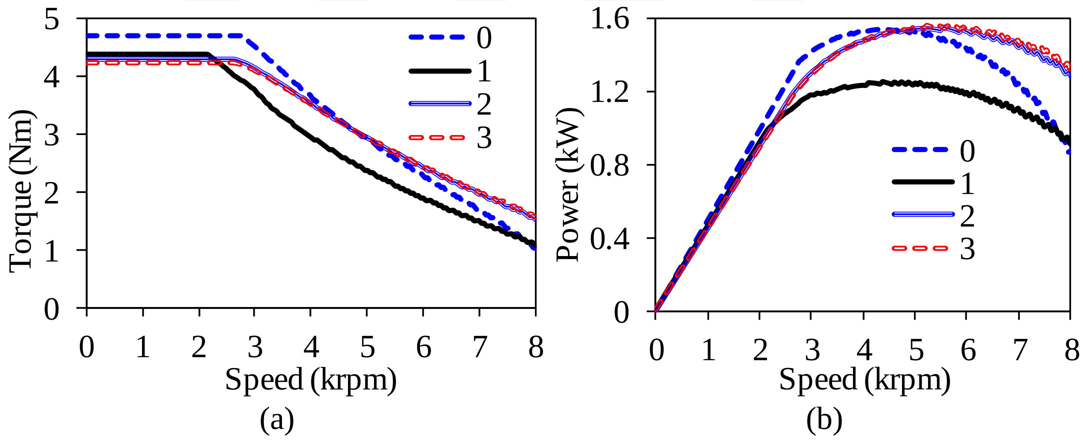


**Figure 6.29 :** Influecen of $N_{PMs}$with iron on FW characteristic: (a) Torque/speed, (b) Power/speed.

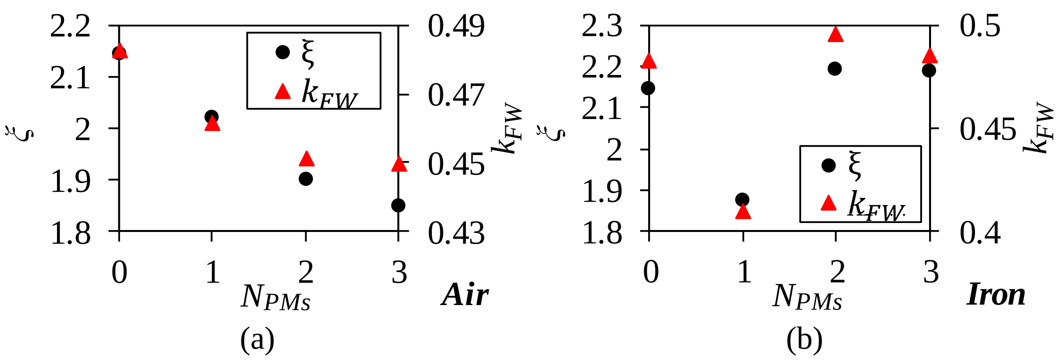


**Figure 6.30 :** Variation of $\xi$ and $k_{FW}$ with respect to $N_{PMs}$ with: (a) Air, (b) Iron.

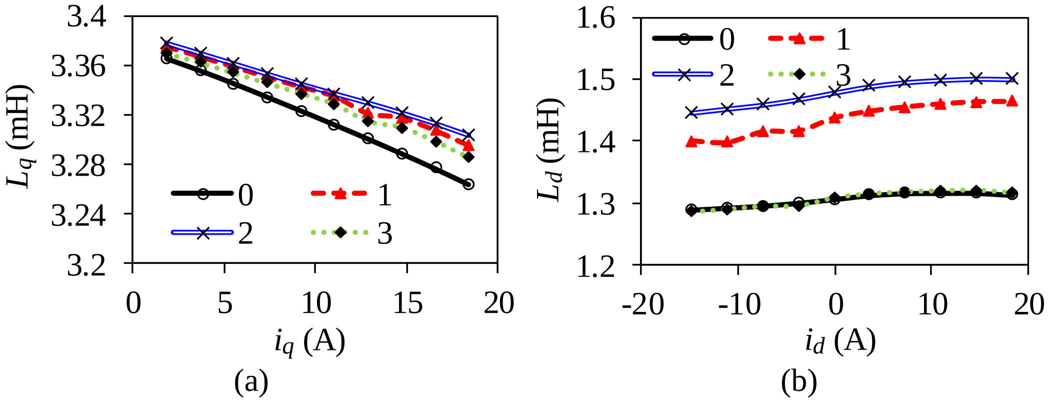


**Figure 6.31 :** Variation of inductance versus current characteristics for various $N_{PMs}$ parameters: (a) $L_q$ vs $i_a$, (b) $L_d$ vs $i_d$.

The influence of segmentation on PM loss due to the eddy current and core losses is also investigated and the obtained results are summarized in Table 6.1. As can be observed, the total and rotor core loss ($P_{core_T}$ and $P_{core_R}$, respectively) generally increase with $N_{PM}$ increasing in both air and iron segmentation cases. On the other hand, the PM loss $P_{PM}$ decreases as $N_{PM}$ increased.

**Table 6.1 :** Comparison of core and PM losses (mW).

| | $P_{core_T}$ | | $P_{core_R}$ | | $P_{PM}$ | |
|---|---|---|---|---|---|---|
| Seg# | **Air** | **Iron** | **Air** | **Iron** | **Air** | **Iron** |
| **0** | 1520 | | 100.13 | | 34.28 | |
| **1** | 1588 | 1600 | 103.4 | 106.4 | 28.67 | 33.91 |
| **2** | 1627 | 1518.2 | 105.3 | 104.1 | 26.32 | 32.2 |
| **3** | 1660 | 1520 | 107.3 | 103.747 | 24.72 | 30.73 |

### 6.3.9 Results Analysis and Discussion

The influence of design parameters on performance characteristics including, CS, maximum torque (MT), maximum power (MP), overall FW ability (FW) and torque ripple (ΔT), are investigated and compared in Table 6.2. It can be concluded that $N_s$, $l_s$, and $B_1$ have a significant effect on the FW ability while $O_1$ has a trivial effect. In addition, other parameters have a moderate effect on FW ability.

It has been revealed that the higher values of the considered design parameters result with lower CS, except for $l_s$ (Case#2). When compared to segmentation with air, the segmentation with iron results with better FW ability. It has also been revealed that performance characteristics at both low- and high-speed operating regions do not necessarily vary linearly with considered design parameters. Moreover, design parameters, except for $l_s$ (both cases) and $N_{PM}$ (Air), having better performance in low-speed region are typically in conflict with those that provide better flux-weakening capability in high-speed region.

**Table 6.2 :** Comparison of the influence of design parameters on performance characteristics.

| *Parameter* | **CS** | **MT** | **MP** | **FW** | **ΔT** |
|---|---|---|---|---|---|
| $N_s$ | $<$ | $>$ | $<$ | 4 | $-$ |
| $l_s$ (Case#1) | $<$ | $>$ | $>$ | 4 | $-$ |
| $l_s$ (Case#2) | $>$ | 0 | $>$ | 4 | $-$ |
| $O_1$ | $<$ | 0 | $<$ | 2 | $-$ |
| $O_2$ | $<$ | $<$ | $<$ | 3 | $<$ |
| $R_{ib}$ | $<$ | $>$ | $<$ | 3 | $\nexists, 4$ |
| $B_1$ | $<$ | $>$ | $<$ | 4 | $>$ |
| $N_{PM}$ (Air) | $<$ | 0 | 0 | 3 | $>$ |
| $N_{PM}$ (Iron) | $<$ | $<$ | $\nexists, 3$ | 3 | $>$ |

**Key**-$>$ :The higher the better. $<$ :The lower the better.$\nexists$: No direct correlation. 0: None. 1: Negligible. 2: Slight. 3: Moderate. 4: Significant.

### 6.4 Conclusion

A systematic analysis on the sole impact of key design parameters, including number of turns, stack length, and six geometric rotor parameters, on the FW ability of NSW IPM for EV applications is presented in this paper. It has been revealed that $N_s$, $l_s$ (both cases), and $B_1$ have a significant effect on the FW ability while $O_1$ has a trivial effect. In addition, $R_{ib}$, $O_2$, and $N_{pm}$ (both cases) have a moderate effect on FW capability. To expose the correlation between the FW capability and$O_2$ parameter, variation of electromagnetic torque components, namely $T_{rel}$ and $T_{pm}$, and inductance components are investigated together with $k_{FW}$ and $\xi$ ratios. In this way, the influence of the considered design parameter on constant-power speed range is predicted at base speed. Furthermore, except for $l_s$ (both cases) and $N_{PM}$ (Air), design parameters that provide better performance in low-speed regions usually conflict with those that have better flux-weakening ability in high-speed regions. Certain findings achieved in this study are specified in Table 6.2.

# 7. EXPERIMENTAL VALIDATIONS

## 7.1 Model and Analysis of Prototyped NSW IPM

To validate the numerical and analytical calculations presented in this thesis, a globally optimized NSW IPM prototype having the specifications given in Table A.1 (NSW-SD) is manufactured. The FEA model of the NSW IPM machine is depicted in Figure 7.1.

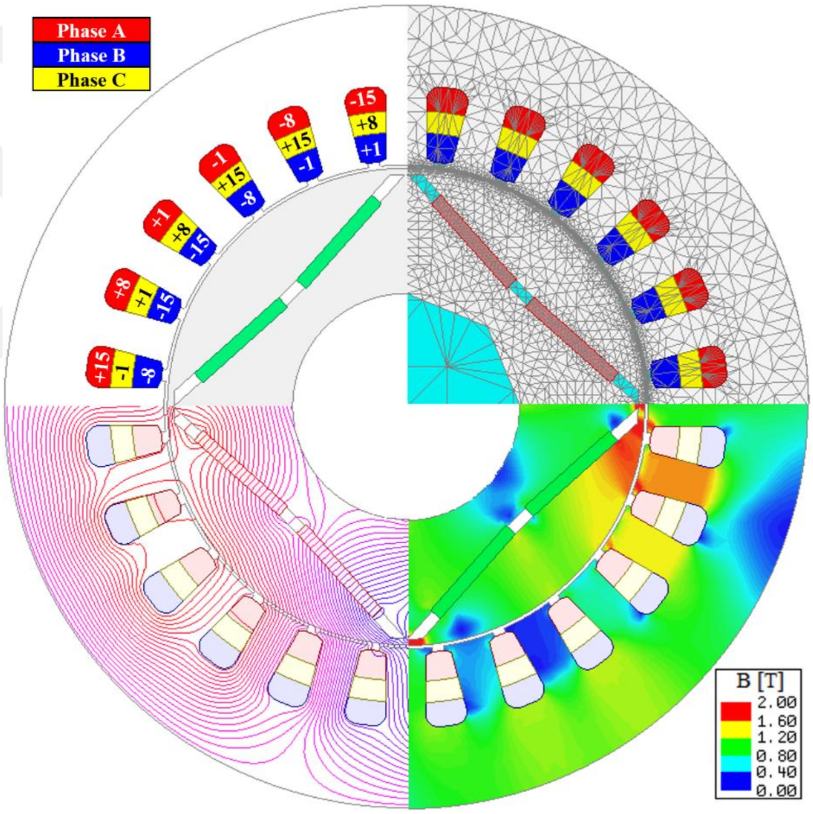


**Figure 7.1 :** FEA Model of prototyped NSW IPM Machine.

## 7.2 Model and Analysis of Prototyped NSW IPM Prototype

The photos of the fabricated prototype and experimental setup are illustrated in Figure 7.2. Performed no-load, full-load, and FW test results are presented as follows. Figure 7.1(a) shows the axial length of the end-winding of the stator, Figure 7.1(b) and (c) shows the whole stator and rotor components, respectively. The established test rig based on the assembled prototype is shown in Figure 7.2.

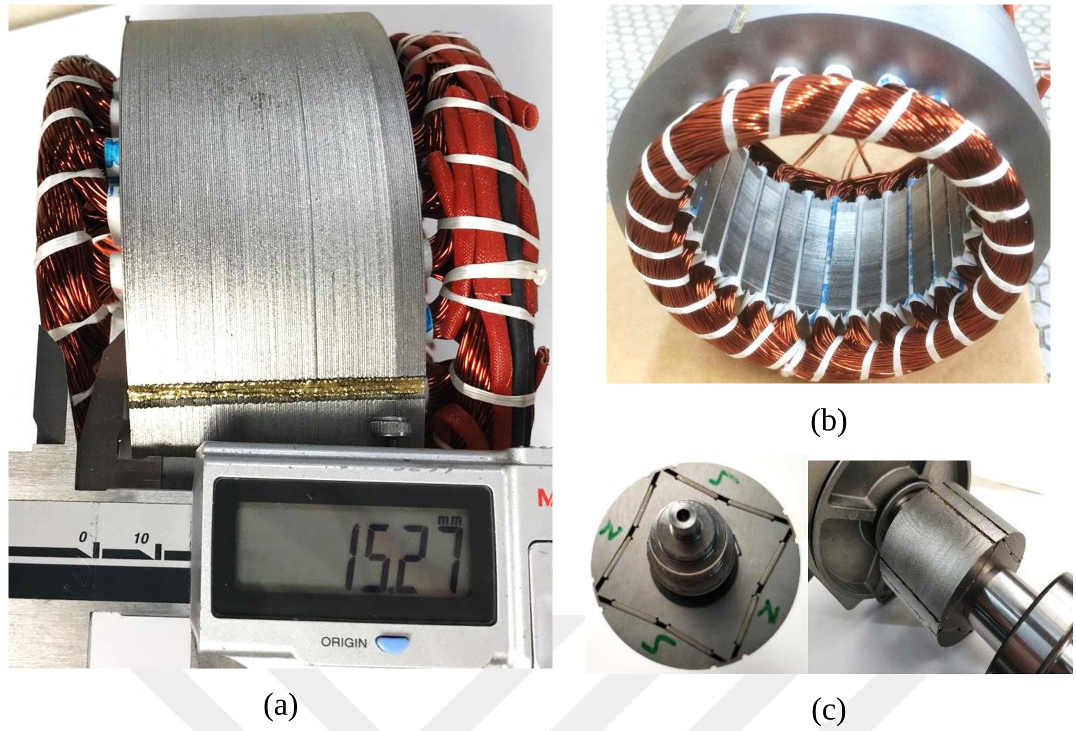


**Figure 7.2 :** Machine constructions: Radial view of Stator with NSWs: end-winding axial length measurement with digital calliper, (b) Axial view of Stator with NSWs, (c) IPM rotor.

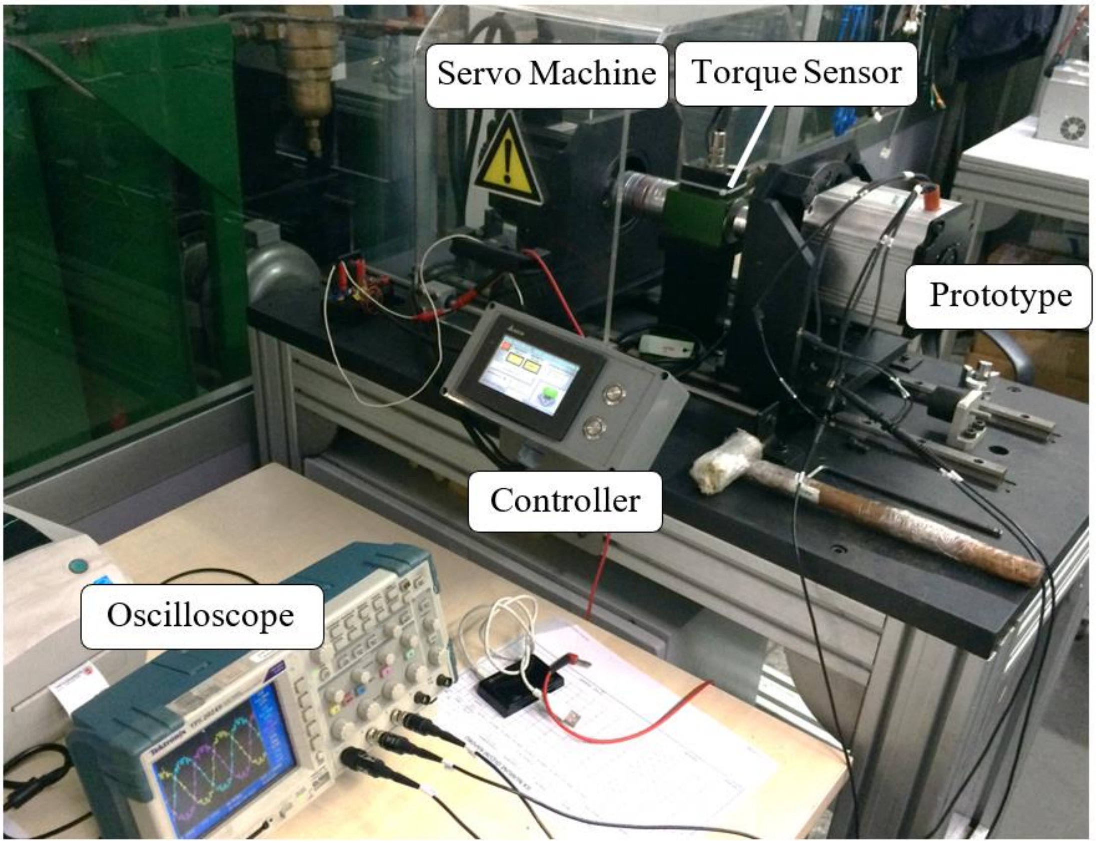


**Figure 7.3 :** Experimental setup (test rig components).

The averaged phase resistance is measured and calculated as 0.101Ω with 0.515 slot fill factor and the one side axial length of the end-winding is calculated as 16.11mm. However, as seen in Figure 7.1(a) it is measured as 15.27mm. This small difference is occurred as a result of not considering the packing of the end-winding in the analytical calculations.

The no-load back-EMF is measured for various rotor speeds ranging from 0.4krpm to 3krpm and the obtained waveforms and variation of the fundamental amplitude are illustrated in Figure 7.3(a) and (b), respectively. In addition, the harmonic specrums of the no-load back-EMFs measured at 0.4krpm and 1.5krpm and the obtained waveforms and their harmonic spectra are shown in Figure 7.4. As clearly seen, the measured back-EMFs agree well with the 2-D FEA predicted results. Note that owing to the end-effects, manufacturing imperfections, and fabrication tolerance such as inconsistent magnetization of PMs, the experimental results are somewhat lower than that of the 2-D FEA predicted results. As clearly seen, the measured back-EMF agrees well with the 2-D FEA predicted results.

The electric current loading test of the prototype has also been conducted and the measured and predicted torque and efficiency curves agree well as illustrated in Figure 7.4. Since no cooling equipment is installed for the prototype machine, it is loaded up to 2.5 times of its nominal current via very short period operating. Note that the current density is 5.96 A/mm$^2$ for nominal operating condition. In addition, it has also been demonstrated that although the prototype is loaded up to 2.5 times of its rated current, no sign of irreversible magnet demagnetization is observed.

As seen in Figure 7.4, torque increases almost linear as the current increases whereas the efficiency decreases. This is because the stator copper loss increases significantly from 0.0032kW to 0.32kW with the excitation from 6.5A to 65A. In addition, verification of the power factor $\cos\varphi$ at 0.4krpm for various phase current injection (Apeak) is given in Table 7.1. The measured $\cos\varphi$ agrees well with the 2-D FEA predicted results.

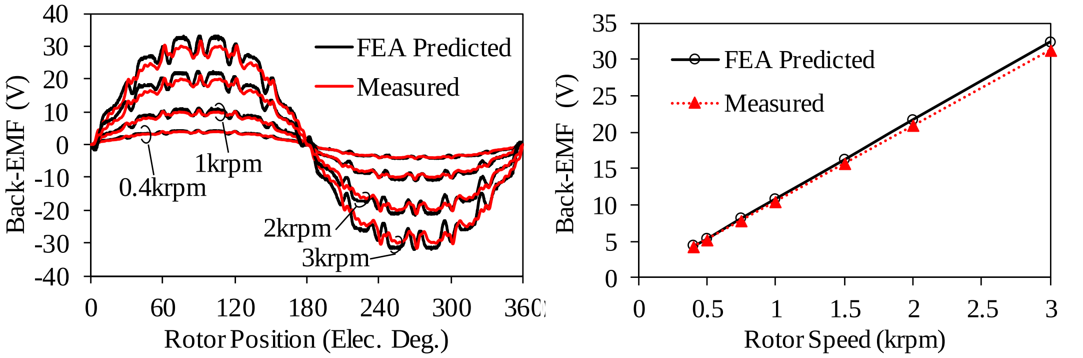


(a) (b)

**Figure 7.4 :** Verification of Back-EMF: (a) waveforms for various rotor speeds, (b) variation of fundamental Back-EMF amplitude with rotor speed.

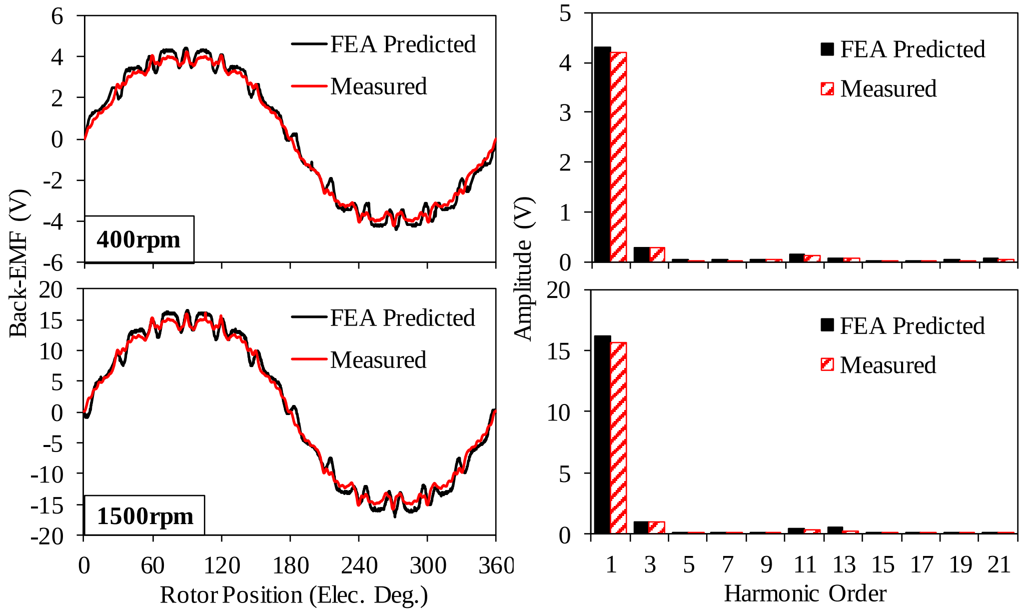


(a) (b)

**Figure 7.5 :** Comparison of predicted and measured Back-EMF: (a) waveforms for different rotor speeds, (b) harmonic spectra of back-EMF waveforms.

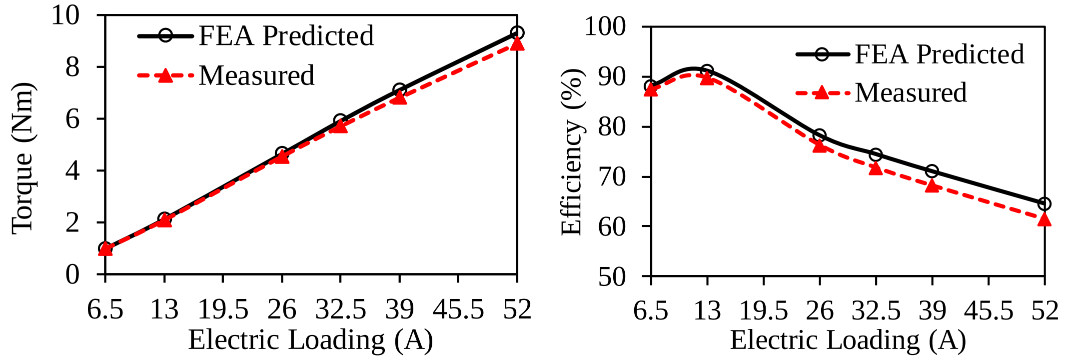


(a) (b)

**Figure 7.6 :** Torque and efficiency $\eta$ against current at 0.4krpm.

**Table 7.1 :** Verification of power factor cos $\varphi$ at 0.4krpm.

| *Is (A)* | *FEA* | *Meas.* | *Is (A)* | *FEA* | *Meas.* |
|---|---|---|---|---|---|
| **6.5** | 0.75 | 0.71 | **26** | 0.67 | 0.64 |
| **13** | 0.71 | 0.68 | **52** | 0.56 | 0.53 |

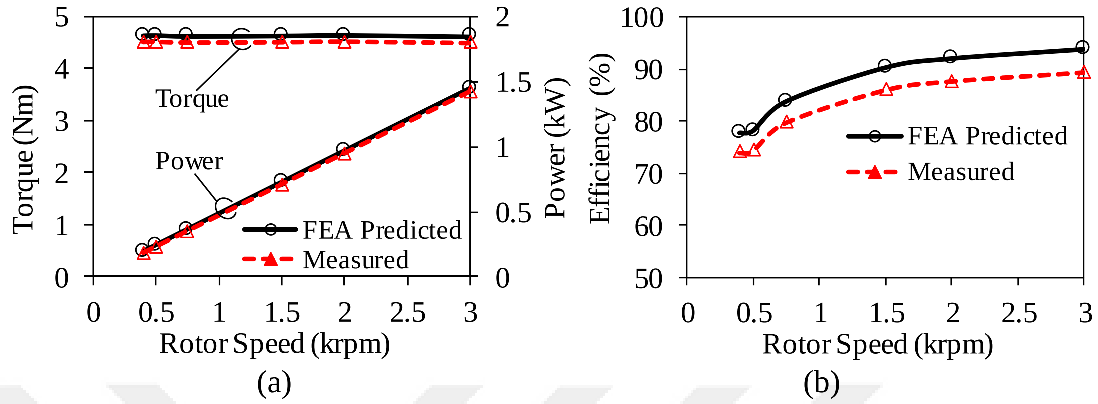


**Figure 7.7 :** Comparison of predicted and measured torque/speed characteristics with simple v/f drive: (a) torque and power vs rotor speed, (b) efficiency vs rotor speed.

In order to conduct the torque-speed curve with simple v/f drive, the inverter having 48Vdc (max) and 30A (peak) has been employed. Note that no control/flux-weakening algorithm could been employed at this stage. The obtained torque/power-speed and efficiency curves at the constant torque operating region only have been illustrated in Figure 7.6. It can be seen that the FEA predicted results agree well with the measurements. Note that owing to the end-effects, manufacturing imperfections and fabrication tolerance, the experimental results are somewhat lower than that of the 2-D FEA predicted results.

### 7.3 No-Load Operating Test

The averaged phase resistance is calculated and measured as ~0.1Ω with 51.5% slot fill factor for 3-layer windings. The coil conductors having 0.7mm diameter with 4 stranded wires (0.7mmx4) have been used in the stator. The coils have been created as to be identical by using winding wheel and assembled as to be started from the yoke side of stator. One side axial length of the end-winding is calculated as 16.11mm and it is measured as 15.27mm (see Fig. 25(b)). Difference with 0.84mm is occurred as a result of not considering the inevitable bending and peening of the end-winding in the analytical calculations. The no-load back-EMF is measured for 0.4krpm and 1.5krpm and the obtained waveforms and harmonic spectra are illustrated in Figure 7.5. Note that owing to the end-effects, manufacturing imperfections, and fabrication tolerance such as inconsistent magnetization of PMs, the experimental results are lower than that of the 2-D FEA predicted results. As clearly seen, the measured back-EMF agrees well with the 2-D FEA predicted results.

### 7.4 Electric Loading Test

The electric loading test of the prototype has also been conducted and the measured and predicted torque and efficiency curves agree well as illustrated in Figure 7.6. Since no additional cooling equipment except for the cooling frame is installed for the prototype machine, it is loaded up to 2.5 times of its nominal current via very short period operating. Note that the current density is 5.96 A/mm2 for nominal operating condition. As seen in Fig. 27, torque increases almost linear as the current increases whereas the efficiency decreases. This is because the stator copper loss increases significantly from 0.0032kW to 0.32kW with the excitation from 6.5A to 65A.

### 7.5 Constant Torque Operating Test

Constant torque operating test has been conducted with inverter limits with 48Vrms and 21Arms. The obtained torque/power-speed and efficiency curves at the constant torque operating region have been illustrated in Figure 7.3. It has been deduced that the FEA predicted results agree well with the measurements.

### 7.6 Flux-Weakening Test

The FW test has been conducted with inverter having the limits of 48Vrms and 18.5Arms and mechanical coupling limit of 6krpm. The predicted and measured torque-speed and power-speed curves have been illustrated in Figure 7.8. As shown in the figure, the MTPA control strategy is adopted below the corner speed while the FW control is used to control the current vector when the speed exceeds the corner speed. FW attempts to use the optimal phase current amplitude to provide the highest torque within the voltage limit imposed by the inverter at any given speed. The predicted and measured efficiency versus speed curves are compared in Figure 7.9. As predicted in Section 5.1 (see Figure 7.10(d)), the maximum efficiency is achieved between 2–5krpm speed range. It has been deduced that the FEA predicted FW performance results agree well with the measurements. The experimental measurements verify at least one predicted FW performance given in Chapter 6.4, where a range of design parameters covering also the optimal values are calculated.

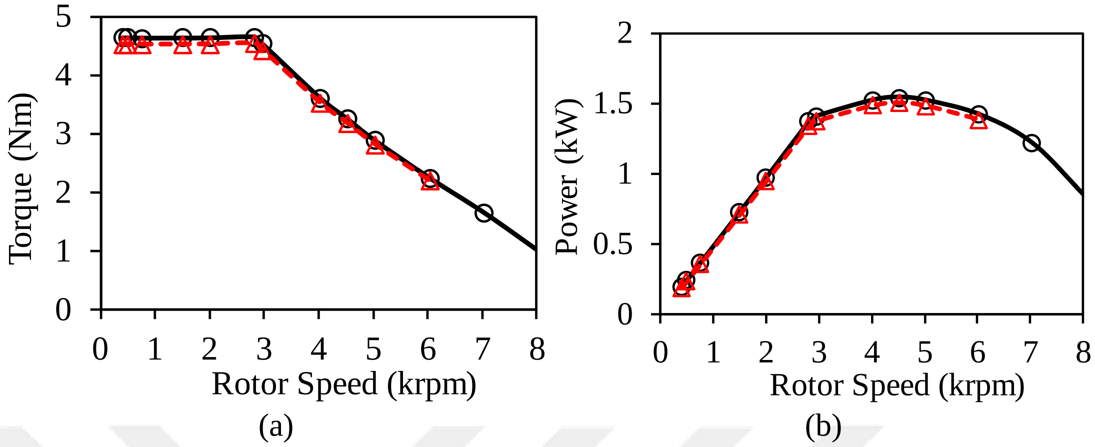


**Figure 7.8 :** Comparison of predicted and measured torque/speed characteristics with simple v/f drive: (a) torque and power vs rotor speed, (b) efficiency vs rotor speed.

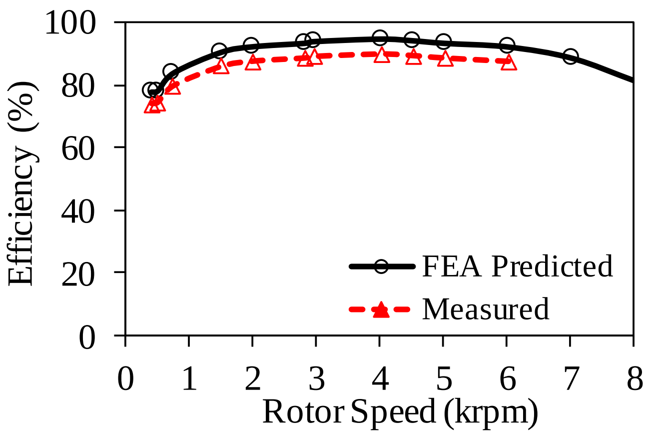


**Figure 7.9 :** Comparison of predicted and measured efficiency-speed characteristic.

Note that although the FW ability of NSW IPM machine with segmented magnets is better, rotor with unsegmented V-shaped magnets are used due to the manufacturing difficulties and material shortage in prototyping stage.

The electromagnetic performance characteristics, including *dq*-axis flux linkage, power loss coefficient, *dq*-axis excitation current matrices, etc, have been calculated under steady-state simulations and the obtained matrices are adapted into the FW algorithm presented in Chapter 6.

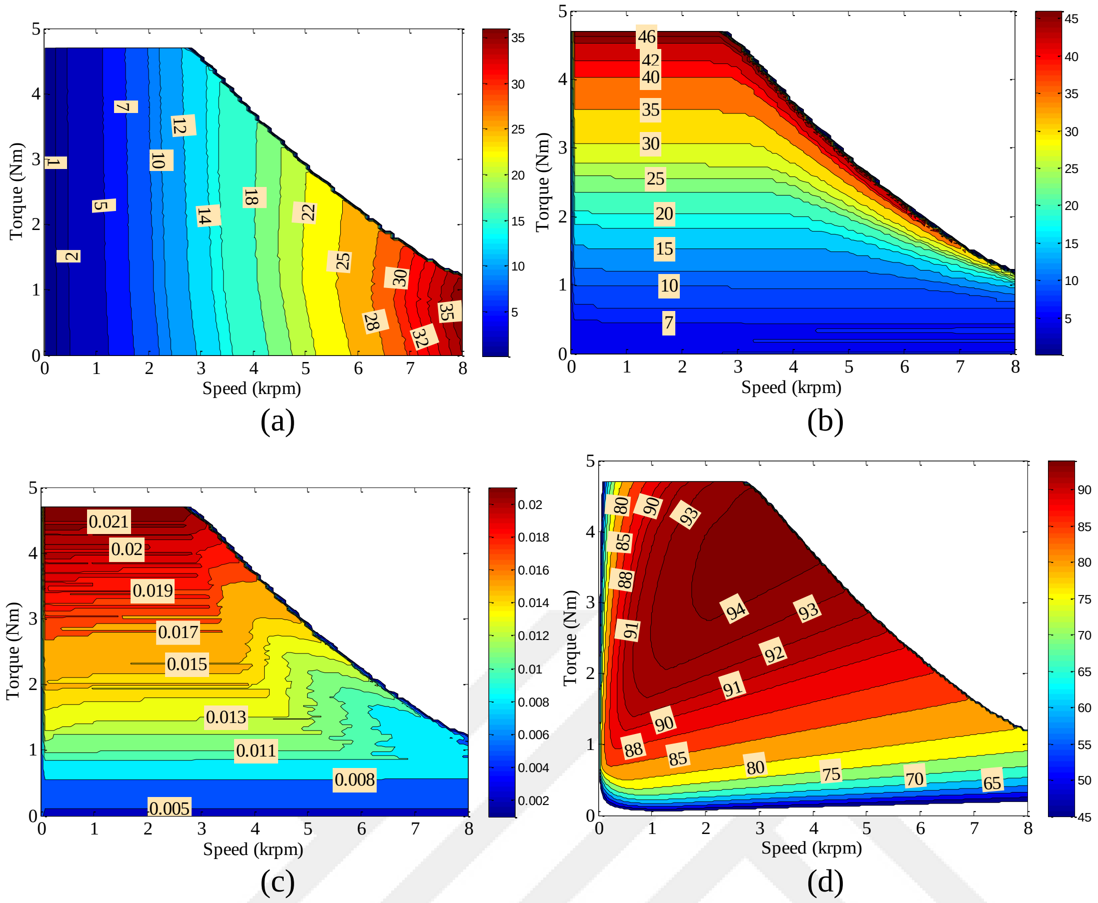


**Figure 7.10 :** Power losses and efficiency maps.

Contours: *(W), $^{\mathbb{W}}$(%) **(a)** $P_{core}{}^{*}$, **(b)** $P_{cu}{}^{*}$, **(c)** $P_{pm}{}^{*}$, **(d)** $\eta_P{}^{\mathbb{W}}$.

Consequently, the FW algorithm, determining the MTPA for each excitation current matrices, is employed and the FW characteristics, including power losses and efficiency maps, illustrated in Figure 7.10 are achieved. In this study, the predicted efficiency $\eta_P$ of each case is calculated with (7.1),

$$\eta_P = \frac{P_{out}}{P_{out} + P_{cu} + P_{pm} + P_{core} + P_{add}} \times 100 \tag{7.1}$$

where $P_{out}$, $P_{core}$, $P_{cu}$, $P_{add}$ are output power, core loss, copper loss, PM loss due to the eddy currents induced in PMs, and additional losses, respectively. Details about the power loss calculations of the IPM machines having NSWs can be found in Chapter 4. As expected, $P_{core}$ increase with speed increasing while the $P_{cu}$and $P_{pm}$ increase with excitation current and hence torque increasing. On the other hand, as a consequence of adopting of FW algorithm, the copper loss increases as a result of increasing current value generated under the same electromagnetic torque. The efficiency map in Figure 7.10(d) represents the steady-state efficiency characteristics of the NSW IPM machine for efficiencies above 45% with a DC link voltage of 48V. The peak efficiency is 94% between about 2krpm and 4.5krpm and efficiencies above 85% are spread over a large area of the operation region.

# 8. CONCLUSIONS AND FUTURE WORK

## 8.1 Conclusions

This thesis mainly investigates a novel winding topology characterized with low MMF harmonic content and short end-winding length. Firstly, the current state-of-the-art of the MMF harmonic reduction techniques for FSCW configurations, including multilayer winding with phase shift, different number of turns per coil side (uneven turn numbers per coil side) and stator flux barriers are investigated. Secondly, a novel winding topology having significantly short end-windings compared to ISDWs and substantially low MMF harmonics compared to FSCWs is developed. For the purpose of establishing the best values of the winding parameters, including the winding layer number, turn number combinations, and S/P combinations, their influences on air-gap flux density and torque characteristics have been examined parametrically. In addition, the proposed winding topology has been implemented into the IPM machines having large and small dimensions. Thirdly, the effectiveness of the proposed winding topology for different machine technologies, namely; IPM, SnyRM, PMaSynRM, and DSRM have been studied by considering the influence of designing with different winding topologies as well. Fourthly, a systematic design optimization method, consisting of a combination of individual and global optimization methods, for IPM machines with NSWs having large and small dimensions is developed. Finally, the FW capability of IPM machine having NSWs is investigated with a particular emphasis on the influence of key design parameters, including the number of turns, stack length, and six geometric rotor parameters, on the FW ability is investigated. The general findings and conclusions drawn from the research demonstrated in thesis are detailed chapter by chapter as follows.

*Chapter 2*

A comprehensive comparative study on the electromagnetic performance characteristics between IPM machines designed with the ISDW technique and the FSCW technique combined with one/some of the used methods has been conducted. In addition, thermal analyses have also been conducted by using the total loss distributions of the IPM machines. In this chapter, the obtained key findings can be summarized as follows.

- The FSCW technique cause a dramatic increase in the eddy losses including the rotor core and PM losses.
- Since the FSCW technique causes a substantially increased leakage flux density, it generates lower averaged torque than its ISDW counterpart.
- Adopting the multilayer winding configuration increases the complexity of the winding structure and causes to obtain lower fundamental winding factor and consequently low torque production capability.
- Adopting the uneven number of turns per coil causes a decrease in the average torque and a slightly decrease in PM loss, but it also leads an increase in the efficiency. In addition, it also causes to less effective utilization of the slots.
- Adopting multilayer and phase-shifting method and using flux barriers on the stator is not favourable in terms of average torque, output power, and efficiency.
- It has been shown that the considered MMF reduction methods have very limited effect on the MMF harmonics of the chosen 12S/8P combination, which has no subharmonics.
- It has been revealed that since the large amount of MMF harmonics of the FSCWs cause a significant increase in the total losses, the temperature of the magnets is quite higher under the same operating condition. In addition, it has also shown that reduction of the number of stator slots causes a remarkable reduction at the heat dissipation area of the windings.
- The IPM machines equipped with FSCWs require more cooling equipment.

*Chapter 3*

The developed winding topology has been implemented into the IPM machines in large and small power applications and the key performance characteristics have been comprehensively compared with other IPM machines equiepped with ISDWs and FSCWs. In this chapter, the obtained key findings are specified as follows.

- It has been validated that thanks to the proposed NSW topology, the end-winding lengths can be successfully shortened without increasing the MMF harmonic content.
- The proposed NSWs do not require a special stator slot geometry. They can be implemented into the stator of any existing electrical machine with ISDWs.
- The MMF distortion level of the proposed NSW is ~80% lower than that of the FSCW.
- The main drawback of the NSW topology is that because of the semi-overlapping windings it is not very suitable for automated manufacturing with today's technology.
- Another disadvantage is that the high winding layer (3L) structure of NSW causes a reduction in the copper fill factor due to the increase in the additional insulation between layers of different phase windings.
- Under the same output power operating, the NSW IPM machine has 4.27% higher efficiency and ~18.7% shorter axial length than its ISDW DL counterpart.
- The torque ripple level of the IPM machine with NSWs is the same as its ISDW counterpart.
- It has been revealed that for the IPM rotor, the FSCW topology is not feasible for large power applications because of its quite large amount of PM loss component.
- The poor power factor of electrical machines can be significantly improved with extended stack length.
- The numerical studies on developing more compact IPMs with improved performance have been successfully verified by the experiments.

*Chapter 4*

Severeal combinations of different rotor and winding topologies have been designed and the obtained electromagnetic performance results have been compared comprehensively and the obtained key findings are summarised as follows.

- It is validated that the electromagnetic performance characteristics of the IPM, SynRM, PMaSynRM, and DSRM with the proposed NSW topology are comparable to design with ISDW and FSCW topologies.
- Implementation of NSWs into the considered machine technologies results with:
    - Significantly improved efficiency over ISDWs.
    - Substantially shortened end-winding axial and radial lengths over ISDWs.
    - Lower rotor losses, particularly PM losses over ISDWs and FSCWs.
    - Lower risk of irreversible demagnetisation of PMs over ISDWs and FSCWs.
    - Higher torque density over ISDWs and FSCW for all reluctance machines.
    - Higher output power over FSCWs for all reluctance machines.
- Since the lower winding factor is compensated by higher reluctance torque component of NSWs, it does not require a greater number of turns compared to FSCWs.
- The highest torque/power density can be achieved by utilising IPM rotor.

*Chapter 5*

In order to determine the optimization parameters and constrains for reaching the optimal solution quickly, sensitivity analyses have been conducted. The most dominant parameters effecting the electromagnetic torque, copper loss, and torque ripple have been determined. Furthermore, optimization parameters and objectives and their weights have been justified for multi-objective global optimization of NSW IPM. Moreover, a comprehensive electromagnetic performance comparison between original (Toyota Prius 2010 IPM having ISDWs), initial (having NSWs), and globally optimized (having NSW) designs have been presented. The key findings obtained successfully within the framework are summarized as follows.

- It has been revealed that among a large number of design parameters, split ratio, stator tooth width ratio bs, stator slot height, rotor outer bridge width between flux barriers, rotor inner bridge radius, flux barrier thickness, rotor inner bridge width between flux barriers, height of flux barriers, magnetwidth, and magnet thickness have been determined as the most dominant geometric parameters effecting the average torque.

- Stator slot opening width ratio, stator slot opening height ratio, rotor outer bridge width between flux barriers, and rotor inner bridge radius parameters have been determined as the most dominant geometric parameters effecting the torque ripple rate.
- Thanks to the global optimization, time-averaged torque and output power are increased by 8.6%, torque ripple is decreased by 21.32%, and the efficiency is increased by 1.45% according to initial design.
- The reliability and effectiveness of the proposed optimization approach is validated over large and small IPM machines.

*Chapter 6*

The FW capability of IPM machine with NSWs and the influence of design parameters on performance characteristics including, corner speed, maximum torque, maximum power, overall FW ability and torque ripple, are investigated and compared in this chapter. The key findings of this study have been summarized as follows.

- It has been revealed that number of tursn, stack length, and width of main magnetic bridge have a significant effect on the FW ability while distance between V-shape magnets has a trivial effect.
- The radius between Λ magnets, distance between shaft and V-shape magnets, and number of magnet segmets have a moderate effect on FW capability.
- It is found that except for stack length and number of segment parameters, design parameters that provide better performance in low-speed regions usually conflict with those that have better FW ability in high-speed regions.

### 8.2 Future Work

Although several research on single-excited synchronous machines having NSWs have been carried out in this thesis, there are still potential directions for developing this study furher, such as:

- It is planned to study on the improvement of IPM machines by using the several different other methods summarized as follows.

- ❖ Investigation of different S/P combinations having both subharmonics and superharmonics (i.e. 9S/8P);
- ❖ Influence of considered MMF reduction methods on the electric loading capability of the IPM machines;
- ❖ Improvement of reluctance torque by optimizing the rotor's design parameters (number and shape of flux barriers, PM diamensions and positions, etc.);
- ❖ Investigation of magnet shape optimization (PM layers, dimension, angles, etc);
- ❖ Investigation of different rotor topologies (U-shape, V-Shape, W-shape, etc.).

- Feasibility analyses of implementing proposed NSW topology into the other machine technologies including the induction machines and machines having outer rotor structures.
- Investigation of the interaction among design parameters (crosseffects between design variables) and feasibility analyses of employing NSW topology into the PMSMs with outer rotors.
- Anayses of thermal, mechanical stress, and fault diagnosis of IPM machine designed with the proposed NSW topology.
- Electromagnetic field and performance analysis of IPM machine designed with the proposed NSW topology by 3-D FEA.

## REFERENCES


[1] **URL-1** *<https://www.globalelectricity.org/content/uploads/New-electricity-frontiers-report.pdf>*, date retrieved 12.12.2020.

[2] **URL-2** *<https://www.tr.undp.org/content/turkey/en/home/projects/promoting-energy-efficient-motors-in-small-and-medium-sized-ente.html>*, date retrieved 12.12.2020.

[3] **BP Statistical Review of World Energy: 2020, 69th ed.** (2020). *<https://www.bp.com/content/dam/bp/business-sites/en/global/corporate/pdfs/energy-economics/statistical-review/bp-stats-review-2020-full-report.pdf>, British Petroleum 2020*.

[4] **BP Energy Outlook: 2020 ed.** (2020). *<https://www.bp.com/en/global/corporate/energy-economics/energy-outlook.html>, British Petroleum 2020*.

[5] **Liu, X., Chen, H., Zhao, J., and Belahcen, A.** (2016). Research on the performances and parameters of interior PMSM used for electric vehicles, *IEEE Trans. Ind. Electron., 63*(6), 3533–3545.

[6] **Pellegrino, G., Vagati, A., Guglielmi, P., and Boazzo, B.** (2012). Performance comparison between surface-mounted and interior PM motor drives for electric vehicle application, *IEEE Trans. Ind. Electron., 59*(2), 803–811.

[7] **Chau, K., Chan, C., and Liu, C.** (2008). Overview of permanent-magnet brushless drives for electric and hybrid electric vehicles, *IEEE Trans. Ind. Electron., 55*(6), 2246–2257.

[8] **Wang, Y., Ho, S.L., Fu, W.N., and Shen, J.X.** (2012). A novel brushless doubly fed generator for wind power generation, *IEEE Trans. Magn., 48*(11), 4172–4175.

[9] **Cheng, M., Sun, L., Buja, G., and Song, L.** (2015). Advanced electrical machines and machine-based systems for electric and hybrid vehicles, *Energies, 8*(9), 9541–9564.

[10] **Villani, M., Tursini, M., Fabri, G., and Castellini, L.** (2012). High reliability permanent magnet brushless motor drive for aircraft application, *IEEE Trans. Ind. Electron., 59*(5), 2073–2081.

[11] **Cheng, M., and Zhu, Y.** (2014). The state of the art of wind energy conversion systems and technologies: A review, *Energy Convers. Manage., 88*, 332–347.

[12] **Zhu, Z.Q., and Howe, D.** (2007). Electrical machines and drives for electric, hybrid, and fuel cell vehicles, *Proc. IEEE, **95***(4), 746–765.

[13] **Chan, C.C.** (2002). The state of the art of electric and hybrid vehicles, *Proc. IEEE, **90***(2), 247–275.

[14] **Yimin, G., Ehsani, M., and Miller, J.M.** (2005). Hybrid electric vehicle: overview and state of the art, *Proc. IEEE Int. Symp. Ind. Electron. (ISIE'05)*, 307–316.

[15] **Zeraoulia, M., Benbouzid, M.E.H., and Diallo, D.** (2006). Electric motor drive selection issues for hev propulsion systems: A comparative study, *IEEE Trans. Veh. Technol.*, *55*(6), 1756–1764.

[16] **Chan, C.C., Bouscayrol, A., and Chen, K.** (2010). Electric, hybrid, and fuel-cell vehicles: Architectures and modeling, *IEEE Trans. Veh. Technol.*, ***59***(2), 589–598.

[17] **Xue, P. and Lin, J.** (2011). Discussion on the rare earth resources and its development potential of Inner Mongolia of China, *Int. Conf. Mater. Renew. Energy Envir.*, 9–12.

[18] **Santiago, J.d., *et al.*** (2012). Electrical motor drivelines in commercial all-electric vehicles: A review, *IEEE Trans. Veh. Technol.*, *61*(2), 475–484.

[19] **El-Refaie, A.M.** (2013). Motors/generators for traction/propulsion applications: A review, *IEEE Trans. Veh. Technol.*, *8*(1), 90–99.

[20] **Estenlund, S., Alaküla, M., and Reinap, A.** (2016). PM-less machine topologies for EV traction: A literature review, *Int. Conf. Elect. Syst. Aircraft Railway Ship Propuls. Road Veh. Int. Transport. Electrif. Conf. (ESARS-ITEC)*, 1–6.

[21] **Shihua, W., Likun, T., and Shumei, C.** (2008). A comparative study of the interior permanent magnet electrical machines rotor configurations for a single shaft hybrid electric bus, *IEEE Veh. Power Propul. Conf. (VPPC'08)*, 1–4.

[22] **Wang, A., Jia, Y., and Soong, W.L.** (2011). Comparison of five topologies for an interior permanent-magnet machine for a hybrid electric vehicle, *IEEE Trans. Magn.*, *47*(10), 3606–3609.

[23] **Yang, Z., Shang, F., Brown, I.P., and Krishnamurthy, M.** (2015). Comparative study of interior permanent magnet, induction, and switched reluctance motor drives for EV and HEV applications, *IEEE Trans. Transport. Electrif.*, *1*(2), 245–254.

[24] **Bowers, B.** (1975). The early history of electric motor, *Philips Tech Review*, *35*(4), 77–95.

[25] **Hofer, M. and Schrödl, M.** (2020). Investigation of permanent magnet assisted synchronous reluctance machines for traction drives in high power flux weakening operation, *IEEE Transport. Electrific. Conf. Expo (ITEC)*, 335–339.

[26] **Vetuschi, M. and Cupertino, F.** (2015). Minimization of proximity losses in electrical machines with tooth- wound coils, *IEEE Trans. Ind. Appl.*, *51*(4), 3068–3076.

[27] **Bauer, D., Mamuschkin, P., Reuss, H., and Nolle, E.** (2015). Influence of parallel wire placement on the AC copper losses in electrical machines, *IEEE Int. Elect. Mach. Drives Conf. (IEMDC'15)*, 1247–1253.

[28] **EL-Refaie, A.M.** (2010). Fractional-slot concentrated windings synchronous permanent magnet machines: opportunities and challenges, *IEEE Trans. Ind. Electron.*, *57*(1), 107–121.

[29] **Mellor, P., Wrobel, R., and Simpson, N.** (2014). AC losses in high frequency electrical machine windings formed from large section conductors, *IEEE Energy Convers. Cong. Expo. (ECCE'14*), 5563–5570.

[30] **Popescu M. and Dorrell, D.G.** (2013). Proximity losses in the windings of high speed brushless permanent magnet AC motors with single tooth windings and parallel paths, *IEEE Trans. Magn.*, *49*(7), 3913–3916.

[31] **Gyselinck, J., *et al.***, (2010). Homogenization of form-wound windings in frequency and time domain finite-element modeling of electrical machines, *IEEE Trans. Magn.*, *46*(8), 2852–2855.

[32] **Sullivan, C.R.** (1999). Optimal choice for number of strands in a litz-wire transformer winding, *IEEE Trans. Power Electron.*, vol. 14, no. 2, 283–291.

[33] **Thang, X. and Sullivan, C.R.** (2003). Stranded wire with uninsulated strands as a low-cost alternative to litz wire, *IEEE Annual Conf. Power Electron. Special., (PESC'03)*, 289–295.

[34] **Hämäläinen, H., Pyrhönen, J., Nerg, J., and Talvitie, J.** (2014). AC resistance factor of litz-wire windings used in low-voltage high-power generators, *IEEE Trans. Ind. Electron.*, *61*(2), 693–700.

[35] **Nan, X. and Sullivan, C.R.** (2009). An equivalent complex permeability model for litz-wire windings, *IEEE Trans. Ind. Appl.*, *45*(2), 854–860.

[36] **Reddy, P.B., Jahns, T.M., and Bohn, T.P.,** (2009). Transposition effects on bundle proximity losses in high-speed PM machines, *IEEE Energy Convers. Cong. Expo. (ECCE'09)*, 1919–1926.

[37] **Geest, M., Polinder, H., Ferreira, J.A., and Zeilstra, D.** (2014). Current sharing analysis of parallel strands in low-voltage high-speed machines, *IEEE Trans. Ind. Electron*., *61*(6), 3064–3070.

[38] **Birnkammer, F., Chen, J., Pinhal, D.B., and Gerling, D.** (2018). Influence of the modeling depth and voltage level on the ac losses in parallel conductors of a permanent magnet synchronous machine, *IEEE Trans. Applied Supercon.*, *28*(3), 1–5.

[39] **Tong, W.** (2014). Mechanical Design of Electric Motors, (Taylor & Francis).

[40] **Merwerth, J.H.J. and Schlangen, G.** (2012). Electrical Drive Motor a Vehicle, US Patent.

[41] **Ozpineci, B.** (2014). Oak Ridge National Laboratory Annual Progress Report for the Power Electronics and Electric Motors Program, Oak Ridge National Laboratory.

[42] **Ozpineci, B.** (2016). Oak Ridge National Laboratory Annual Progress Report for the Electric Drive Technologies Program, Oak Ridge National Laboratory.

[43] **Agamloh, E. J. and Yokochi, A.** (2020). An overview of electric machine trends in modern electric vehicles, *Machines*, *8*(20), 1–16.

[44] **Chan, C.C.** (2002) The state of the art of electric and hybrid vehicles. *Proc IEEE, 90*(2), 247–275.

[45] **Zhu, Z.Q. and Howe, D.** (2007) Electrical machines and drives for electric, hybrid, and fuel cell vehicles. *Proc IEEE.*, *95*(4), 746–765.

[46] **URL-3** <*https:// www.toyota.co.uk/new-cars/prius* >, date retrieved 26.03.2018.

[47] **Chau, K.T., Chan, C.C. and Liu, C.** (2008) Overview of permanent magnet brushless drives for electric and hybrid electric vehicles. *IEEE Trans Ind Electron*., *55*(6), 2246–2257.

[48] **Wang, A., Jia, Y. and Soong, W.L.** (2011) Comparison of five topologies for an interior permanent-magnet machine for a hybrid electric vehicle. *IEEE Trans Magn*., *47*(10), 3606–3609.

[49] **Wang, J., Yuan, X. and Atallah, K.** (2013) Design optimization of a surface-mounted permanent-magnet motor with concentrated windings for electric vehicle applications. *IEEE Trans Veh Technol*., *62*(3),1053-1064.

[50] **Chen, X., Wang, J., Lazari, P., Chen, L.** (2013) Permanent magnet assisted synchronous reluctance machine with fractional-slot winding configurations. *Int Elect Mach Drives Conf (IEMDC'13)*, Chicago, 374-381.

[51] **Boldea, I., Tutelea, L.N., Parsa, L., Dorrell, D.** (2014) Automotive electric propulsion systems with reduced or no permanent magnets: an overview. *IEEE Trans Ind Electron., 61*(10), 5696-5711.

[52] **Dorrell, D., Parsa, L., Boldea, I.** (2014) Automotive electric motors, generators, and actuator drive systems with reduced or no permanent magnets and innovative design concepts. *IEEE Trans Ind Electron., 61*(10), 5693-5695.

[53] **Li, J., *et al*.** (2015)Analysis and reduction of magnet loss by deepening magnets in interior permanent-magnet machines with a pole/slot ratio of 2/3. *IEEE Trans Magn., 51*(11),1-4.

[54] **Reddy, P.B., *et al.*** (2012) Comparison of interior and surface PM machines equipped with fractional-slot concentrated windings for hybrid traction applications. *IEEE Trans Energy Convers., 27*(3), 593-602.

[55] **El-Refaie, A.M. and Jahns, T.M.** (2005) Optimal flux weakening in surface PM machines using fractional-slot concentrated windings. *IEEE Trans Ind Appl., 41*(3), 790-800.

[56] **Cros, J., Viarouge, P.** (2002) Synthesis of high performance PM motors with concentrated windings. *IEEE Trans Energy Convers., 17*(2), 248-253.

[57] **Bianchi, N., Fornasiero, E.** (2008) Impact of MMF space harmonic on rotor losses in fractional-slot permanent-magnet machines. *IEEE Magn., 14*(2), 323-328.

[58] **Fornasiero, E., Bianchi, N., Bolognani, S.** (2012) Slot harmonic impact on rotor losses in fractional-slot permanent-magnet machines, *IEEE Trans Ind Electron., 59*(6), 2557-2564.

[59] **El-Refaie, A.M.** (2010) Fractional-slot concentrated-windings synchronous permanent magnet machines: opportunities and challenges. *IEEE Trans Ind Electron.*, *57*(1), 107-121.

[60] **Tangudu, J.K. and Jahns, T.M.** (2011) Comparison of interior PM machines with concentrated and distributed stator windings for traction applications. *IEEE Veh Power Propul Conf (VPPC'11)*; Chicago, 1-8.

[61] **Magnussen, F., Thelin, P., Sadarangani, C.** (2004) Performance evaluation of permanent magnet synchronous machines with concentrated and distributed windings including the effect of field-weakening. *Int Conf Power Electron Mach Drives (PEMD'04).* Edinburgh, 679-685.

[62] **Amin, B.** (1992) Electromagnetic performance comparison in electrical machines. *Eur Trans Electr Power*., *2*(2), 83-90.

[63] **Caruso, M., Tommaso, A.O.D., Miceli, R., Rizzo, R.** (2018) The use of slightly asymmetrical windings for rotating electrical machines. *Int Trans Electr Energ Syst*., *e2569*, 1-19.

[64] **Monteiro, J.R.B.A., *et al*.** (2012) Electromagnetic torque ripple and copper losses reduction in permanent magnet synchronous machines. *Eur Trans Electr Power*, *22*(5), 627-644.

[65] **Neji, R., Tounsi, S. and Sellami, F.** (2006) Contribution to the definition of a permanent magnet motor with reduced production cost for the electrical vehicle propulsion. *Eur Trans Electr Power*, *16*, 437-460.

[66] **Kouchih, D., Boumalha, N., Tadjine, M., Boucherit, M.S.** (2016) New approach for the modeling of induction machines operating under unbalanced power system. *Int Trans Electr Energ Syst.*, *26*(9),1832-1846.

[67] **Busch, R.** (1998) About the concept of consumed life of electrical machine windings and its application. *Eur Trans Electr Power*, *8*(2), 105-110.

[68] **Dajaku, G.** (2010) Elektrische maschine. *German Patent*. DE 10 2008 057 349 B3.

[69] **Dajaku, G., Gerling, D.** (2011) Eddy current loss minimization in rotor magnets of PM machines using high-efficiency 12-teeth/ 10-slots winding topology. *Int Conf Elect Mach Syst (ICEMS'11).* Beijing, 1-6.

[70] **Cistelecan, M.V., Ferreira, F.J.T.E., Popescu, M.** (2010) Three phase tooth-concentrated multiple-layer fractional windings with low space harmonic content. *IEEE Energy Convers Cong Expo (ECCE'10)*. Atlanta, 1399-1405.

[71] **Cistelecan, M.V., Ferreira, F.J.T.E., Popescu, M**. (2010) Three phase tooth-concentrated interspersed windings with low space harmonic content. *Int Conf Elect Mach (ICEM'10).* Rome, 1-6.

[72] **Chen, X., Wang, J., Patel, V.I.** (2014) A generic approach to reduction of magnetomotive force harmonics in permanent magnet machines with concentrated multiple three-phase windings. *IEEE Trans Magn.*, *50*(11), 1-4.

[73] **Abdel-Khalik, A.S., Ahmed, S., Massoud, A.M.** (2016) Effect of multilayer windings with different stator winding connections on interior PM machines for EV applications. *IEEE Trans Magn.*, *52*(2), 1-7.

[74] **Dajaku, G., Gerling, D.** (2012) A novel 12-teeth/10-poles PM machine with flux barriers in stator yoke. *Int Conf Elect Mach (ICEM'12).* Marseille, 36-40.

[75] **Dajaku G, Xie W, Gerling D.** (2014) Reduction of low space harmonics for the fractional slot concentrated windings using a novel stator design. *IEEE Trans Magn.*, *50*(5), 1-12.

[76] **Dajaku, G., Gerling, D.** (2014) Analysis of different PM machines with concentrated windings and flux barriers in stator core. *Int Conf Elect Mach (ICEM'14)*. Berlin, 375-384.

[77] **Bilyi, V., Gerling, D.** (2015) Design of high-efficiency interior permanent magnet synchronous machine with stator flux barriers and single-layer concentrated windings. *IEEE Int Elect Mach Drives Conf (IEMDC'15)*. Coeur d'Alene, 1177-1183.

[78] **Chen, X., Wang, J.** (2017) Magnetomotive force harmonic reduction techniques for fractional-slot non-overlapping winding configurations in permanent-magnet synchronous machines. *Chinese J. Elect Eng.*, *3*(2), 102-113.

[79] **Lipo, T.A.** (2017) Introduction to AC machine design. New Jersey: John Wiley & Sons, Ch.3.

[80] **Gundogdu, T., Zhu, Z.Q., Mipo, J.C., Farah, P.** (2016) Influence of magnetic saturation on rotor bar current waveform and performance in induction machines. *Int Conf Elect Mach (ICEM'16)*. Lausanne, 391-397.

[81] **Gundogdu, T., Zhu, Z.Q., Mipo, J.C., Farah, P.** (2016) Investigation of non-sinusoidal rotor bar current phenomenon in induction machines — Influence of slip and electric loading. *Int Conf Elect Mach (ICEM'16)*. Lausanne, 391-397.

[82] **Chau, K.T., Chan, C.C., Liu, C**. (2008) Overview of permanent-magnet brushless drives for electric and hybrid electric vehicles, *IEEE Trans. Ind. Electron.*, *55*(6), 2246–2257.

[83] **Boldea, I., Tutelea, L.N., Parsa, L., Dorrell, D.** (2014) Automotive and electric vehicle propulsion systems with reduced or no permanent magnets: An overview, *IEEE Trans. Ind. Electron.*, ***61***(10), 5696–5711.

[84] **Dorrell, D., Parsa, L., Boldea, I.** (2014) Automotive electric motors, generators, and actuator drive systems with reduced or no permanent magnets and innovative design concepts, *IEEE Trans. Ind. Electron.*, *61*(10), 5693–5695.

[85] **Reddy, P.B., *et al.*** (2012) Comparison of interior and surface PM machines equipped with fractional-slot concentrated windings for hybrid traction applications, *IEEE Trans. Energy Convers. 27*(3), 593–602.

[86] **Magnussen, F., Thelin, P., Sadarangani, C.** (2004) Performance evaluation of permanent magnet synchronous machines with concentrated and distributed windings including the effect of field-weakening, *Int. Conf. Power Electron., Mach. Drives (PEMD'04)*, Edinburgh, 679–685.

[87] **Dajaku, G., Gerling, D.** (2011) Eddy current loss minimization in rotor magnets of PM machines using high-efficiency 12-teeth/10-slots winding topology, *Int. Conf. Elect. Mach. Syst. (ICEMS'11)*, Beijing, 1–6.

[88] **Cistelecan, M.V., Ferreira, F.J.T.E., Popescu, M.** (2010) Three phase tooth-concentrated interspersed windings with low space harmonic content. *Int. Conf. Elect. Mach. (ICEM'10),* Rome, 1-6.

[89] **Chen, X., Wang, J., Patel, V.I.** (2014) A generic approach to reduction of magnetomotive force harmonics in permanent-magnet machines with concentrated multiple three-phase windings, *IEEE Trans. Magn.*, ***50***(11), 1–4.

[90] **Abdel-Khalik, A.S., Ahmed, S., Massoud, A.M.** (2016) Effect of multilayer windings with different stator winding connections on interior PM machines for EV applications, *IEEE Trans. Magn.*, *52*(2), 1–7.

[91] **Dajaku, G., Gerling, D.** (2012) A novel 12-teeth/10-poles PM machine with flux barriers in stator yoke. *Int. Conf. Elect. Mach. (ICEM'12),* Marseille, 36–40.

[92] **Dajaku, G., Xie, W., Gerling, D.** (2014) Reduction of low space harmonics for the fractional slot concentrated windings using a novel stator design, *IEEE Trans. Magn.*, *50*(5), 1–12.

[93] **Zhu, S., Cox, T., Xu, Z., Gerada, C**. (2018) A novel 24-slots14-poles fractional-slot concentrated winding topology with low space harmonics for electrical machine, *Int. Conf. Power Electron. Mach. Drives (PEMD'18)*, Liverpool, 1–6.

[94] **Zhu, Z.Q., Li, Y.X.** (2018) Modularity techniques in high performance permanent magnet machines and applications, *CES Trans. Elect. Mach. Syst.*, *2*(1), 93–103.

[95] **Wang, J., Patel, V.I., Wang, W.** (2014) Fractional-slot permanent magnet brushless machines with low space harmonic contents, *IEEE Trans. Magn.*, *50*(1), 1–9.

[96] **Cox, T., Eastham, J.F.** (2011) Multi layer planar concentrated windings. *IEEE Int. Elect. Mach. Drives Conf. (IEMDC'11)*, Niagara Falls, 1439–1444.

[97] **Kabir, M.A., Husain, I**. (2016) New multilayer winding configuration for distributed MMF in AC machines with shorter end-turn length'. *IEEE Power Energy Soc. Gen. Meeting (PESGM'16)*, Boston, 1–5.

[98] **Kabir, M.A., Husain, I.** (2018) Application of a multilayer AC winding to design synchronous reluctance motors, *IEEE Trans. Ind. Appl.*, *54*(6), 5941–5953.

[99] **Dajaku, G., Gerling, D.** (2013) A novel tooth concentrated winding with low space harmonic contents, *Int. Elect. Mach. Drives Conf.* (IEMDC'13), Chicago, 755–760.

[100] **Dajaku, G., Gerling, D.** (2013) Novel winding topologies for synchronous and asynchronous machines', *Haus der Technik*, *1*(14)., 26–40.

[101] **Wang, K., Zhu, Z.Q., Ombach, G.** (2014) Synthesis of high performance fractional-slot permanent-magnet machines with coil-pitch of two slot-pitches, *IEEE Trans. Energy Convers., 29*(3), 758–770.

[102] **Dajaku, G., Gerling, D.** (2014) Low costs and high efficiency asynchronous machine with stator cage winding. *IEEE Int. Elect. Veh. Conf. (IEVC'14)*, Florence, 1-6

[103] **Dajaku, G., Bachheibl, F., Patzak, A., Gerling, D.** (2015) Intelligent stator cage winding for automotive traction electric machines. *Int. Elect. Veh. Symp. Exhib. (EVS'28)*, Kintex, 1–8.

[104] **Abdel-Khalik, A.S., Ahmed, S., Massoud, A.M.** (2015) Low space harmonics cancelation in double-layer fractional slot winding using dual multiphase winding, *IEEE Trans. Magn.*, *51*(5), 1–10.

[105] **Raziee, S.M., Misir, O., Ponick, B.** (2018) Combined star-delta winding analysis, *IEEE Trans. Energy Convers.*, *33*(1), 383–394.

[106] **Chen, J.Y., Chen, C.Z.** (1998) Investigation of a new AC electrical machine winding, *IEE Proc. – Elect. Power Appl.*, *145*(2), 125-132.

[107] **Vansompel, H., Sergeant, P., Dupre, L., Bossche, A.** (2012) A combined wye-delta connection to increase the performance of axial-flux PM machines with concentrated windings, *IEEE Trans. Energy Convers. 27*(2), 403–410.

[108] **Sundaram, V.M., Toliyat, H.A.** (2015) A fractional slot concentrated winding (FSCW) configuration for outer rotor squirrel cage induction motors. *IEEE Int. Elect. Mach. Drives Conf. (IEMDC'15)*, Coeur d'Alene, 20–26.

[109] **Dajaku, G., Spas, S., Dajaku, X., Gerling, D.** (2016) An improved fractional slot concentrated winding for low-poles induction machines. *Int. Conf. Elect. Mach. (ICEM'16)*, Lausanne, 114-119.

[110] **Abdel-Khalik, A.S., Diab, M.S., Ahmed, S., Massoud, A.M.** (2015) A new single tooth winding layout for a single-phase induction motor with segmented stator. *IEEE Ind. Electron. Soc. Conf. (IECON'15)*, Yokohama, 102-107.

[111] **Gundogdu, T.** (2018) Advanced non-overlapping winding induction machines for electrical vehicle applications, Ph.D. Thesis, Dept. Electron. Elect. Eng., Sheffield Univ.

[112] **Sakai, K., Suzuki, M., Takishima, K.** (2017) Induction machines with novel concentrated windings. *IEEE Int. Elect. Mach. Drives Conf. (IEMDC'17)*, Miami, 1–7.

[113] **Spargo, C., Mecrow, B., Widmer, J.** (2014) Synchronous reluctance motors with toroidal windings. *IEEE Energy Convers. Cong. Expo. (ECCE'14)*. Pittsburgh, 1374–1378.

[114] **Bianchi, N., Fornasiero, E.** (2009) Impact of MMF space harmonic on rotor losses in fractional-slot permanent-magnet machines. *IEEE Trans. Energy Convers. 24*(2), 323–328.

[115] **Fornasiero, E., Bianchi, N., Bolognani, S.** (2012) Slot harmonic impact on rotor losses in fractional-slot permanent-magnet machines. *IEEE Trans. Ind. Electron.*, *59*(6), 2557–2564.

[116] **EL-Refaie, A.M.** (2010) Fractional-slot concentrated-windings synchronous permanent magnet machines: opportunities and challenges. *IEEE Trans. Ind. Electron.*, *57*(1), 107–121.

[117] **Tangudu, J.K., Jahns, T.M.** (2011) Comparison of interior PM machines with concentrated and distributed stator windings for traction applications. *IEEE Veh. Power Propuls. Conf. (VPPC'11)*, Chicago, 1–8.

[118] **Gundogdu, T., Komurgoz, G.** (2018) Investigation of winding MMF harmonic reduction methods in IPM machines equipped with FSCWs. *Int. Trans. Electr. Energ. Syst.*, *29*(1), 1–27.

[119] **Gundogdu, T., Komurgoz, G.** (2019) Design of interior permanent-magnet machines with novel semi-overlapping windings. *IEEE Global Power, Energy Commun. Conf. (GPECOM'19)*, Nevsehir, 180–187.

[120] **Alberti, L., Bianchi, N.** (2013) Theory and design of fractional-slot multilayer windings. *IEEE Trans. Ind. Appl. 49*(2), 841-849.

[121] **Pyrhonen, J., Jokinen, T., Hrabovcova, V.** (2014) Design of Rotating Electrical Machines. Wiley, Chichester, U.K., 2nd edn.

[122] **Magnussen, F., Sadarangani, C.** (2003) Winding factors and Joule losses of permanent magnet machines with concentrated windings. *IEEE Int. Elect. Mach. Drives Conf. (IEMDC'03)*, Madison, 333-339.

[123] **Caruso, M., et. al.** (2018) Computer-aided analysis and design procedure for rotating induction machine magnetic circuits and windings. *IET Elect. Power Appl.*, *12*(6), 885–893.

[124] **Xu, L. et al.** (2015) Quantitative comparison of integral and fractional slot permanent magnet vernier motors. *IEEE Trans. Energy Convers.*, ***30***(4), 1483–1495.

[125] **Cros, J., Viarouge, P.** (2002) Synthesis of high performance PM motors with concentrated windings. *IEEE Trans. Energy Convers.*, *17*(2), 248–253.

[126] **ANSYS Electromagnetics** Suite 19.2, Maxwell Help, Maxwell 2D/3D Technical Notes, AC Resistance Extracting and Eddy Current Field Simulation. Last access: Jan. 14 2020.

[127] **Rahman, M.A.** (2013) History of interior permanent magnet motors, *IEEE Ind. Appl. Mag.*, *19*(1), 10-15.

[128] **Zhu, Z.Q., Chu, W.Q., Guan, Y.** (2017) Quantitative comparison of electromagnetic performance of electrical machines for HEVs/Evs. *CES Trans. Elect. Mach. Syst.*, *1*(1), 37-47.

[129] **Gamba, M., Pellegrino, G., Vagati, A.** (2014) A new PM-assisted synchronous reluctance machine with a nonconventional fractional slot per pole combination. *Int. Conf. Optim. Elect. Electron. Equip. (OPTIM'14)*, Brasov, 268-275.

[130] **Barcaro, M. Bianchi, N.** (2014) Interior PM machines using ferrite to replace rare-earth surface pm machines. *IEEE Trans. Ind. Appl., 50*(2), 979-985.

[131] **Cai, H., Guan, B., Xu, L.** (2014) Low-cost ferrite pm-assisted synchronous reluctance machine for electric vehicles. *IEEE Trans. Ind. Electron., 61*(10), 741-5748.

[132] **Zhao, W., *et al.*** (2015) Performance improvement of ferrite-assisted synchronous reluctance machines using asymmetrical rotor configurations. *IEEE Trans. Magn., 51*(11), 1-4.

[133] **Zhu, S., *et al.*** A novel 24-slots14-poles fractional-slot concentrated winding topology with low space harmonics for electrical machine. *Int. Conf. Power Electron. Mach. Drives (PEMD'18)*, Liverpool, 1-6.

[134] **Zhu, Z.Q., Li, Y.X.** (2018) Modularity techniques in high performance permanent magnet machines and applications. *CES Trans. Elect. Mach. Syst., 2*(1), 93-103.

[135] **Ma, X.Y., *et al.*** (2018) Recent development of reluctance machines with different winding configurations, excitation methods, and machine structures. *CES Trans. Elect. Mach. Syst., 2*(1), 82-92.

[136] **Boldea, I.** (2017) Electric generators and motors: An overview, *CES Trans. Elect. Mach. Syst., 1*(1), 3-14.

[137] **Wang, Y., Bacco, G., Bianchi, N.** (2017) Geometry analysis and optimization of pm-assisted reluctance motors, *IEEE Trans. Ind. Appl., 53*(5), 4338-4347.

[138] **Barcaro, M., Bianchi, N., Magnussen, F.** (2012) Permanent-magnet optimization in permanent-magnet-assisted synchronous reluctance motor for a wide constant-power speed range. *IEEE Trans. Ind. Electron., 59*(6), 2495-2502.

[139] **Mohanarajah, T., Nagrial, M., Rizk, J., Hellany, A.** (2018) Permanent magnet optimization in pm assisted synchronous reluctance machines. *IEEE Int. Symp. Ind. Electron. (ISIE'18)*, Cairns, 1347-1351.

[140] **Gaussens, B., *et al.*** (2017) Torque ripple mitigation of PM-assisted synchronous reluctance machine: Design and optimization. *Int. Conf. Elect. Mach. Syst. (ICEMS'17)*, Sydney, 1-6.

[141] **Zhang, X., *et al.*** (2018) Improvement of reluctance torque in fault-tolerant permanent-magnet machines with fractional-slot concentrated-windings. *IEEE Trans. Applied Supercon., 28*(3), 1-5.

[142] **Tursini, M., *et al.*** (2017) A switched-reluctance motor for aerospace application: Design, analysis and results. *Elect. Power Syst. Res., 142*, 74-83.

[143] **Moghaddam, R., Magnussen, F., Sadarangani, C.** (2012) Novel rotor design optimization of synchronous reluctance machine for low torque ripple. *Int. Conf. Elect. Mach. (ICEM'12)*, Marseille, 720-724.

[144] **Yang, H., *et al*.** (2017) Novel reluctance axis shifted machines with hybrid rotors. *IEEE Energy Convers. Cong. Expo. (ECCE'17)*, Cincinnati, 2362-2367.

[145] **Yang, Z., *et al.*** (2015) Comparative study of interior permanent magnet, induction, and switched reluctance motor drives for EV and HEV applications. *IEEE Trans. Transport. Electrific.*, *1*(3), 245-254.

[146] **Zhu, Z.Q., *et al*.** (2015) Comparative study of the electromagnetic performance of switched flux permanent magnet machines. *IET Elect. Power Appl.*, *9*(4), 297-306.

[147] **Kim, K., *et al.*** (2016) Comparative study of electromagnetic performance of high-speed synchronous motors with rare-earth and ferrite permanent magnets. *IEEE Trans. Magn., 52*(7), 1-4.

[148] **Taras, P., Li, G., Zhu, Z.Q.** (2017) Comparative study of fault-tolerant switched-flux permanent-magnet machines. *IEEE Trans. Ind. Electron.*, *64*(3),1939-1948.

[149] **Huynh, T.A., Hsieh, M.** (2017) Comparative study of PM-assisted SynRM and IPMSM on constant power speed range for EV applications. *IEEE Trans. Magn.*, *53*(11), 1-6.

[150] **Bostanci, E., *et al*.** (2017) Opportunities and challenges of switched reluctance motor drives for electric propulsion: a comparative study', *IEEE Trans. Transport. Electrific.*, *3*(1), 58-75.

[151] **Gundogdu, T., Komurgoz, G.** (2017) Influence of winding configuration on the performance of surface-mounted PM machines. *Int. J. Mechanic. Eng. Robo. Res.*, *6*(1), 46-49.

[152] **Wang, A., Wang, C., Wang, Y.** (2013) Performance analysis and comparison of interior permanent magnet machine with FSCW and distributed windings for a hybrid electric vehicle. *Int. Conf. Electr. Mach. Syst. (ICEMS'13),* Busan, 1044-1047.

[152] **Wang, A., Wang, C., Soong, W.L.** (2014) Design and optimization of interior PM machines with distributed and fractional-slot concentrated-windings for hybrid electric vehicles. *IEEE Conf. Expo Transport. Electrific. Asia-Pacific (ITEC Asia-Pacific),* Beijing, 1-5.

[153] **Ponomarev, P., Petrov, I., Pyrhönen, J.** (2014) Influence of travelling current linkage harmonics on inductance variation, torque ripple and sensorless capability of tooth-coil permanent-magnet synchronous machines. *IEEE Trans. Magn., 50*(1), 1-8.

[154] **Chen, X., *et al.*** (2014) Reluctance torque evaluation for interior permanent magnet machines using frozen permeability. *IET Int. Conf. Power Electron. Mach. Drives (PEMD'14),* Manchester.

[155] **Chen, Q., Liu, G., Zhao, W., Xu, G.** (2019) Separation and comparison of average torque in five-phase IPM machines with distributed and fractional slot concentrated windings. *IET Elec. Power Appl., 13*(3), 285-293.

[156] **Lipo, T.A**. (2017) Calculation of induction machine losses and Permanent magnet machines', in Samad, T. (Ed.): 'Introduction to AC Machine Design' (John Wiley & Sons, Inc., 2017, 1st edn.), Hoboken, 193-400.

[157] **Caruso, M., *et al.*** (2018) Computer-aided analysis and design procedure for rotating induction machine magnetic circuits and windings. *IET Elect. Power Appl., 12*(6), 885-893.

[158] **Bianchi N., Bolognani S**. (1998) Design optimisation of electric motors by genetic algorithms. *IEE Proceedings – Elect. Power Appl. 145*, 475-483.

[159] **Bianchi, N., Canova A.** (2002) FEM analysis and optimisation design of an IPM synchronous motor. *International Conference on Power Electronics, Machines and Drives*, 49-54.

[160] **Dong-Hyeok, C., Hyun-Kyo, J., Dong-Joon, S.** (1999) Multiobjective optimal design of interior permanent magnet synchronous motors considering improved core loss formula. *IEEE Trans. Energy Convers.14*(2),1347-1352.

[161] **Dong-Joon S., *et al.*** (1997) Efficiency optimization of interior permanent magnet synchronous motor using genetic algorithms. *IEEE Trans. Magn. 33*(8).1880-1883.

[162] **Iles-Klumpner, D., Risticevic, M., Boldea, I.** (2005) Advanced optimization design techniques for automotive ınterior permanent magnet synchronous machines. *IEEE Int. Conf. Elect. Mach. Drives*, 227-234.

[163] **Jannot, X, *et al.*** (2011) Multiphysic modeling of a high-speed ınterior permanent-magnet synchronous machine for a multiobjective optimal design. *IEEE Trans. Energy Convers. 26*(8), 457-467.

[164] **Jolly, L., Jabbar, M.A., Liu, Q**. (2005) Design optimization of permanent magnet motors using response surface methodology and genetic algorithms. *IEEE Trans. Magn. 41*(5), 3928-3930.

[165] **Kim, H., You Y., Kwon B.** (2013) Rotor shape optimization of ınterior permanent magnet BLDC motor according to magnetization direction. *IEEE Trans.Magn. 49*(12), 2193-2196.

[166] **Liu, Q., Jabbar, M.A., Khambadkone, A.M.** (2001) Design optimization of interior permanent magnet synchronous motors for wide- speed operation. IEEE Int. Conf. Power Electron. Drive Sys. Indonesia. 475-478.

[167] **Mirahki, H., Moallem, M., Rahimi, S.A.** (2014) Design optimization of IPMSM for 42V ıntegrated starter alternator using lumped parameter model and genetic algorithms. *IEEE Trans. Magn. **50***(11),114-119.

[168] **Pellegrino, G., Cupertino, F.** (2010) FEA-based multi-objective optimization of IPM motor design including rotor losses. *IEEE Energy Conversion Congress and Exposition*, 3659-3666.

[169] **Du, Z.S., Lipo, T.A.** (2017) Efficient utilization of rare earth permanent-magnet materials and torque ripple reduction in ınterior permanent-magnet machines. *IEEE Trans. Ind. Appl. 53*(2), 3485-3495.

[170] **Fatemi, A., *et al.*** (2016) Large-scale design optimization of pm machines over a target operating cycle, *IEEE Trans. Ind. Appl. 52*(3), 3772-3782.

[171] **Günther, S., Ulbrich, S., Hofmann, W.** (2014) Driving cycle-based design optimization of interior permanent magnet synchronous motor drives for electric vehicle application, *Int. Symp. Power Electron. Elect. Drives Auto, Motion*, 25-30.

[172] **Ouyang, W., Zarko, D., Lipo, T.A.,** Permanent magnet machine design practice and optimization. *IEEE Industry Applications Conference Forty-First IAS Annual Meeting*, 1905-1911.

[173] **Sizov, G.Y., *et al.*** (2013) Automated multi-objective design optimization of pm ac machines using computationally efficient FEA and differential evolution. *IEEE Trans. Ind. Appl. 49*, 2086-2096.

[174] **Zarko, D., Ban. D., Lipo, T.A.**, (2010) Design optimization of interior permanent magnet (IPM) motors with maximized torque output in the entire speed range. *Euro. Conf. Power Electron. Appl.*1-10.

[175] **Zhang, P., Ionel, D.M., Demerdash, N.A.O.** (2013) Morphing parametric modeling and design optimization of spoke and V-type permanent magnet machines by combined design of experiments and differential evolution algorithms. *IEEE Energy Conversion Congress and Exposition*, 5056-5063.

[176] **Zhang, P., Ionel, D.M., Demerdash, N.A.O.** (2016) Saliency ratio and power factor of ıpm motors with distributed windings optimally designed for high efficiency and low-cost applications. *IEEE Trans. Ind. Appl. 52*(4), 4730-4739.

[177] **Zhang, P., Sizov, G.Y., Ionel, D.M., Demerdash, N.A.O.** (2015) Establishing the relative merits of ınterior and spoke-type permanent-magnet machines with Ferrite or NdFeB through systematic design optimization. *IEEE Trans. Ind. Appl. 51*(10), 2940-2948.

[178] **Alotto, P., Barcaro, M., Bianchi, N., Guarnieri, M.** (2011) Optimization of interior PM motors with machaon rotor flux barriers, *IEEE Trans. Magn. 47*, 958-961.

[179] **Ashabani, M., Mohamed, Y.A.I.** (2011) Multiobjective shape optimization of segmented pole permanent-magnet synchronous machines with ımproved torque characteristics. *IEEE Trans. Magn. 47*(12), 795-804.

[180] **Lee, J.H., *et al*.** (2018) Particle swarm optimization algorithm with ıntelligent particle number control for optimal design of electric machines. *IEEE Trans. Ind. Electron.* ***65***(13), 1791-1798.

[181] **Jolly, L., Jabbar, M.A., Liu, Q.** (2006) Optimization of the constant power speed range of a saturated permanent-magnet synchronous motor. *IEEE Trans. Ind. Appl. 42*(12),1024-1030.

[182] **Kim, S., Bhan, J., Hong, J., Lim, K.** (2006) Optimization technique for ımproving torque performance of concentrated winding ınterior PM synchronous motor with wide speed range. *IEEE Industry Applications Conference Forty-First IAS Annual Meeting*, 1933-1940.

[183] **Duan, Y., Ionel, D.M.** (2013) A Review of recent developments in electrical machine design optimization methods with a permanent-magnet synchronous motor benchmark study. *IEEE Trans. Ind. Appl. 49*(15), 1268-1275.

[184] **Choi, J.S., Izui, K., Nishiwaki, S., Kawamoto, A., Nomura, T.** (2012) Rotor pole design of IPM motors for a sinusoidal air-gap flux density distribution. *Structural and Multidisciplinary Optimization 46*(3), 445-455.

[185] **Chong, L., Rahman, M.F.** (2010) Saliency ratio derivation and optimisation for an interior permanent magnet machine with concentrated windings using finite-element analysis, *IET Elec. Power Appl.* ***4***(8), 249-258.

[186] **Kuci, E., Henrotte, F., Duysinx, P., Geuzaine, C.** (2019) Combination of topology optimization and Lie derivative-based shape optimization for electro-mechanical design. *Structural and Multidisciplinary Optimization 59*(1), 1723-1731.

[187] **Reichert, T., Nussbaumer, T., Kolar, J.W.** (2013) Split ratio optimization for high-torque pm motors considering global and local thermal limitations. *IEEE Trans. Energy Convers. 28*(5), 493-501.

[188] **Sizov, G.Y., Ionel, D.M., Demerdash, N.A.O.** (2012) Modeling and parametric design of permanent-magnet ac machines using computationally efficient finite-element analysis. *IEEE Trans. Ind. Electron. 59*(12), 2403-2413.

[189] **Xia, C., Guo, L., Zhang, Z., Shi, T., Wang, H.** (2015) Optimal designing of permanent magnet cavity to reduce ıron loss of ınterior permanent magnet machine. *IEEE Trans. Magne. 51*, 1-9.

[190] **Yamazaki, K., Ohki, S., Nezu, A., Ikemi, T.** (2007) Development of ınterior permanent magnet motors reduction of harmonic ıron losses by optimizing rotor structures. *IEEE International Electric Machines & Drives Conference*, 489-494.

[191] **Lee S,** ***et al.*** (2014) Optimal design of interior permanent magnet synchronous motor considering the manufacturing tolerances using Taguchi robust design. *IET Elect. Power Appl. 8*(15), 23-28.

[192] **Zhu, Z.Q., Liu, X.** (2011) Individual and global optimization of switched flux permanent magnet motors. *Int. Conf. Elect. Mach. Syst.* 1-6.

[193] **Olszewski, M.** (2011) Evaluation of the 2010 Toyota Prius hybrid synergy drive system vol FY2011. Oak Ridge National Laboratory, U.S. Department of Energy Vehicle Technologies, EE-2G.

[194] **Material Market Priced**: https://www.lme.com/ date retrieved 21.05.2019.

[195] **N35SH Market Price**: https://magnetsim.com/grades/N35SH. date retrieved 28.05.2019.

[196] **Ponomarev, P., Petrov, I., Pyrhönen, J.** (2014) Influence of travelling current linkage harmonics on ınductance variation, torque ripple and sensorless capability of tooth-coil permanent-magnet synchronous machines. *IEEE Trans. Magn. 50*, 1-8.

[197] **Haftka, R.T., Zhou, M., Queipo, N.V.** (2019) Replication of results. *Struct. Multidiscip. Optim.* ***60***(2), 400-405.

[198] **Climate Change 2014**: Synthesis Report. hdl:10013/epic.45156.

[199] **Soong, W.L., Ertugrul, N.** (2002) Field-weakening performance of interior permanent-magnet motors. *IEEE Trans. Ind. Appl.*, 2002, ***38***(5), 1251-1258.

[200] **Zeraoulia, M., Benbouzid, M.E.H., Diallo, D.** (2006) Electric motor drive selection issues for hev propulsion systems: A comparative study. *IEEE Trans. Veh. Technol. 55*(6), 1756-1764.

[201] **Chan, C.C.** (2007) The state of the art of electric, hybrid, and fuel cell vehicles, *Proc. IEEE, 95*(4), 704-718.

[202] **Boldea, I., Tutelea, L.N., Parsa. L., Dorrell, D.** (2014) Automotive electric propulsion systems with reduced or no permanent magnets: An overview. *IEEE Trans. Ind. Electron. 61*(10), 5696-5711.

[203] **Fasolo, A., Alberti, L., Bianchi, N.** (2014) Performance comparison between switching-flux and IPM machines with rare-earth and ferrite PMs. *IEEE Trans. Ind. Appl.*, 2014, *50*(6), 3708-3716.

[204] **Wang, A., Jia, Y., Dong, S.** (2011) Design and analysis of a novel interior permanent magnet machine for hybrid electric vehicle traction. *Int. Conf. Elect. Mach. Syst. (ICEMS11)*, Beijing, 1-4.

[205] **Reddy, P.B., Huh, K., El-Refaie, A.M.** (2012) Effect of stator shifting on harmonic cancellation and flux weakening performance of interior PM machines equipped with fractional-slot concentrated windings for hybrid traction applications. *IEEE Energy Convers. Cong. Expo. (ECCE12)*, Raleigh, 525-533.

[206] **Reddy, P.B., EL-Refaie, A.M., Huh, K**. (2015) Effect of number of layers on performance of fractional-slot concentrated-windings interior permanent magnet machines, *IEEE Trans. Power Electron. 30*(4), 2205-2218.

[207] **Wang, Y., Qu, R., Li, J.** (2015) Multilayer windings effect on interior pm machines for EV applications. *IEEE Trans. Ind. Appl.*, 2015, *51*(3), 2208-2215.

[208] **Honda, Y., Nakamura, T., Higaki, T., Takeda, Y.** (1997) Motor design considerations and test results of an interior permanent magnet synchronous motor for electric vehicles. *IEEE Ind. Appl. Conf. (IAS 97)*, New Orleans, 75-82.

[209] **Morimoto, S.** (2007) Trend of permanent magnet synchronous machines, *IEEJ Trans. Elec. Electron. Eng.* 2, 101-108.

[210] **Pouramin, A., Madani, S.M.** (2009) New interior PM rotor design with high flux-weakening capability. *IEEE Int. Elect. Mach. Drives Conf. (IEMDC09)*, Miami, 958-963.

[211] **Kim, K., Lee, J., Kim, H.J., Koo, D.** (2009) Multiobjective optimal design for interior permanent magnet synchronous motor. *IEEE Trans. Magn.*, 2009, *45*(3), 1780-1783.

[212] **Kim, S., Kim, Y., Lee, G., Hong, J.** (2012) A novel rotor configuration and experimental verification of interior PM synchronous motor for high-speed applications. *IEEE Trans. Magn. 48*(2), 843-846.

[213] **Xu, L., Ye, L., Zhen, L., El-Antably, A.** (1995) A new design concept of permanent magnet machine for flux weakening operation. *IEEE Trans. Ind. Appl. 31*(2), 373-378.

[214] **Stumberger, B., *et al*.** (2008) Design and finite-element analysis of interior permanent magnet synchronous motor with flux barriers. *IEEE Trans. Magn. 44*(11), 4389-4392.

[215] **Yamazaki, K., *et al*.** (2010) Reduction of magnet eddy-current loss in interior permanent-magnet motors with concentrated windings, *IEEE Trans. Ind. Appl. 46*(6), 2434-2441.

[216] **Barcaro, M., Bianchi, N., Magnussen, F.** (2010) Rotor flux-barrier geometry design to reduce stator iron losses in synchronous IPM motors under FW operations. *IEEE Trans. Ind. Appl. 46*(5), 1950-1958.

[217] **Zhu, X., e*t al.*** (2018) Comparative design and analysis of new type of flux-intensifying interior permanent magnet motors with different q-axis rotor flux barriers. *IEEE Trans. Energy Convers. **33***(4), 2260-2269.

[218] **Liu, F., *et al.*** (2018) Design and analysis of an interior permanent magnet synchronous machine with multiflux-barriers based on flux-intensifying effect. *IEEE Trans. Appl. Supercon. 28*(3), 1-5.

[219] **Bianchi, N., Bolognani, S**. (1999) Performance analysis of an IPM motor with segmented rotor for flux-weakening applications. *Int. Conf. Elect. Mach. Drives, Canterbury*, 49-53.

[220] **Stumberger, B., Hamler, A., Trlep, M., Jesenik, M.** (2001) Analysis of interior permanent magnet synchronous motor designed for flux weakening operation. *IEEE Trans. Magn. 37*(5), 3644-3647.

[221] **Dutta, R., Rahman, M.F.** (2008) Design and analysis of an interior permanent magnet (IPM) machine with very wide constant power operation range, *IEEE Trans. Energy Convers. 23*(1), 25-33.

[222] **Duan, S., Zhou, L., Wang, J.** (2014) Flux weakening mechanism of interior permanent magnet synchronous machines with segmented permanent magnets, *IEEE Trans. Appl. Supercon. 24*(3), 1-5.

[223] **Zhu, X., *et al.*** (2016) Electromagnetic performance analysis and verification of a new flux-intensifying permanent magnet brushless motor with two-layer segmented permanent magnets. *IEEE Trans. Magn. 52*(7), 1-4.

[224] **Qi, G., *et al.*** (2009) Influence of skew and cross-coupling on flux-weakening performance of permanent-magnet brushless AC machines. *IEEE Trans. Magn.*, *45*(5), 2110-2117.

[225] **Wang, A., Li, H., Lu, W., Zhao, H**. (2009) Influence of skewed and segmented magnet rotor on IPM machine performance and ripple torque for electric traction. *IEEE Int. Elect. Mach. Drives Conf. (IEMDC09)*, Miami, 305-310.

[226] **Zhang, J.C., Huang, X.Y., Fang, Y.T., Ma, Z.K.** (2012) Design of interior PM synchronous traction motor with novel approximate skewed rotor. *Annu. Conf. IEEE Ind. Electron. Soc. (IECON12)*, Montreal, 1726-1730.

[227] **Barman, D., Pillay, P.** (2018) Effect of skewing in a variable flux interior permanent magnet synchronous machine. *IEEE Int. Conf. Power Electron. Drives Energy Syst. (PEDES28)*, Chennai, 1-6.

[228] **Deak, C., Binder, A., Funieru, B., Mirzaei, M.** (2009) Extended field weakening and overloading of high-torque density permanent magnet motors. *IEEE Energy Convers. Cong. Expo. (ECCE09)*, San Jose, 2347-2353.

[229] **Tessarolo, A., Mezzarobba, M. Menis, R.** (2012) A novel interior permanent magnet motor design with a self-activated flux-weakening device for automotive applications. *Int. Conf. Elect. Mach. (ICEM12)*, Marseille, 2603-2609.

[230] **Tessarolo, A., Mezzarobba, M. Menis, R.** (2015) Modeling, analysis, and testing of a novel spoke-type interior permanent magnet motor with improved flux weakening capability. *IEEE Trans. Magn. 51*(4), 1-10.

[231] **Seo, J., Kim, S., Jung, H.** (2010) Rotor-design strategy of IPMSM for 42 V integrated starter generator. *IEEE Trans. Magn. 46*(6), 2458-2461.

[232] **Yamazaki, K., Ishigami, H.** (2010) Rotor-shape optimization of interior-permanent-magnet motors to reduce harmonic iron losses. *IEEE Trans. Ind. Electron. 57*(1), 61-69.

[233] **Du, J., Wang, X., Lv, H.** (2016) Optimization of magnet shape based on efficiency map of IPMSM for Evs. *IEEE Trans. Appl. Supercon. 26*(7), 1-7.

[234] **Soong, W.L., Staton, D.A., Miller, T.J.E.** (1995) Design of a new axially-laminated interior permanent magnet motor. *IEEE Trans. Ind. Appl.*, *31*(2), 358-367.

[235] **Lu, X., *et al.*** (2015) Investigation of permanent-magnet motor drives incorporating damper bars for electrified vehicles. *IEEE Trans. Ind. Electron. 62*(5), 3234-3244.

[236] **Li, J.,Wang, K., Zhang, H.** (2020) Flux-focusing permanent magnet machines with modular consequent-pole rotor. *IEEE Trans. Ind. Electron. 67*(5), 3374-3385.

[237] **Lu, D., Kar, N.C.** (2010) A review of flux-weakening control in permanent magnet synchronous machines. *IEEE Veh. Power Propul. Conf. (VPPC10)*, Lille, 1-6.

[238] **Cao, R., Mi, C., Cheng, M.** (2012) Quantitative comparison of flux-switching permanent magnet motors with interior permanent magnet motor for EV, HEV, and PHEV applications. *IEEE Trans. Magn. 48*(8), 2374–2384.

[239] **Pellegrino, G., Vagati, A., Guglielmi, P.** (2003) Design tradeoffs between constant power speed range, uncontrolled generator operation, and rated current of IPM motor drives. *IEEE Trans. Ind. Appl.* 47(5), 1995–2003.

[240] **Chen, C.H., Cheng, M.Y., Tsai, M.S.** (2005) Study on a wide speed range integrated electrical transmission system. *Int. Conf. Power Electron. Drives Syst.* Kuala Lumpur, 781-786.

[241] **Seol, H.,** ***et al.*** (2017) Design of winding changeable BLDC motor considering demagnetization in winding change section. *IEEE Trans. Magn. 53*(11), 1-5.

[242] **Im, S., Park, G., Gu, B.** (2019) Novel winding changeover method for a high efficiency ac motor drive. *IEEE Energy Convers. Conger. Expo. (ECCE19)*, Baltimore, 2347-2352.

**APPENDICES**

**APPENDIX A:** The main specifications of the IPM machines analyzed in Chapter 2.

**APPENDIX B:** The main specifications of the IPM machines analyzed in Chapter 3.

**APPENDIX C:** Open layout of the NSW for 24S/4P combination

**APPENDIX D:** Current waveforms and their *dq* representation

**APPENDIX E:** Power factor comparison for machines having large and small dimensions

**APPENDIX F:** Clarification of MMF sub- and super-harmonics

**APPENDIX G:** Determination of torque ripple’s order

**APPENDIX H:** Definition of concentiric winding

**APPENDIX I:** Definition of slot fill factor used in the thesis

**APPENDIX J:** No Load Back-EMF scope screen shots for various rotor speeds

**APPENDIX K:** Optimization parameters and justifications

## APPENDIX A

The 2-D cross-sections and main specifications of the Toyota Prius 2010 IPM machine (ISDW) and its FSCW counterpart, analyzed in Chapter 2, are presented in Figure A.1 and A.2 and Table A.1.

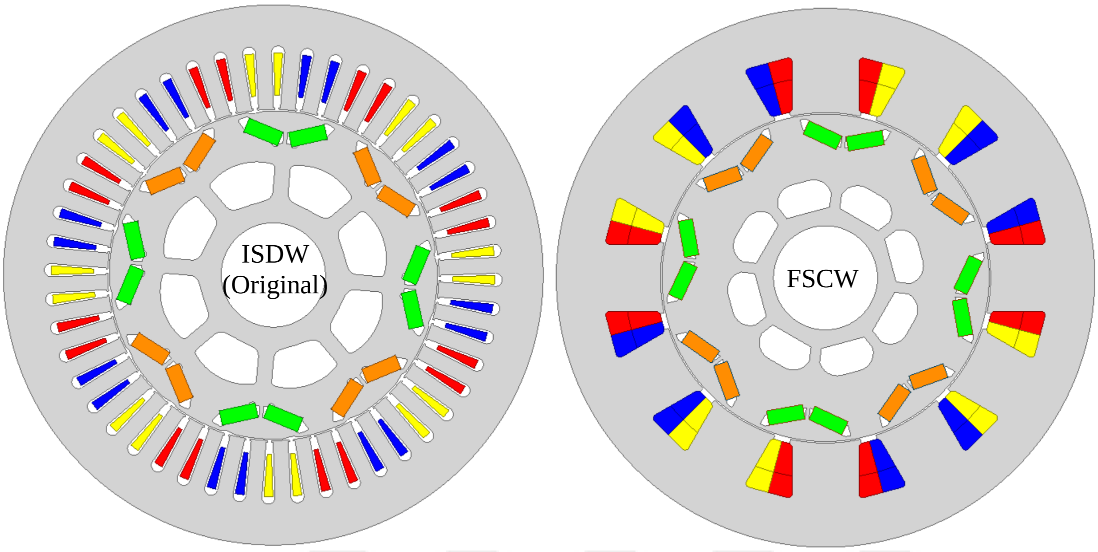


**Figure A.1 :** Cross-section of the designed IPM machines.

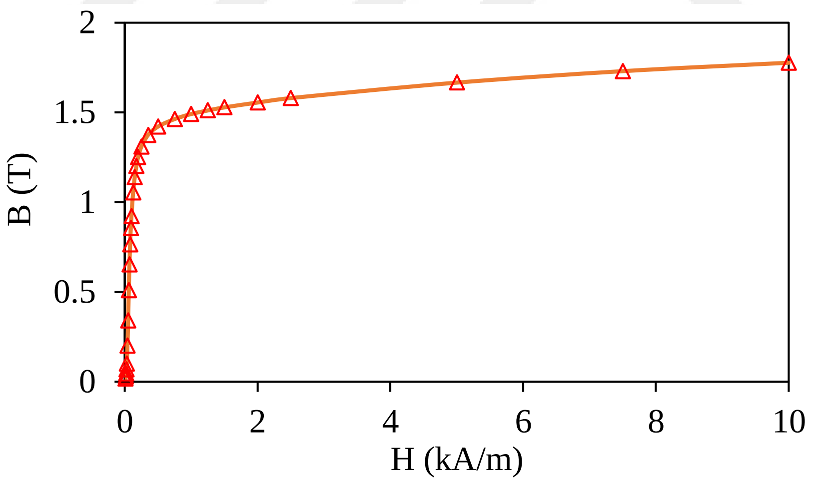


**Figure A.2 :** BH curve of the W330_35 material.

**Table A.1 :** Parameters of analysed IPM machines in Chapter 2.

| ***Parameter*** | ***ISDW*** | ***FSCW*** | ***Unit*** |
|---|---|---|---|
| Peak power | 60 | | kW |
| Peak torque | 240 | | Nm |
| Max. speed | 13500 | | rpm |
| Rated speed | 1000 | | rpm |
| Voltage range (DC) | 200-650 | | V |
| Max. phase current (peak) | 236 | | A |
| Pole number | 8 | | – |
| Slot number | 48 | 12 | – |
| Number of turns per coil | 11 | 26 | – |
| Coil pitch | 5 | 1 | – |
| Air-gap length | 0.73 | | mm |
| Stack length | 50.8 | | mm |
| Stator outer diameter | 264 | | mm |
| Stator inner diameter | 161.9 | | mm |
| Rotor outer diameter | 160.44 | | mm |
| Rotor inner diameter | 51 | | mm |
| Lamination thickness | 0.305 | | mm |
| Slot depth | 30.9 | 27.9 | mm |
| Tooth width | 7.55 | 32.8 | mm |
| Slot opening | 1.88 | 8 | mm |
| Tooth tip height | 0.85 | 2 | mm |
| PM width | 17.88 | | mm |
| PM Thickness | 7.16 | | mm |
| Permeability | 1.05 | | $Hm^{-1}$ |
| Conductivity | 625000 | | s/m |
| Coercivity | -805399.8 | | A/m |

## APPENDIX B

The main specifications of the designed IPM machines with small (*SD*) and large (*LD*=Toyota Prius 2010) dimensions are listed in Table B.1. The geometric dimensions of the IPM machines designed in this study (except for the original Toyota Prius 2010 IPM machine) have been globally optimized by adopting Genetic Algorithm for maximum average torque by keeping the current density, slot fill factor, outer diameter, stack length, air-gap length, and PM volume constant (same as the Toyota Prius 2010 IPM machine).

**Table B.1 :** Parameters of analysed IPM machines in Chapter 3.

| IPM Mach. / Parameter | ISDW | | FSCW | | NSW | |
|---|---|---|---|---|---|---|
| | *SD* | *LD* | *SD* | *LD* | *SD*§ | *LD* |
| Peak current (A) | 26 | 236 | 26 | 236 | 26 | 236 |
| Rated Speed (rpm) | 400 | 1000 | 400 | 1000 | 400 | 1000 |
| Slot number | 24 | 48 | 6 | 12 | 24 | 48 |
| Pole number | 4 | 8 | 4 | 8 | 4 | 8 |
| Number of turns per phase | 96 | 88 | 96 | 100 | 96 | 88 |
| Number of strands per wire | 1 | 12 | 1 | 12 | 1 | 12 |
| Coil pitch | 5 | 5 | 1 | 1 | 5/3/1 | 5/3/1 |
| Stack length | 50 | 50.8 | 50 | 50.8 | 50 | 50.8 |
| Stator outer dia. | 124 | 264 | 124 | 264 | 124 | 264 |
| Split ratio | 0.602 | 0.613 | 0.59 | 0.635 | 0.602 | 0.613 |
| Air-gap length | 0.5 | 0.73 | 0.5 | 0.73 | 0.5 | 0.73 |
| Shaft dia. | 35 | 51 | 35 | 51 | 35 | 51 |
| Slot depth | 9.2 | 26.75 | 5.2 | 26.75 | 9.2 | 26.75 |
| Slot tip height | 0.7 | 0.85 | 0.7 | 0.85 | 0.7 | 0.85 |
| Tooth width | 6.063 | 7.526 | 22.13 | 30.02 | 6.063 | 7.526 |
| Slot opening width | 1.8 | 1.9 | 3 | 7.6 | 1.8 | 1.9 |
| PM width | 17.5 | 17.88 | 17.5 | 17.88 | 17.5 | 17.88 |
| PM thickness | 2 | 7.16 | 2 | 7.16 | 2 | 7.16 |
| PM Material | N35UH_80C | | N35UH_80C | | N35UH_80C | |
| PM Remanence (T) | 1.21 | 1.05 | 1.21 | 1.05 | 1.21 | 1.05 |
| PM Coercive force (kA/m) | -905 | -932 | -905 | -932 | -905 | -932 |
| Iron lamination | M270 | Steel | M270 | Steel | M270 | Steel |

*All dimensions are in mm. NSW (S) is the prototyped IPM machine.
§Prototyped machine.

## APPENDIX C

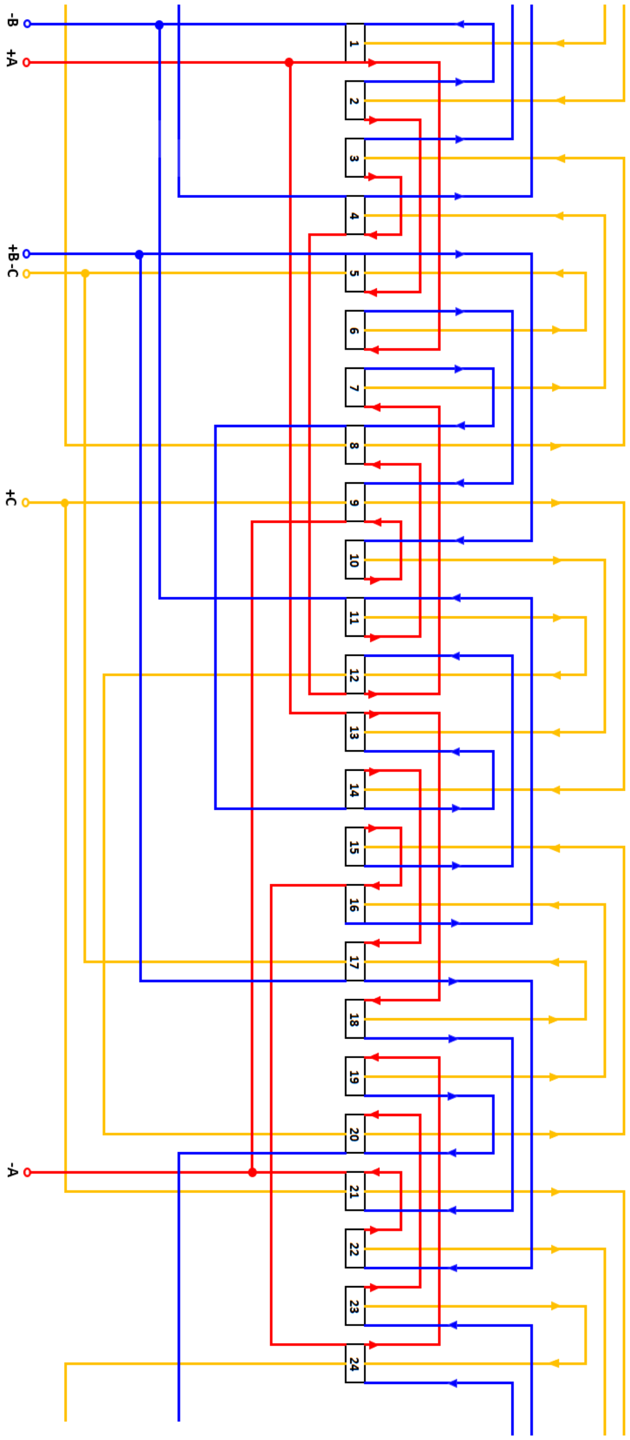


**Figure C.1 :** Winding layour of 24S/4P (3*L*) NSW.

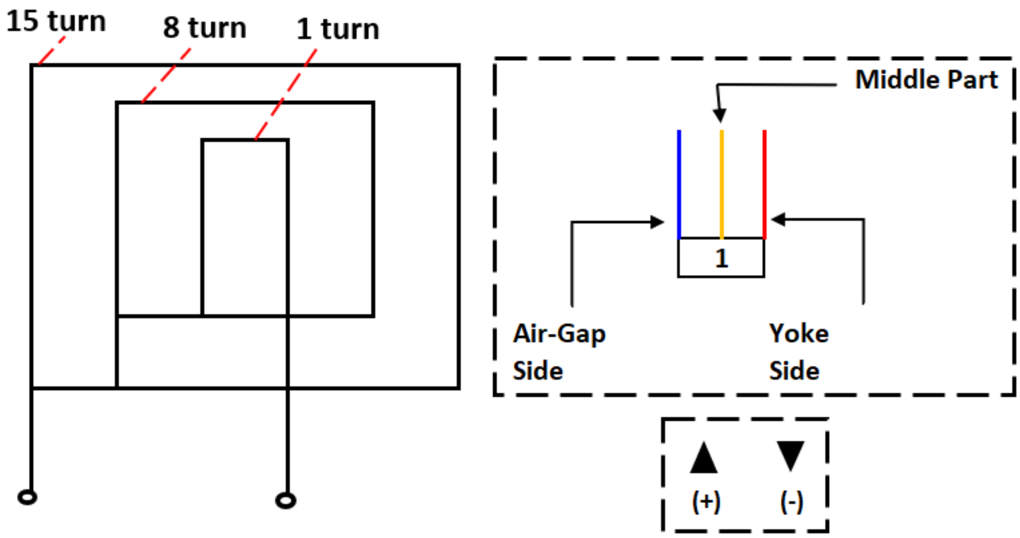


**Figure C.2 :** Details of winding layout illustrated in Fig. A.1.

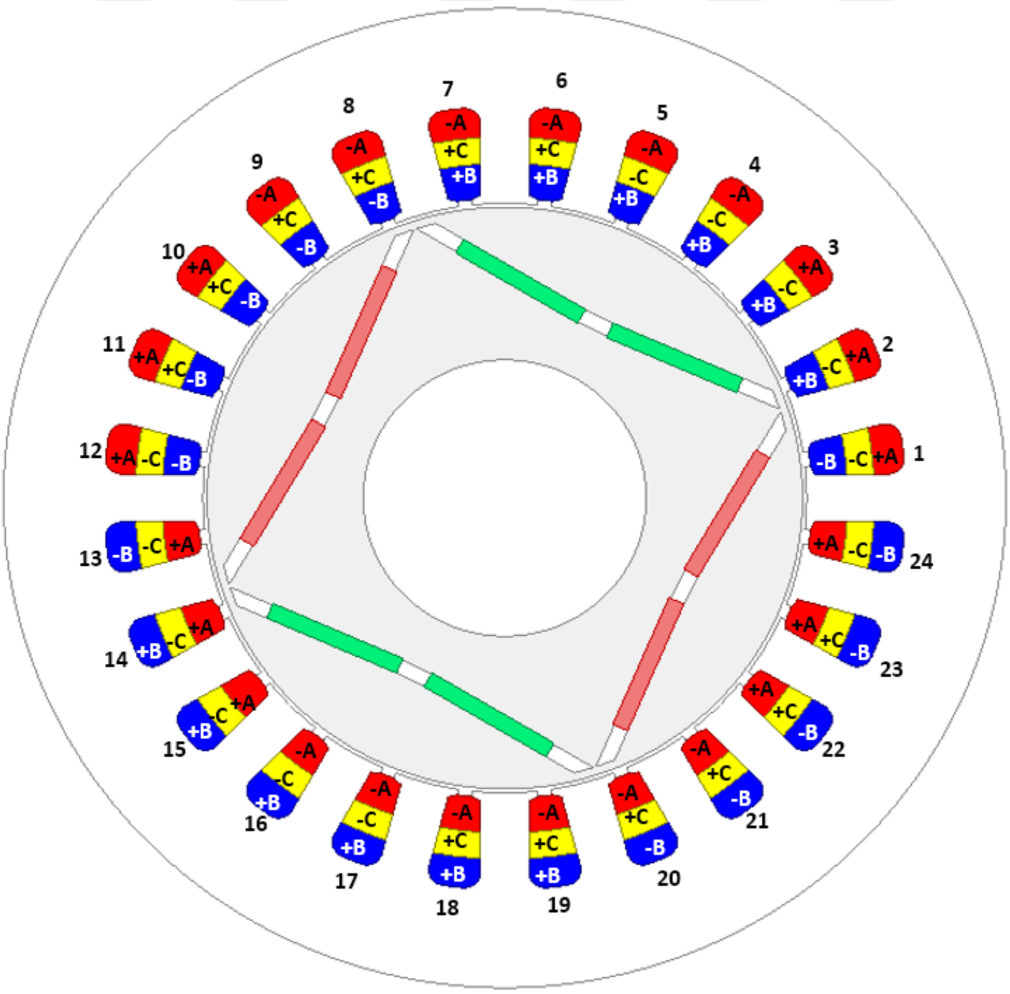


**Figure C.3 :** Winding configuration with slot numbers and winding polarizations.

## APPENDIX D

Initially, the machines are modelled in the *dq* plane and all the analyses done for *dq* model of the machine. To be able to simplify the model and obtain the analysis results a bit faster, current is directly injected to the stator windings. Since the current source is used for the excitation source for the designed IPM machines, it is purely sinusoidal as illustrated in Fig. A.1. However, the distortions of the excitation can also be observed from the back-EMF (namely induced phase voltage) waveforms illustrated in Fig. 13, Fig. 14, and Fig. 23 in Chapter 2.

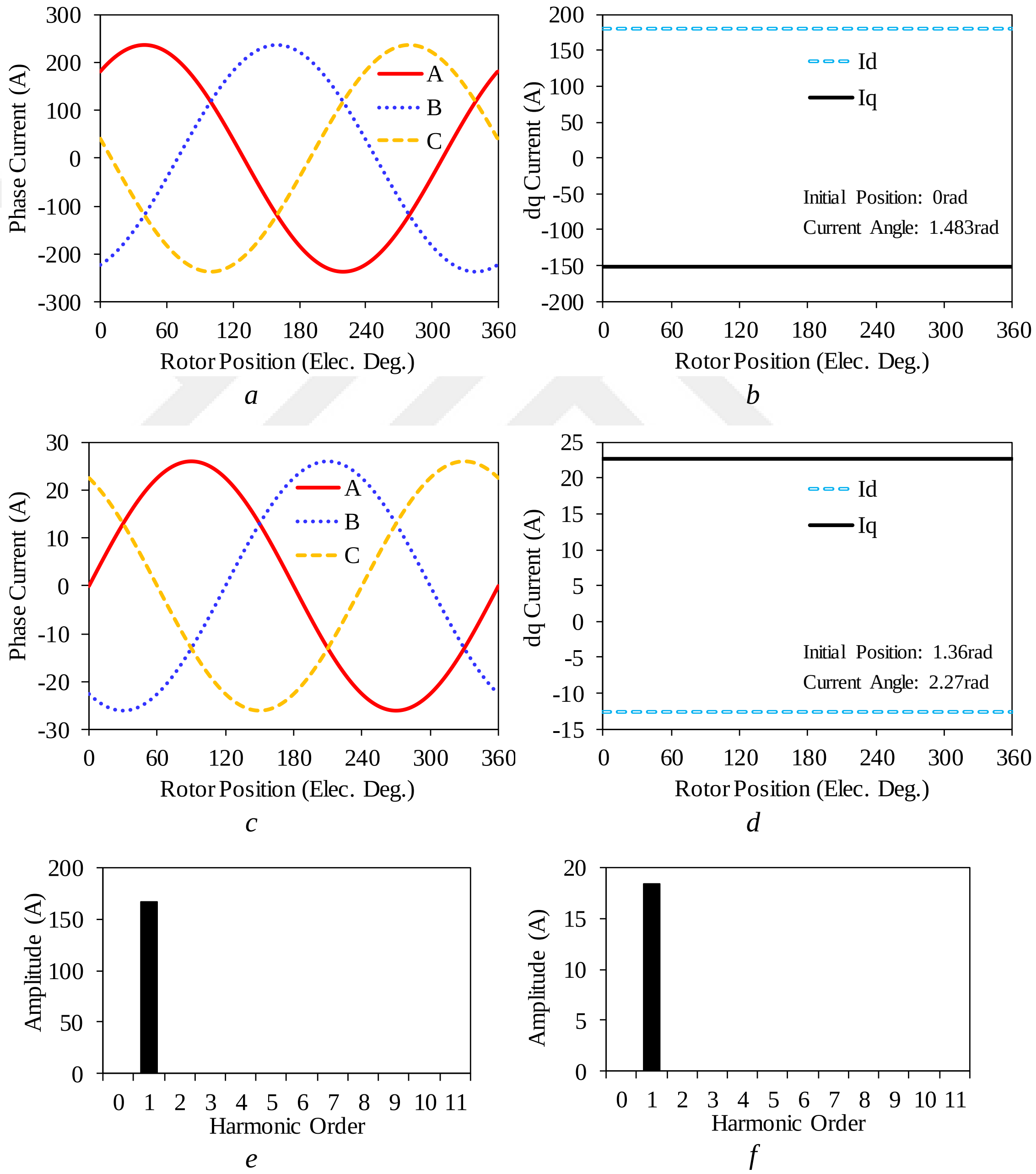


**Figure D.1.** Injected stator currents for LD and SD IPM machines: (a) Phase ABC current waveform for LD, (b) Stator *dq* currents for LD, (c) Phase ABC current waveform for SD, (d) Stator *dq* currents for SD, (e) Harmonic spectrum of (a) for LD, (f) Harmonic spectrum of (c) for SD.

**APPENDIX E**

It has been explained previously that there is not a simple explanation revealing the difference between the power factors of different machine topologies since the power factor is affected by a large number of design and operating parameters. The variation of the power factor in different designs at the fixed operating conditions (operating with the same rotor speed, excitation current, etc.) could be as a consequence of:

- Difference in magnetic circuit elements, particularly in leakage reluctances, leakage flux levels, and winding reactance;
- Different saturation levels of magnetic cores of different machines;
- Difference in flux linkage/air-gap flux density;
- Different number of turns and/or back-EMF magnitude;
- Different electromagnetic torque and hence output power;
- Different inductance magnitude and fundamental harmonic orders;
- Different phase resistance and phase current levels;
- Different power loss and efficiency levels of different machines.

The power factor $\cos\varphi$ of the designed machines have been calculated by using the expression given in (E.1), where $P_{out}$ is output power, $E_0$ is the back-EMF fundamental amplitude, $I_s$ is the rms stator current, $R_{phase}$ is the stator phase resistance, $R_c$ is the equivalent iron core loss resistance, $I_c$ is the core loss current and $\eta$ is the efficiency.

$$\cos\varphi = \frac{P_{out}}{3\left(E_0 + I_s R_{phase} + I_c R_c\right) I_s \eta} \quad \text{(E.1)}$$

The calculated power factors have been given in Table 2.5 (in Chapter 2) for *LD* (large power) machines and *SD* (small power) machines in Table 2.7 (in Chapter 2).

As clearly seen in equation (C1), the direct proportion between power factor and output power while there is an inverse proportion between power factor and the summation of terminal voltage and voltage drop due to magnetic circuit parameters, multiplied by phase current and efficiency. Please not that, to be able to simplify the explanations, the contribution of $I_c R_c$ has not been investigated in here because of it is negligibly low value when compared to level of $E_0 + I_s R_{phase}$. However, its contribution is included in the calculations for more accurate power factor values.

The key parameters affecting the power factor is summarized in Table E.1. for all considered IPMs. Please not that Table E.1. is created from the data taken from Table 2.4, 2.5, and 2.7 of the manuscript. The abbreviation Incr. indicates the increase of related parameter in percentage. Now, it can be clearly seen that the larger and longer machines have higher output power and higher power factor while small machines have lower power factor. Therefore, it can be expected that the higher power factor can be achievable with higher output power but lower phase resistance and lower back-EMF amplitude. Also, this direct correlation can easily be observed from Table E.1.

**Table E.1.** Parameters of power factor and their variation with stack length.

| | *IPM* | $l_{stack}$ (mm) | *Incr.* (%) | $R_{phase}$ (Ω) | *Incr.* (%) | $P_{out}$ (kW) | *Incr.* (%) | $\eta$ (%) | *Incr.* (%) | $E_0$ (V) | *Incr.* (%) | $\frac{L_d}{L_q}$ | *Incr.* (%) | $\cos\varphi$ | *Incr.* (%) |
|---|---|---|---|---|---|---|---|---|---|---|---|---|---|---|---|
| LD* | ISDW SL | 50.8 | | 0.101 | | 25.057 | | 78.706 | | 128.13 | | 1.51 | | 0.82 | |
| | ISDW DL | 50.8 | | 0.084 | | 24.381 | | 81.051 | | 122.82 | | 1.19 | | 0.78 | |
| | FSCW | 50.8 | 15.16 | 0.074 | 8.11 | 24.739 | 61.95 | 77.544 | 5.18 | 145.98 | 15.16 | 0.93 | 26.88 | 0.73 | 30.1 |
| | FSCW(L) | **58.5** | | 0.08 | | **40.064** | | **81.562** | | **168.11** | | 1.18 | | 0.95 | |
| | NSW | 50.8 | 10.23 | 0.079 | 5.06 | 25.025 | 40.82 | 82.231 | 4.5 | 108.6 | 10.23 | 1.73 | 5.2 | 0.89 | 9 |
| | NSW(L) | **56** | | 0.083 | | **35.239** | | **85.927** | | **119.71** | | 1.82 | | 0.97 | |
| SD** | ISDW DL | 50 | | 0.1682 | | 0.216 | | 74.814 | | 21.907 | | 0.65 | | 0.67 | |
| | FSCW | 50 | | 0.1062 | | 0.197 | | 81.895 | | 20.487 | | 0.83 | | 0.69 | |
| | NSW | 50 | | 0.1354 | | 0.195 | | 78.008 | | 18.822 | | 0.67 | | 0.68 | |

$^*I_{s_{LD}} = 236Apeak$ $\quad ^{**}I_{s_{SD}} = 26Apeak$

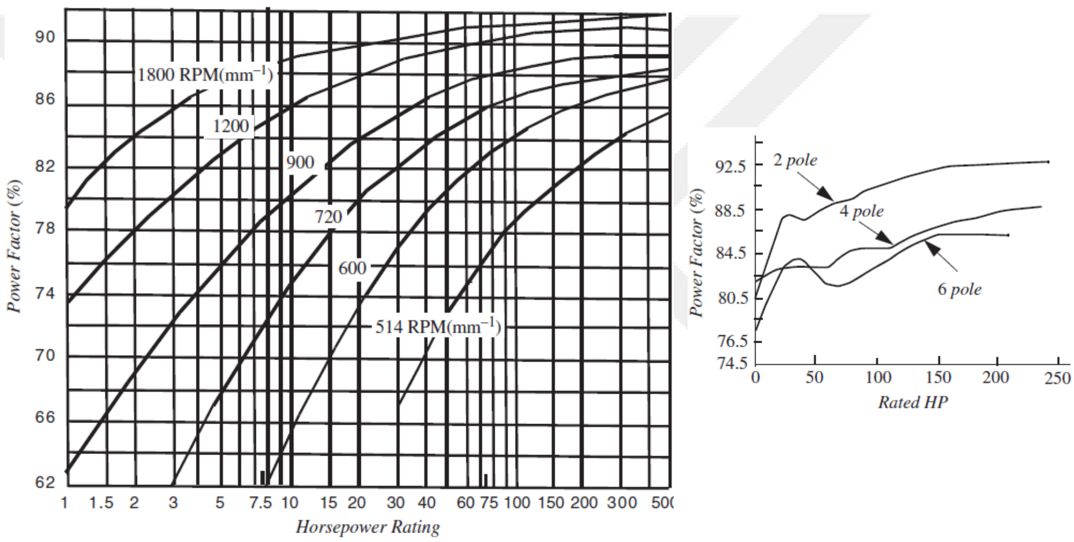


(a) (b)

**Figure E.1.** Approximate power factors[6]: (a) Approximate power factors of NEMA Class B three-phase 60-Hz induction motors, (b) Power factors of standard class B induction machines corresponding to (a).

Furthermore, it can be seen that the power levels of IPMs with SDs and LDs are quite different. As clearly shown in Figure E.1 and E.2, the higher the output power rate, the higher the power factor. This is mainly because of the fact that the IPMs having SDs have higher phase reactance and hence require much more magnetizing current [Ch2/42], [Ch2/48]. Moreover, it has been reported in Chapter 2 that a high inductance ratio ($L_d/L_q$) leads to a small current angle, and thus to a small load angle and a good

[6] P. Pillay, "Applying energy-efficient motors in the petrochemical industry," *IEEE Industry Applications Magazine*, vol. 3, no. 1, January/February 1997, 32–40.

power factor. As a consequence, the higher the $L_d$, the lower the current need to magnetize the $d$-axis, and the better the power factor. This finding is also validated in Table R.1. As clearly seen, the higher the $L_d/L_q$ ratio, the higher the power factor.

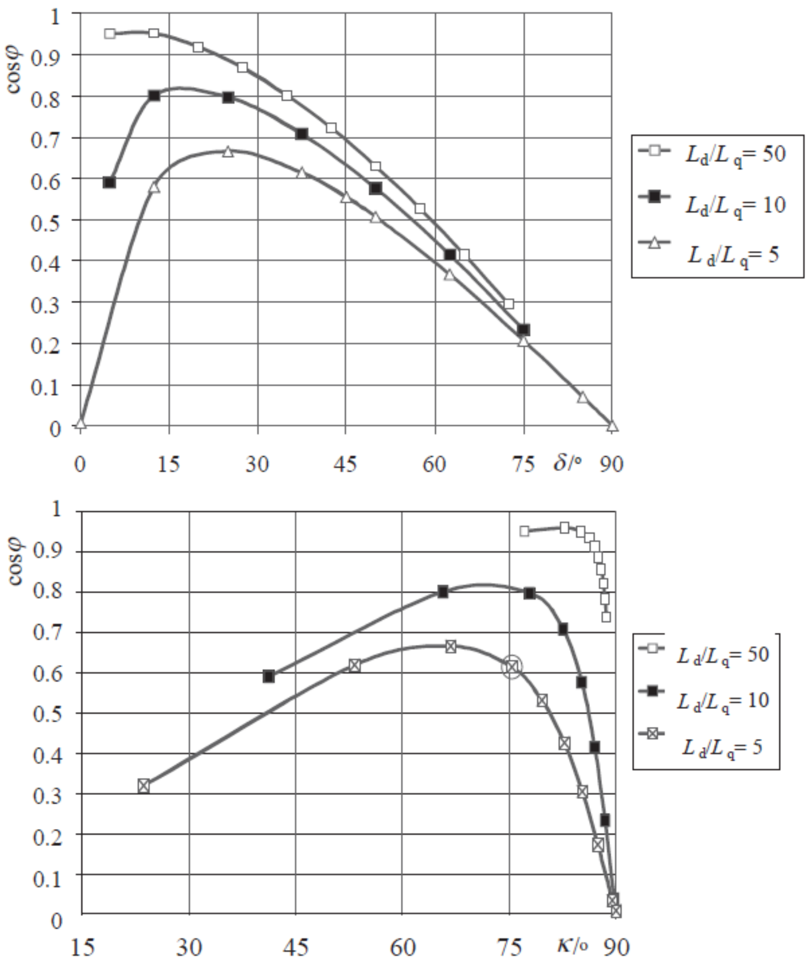


**Figure E.2**. Power factor of a synchronous reluctance machine as a function of current angle and load angle at various inductance ratios. The values are calculated for a 30kW, four-pole, 50 Hz machine. The impractical $Ld/Lq$ = 50 is indicated in the figure only for academic interest [Ch2/42] (pp-401-403).

**APPENDIX F**

In order to make a much fairer comparison, the combinations having no sub-harmonics have been chosen. Because, as known very well, the higher the MMF harmonic content, the higher the rotor losses, particularly PM loss. Although the 12S/10P combination has very high fundamental winding factor, it has both sub- and super-harmonics with very high amplitudes (please see Figure F.1). On the other hand, since $q = 0.5$ families show competitive results to the families $q \geq 1$ (any integer number) in terms of MMF harmonic content, 6S/4P combination has been selected. Alternatively, again in order to make a fair analysis, 4P combinations have been chosen for all considered machines. If the pole number is not fixed, then the comparison results will not be very fair because of significantly chancing winding factor, inductance, reluctance, etc. By keeping the pole number at the same, these factors have been limited considerably.

Another reason is that because of the low budget of the project, only a small prototype can be built. Therefore, for such a small dimension, it is not very feasible to use high pole number combinations for especially ISDW and NSW topologies, i.e. for 10-pole counterparts of ISDW and NSW topologies, at least 60-stator slots are required for 5-coil pitch (even short slot pitch). However, in order to verify the information given above, IPM having 12S10P, 15S10P (which is non-sub-harmonic counterpart of 10P family), and 6S4P have been designed by using exactly the same geometric and operating parameters and the obtained characteristics have been comprehensively compared for your consideration. Note that all the considered IPMs are optimized by using the same method presented in the major revised paper. The obtained key performance characteristics, including winding factor and MMF harmonic spectra, back-EMF, air-gap flux density, flux-line and flux density distributions, electromagnetic torque, and efficiency have been illustrated from Figure F.1 to F.5.

As clearly seen from Figure F.1, although the 12S10P has higher fundamental winding factor and MMF amplitude, its order and level of winding factor and MMF harmonics are significantly higher than those of 15S10P and 6S4P. The MMF THD level is close to almost 100% (please see also the higher order MMF harmonics in Figure F.2). Therefore, it can be predicted that these rich harmonics of 12S10P combination will cause a significant increase in the level of rotor losses, particularly PM loss component.

The 2D geometries and flux density and flux line distributions of the designed IPMs are illustrated in Figure F.3. As clearly seen, there are some local saturations, particularly stator toot tip and rotor flux bridge parts. Figure F.4 presents the key electromagnetic performance characteristics including back-EMF, air-gap flux density, $dq$-axes inductances, and torque. As can be seen, the distortion level of the

10P combinations are lower than that of the 6P. This is due to the reduced effect of slotting. On the other hand, considering the peak to peak variation of *dq*-axis inductances, it can be concluded that the saturation level of 4P IPM is higher than the others. As expected, under the same number of turns per phase and phase current amplitude, the time averaged torque of 12S10P IPM is the highest due to its higher fundamental winding factor (see Fig. D.1(b) and Fig. D.4(f)). On the other hand, although the 15S10P and 6S4P has the same fundamental winding factor amplitude, 15S10P has higher torque. This is because of its lower saturation level and consequently higher reluctance toque component.

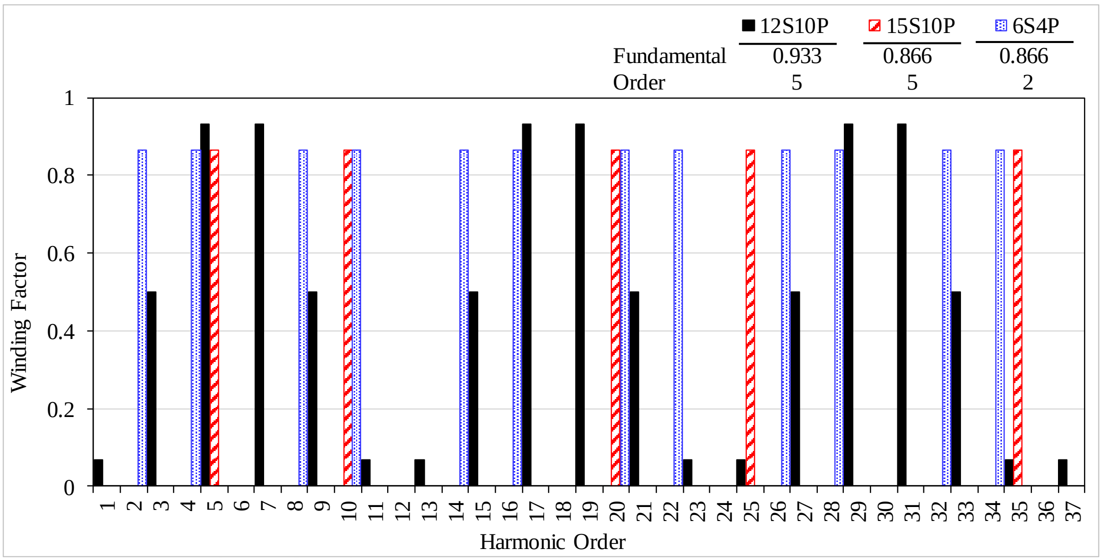


(a)

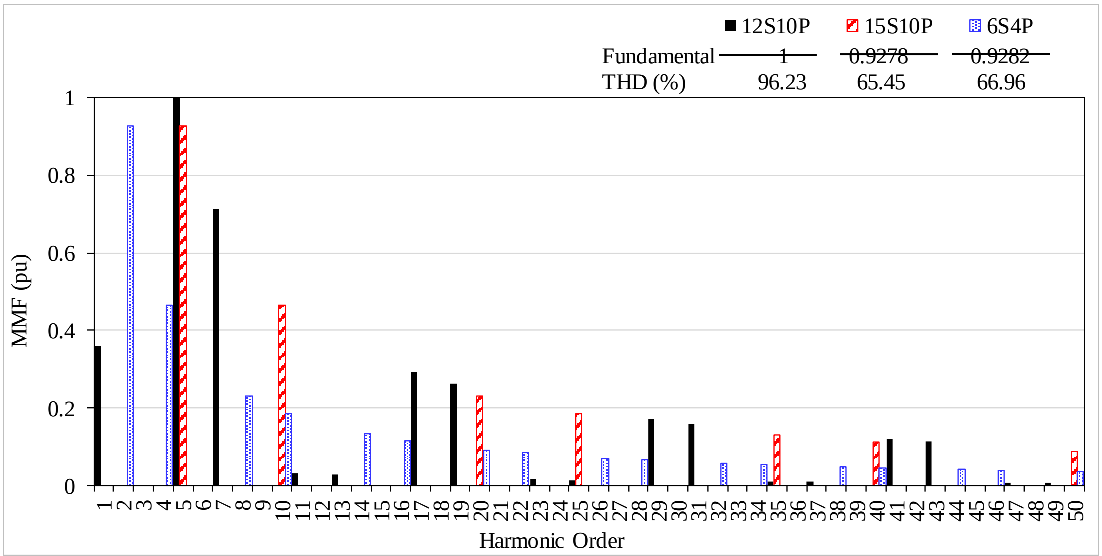


(b)

**Figure. F.1 :** Winding factor and MMF harmonic comparison for different S/P combinations: (a) Comparison of winding factor harmonics; (b) Comparison of MMF harmonics.

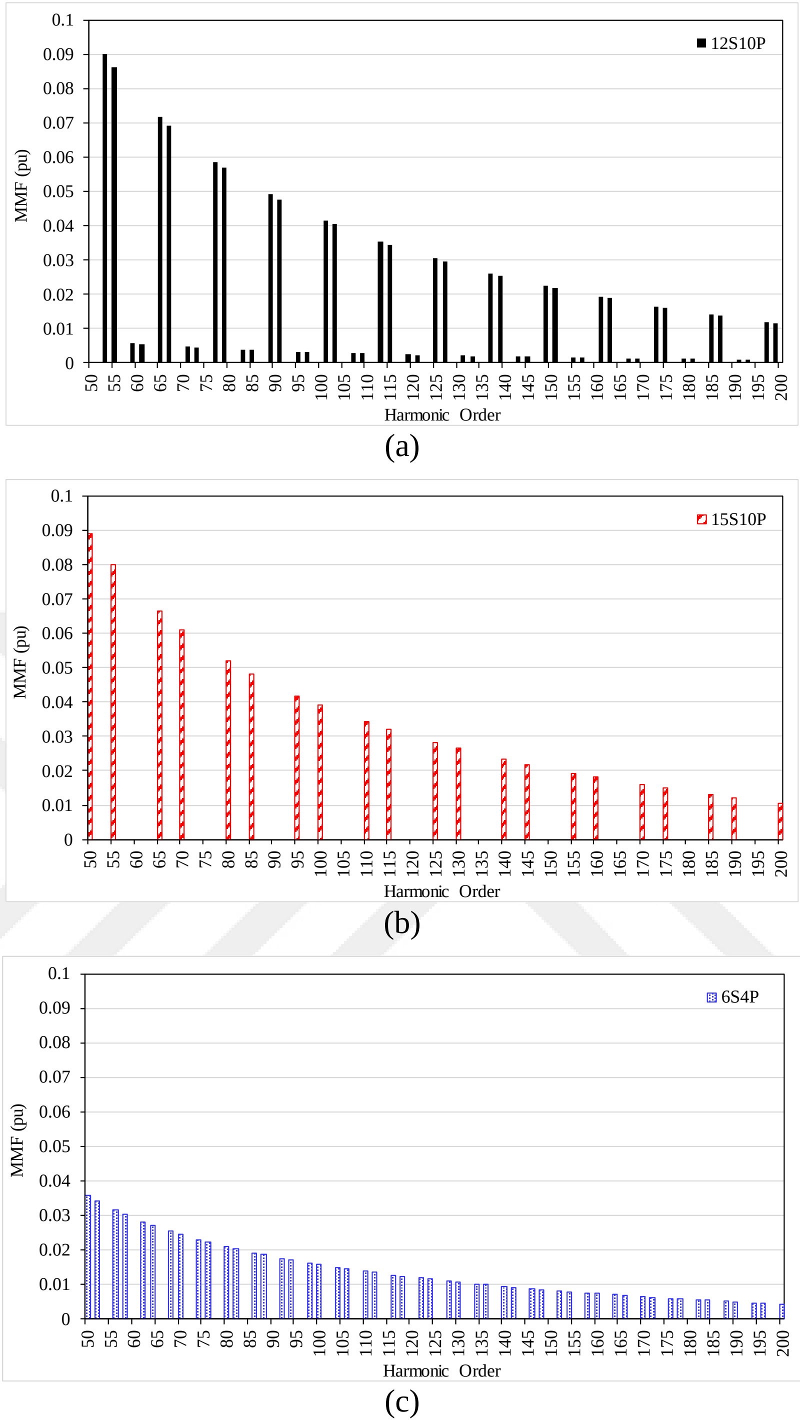


**Figure F.2 :** High order MMF harmonics of different S/P combinations (a) 12S10P; (b) 15S10P; (c) 6S4P.

Finally, the power losses and efficiency of the IPMs are illustrated in Fig. D.5. Since the same number of turns, slot fill factor, and current density is assigned for all the machines, their copper losses are similar. However, since the 10P combinations have shorter end-winding lengths, they have lower end-winding copper losses. It is obvious that the 12S10P has the highest core and PM losses due to its high MMF harmonic content. Note that, 10P combinations have 20 pieces of PMs while 4P combination has

8 pieces only. Therefore, the eddy current amplitude in the PMs of the 6S4P IPM is 2.5 times higher than that of 15S10P IPM. That is why no sub-harmonic counter part of 12S10P combination, which is 15S10P, is considered in the analyses. As clearly seen in Figure F.5(b), under the same amount of PM pieces, the 15S10P IPM has significantly low PM loss than that of 12S10P IPM. As a result, the high PM loss of 6S4P is not due to the MMF harmonics, it is a consequence of low piece of PMs. In conclusion, although the output power of the 15S10P IPM is quite lower than that of 12S10P, it has higher efficiency due to lower PM loss.

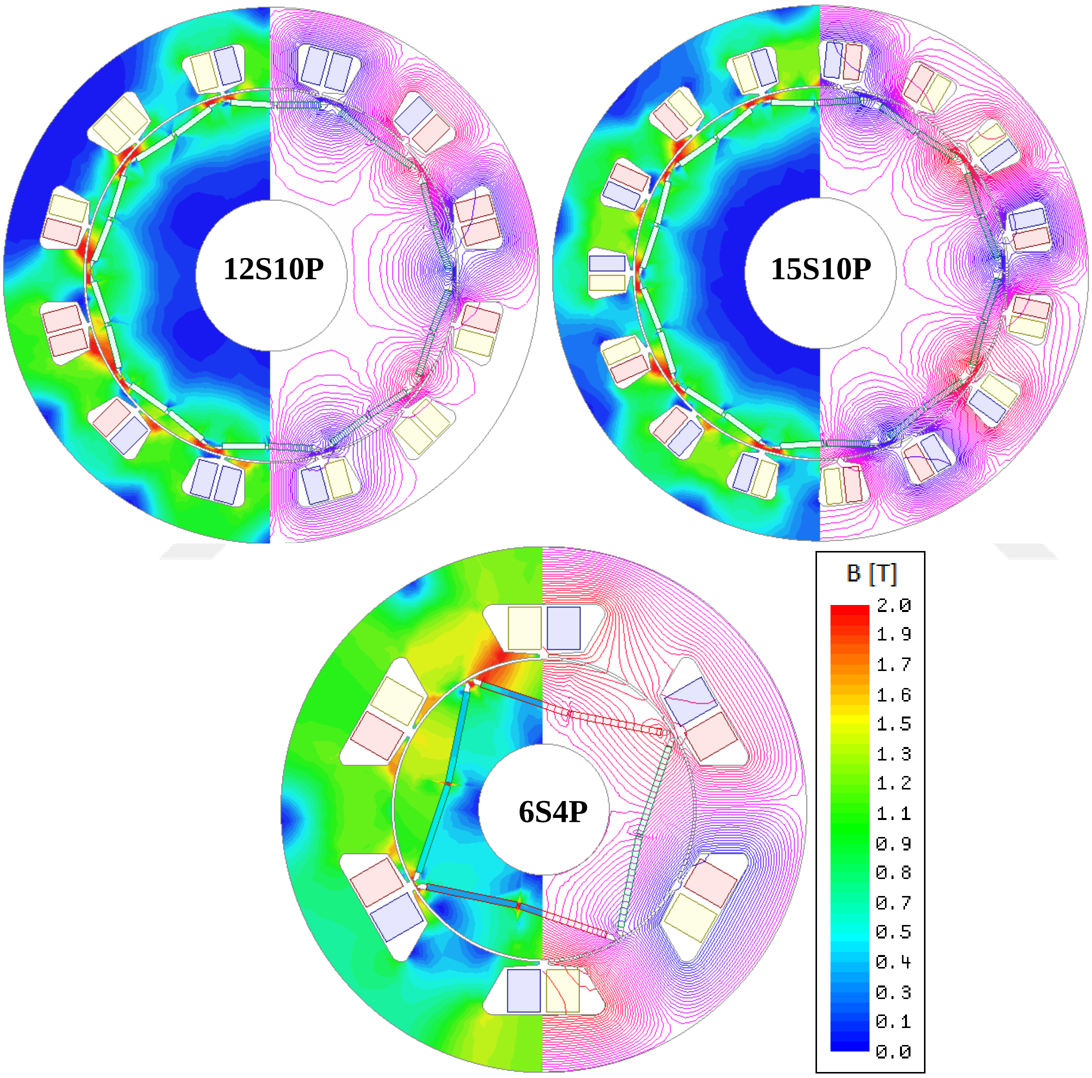


**Figure F.3 :** Flux density and flux line distributions of IPMs having different S/P combinations.

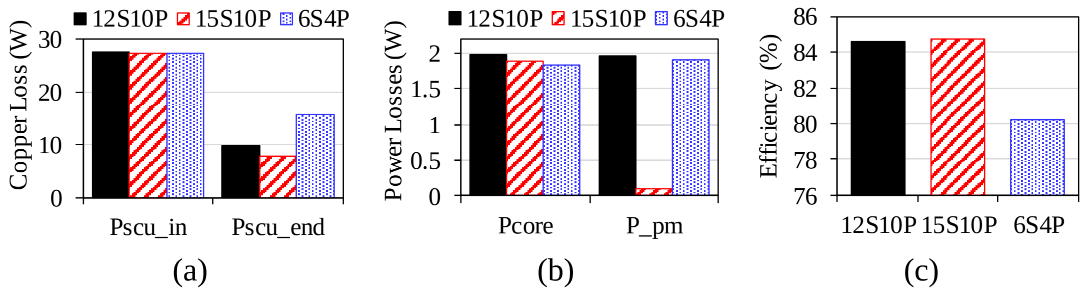


**Figure F.4 :** Comparison of power losses and efficiency for considered IPMs: (a) Copper loss; (b) Core and PM losses; (c) Efficiency.

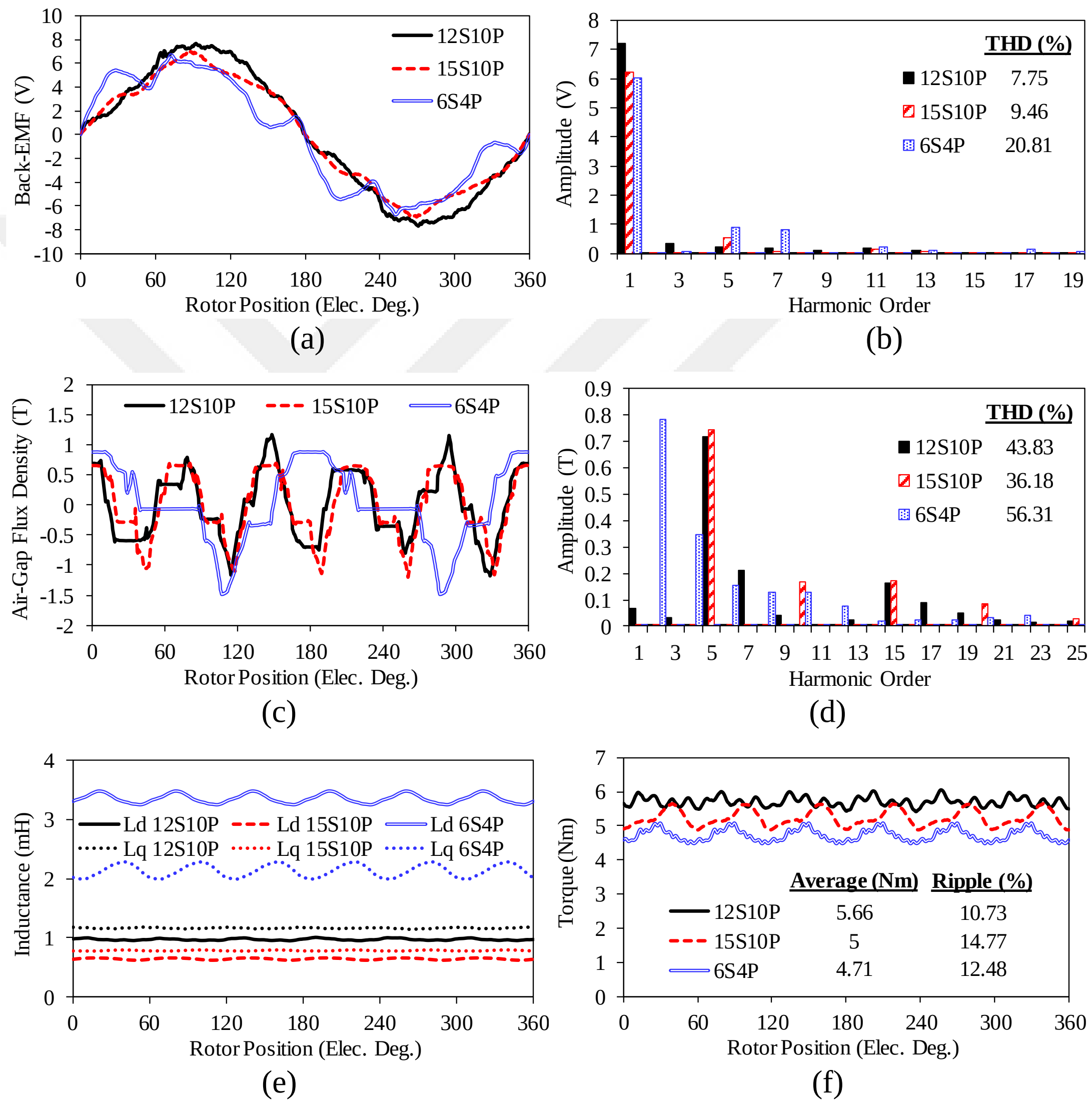


**Figure F.5 :** Comparison of performance characteristics of IPMs having different S/P combinations: (a) Back-EMF waveform; (b) Harmonic spectra of back-EMF; (c)Air-gap flux density waveform; (d) Harmonic spectra of air-gap flux density; (e) dq-axis inductance waveform; (f) Electromagnetic waveform.

## APPENDIX G

The order of the torque ripple is related to the interaction between the stator slot number and pole number. The order of the torque ripple $O_{\Delta T}$ can be predicted by using (G.1) as follows.

$$O_{\Delta T} = \frac{S}{p} \rightarrow \text{for ISDW and NSW}$$
$$O_{\Delta T} = S \rightarrow \text{for FSCW} \tag{G.1}$$

where $S$ is the slot number and $p$ is the pole pair number. As clearly seen in Figure G.1 (which is the zoomed version of Fig, 16 in the manuscript), the torque ripple order of the machines with ISDW and NSWs are 12 (360° Elec. Deg.) while it is 6 for FSCW. This is because of the fact that the FSCW has one phase winding per tooth while others have not. If Figure G.1 is investigated closely, it can be revealed that the expressions in (G.1) are consistent.

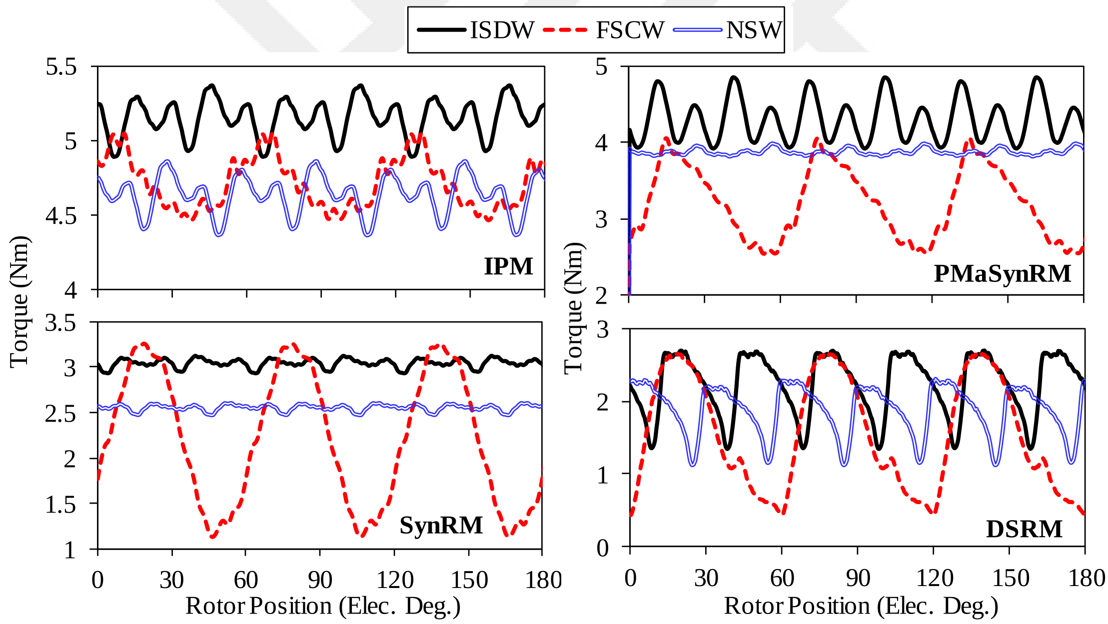


**Figure G.1 :** Variation of torque $T_e$ with respect to rotor position.

## APPENDIX H

It is a fact that the proposed winding topology is difficult to manufacture because of its different number of turns per coil arms. Some other key disadvantages of the NSWs over FSCWs are given as follows.

- *Slightly lower winding factor than ISDW and FSCW counterparts*: requires slightly a greater number of turns to generate the same amount of torque with its ISDW and FSCW counterparts under the same amount of phase current excitation. However, due to higher reluctance torque component of the NSW, it can generate higher electromagnetic torque than its FSCW counterpart.
- *Difficulty in manufacturing*: Increased manufacturing process time and cost

Nevertheless, as presented in Chapter 3, the disadvantages of similar winding topologies presented in [35]-[38] of Chapter 3 and summarized as follows have been eliminated successfully thanks to the proposed NSW topology.

- Fairly low (usually <0.63) fundamental winding factor (the proposed NSW has minimum 0.834);
- the number of turns between the winding sets are restricted to a constant rate, otherwise it is impossible to cancel/reduce the MMF harmonic content;
- half of the stator slots have not been fully filled causing to obtain quite low torque/power density and efficiency.

In addition, the winding layout of the NSW seems to be comparable to a conventional winding layout known as "concentric winding"[7,8,9] as shown in Figure H.1. The differences are: (i) different number of turns per coil arm; (ii) only some coils are over-lapped i.e. for 12-coils winding, only 2-coils are overlapped.

---

[7] Buksnaitis, J.J.: 'Sinusoidal three-phase windings of electric machines'. (Springer Press, Cham, Switzerland, 2016)
[8] Pyrhonen, J., Jokinen, T., Hrabovcova, V.: 'Design of rotating electrical machines' (Wiley and Sons Ltd., West Sussex, 2007, 2nd edn. 2013)
[9] Hendershot, J.R., T.J.E. Miller: 'Design of brushless permanent-magnet machines' (Motor Design Book LLC, Florida, 2010)

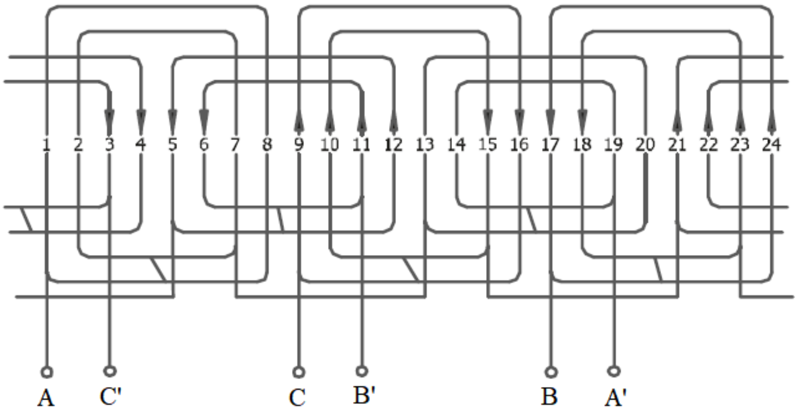

**Figure H.1 :** Winding layout of a concentric winding.

## APPENDIX I

The slot fill factor is copper packing factor. In other words, it indicates the occupancy rate of stator slots. A winding topology with high slot fill factor is favourable due to its tremendous advantages over winding topologies with low slot fill factor, such as high-power density or improved efficiency, high torque density, etc. However, achieving high slot fill factor is not easy since it requires segmented stator structure and prepressed windings.

One of the key advantages of FSCW (non-overlapping winding) is the ability to achieve significantly higher copper slot fill factor (compared to conventional laminated stator structures) if coupled with segmented stator structures particularly if the windings are prepressed [10,11]. This can have a significant impact on the machine power density. Jack et al.[7] reported a significantly high slot fill factor (ratio of copper area to total slot area) of ∼78% by using 450MPa pressed preformed windings known as “soft magnetic composite (SMC) structures”, as shown in Fig. G.1. Furthermore, Akita et al. reported a 75% slot fill factor using a “joint-lapped core” (please see Fig. G.2). On the other hand, as a natural consequence of overlapping between the phase coils of ISDWs, it is neither possible to use prepressed coils nor segmented stator structures.

In Chapter 3, it is reported that compared to the FSCW configurations, the integer-slot distributed winding (ISDW) configurations have lower copper packing (fill) factor since prepressed windings with segmented stator structures cannot be used, and have longer end-winding length, higher cogging torque, and less fault tolerant owing to higher mutual inductance and winding overlapping.

As presented in Chapter 3, the slot fill factor of NSW topology is moderate when compared to overlapping and non-overlapping windings. For NSW topology, a high slot fill factor is required due to the increased winging layer and hence phase winding insulation material. As can be seen from Figure I.1, the proposed NSW topology has 3 winding layers. Therefore, it requires more fill factor that that of ISDWs (considering both windings having the same number of turns per coil will be placed into same stator slot). However, since a large number of windings coils are non-overlapping, partly prepressed windings can be used. Therefore, a higher slot fill factor according to overlapping windings can be achieved as evidenced from the prototype. We achieved 51.5% fill factor.

---

[10] EL-Refaie, A.M.: ‘Fractional-slot concentrated-windings synchronous permanent magnet machines: opportunities and challenges’, IEEE Trans. Ind. Electron., 2010, 57, (1), 107–121

[11] Tangudu, J.K., Jahns, T.M.: ‘Comparison of interior PM machines with concentrated and distributed stator windings for traction applications’. IEEE Vehicle Power Propulsion Conf. (VPPC'11), Chicago, 2011, 1–8

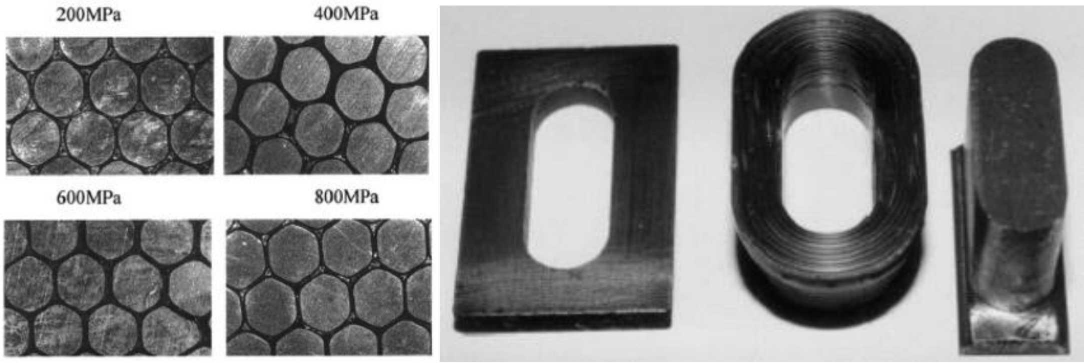


(a) Coil sections: Pressing trial results (b) Manufactured core components and coil

**Figure I.1 :** Segmented stator structure with coil sections and stator core components and coils [12].

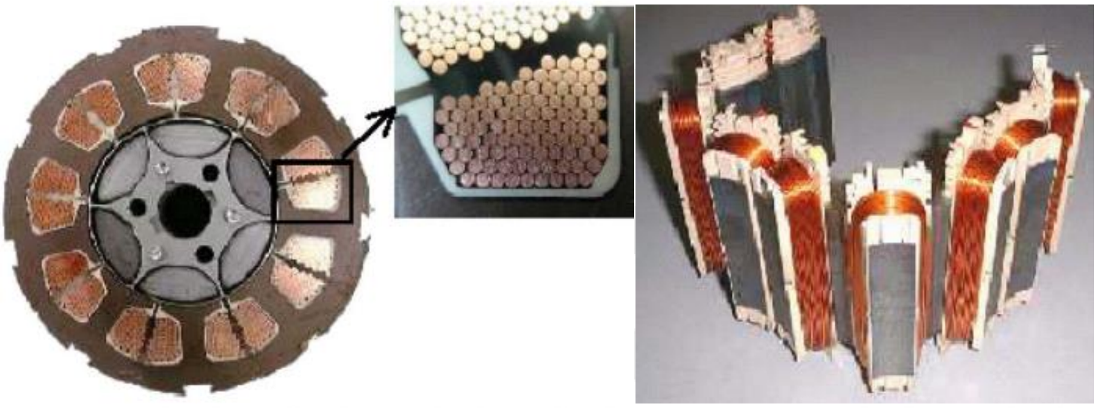

(a) Cross section of a joint-lapped core machine (b) Joint-lapped core after winding

**Figure I.2 :** Joint-lapped stator structure with pressed coils and stator components [13].

[12] Jack, A.G., et al:, 'Permanent magnet machines with powdered iron cores and pre-pressed windings'. IEEE Ind. Appl. Conf. Thirty-Forth IAS Annual Meeting, Phoenix, 1999, 97-103. doi: 10.1109/IAS.1999.799934

[13] Akita, H., Nakahara, Y., Miyake, N., Oikawa, T.: 'New core structure and manufacturing method for high efficiency of permanent magnet motors'. 38th IAS Annual Meeting of Ind. Appl. Conf., Salt Lake City 2003, 367-372. doi: 10.1109/IAS.2003.1257527

## APPENDIX J

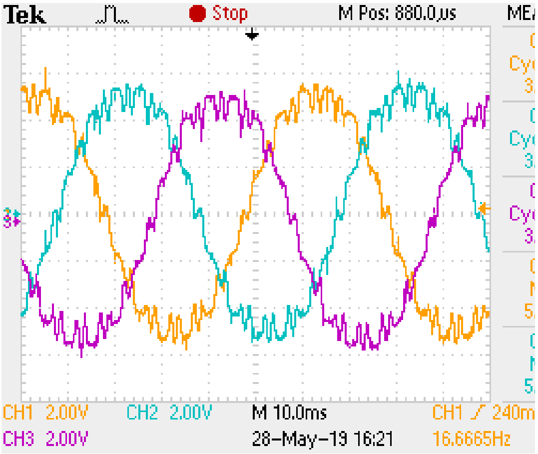


500rpm

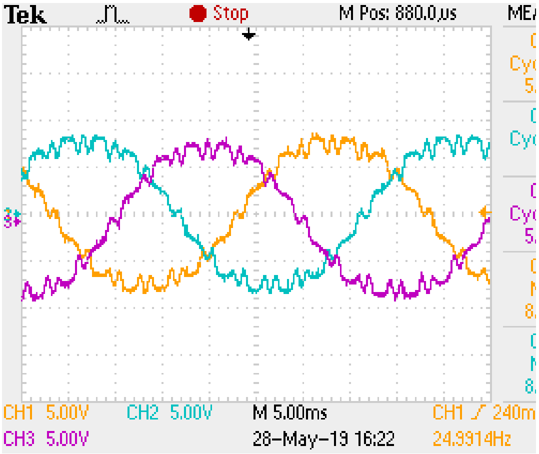


750rpm

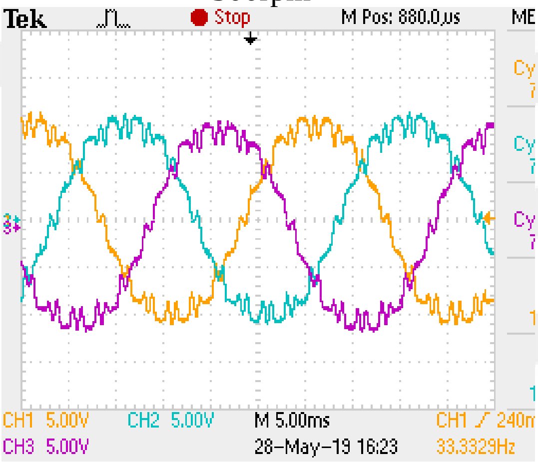


1000rpm

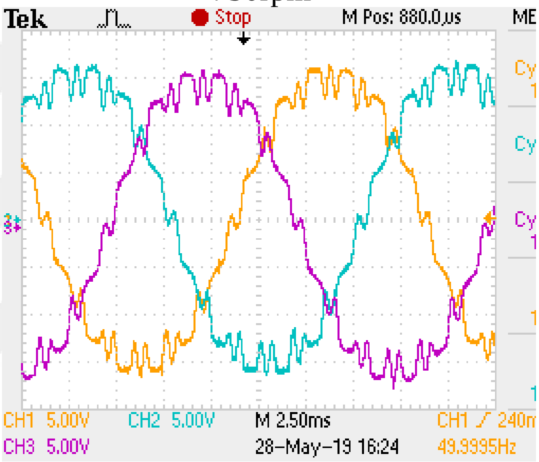


1500rpm

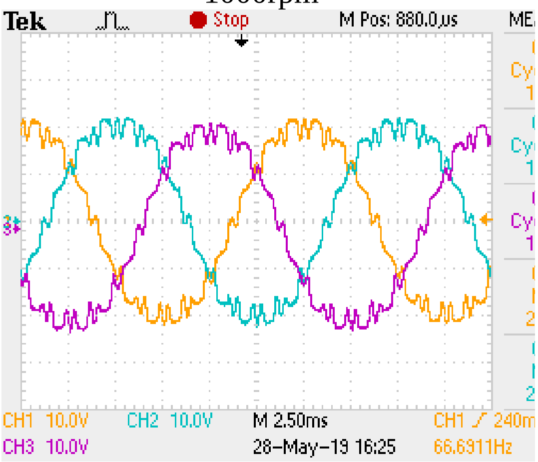


2000rpm

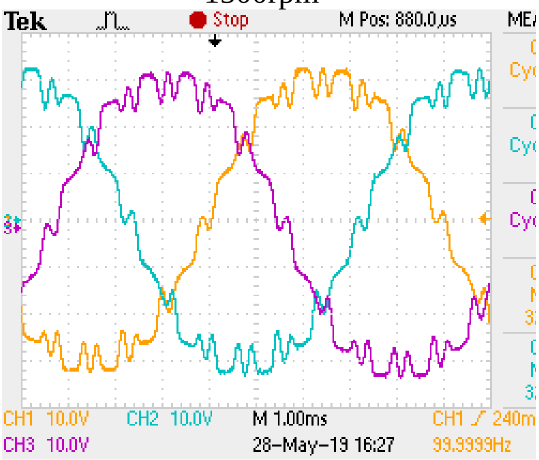


3000rpm

**Figure J.1 :** Oscilloscope screen shots under no-load operating for different speeds.

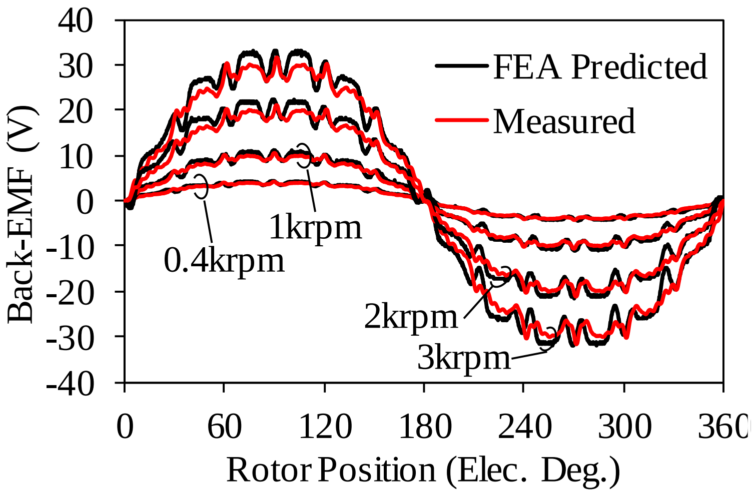


**Figure J.2 :** Back-EMF waveform comparison for different speed at no-load operating condition.

## APPENDIX K

The considered design parameters are chosen as a result of experience gained through numerous investigations and comprehensive literature presented in Chapter 5. On the other hand, following table is created for simply clarifying the unconsidered parameters and reasons underlaying.

**Table K.1 :** Unconsidered parameters and underlying causes

| ***Parameter*** | ***Reason*** |
|---|---|
| Stator outer diameter | • It will affect the complete behaviour of the machine as being in influence of number of turns and stack length (see Figure 5.6). It can be predicted that the higher the stator outer diameter, the better the electromagnetic performance characteristics;<br>• The individual effect of stator outer diameter cannot be investigated since it will affect all the geometrical parameters. |
| Stator slot geometry | • Considering the number of turns, current density, and magnetic saturation level, very limited range can be investigated;<br>• Effects too many design parameters such as number of turns, phase voltage and current, slot fill factor, current density, slotting effect, etc. |
| Shaft diameter | • It is determined by the mechanical constrains;<br>• Trivial effect can be predicted. |
| Air-gap length | • It will affect the complete behaviour of the machine as being in stack length (see Figure 5.6);<br>• Limited by mechanical constraints. |
| $D_2$ | • Minimum value is determined by mechanical constraints;<br>• Maximum value causes a significant amount of leakage flux; hence a poor performance can be predicted. |
| $HR_{ib}$ | • It has similar effect with $B_1$ parameter. |
| $w_s$ | • Considering the dimensions of PMs (which fixed for all analyses), very limited range can be investigated;<br>• It can be predicted that the large values can cause a significant increase in the level of flux leakage and consequently increases the saturation level of rotor. |

## CURRICULUM VITAE

**Name Surname** : Tayfun GÜNDOĞDU

**Place and Date of Birth** :

**EDUCATION** :

- **B.Sc.** : 2009, Gazi University, Technical Education Faculty, Electrical Education Department.
- **M.Sc.** : 2012, Istanbul Technical University, Faculty of Electrical and Electronics Engineering, Electrical Engineering Department.
- **Ph.D.** : 2018, The University of Sheffield, Faculty of Engineering, Department of Electronic and Electrical Engineering.

**PUBLICATIONS, PRESENTATIONS AND PATENTS ON THE THESIS:**

- **Gundogdu, T.** and Komurgoz, G. 2019 Investigation of winding MMF harmonic reduction methods in IPM machines equipped with FSCWs, *Int. Trans. Elect. Energy Syst*, *29*(1), e2688, 1-27.
- **Gundogdu, T.** and Komurgoz, G. 2019 Design of interior permanent-magnet machines with novel semi-overlapping windings, *Global Power, Energy and Communication Conference (GPECOM)*, Cappadocia, Turkey, 180-187.
- **Gundogdu, T.** and Komurgoz, G. 2020 Design and analysis of interior permanent magnet machines equipped with novel semi-overlapping windings, *IET Elect. Power Appl.*, *14*(8), 1446-1457.
- **Gundogdu, T.** and Komurgoz, G. 2020 Comparative study on performance characteristics of pm and reluctance machines equipped with overlapping, semi-overlapping, and non-overlapping windings, *IET Elect. Power Appl.*, *14*(6), 991-1001.
- **Gundogdu, T.** and Komurgoz, G**.** 2021 A systematic design optimization approach for interior permanent magnet machines equipped with novel semi-overlapping windings, *Struct. Multidis. Optim.*, *63*(3), 1491-1512.

- **Gundogdu, T.** and Komurgoz, G. 2020 Influence of design parameters on flux-weakening performance of interior permanent magnet machines with novel semi-overlapping windings, *IET Elect. Power Appl.*, *14*(13), 2547-2563.

**OTHER PUBLICATIONS, PRESENTATIONS AND PATENTS:**

- **Gundogdu, T.**, Zhu, Z.Q., and Mipo, J.C. 2020 Analysis of coil pitch in induction machines for electric vehicle applications, *IET Electric Power Appl.*, *14*(12), 2525-2536.
- **Gundogdu, T.**, Zhu, Z.Q., Mipo J.C. and Personnaz, S. Influence of stator and rotor geometric parameters on rotor bar current waveform and performance of IMs, *J. Eng*, *2019*(17), 3649-3654.